AD NUMBER

AD857343

NEW LIMITATION CHANGE

TO

Approved for public release, distribution unlimited

FROM

Distribution authorized to U.S. Gov't. agencies and their contractors; Administrative/Operational Use; Feb 1969. Other requests shall be referred to Air Force Rocket Propulsion Lab., Edwards AFB, CA 93523.

AUTHORITY

AFRPL ltr, 29 Sep 1971

AFRPL TR-69-89

URS 706-5

HEAT TRANSFER HAZARDS OF LIQUID ROCKET PROPELLANT EXPLOSIONS

Final Report February 1969

PREPARED UNDER
CONTRACT F04611-69-C-0004

FOR
AIR FORCE ROCKET PROPULSION LABORATORY
AIR FORCE SYSTEMS COMMAND
UNITED STATES AIR FORCE
EDWARDS, CALIFORNIA

URS SYSTEMS
CORPORATION

965

AFRPL TR-69-89

URS 706-5

HEAT TRANSFER HAZARDS OF LIQUID ROCKET PROPELLANT EXPLOSIONS

Final Report February 1969

by
Joseph A. Mansfield

URS RESEARCH COMPANY
1811 Trousdale Drive
Burlingame, California 94010

PREPARED UNDER
CONTRACT F04611-69-C-0004

FOR
AIR FORCE ROCKET PROPULSION LABORATORY
AIR FORCE SYSTEMS COMMAND
UNITED STATES AIR FORCE
EDWARDS, CALIFORNIA

FOREWORD

This report was prepared by URS Research Company, Burlingame, California, under Air Force Contract F04611-69-C-0004. The work documented herein constitutes a part of an extensive experimental program, designated Project PYRO, which was devoted to improving the definition of the potential hazards of liquid rocket propellant explosions. Project PYRO was jointly sponsored by the Air Force, NASA, and AEC (Sandia Corporation), and was conducted at the Air Force Rocket Propulsion Laboratories, Edwards Air Force Base, California.

Project PYRO was initiated in August 1963 under the direction of Dr. John B. Gayle of the NASA Marshall Space Flight Center. The AFRPL Program Managers have been Mr. Charles R. Cooke, Mr. John Marshal, and Mr. Robert L. Thomas. General management was also provided by Mr. Bill Richl of the NASA Marshall Space Flight Center, Mr. Paul King and Mr. John Atkins of the NASA Kennedy Space Center, Mr. Louis Ullian of the Air Force Eastern Test Range, and Mr. Frank Kite of the Sandia Corporation. URS Research Company provided analytical services and experimental design, with Mr. A. B. Willoughby the principal investigator and Mr. C. Wilton the program manager.

The propellant explosion hazards considered in Project PYRO were primarily those associated with the blast or shock wave generated by the explosion and, with less priority, the heat transfer or thermal hazards associated with the fireball created by the explosion. This report pertains solely to and is a summary of the thermal hazards.

This technical report has been reviewed and approved.

ABSTRACT

An extensive experimental program, designated Project PYRO, was conducted in order to improve the definition of the hazards associated with liquid rocket propellant explosions. This report is a summary of the thermal or heat transfer measurements from this program. Tests were conducted with propellant quantities ranging from 200 to approximately 100,000 lb for the propellant combinations of LO_2/RP-1 and LO_2/LH_2, and up to 1000 lb for the hypergolic propellant combination of N_2O_4/50% UDMH-50% N_2H_4. From measurements within the fireball, data are given for the total (convective plus radiant) heat flux density, radiant flux density, and fireball temperature, and – from remote measurements – for the fireball temperature (photo-pyrometric) and radiant flux density. The total heat flux density was evaluated through computation from surface temperature vs time measurements of metal slabs; an error analysis of this technique is included. Curves representing conservative upper bounds of the total heat flux density vs time for a given propellant type and quantity are developed from the data. A recommended procedure for extrapolating these curves to comparatively large propellant quantities is given, along with the basis and limitations of extrapolation.

ACKNOWLEDGEMENTS

The author wishes to particularly acknowledge the assistance of Mr. James Wanchek, Mr. Robert L. Thomas, and Mr. Richard E. McQuown of the Air Force Rocket Propulsion Laboratories, Edwards Air Force Base, California. Mr. Wanchek was intimately involved in virtually all phases of thermal program planning and instrument design. Mr. Thomas provided invaluable technical and administrative support and gave substantial assistance and advice in the writing of this report.

I wish also to express appreciation to Mr. Frank Kite of the Sandia Corporation, Albuquerque, New Mexico, for assistance gained through our many technical conversations, as well as thanks for the fireball temperature data that Mr. Kite, as representative of the Sandia Corporation, obligingly provided.

Especial acknowledgement is certainly also made of the role of Mr. A.B. Willoughby of URS Research Company, who originally proposed inclusion of thermal measurements in the total program and who is chiefly responsible for the initial technical planning of the thermal portion of the program.

CONTENTS

ILLUSTRATIONS

ILLUSTRATIONS (Continued)

TABLES

Section 1
INTRODUCTION

With the comparatively large quantities of liquid propellants that are now contained in missiles and aerospace vehicles, the need arose for an improvement in the definition of the potential hazards of liquid propellant explosions which may occur during the launch or pre-launch operation. To satisfy this need, an experimental program (Project PYRO) was undertaken to determine the dependence of the blast or shock wave hazards on various test conditions, and – with lesser priority – to evaluate the heat transfer or thermal hazard. This report pertains solely to the thermal hazards portion of this program. The overall program is described in Ref. 1.

The objective of the thermal portion of the study was to make measurements which would enable "reasonable" bounds to be placed on, or which would substantiate theoretical predictions of, the heat transfer to objects in and about the "fireball" created by liquid propellant explosions. Residual fires are not included.*

The PYRO program was composed of over 300 propellant tests. In each test, quantities of fuel and oxidizer were permitted to flow together and mix under any of several controlled conditions and the mixture ignited at a selected time. The quantity of propellants per test ranged from 200 to about 100,000 lb for the cryogenic propellant combinations of liquid oxygen/RP-1 (LO_2/RP-1) and liquid oxygen/liquid hydrogen (LO_2/LH_2), and a comparatively few tests were conducted at the 200- and 1000-lb levels with the hypergolic propellant nitrogen tetroxide/50% unsymmetrical dimethylhydrazine-50% hydrazine (N_2O_4/50% UDMH-50% N_2H_4).

---

*For thermal hazards of residual fires see, for example, Ref. 2.

The major test condition categories considered for the thermal analysis were the propellant type, propellant weight, propellant configuration, and ignition time.* Ignition time is defined as the time from commencement of propellant mixing to ignition of the mixture. There were two basic propellant configurations, termed the confinement-by-the-missile (CBM) configuration, and the confinement-by-the-ground-surface (CBGS) configuration. For the CBM case, a portion of the internal diaphragm or intertank bulkhead that initially separates the fuel and oxidizer was rapidly removed, thereby permitting the propellants to commence mixing within their tankage. The propellant mixture was ignited at or prior to tank rupture, which would eventually occur as a result of the pressure rise that is created by the mixing of the propellants. For the CBGS case, the propellants were permitted to spill from the tankage and spread (and mix) along the ground surface prior to their ignition. The testing sequence for this case was typically as follows: the propellant tank was dropped from a tower (from a height of from 10 to 100 ft); when the tank was a few feet above the ground surface, both the internal tank diaphragm that separates the fuel and oxidizer and the bottom of the tank were rapidly removed; finally the tank motion was stopped about one tank diameter above the ground surface, thereby permitting the propellants to impact with and disperse radially along the ground surface with an initial velocity that depended on the height of drop. Three velocities (22, 44, and 77 ft/sec) were tested, and velocity constituted a secondary test condition under the CBGS case.

One further secondary test condition should be mentioned. For most CBM tests, both the fuel and oxidizer tank compartments were filled to within a few percent of their capacity. For a few tests (for one of which there are thermal data), both the fuel and oxidizer were at about two-thirds capacity. The result of this reduction was to increase the magnitude of the explosion.

---

*The test conditions considered in this report do not include all those described in Ref. 1 (the general documentation of Project PYRO) because thermal data were either not obtained or not analyzed for all cases tested. In addition, the emphasis in descriptions differ since factors that affect blast hazards are not always of importance to heat transfer.

The contents and organization of this report are as follows:

- Section 2 is a general discussion describing the fireball characteristics, the nature of the heat transfer within the fireball, and the general experimental approach that was taken.
- Section 3 contains a brief summary of the instrumentation. (A more detailed description of the thermal instrumentation is presented in Appendix A.)
- Section 4 is the presentation of results.
- Section 5 is a brief summary of the results.
- Appendix A consists of a detailed description of the thermal instruments, their mounting and location, and the errors of the associated measurements.
- Appendix B contains the basic thermal data records. Data are given regarding the:
  (1) Heat flux density into slabs immersed in the fireball for the 200-, 1000-, and 25,000-lb tests and the Titan test.
  (2) Radiant flux density within the fireball for the 25,000-lb tests.
  (3) Radiant flux density outside the fireball from the 25,000-lb and Titan tests.
  (4) Temperature of thermocouple probes selected from the 25,000-lb test data.
- Appendix C lists the symbols used in this report and their definitions.

The expressions "heat flux density," "total heat flux density," "heat flux," and "flux density" are used interchangeably and represent the energy per unit area per unit time transported through a material surface due to both the radiant and convective modes of heat transfer. Similarly, the expressions "radiant flux density" and "radiant flux" represent the energy in radiant form per unit area per unit time.

It should be noted that the Sandia Corporation obtained and provided the pyrometric gas temperature data and the thermocouple probe data that are presented in this report.

Section 2
GENERAL DISCUSSION

CHARACTERISTICS OF THE FIREBALL

The size, duration, and gross motion of the propellant fireball depends on the total quantity of propellants. During its growth and the early stages thereafter, the fireball from a propellant mixture on or near the ground surface is more or less hemispherical, reaching a maximum diameter that is approximately proportional to the cube root of the propellant weight. More specifically, an empirically derived expression relating the maximum diameter D (in feet) to the total propellant weight W (in pounds) is given by*

$$D = 9.56\ W^{0.325} \qquad (2.1)$$

where the estimated standard error of the diameter is 30 percent. Thus, diameters, for instance, for 1,000 and 1,000,000 lb are about 93 and 850 ft, respectively. It is emphasized, however, that Eq. (2.1) does not always indicate maximum fireball dimensions, in part, because it was derived on the basis that "in those instances where the fireballs were markedly asymmetrical, attempts were made to estimate equivalent spherical diameters."** Moreover, in the tests from which Eq. (2.1) was obtained, there was a tendency for the spatial dispersal of propellants prior to their ignition to be less extensive than can practically occur, and comparatively extensive dispersal can lead to correspondingly large maximum dimensions. Larger fireballs would tend to result from propellant spills, for instance, if the propellants spread sufficiently along the ground surface prior to their ignition. The Titan test (involving about 100,000 lb of LO_2/RP-1) provides an illustration, first, of the departure of the maximum dimensions that can occur from the diameter given by Eq. (2.1), and second, of still another

---

* Equations (2.1) and (2.2) have been extracted from Ref. 3. The equations were obtained through the statistical analysis of data from either the literature or by reduction of photographic records from a total of 71 tests or incidents with the propellant combinations of LO_2/RP-1 or LO_2/LH_2 and which ranged in propellant weight from 10 to 250,000-lb.

** See Ref. 3.

mechanism of propellant dispersal. In this test, a fraction of the propellants were intentionally allowed to mix and subsequently ignite while within the confines of the missile tankage. However, the forces of the explosion evidently caused part of the remaining unmixed propellants to be displaced in such a manner that they did not mix and react until they had been substantially displaced laterally from the center of explosion. The maximum dimension of the resultant fireball was estimated to be from 800 to 1000 ft, while the diameter as given by Eq. (2.1) is approximately 400 ft.

Fireball durations, i.e., the period over which visible radiation exists, also increase approximately with the cube root of propellant weight as given by

$$\tau = 0.196\ W^{0.349} \qquad (2.2)$$

where the duration, τ, is in seconds for a weight in pounds, with a standard error of 84 percent; 1,000- and 1,000,000-lb durations are 2.2 and 24 sec, respectively. For large enough propellant quantities, the duration is sufficient for the fireball to rise to heights of the order of a few fireball diameters, the rise occurring with accompanying modifications of the shape of the fireball, first to that resembling a sphere, and finally approaching, should it continue to persist, the characteristic toroidal geometry. Vertical motion is, for practical purposes, generally nonexistent at the 1,000-lb (or lower) level, while significant heights are generally attained with quantities of 25,000 lb or more. A significant rise is accompanied also by the formation of a vertical and temporarily rising column, generally referred to as the stem, which extends from the lower region of the fireball to the ground surface. While this column may become heated due to its proximity to the fireball, it essentially does not consist of the products of explosion, but rather of gases and particulate matter that have been swept from regions lateral to the initial fireball.

Velocities that accompany fireball growth are at first supersonic but rapidly decay to subsonic levels. From film coverage of 25,000-lb tests, radial expansions of 60 ft (about one-half maximum dimension) typically occur in about

50 msec, giving an average velocity during that time of 1200 ft/sec. While the growth velocities thereafter rapidly subside, randomly directed local motion persists throughout the duration of the fireball.

Temperatures that prevail in the fireball are typically of the order of 2,500°K (~ 4,000°F), with spatial variations tending to occur particularly after the period of fireball growth. Unlike explosions of high explosives of "well-mixed" propellants, there is evidence suggesting that the process of fuel-oxidizer mixing and subsequent chemical reaction continues during and perhaps somewhat after fireball growth. Since the rate of chemical reaction in, and the consequent energy emitted from, an elemental region depends on the quantities of fuels and oxidants in the region that are in sufficient proximity to interact and since the spatial distribution of these potential reactants can easily be nonuniform, there is no guarantee of thermodynamic equilibrium, and radiation from any such region is therefore not necessarily governed by the Planck radiation laws. With time, of course, uniformity throughout any given elemental region will be approached, thereafter making it sensible to consider Planckian radiation and its associated laws. When laws such as Stefan's radiation law are applied, however, there remains the uncertainty of the emissivity, an uncertainty stemming primarily from ignorance of the fireball constituents at a given instant.

HEAT TRANSFER WITHIN THE FIREBALL

The transfer of energy to material surfaces immersed in and moving relative to a "high-temperature" gas is effected through some combination of the mechanisms of radiation and forced convection. An object whose surface is everywhere convex or planar will be uniformly irradiated, provided the mean free photon distance, the mean distance that a photon travels through the fireball before being absorbed, is significantly less than the distance to either the edge of the fireball or some other object that can obstruct its irradiance. With the quantities of carbon that are present in the LO_2/RP-1 fireballs, this mean distance is evidently small compared with the dimensions of the fireball, so that for most circumstances there would be uniform irradiance. This is less clear for fireballs from the LO_2/LH_2 propellant combinations.

For the LO_2/RP-1 propellant combination, particulate carbon is present in sufficient quantities to suggest that the emissivity of a layer of the fireball would approach that of carbon for a thickness that is small compared with the fireball diameter. If this is assumed, along with a gas temperature of 2,500°K, a radiant flux density of about 215 watts/cm^2 (190 Btu/ft^2-sec) is obtained.

Convective transfer from ordinary gases at these temperatures tends to be small compared with the radiant transfer mentioned above except as flow velocities approach supersonic levels. As noted previously, the velocities that accompany the fireball growth commence at supersonic levels, but the growth approaches completion within tens or hundreds of milliseconds. Consequently, while convective transfer rates can be comparable to expected radiative rates during this time, the short duration renders their contribution negligible compared with the total transfer. However, high-speed motion does not cease with the completion of growth. Local and randomly directed "swirling" motion continued throughout the duration of the fireball, with velocities, as photographically indicated, typically ranging from 100 to 400 ft/sec. An immersed object, therefore, will tend to receive "surges" of convectively transferred energy at levels that are not negligible compared with radiant transfer, and the object may experience several such surges from more or less random directions. It is again emphasized that this discussion pertains to ordinary gases.

There is a difference of potential importance between a gas and a so-called fireball "gas" in that the fireball contains particulate matter, a fact which can greatly affect energy transfer. To illustrate the possible extent of the effect, consider a flow of high-temperature gas within which are particles that have the same temperature and velocity as the gas. On approaching an object, the comparatively large momentum of the particles will tend to permit their impingement on the object, and during the time of contact, energy will be conducted from the particles to the object. As an example, a 500-μ carbon particle at 2,500°K has about 3 joules of internal energy that can be transferred to a room-temperature heat sink, and if the particle is assumed to temporarily deform on impact in such a way that a circular area whose diameter is equal to that of

the particle is in contact for 0.01 sec, approximately 1 joule of energy will be transferred from the particle. The continual bombardment from the flow of a concentration of particles will, of course, result in a heat flux to the object, as illustrated in Table 2-1, where the heat flux density associated with ranges of particle size, particle concentration, and duration of contact are considered for a velocity of 200 ft/sec.

Table 2-1
ESTIMATES OF HEAT FLUX DENSITY $\left(\text{in watts/cm}^2\right)$ BY PARTICLE IMPINGEMENT

		DIAMETER (μ)			
		50		250	
		CONCENTRATION (particles/cm³)		CONCENTRATION (particles/cm³)	
		10^{-2}	1	10^{-2}	1
Duration of Contact (ms)	0.1	0.01	1.2	0.5	50
	10	0.01	1.5	1.8	180

While it is difficult to obtain clearly realistic assumptions, the results of Table 2-1 suggest that energy transfer by particle bombardment can not easily be ignored. At the outset, the assumption that the contact of all of the impinging particles is temporary may be unrealistic, since the explosions are accompanied by a permanent deposition of particles, a case in which a greater fraction of the internal energy of a particle will be conducted to the object. It thus becomes important whether some permanent particle adherence occurs during the heating pulse or whether the deposition is confined to a later settling of cooled particles.

EXPERIMENTAL APPROACH

A completely general experimental approach would require measurement of all properties and variables of the fireball which are necessary to evaluate heat transfer to any object, and while ideal, it is prohibitive, aside from the difficulty of evaluation, in terms of the required instrumentation. Diminishing the scope of this approach by measuring only the most essential or dominant

variables, such as the gas temperature, introduces an uncertainty in evaluating the heat flux density, of course, since assumptions about the fireball are required. A case in point is that of the effect of heat transfer through particle impingement mentioned above, a case which is difficult to evaluate realistically. However, an approximate gas temperature, a most critical variable, can be measured remotely, which permits selecting the fireball region to be measured, and thus enables a measurement of the highest apparent temperature region of the fireball. This is important because an upper bound of the heat flux density is sought. Indeed, remote gas temperature measurements of this kind have been made throughout the program by the Sandia Corporation, using a photographic recording pyrometer. The pyrometer is described in Appendix A and is illustrated in Fig. A-12.

A less general though more direct approach is that of simply measuring the heat flux into various immersed objects, the distinct advantage being that no assumptions regarding the fireball are required. The most serious disadvantage of measurements of this sort within the fireball is that the instrument is not always in the most severe environment, the environment of primary interest. Thus, a statistical sampling of measurements must be obtained, and several direct measurements of heat flux density were made per test at locations distributed throughout the fireball.

Two additional types of measurements were made that pertain to heat transfer within the fireball, in particular, the radiant flux density and the thermocouple probe measurement, although there is a tendency to regard them as secondary measurements with respect to the two measurements mentioned above, in part because of certain experimental uncertainties associated with these measurements. The associated inaccuracies do not necessarily exist; rather, it is difficult without further, and perhaps unwarranted, effort to firmly establish that they are negligible or to determine a suitable correction. The problems are discussed in the instrument and error analysis sections, although, in summary, it can be said that for most circumstances, the radiant flux density errors are not expected to be "excessive" nor are those of the thermocouple probe, except as the probe approaches its melting temperature.

These two measurements are also considered secondary in that they cannot satisfactorily accomplish by themselves the primary objectives of the thermal program; rather, they tend to support (or depreciate) the heat flux density and pyrometric gas temperature measurements discussed above. It should be recognized, however, that supporting measurements are relatively important in light of the ease with which a substantial error can occur with any one type of measurement.

In summary, the experimental approach used to accomplish the objective of determining a bound to the heat flux density within the fireball consisted of a combination of the general and the direct approach, supplemented by supporting measurements.

Section 3
SUMMARY OF INSTRUMENTATION

This summary of instrumentation permits comprehensive reading of the presentation of results without requiring reference to the detailed description of instrumentation given in Appendix A.

The heat flux density is measured just beneath the surface of various slabs located within the fireball. The dimensions of the slabs are of the order of 1.5 in. in thickness (normal to their exposed surface) and range from 1 to 3 in. laterally. Over the heating duration, however, the slabs are thermally representative of semi-infinite slabs, that is, they effectively occupy half of space. The heat flux density is evaluated by measuring the temperature with time just beneath the exposed surface of the slab and applying these temperature data to the computation of the heat flux density through the following relation (or its equivalent):

$$q(t) = K' \int_0^t \frac{\frac{\partial T_s(\tau)}{\partial \tau}}{\sqrt{t - \tau}} d\tau \qquad (3.1)$$

where q is the heat flux density; $K' = (K\rho c/\pi)^{1/2}$; K, ρ, and c are the conductivity, density, and specific heat, respectively, of the slabs; T_s is the slab surface temperature; and t is time. The slab temperature is measured by means of a thermocouple junction embedded just beneath the slab surface.

Radiant flux density is measured with a "Gardon" type radiometer. The energy-sensitive element of the radiometer consists of a circular metallic foil whose circumferential edge is joined to a heat sink. Irradiance of the foil induces a temperature differential between the center and edge of the foil that is proportional to the incident radiant flux density. The temperature differential is measured with a differential thermocouple whose output, then, is a measure of radiant flux density.

There are four instrument stations within the fireball designated stations H, S,* and the Sandia station with one or more instruments being associated with each, as well as several additional instruments located external to the fireball. The relative azimuthal position of the instruments or instrument stations (azimuth is important only with regard to the position of a given instrument relative to the others) is indicated by specifying the position of the stations or instruments with respect to three radial gauge lines, designated gauge lines A, B and C, which are 120 deg from each other. The arrangement of the gauge lines and the relative locations of the instrument stations are shown in Fig. 3-1.

Heat flux density measurements were obtained at instrument stations H, S, and P, two each at stations H and S and five at station P, and up to four radiant flux density measurements were obtained at station H. Station H was elevated approximately 52 in. above the ground surface at a horizontal distance from the test pad center of 38 ft for the 25,000-lb tests and the Titan I test and of 13 ft for the 200- and 1000-lb tests. The two slabs of Station H are adjacent and, for the 25,000-lb tests, are arranged so that the flow of hot gas along the exposed surface of each is similar. Station S, consisting of two slabs, is located 13 ft above the ground surface and as near to the center of the explosion as practical. In tests 275 through 285 (25,000-lb tests), it was located at a ground distance of 23 ft along gauge line A, and thereafter (for the remaining 25,000-lb tests and the Titan I test) was 32 ft from the test pad center at a point approximately intersecting gauge lines A and B. For the 200- and 1000-lb tests, it was positioned almost directly above the test pad center. Station P, installed after Test 285 (for the 25,000-lb LO_2/LH_2 tests and the Titan I test only), consists of a series of five instrumented slabs (designated as being at positions "1" through "5") distributed at 60-deg intervals along the circumference of a 12-in.-diameter, vertically oriented pipe. The station is 11 ft above the ground surface and is part of the support structure of station S.

---

* Sketches of instrument stations H and S are given in Figs. A-18 through A-20.

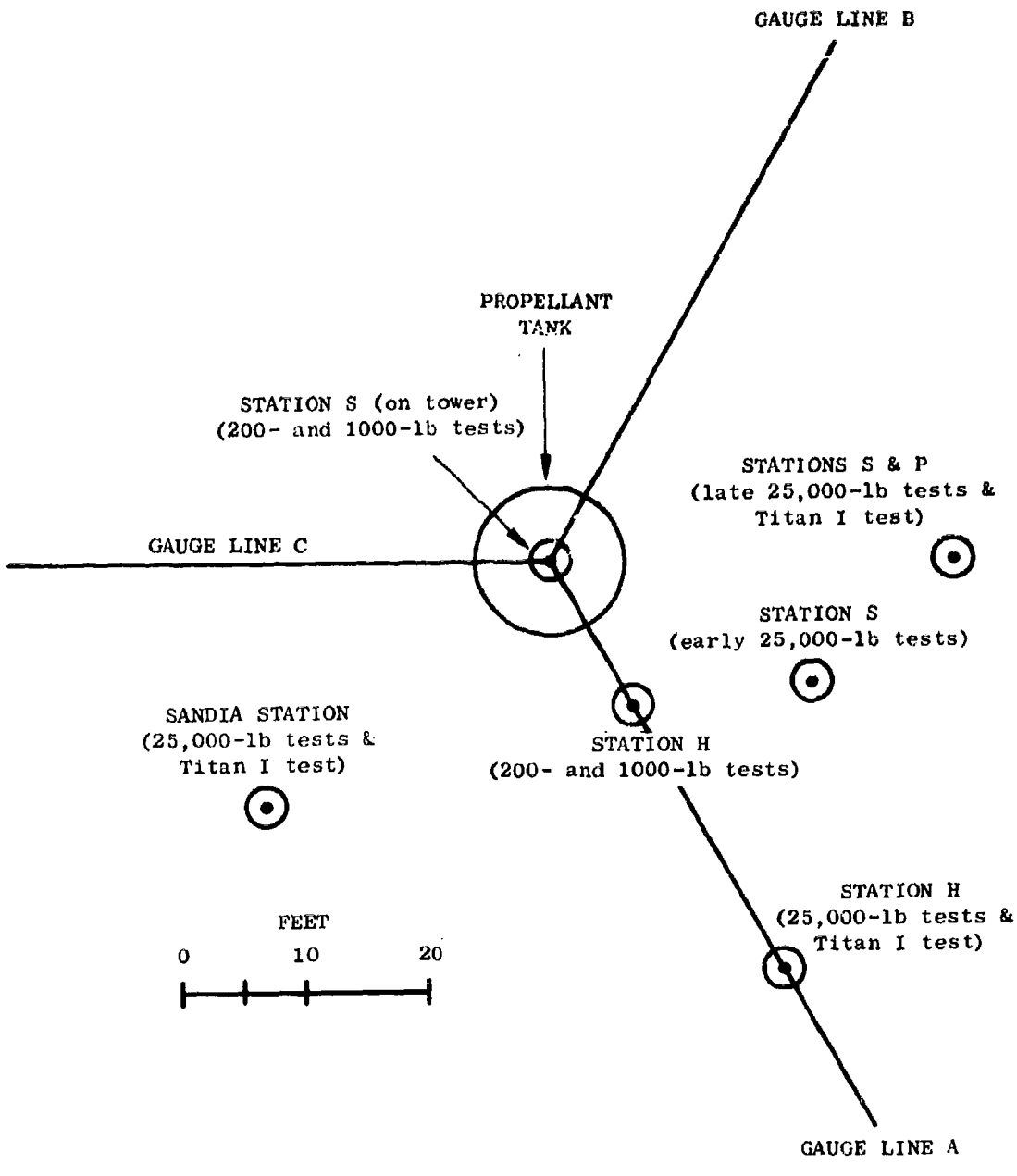

Fig. 3-1. Instrument Station Locations

The primary gas temperature measurement was obtained from a photographic recording pyrometer. This measurement technique consists of matching, over a portion of the visible spectrum, the intensity of an image of a region of the fireball with the intensity of a similar image of one of several tungsten filaments, each of which is at a known and preset temperature. Since the intensity from the tungsten in the optical spectrum approximates that of a blackbody, the measured fireball temperature is near the blackbody equivalent temperature. It was the policy to measure the fireball region having the highest intensity or temperature. The pyrometer was located about 450 ft from the test pad along gauge line A.

The secondary gas temperature measurement was obtained with a thermocouple probe, which consists of a metallically sheathed therm couple junction, with the thermocouple leads insulated from the sheath except at the junction. One or more thermocouple probes per test were mounted on the Sandia instrument station, located 13 ft above the ground surface about 30 ft from the test pad center at a point approximately intersecting gauge lines A and C.

Radiant flux density was also measured at locations external to the fireball by means of the Gardon-type radiometer described above. Generally, three radiometers were used per test, two at the same distance (335 ft) from ground zero along radial gauge lines (A and B) 120 deg from each other, with the third more remotely located (600 ft) along gauge line A. These distances are such that with the existing field-of-view of the instruments, radiant energy originating in any region of the fireball prior to its rise was not restricted from falling incident on the sensitive foil of the instrument.

Section 4
PRESENTATION OF RESULTS

GENERAL ORGANIZATION

Results of the primary measurements of slab heat flux density and pyrometric gas temperature are presented first. This commences with a graphical summary of the pyrometric temperature that shows the range and mean value of the measurements for each propellant type (LO_2/RP-1 and LO_2/LH_2) for the 25,000-lb tests. (No Titan I data are available.) In addition, a graph indicating the spatial variation of temperature over the fireball from a single test is presented.

The results of the heat flux density measurements are presented next, including curves which represent the upper bound of this parameter (bounding curves) and curves which represent values of this parameter that are suitable to anticipated applications (recommended curves). Indications of the basis and limitations of both the bounding and recommended curves are also given. The correspondence between the heat flux density measurements and the pyrometric gas temperature measurements is given next by comparing the radiant flux density computed from the gas temperature measurements with the heat flux density measurements.

The secondary measurements from the 25,000-lb tests are then considered, commencing with illustrations of the degree that the radiant flux density measurements within the fireball support the primary measurements. (The corresponding measurements for the Titan I test were unsuccessful.) This is followed by similar illustrations of support from the temperature measurements obtained from the thermocouple probes.

Heat flux vs time at "large" propellant weight scales is then considered. A recommended scaling relationship for heat flux vs time is given, along with a listing of the experimental evidence upon which the relationship is based.

The Titan I heat flux data are then compared with the LO_2/RP-1 bounding heat flux – time curve that has been scaled, using the recommended scaling, to the 100,000-lb level.

The heat flux data from the 200- and 1000-lb LO_2/RP-1 and LO_2/LH_2 tests are presented next, and this is followed by the 200- and 1000-lb N_2O_4/50% UDMH-50% N_2H_4 data.

Finally, the radiant flux density measurements from outside the fireball are considered. The results of the 25,000-lb tests are presented only in terms of summary data plots indicating the data mean and range. A single measurement from the Titan I test is given.

RESULTS OF THE 25,000-LB TESTS

Gas Temperature from the Photo-Recording Pyrometer

A summary of the pyrometric gas temperature measurements for the 25,000-lb tests is presented in Fig. 4-1 for both the LO_2/RP-1 and the LO_2/LH_2 tests. (No equivalent Titan data are available.) The plots include a curve of the mean temperature and an indication of the highest and lowest measured temperature, where the plotted values are time averages over, in most cases, 100- and 200-msec time intervals for the LO_2/RP-1 and LO_2/LH_2 tests, respectively. The number of data curves from which the summary plots are constructed changes with time because the fireballs have a range of durations, and this number is indicated just beneath the plot. It should be remarked also that the temperature range of the pyrometer for these tests was such that temperatures below about 1900°K could not be measured. For two tests (Tests 279 and 282), the temperature during the fireball duration fell temporarily to levels at or somewhat below 1900°K, and for this time and these two tests, a value of 1900°K was used in obtaining the temperature average over the tests.

A most evident feature of the gas temperature values is their consistency from test to test. The variation appears to be somewhat larger for LO_2/LH_2 than for LO_2/RP-1 with – for instance – the greatest deviation of a single

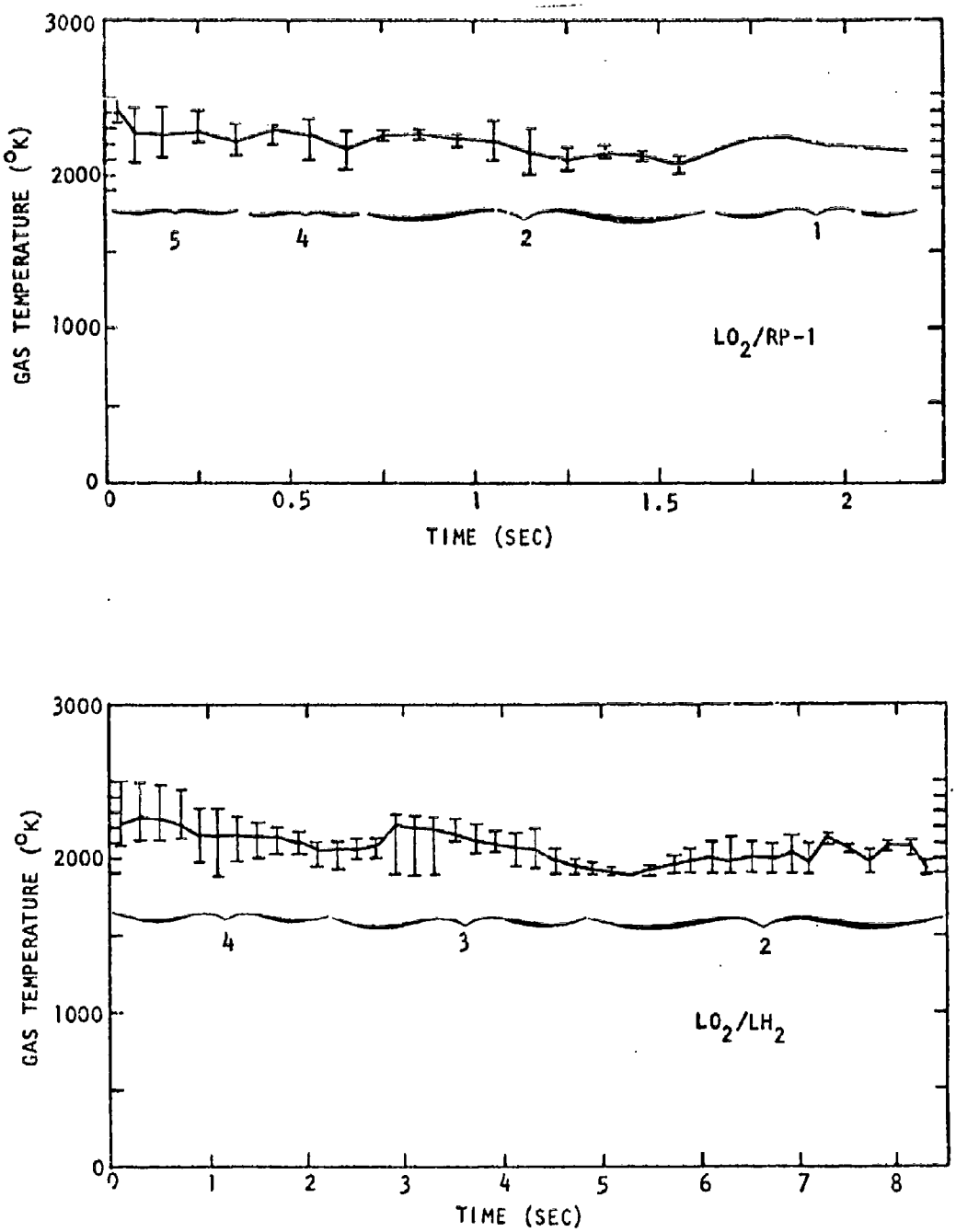

Fig. 4-1. Pyrometric Gas Temperature Measurement Summary for the 25,000-lb Tests

measurement from the mean of the measurements being about 300°K. There is a notably short duration for the LO_2/RP-1 compared with both the LO_2/LH_2 gas temperature duration and, more importantly, with the measured LO_2/RP-1 heat flux durations that will be considered below. Substantial temperatures appear to have persisted within the fireball for significantly longer periods than could be measured by the remote temperature instruments, evidently due to obscuration by "cooler" gases and/or particulate matter along the surface of the fireball.

A feature of the temperature data that does not appear in Fig. 4-1 is the frequent occurrence of a comparatively high but abruptly decreasing temperature in the initial stage of fireball expansion; these temperature "pulses" are not resolved in Fig. 4-1 since their duration is generally a small fraction of the 100- and 200-msec time intervals of Fig. 4-1. A listing of the highest magnitude and the duration of the pulses is given in Table 4-1, where the duration is defined as the time from ignition for the temperature to decay to (and remain below) 2450°K; a radiant flux density of 200 watt/cm^2 corresponds to a temperature of 2450°K for an emissivity of 1. Also included in the table are maximum values of the radiant flux density during this time for an emissivity of 1.

Table 4-1

FIREBALL TEMPERATURE DURING INITIAL STAGE
OF FIREBALL EXPANSION FROM PHOTO-RECORD PYROMETER

PROPELLANT TYPE	TEST NO.	TIME FOR TEMPERATURE TO DECREASE TO 2450°K (msec)	MAXIMUM TEMPERATURE (°K)	MAXIMUM RADIANT FLUX FOR AN EMISSIVITY OF 1 (watts/cm^2)
LO_2/RP-1	275	30	>2650	>270
	278	25	>2500	>210
	282	15	>2600	>250
	284	10	2560	235
	285	10	2860	360
LO_2/LH_2	277	0	2380	175
	279	0	2320	160
	281	0	2250	140
	288	25	2900	285

While comparatively large temperatures or corresponding magnitudes of heat flux frequently occur, the damaging response of most structures or objects to these pulses is small compared with the response from the remaining or subsequent heat transfer.

An indication of the spatial variation of gas temperature over the fireball is given in Fig. 4-2, where the temperature over three separate regions of the fireball from Test 288 is given. A crude indication of the size of each region of measurement relative to the fireball dimensions and the location of each region is given in the upper right hand corner of the figure.

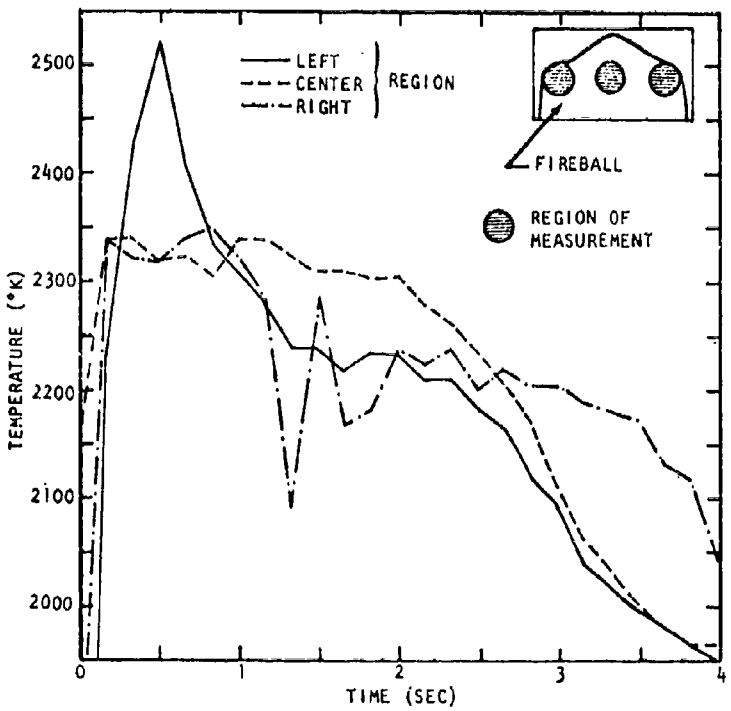

Fig. 4-2. Spatial Variation in Gas Temperature for Test 288

It can be seen that spatial differences of the temperature at given times are commonly of the order of 200°K, and it should be remarked that comparative examination of film coverage of the various 25,000-lb tests suggests that the fireball from Test 288 was relatively uniform. Temperature variations of this

magnitude result in comparatively large spatial variations in heat flux, particularly since the radiant flux varies with the fourth power of the temperature. For an emissivity of 1, the radiant flux computed from the temperatures of about 2320 and 2520°K at 0.5 sec in Fig. 4-2, for example, are 160 and 220 watt/cm^2, respectively. Similarly, temperatures of 2090 and 2320°K at 1.3 sec correspond to flux densities of 103 and 160 watt/cm^2. In addition to spatial variations in heat flux of this magnitude, temporal variations (at a stationary point) of the same magnitude can be expected to occur in small fractions of a second, as evidenced, first, by the abrupt temperature changes in Fig. 4-2, and more vividly through high-speed coverage of the apparent motion of high- or low-temperature regions about the fireball.

Heat Flux Density

All heat flux density data from the 25,000-lb tests are presented in Figs. B-1 through B-28. Included in the present section are discussions of the results and comparisons of the data with other data. More importantly, however, it is desirable to use the heat flux density data to obtain a "conservative yet realistic" bound to the heat flux that a structure or object immersed in the fireball can receive, and this section commences with the discussion and presentation of this upper bound.

Two complications occur in acquiring the upper bound. First, the flux instruments are not continuously in the most severe region of the fireball; and second, because the test design was based on blast rather than thermal considerations, there are some difficulties with regard to identifying thermal test conditions.

Regarding the first complication, the fireball parameters of potential importance to heat transfer, such as the gas temperature, are not generally uniform throughout the fireball. This is particularly evident from film coverage of the tests, and was illustrated for gas temperature specifically in Fig. 4-2. It would be expected, therefore, that a direct flux density measurement from a stationary instrument would approach or attain the maximum possible value only occasionally, that is, for some times for some tests. It is an observed characteristic of the measured flux density–time curves to

exhibit periodic "surges" or maxima, evidently reflecting the variations in the gas parameters as the gas flows past the instrument, and statistically, some of these maxima will be, or will approach, the highest value possible at that time for the fireball in question. Provided there is a sufficiently large number of measurements per test and a sufficiently large group of tests having identical test conditions, the upper bound to the heat flux density for this set of test conditions will be revealed by superimposing the flux density pulses having the higher maxima on a single flux density – time graph; or more specifically, a smooth curve fitted to the highest maxima of this graph will represent an upper bound. This approach of estimating an upper bound, or a bounding curve, has been applied, and the results obtained from it, along with indications of the limitations associated with the approach, are presented below.

With this approach, it is essential that the data that are combined to obtain an upper bound are from tests which have identical test conditions. The discussion in the following paragraphs serves primarily to indicate how closely we are able to comply with this requirement. It will be seen that a practical choice of separating the tests into thermal test condition categories is made without complete technical justification for the choice. The discussion commences with a brief description of test conditions.

There were variations of the propellant test tankage, propellant ignition time, etc., which were introduced to determine their effect on blast wave hazards, and these will be referred to as blast wave test conditions. These conditions may or may not influence the thermal hazard and, thus, may or may not constitute a thermal test condition. There were three blast wave test conditions for the 25,000-lb tests. The first is the propellant type, and is specified by indicating either the LO_2/RP-1 or the LO_2/LH_2 combination. A second condition, which we will refer to as the propellant configuration, separates the tests on the basis of whether they were of the confinement-by-the-missile condition (CBM) or the confinement-by-the-ground-surface condition (CBGS). For the CBM condition, the propellants were permitted to mix within the propellant tankage by the abrupt creation of an opening in the diaphragm that originally separated the two propellants. For the CBGS condition, the propellants were permitted to spill from the tankage and to spread (and mix) along the ground

surface. For each of the several tests conducted for each of these conditions the propellants were permitted to mix for varying lengths of time prior to their ignition, and "ignition time" constitutes a third condition. In order to describe a test, then, it is necessary to specify the propellant type, propellant configuration, and the ignition time. The blast wave test conditions for each 25,000-lb test (for which there are heat flux data) are indicated in Table 4-2 for reference in the discussion to follow.

Table 4-2

TEST CONDITIONS FOR THE 25,000-LB TESTS

Test Number	Propellant Type	Propellant Configuration	Ignition Time (sec)
275	LO_2/RP-1	CBM	0.51
278			0.53
284		CBGS	0.00
285			0.46
279	LO_2/LH_2	CBM	0.03
288		CBGS	0.36
289			0.17
290			0.11

Since the approach used to construct the bounding curves requires a number of individual flux-time curves for each test condition, it is desirable to combine all tests whose blast wave test conditions do not differ in ways that are of importance to heat transfer. To the extent that it is practical, then, we will consider the effect of blast wave test conditions on the heat flux density and on the heating duration. Commencing with the effect on heat flux, the photorecording pyrometer measurements were first considered, and it was found that the gas temperature in the fireball region where the temperature was maximum does not, for practical purposes, depend on blast wave test conditions other than propellant type. (The consistency of gas temperature for all conditions for a given propellant was indicated in Fig. 4-1.) Gas temperature, moreover, is expected to be the most critical parameter; that is, it will have the greatest influence on the magnitude of the heat flux.

The test conditions of propellant configuration and ignition time can affect the flow velocity (and pattern) and so, in turn, can affect the heat flux. For "ordinary" gases, however, estimates of the flux contribution from convective heat transfer at the most extreme flow velocities (except during the early fireball growth stages) are small compared with the radiant transfer. The possible presence of particulate matter in the explosive products of the LO_2/RP-1 tests, however, makes it mandatory that test conditions influencing flow velocity be considered as possible thermal test conditions. Since particulate matter is present, any condition which affects either the flow velocity or particle concentration may constitute a thermal test condition. The only practical means of attempting to establish the dependence or independence of the heat flux on particulate concentration is through analysis of the heat flux density data themselves. The assortment of test conditions that existed for the 25,000-lb tests, as indicated in Table 4-2, is not readily amenable to analysis, and we resorted to the following method. We first compared the mean value of the time average of each flux trace from Test 285 with the corresponding mean of the combined test data from Tests 275 and 278, where the test conditions of these two test groups differ only in propellant configuration. It was concluded that there is no reason to believe that the two mean values are different. That is, there is no reason to believe the flux depends on propellant configuration, and the probability that this analysis has failed to reveal a difference that really exists is about 0.01. Next, with the assumption that this conclusion also applies to the LO_2/LH_2 propellant combination, the analysis of the flux data from several tests may be used to determine the effect of propellant type on the time average of the flux. Specifically, the mean of the time average of each flux trace from Tests 275, 278, and 285 was compared with the corresponding mean from Tests 288 and 289, and it is concluded that the flux does not depend on propellant type, and the probability that this part of the analysis has failed to reveal an existing difference is about 0.30. Since the ignition time for Test 289 is substantially less than that of the other four tests, as can be seen in Table 4-2, the analysis was also performed with the data from Test 289 excluded, and the conclusion was the same. If there is no significant effect of propellant type on heat flux as the analysis suggests, the presence of particulate matter evidently has no pronounced effect; the flow velocity, then,

should not have a pronounced effect: and finally, there should be no pronounced effect of either propellant configuration (which was already concluded from the crude data analysis above) or ignition time. Regarding ignition time, a crude analysis was performed with the data from Tests 288 and 289, which differ only in ignition time, and it indicated that the average heat flux does increase with increasing ignition time, in contradiction to the conclusion above. In searching for a way to account for the contradiction, it was noticed that the pyrometric gas temperature for Test 288 was somewhat higher during the time of interest than for the other LO_2/LH_2 tests, although there are no pyrometric data available from Test 289 with which to make a direct comparison. If the abnormally high temperature for Test 288 was the cause of the influence of ignition time on average heat flux, this tends to detract from the first conclusion above, namely, that the gas temperature is, for practical purposes, independent of these test conditions. This conflicting result illustrates the limitations of separating the tests into distinct test condition categories. In the case above, for purposes of estimating upper bounds of the heat flux, we have chosen to disregard propellant configuration and ignition time as test conditions, although we were unable to establish a firm basis for the choice.

In order to consider the effect of test conditions on heating duration, the time from propellant ignition for the fireball to lift from the ground surface was obtained from film coverage of the tests, this time being a measure of the potential heating duration at the location of the instruments. These durations are listed in Table 4-3.* In this case, there appears to be a decidedly longer duration for LO_2/RP-1 tests than for LO_2/LH_2 tests, and analysis (using all data given) supports this. The suggestion from a comparison of Tests 284 and 285 that duration decreases with increasing ignition time is offset by the opposite trend suggested by a corresponding comparison of Tests 288 and 290. (It should be noted that the duration of 3.4 sec for Test 285 is particularly uncertain.) There appears to be no reasonable means to ascertain the effect of propellant configuration. As a practical choice, propellant type is treated as the only test condition affecting heating duration (or heat flux magnitude), and the flux data will be combined on this basis.

* The details of these durations are described in a later discussion.

Table 4-3

HEATING DURATIONS FROM THE 25,000-LB TESTS

Propellant Type	Test Number	Heating Duration (sec)
LO_2/RP-1	275	4.7
	278	4.0
	282	5.2
	284	6.8
	285	3.4
	LO_2/RP-1 Average	4.8
LO_2/LH_2	281	3.7
	288	3.8
	290	3.5
	LO_2/LH_2 Average	3.7

Heat flux density maxima plots are presented for LO_2/RP-1 and LO_2/LH_2 tests in Figs. 4-3 and 4-4, respectively. Each flux density "pulse" is labeled with the letter H, S, or P to indicate the instrument station (as designated in Appendix A) from which it was obtained, and the test number is identified by the type of curve as indicated in the legend. The numbers "1" through "5" adjacent to the station letter "P" on Fig. 4-4 designate the instrument position at that station. Bounding curves, or curves which are estimates of the upper bound, are also indicated in the figures.

Regarding these graphs, a high concentration of maxima near the bounding curve tends to support the firmness of the curve, and, of course, suggests that it would not be unusual to obtain values that approach the curve in a subsequent test. A reasonably large concentration near the curve is in fact required for the construction of a bounding curve to be a sensible endeavor. This requirement is clearly satisfied for the LO_2/RP-1 test condition. Examination of Fig. 4-3 indicates, for instance, that the absence of any measurement would not require marked revision of the bounding curve, perhaps the worst case being a minor modification in the 3- to 5-sec region associated with the elimination of the

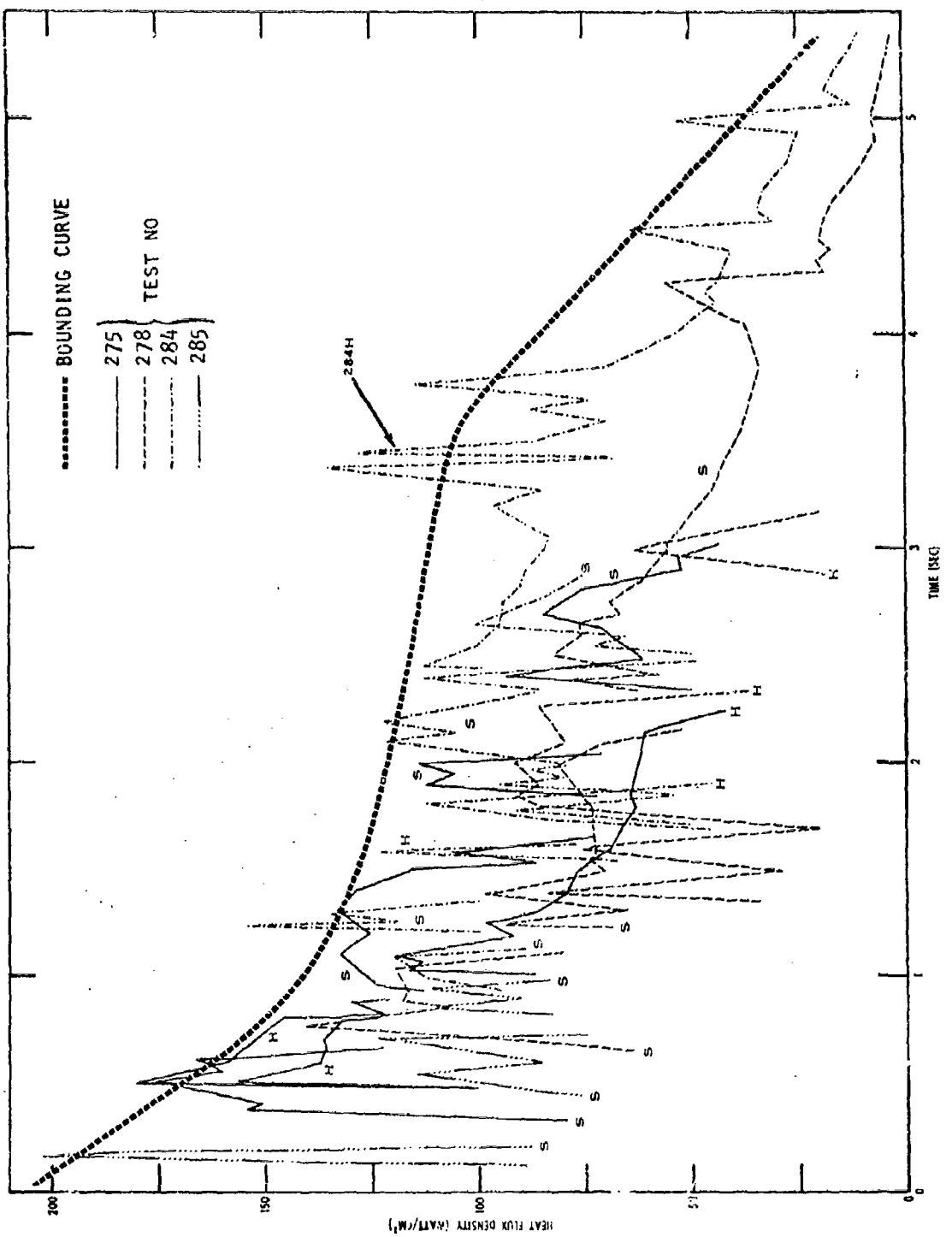

Fig. 4-3. Heat Flux Density Pulses from the 25,000-lb LO_2/RP-1 Tests

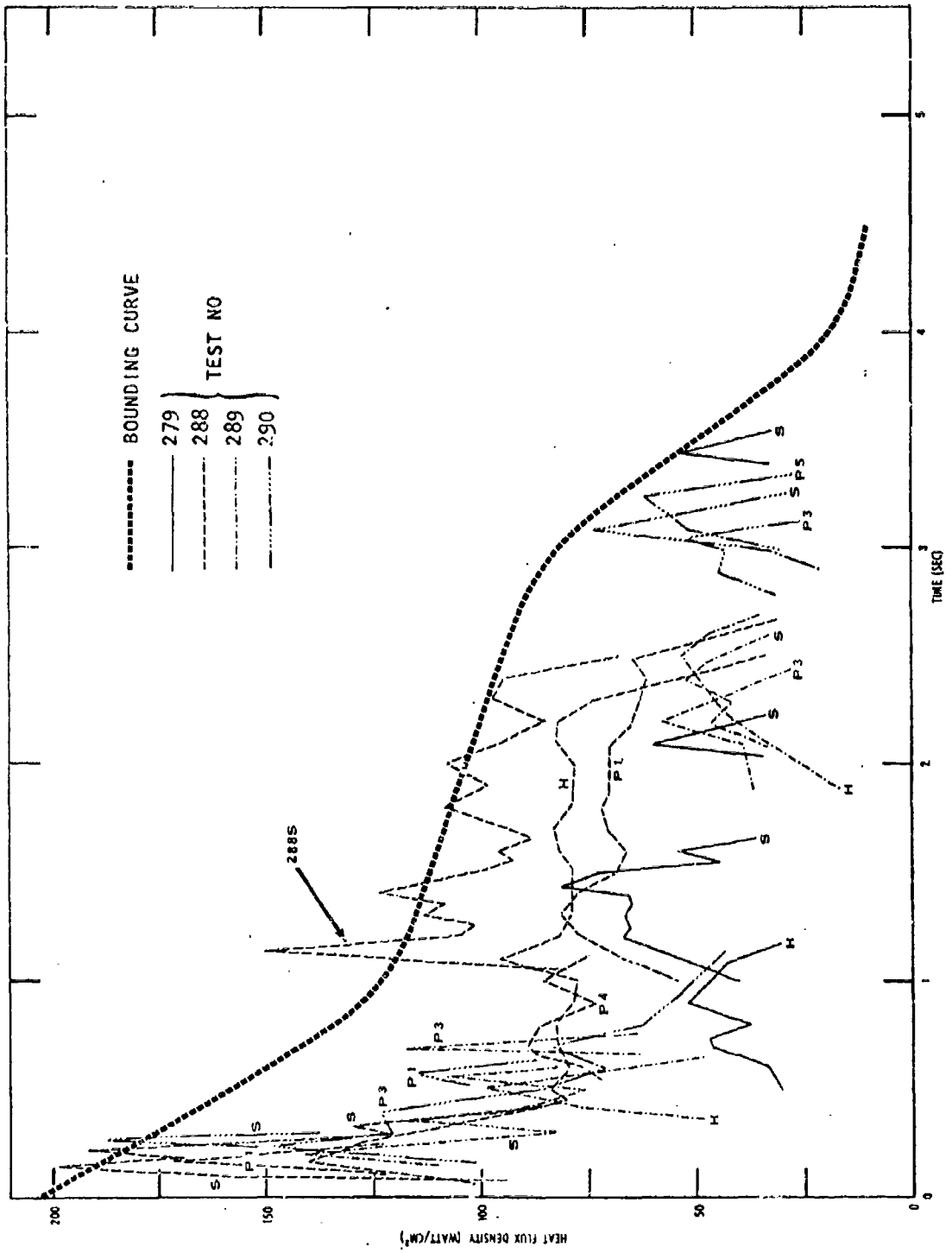

Fig. 4-4. Heat Flux Density Pulses from the 25,000-lb LO_2/LH_2 Tests

pulse labeled "284H." For the LO_2/LH_2 plots, the distribution of maxima does not as firmly support the position of the curve. It can be seen in Fig. 4-4 that the elimination of the particular pulse labeled "288S," for example, would result in a substantial modification of the curve and would reduce the associated cumulative flux by approximately 10 percent. With the statistical sampling at this limited level, it is not clear if this particular measurement is unusual or reasonably typical, and the position of the bounding curve is evidently somewhat less certain than the previous LO_2/RP-1 case. It would be expected that the addition of further measurements would more substantially alter the LO_2/LH_2 curve than that of the LO_2/RP-1. The LO_2/LH_2 curve is included, however, since it represents the best (and evidently a reasonable) approximation to the bound for this test condition that can be made with the available data.

As noted above, the flux density associated with the bounding curves is indicative of the energy that an immersed object can receive and is, for most applications, a reasonably conservative condition to impose, both in terms of the magnitudes and, particularly, in terms of the length of time that such magnitudes would be sustained. No object tested, for instance, received a cumulative flux density in excess of 60 percent of that associated with the bounding curve. Since the bounding curve is evidently somewhat conservative, it is desirable both to investigate the degree of conservatism, and to provide a curve which is more suitable to anticipated applications. Both of these require statistical investigations and several associated points should be emphasized. The first is, simply, that the quantity of data is sufficiently limited that the analysis will provide only a reasonable approximation to the numerical results. Secondly, as noted above, an assumption has been made with regard to what constitutes a test condition, so that some of the data scatter is probably attributable to unrecognized test conditions. Finally, it is not clear how extensive would be the variation of heat transfer with test condition outside the range that has been tested; for instance, failures leading to more thoroughly mixed propellants at ignition may, in turn, lead to somewhat higher temperatures and heat transfer rates. Thus, the restricted range of test conditions over which these data were obtained should be considered in any application.

The conservatism of the bounding curve is illustrated in Table 4-4, which lists the ratio of the energy accumulated in 5.4 sec at each instrument station to that of the bounding curve for the same time, the latter being 590 and 420 watt-sec/cm^2 for the LO_2/RP-1 and LO_2/LH_2 curves, respectively. Also included in the table are the magnitudes of the cumulative flux density for 5.4 sec. The measured cumulative flux density can be seen to range from 9 to 60 percent of that associated with the bounding curve. If one assumes that the measured values conform to a Gaussian distribution, the probablity of obtaining, for instance, 75 percent of the cumulative bounding flux is 0.02 and 0.002 for LO_2/RP-1 and LO_2/LH_2, respectively, and the corresponding figures for 65 percent are 0.07 and 0.02

Table 4-4

CUMULATIVE FLUX DENSITY FOR 25,000-LB TESTS

PROPELLANT TYPE	TEST NO.	INSTRUMENT STATION					
		H		S		P	
		CUMULATIVE FLUX (watt-sec/cm^2)	FRACTION OF BOUNDING CURVE	CUMULATIVE FLUX (watt-sec/cm^2)	FRACTION OF BOUNDING CURVE	CUMULATIVE FLUX (watt-sec/cm^2)	FRACTION OF BOUNDING CURVE
LO_2/RP-1	275	249	0.44	334	0.60	-	-
	278	165	0.29	280	0.50	-	-
	284	304	0.54	265*	0.47*	-	-
	285	49	0.09	140	0.25	-	-
LO_2/LH_2	279	89	0.20	163	0.37	-	-
	288	234	0.53	259	0.58	242	0.54
	289	135	0.30	145	0.33	116	0.26
	290	98*	0.22*	139	0.31	177	0.40

* The cumulative flux values for Station S, Test 284 and for Station H, Test 290 are to a time of 2.8 and 2.6 sec, respectively, and these two values were not used in the analyses.

In obtaining a curve more suitable for application (than the bounding curve), a difficulty arises in that a recommended curve depends on the particular application (e.g., on the degree of conservatism the application calls for, on the materials and geometry that the structure whose response to the environment is desired, and so on). It is not possible then to provide a curve that is applicable to all situations, and one is given which is suitable to many anticipated applications. The criteria upon which this curve, hereafter referred to as the recommended curve, is based are discussed below.

The first criterion is that the cumulative flux density associated with the recommended curve, that is, the area under the recommended flux density - time plot, is such that the probability of exceeding this cumulative flux density is 0.01. With this criterion, analysis of the cumulative flux distributions in Table 4-4 (again assuming a Gaussian distribution) indicates that the cumulative flux densities of the recommended curve are approximately 450 and 300 watt-sec/cm^2 for LO_2/RP-1 and LO_2/LH_2, respectively.

Several difficulties arise when consideration is subsequently given to time distributions of flux density that are appropriate and consistent with these cumulative flux values. It is typical for the measured flux density surges to approach and temporarily remain near the bounding curve and for the heating activity during the time periods separating these surges to be comparatively moderate or negligible. (This is perhaps most easily observed by scanning the individual flux-data curves in Figs. B-1 through B-28.) This suggests that the recommended curves should be superimposed on the corresponding bounding curves and that the reduced cumulative flux values of 450 and 300 watt-sec/cm^2 be obtained by imposing flux voids (or more moderate flux values) over one or more time periods, and the remaining question, in that case, would be in regard to a suitable selection of voids and their distribution. No evident pattern in this distribution is suggested by examination of the individual flux - time measurements. However, it is not uncommon for the flux to remain uninterruptedly near the bounding curve for large fractions of the heating duration. This is illustrated by the example data presented in Figs. 4-5 and 4-6. The flux shown in Fig. 4-5 from Test 288, for instance, remains near the bounding curve from about 1 to 2.5 sec, and similarly for Test 284 in Fig. 4-6 from about 2.5 to

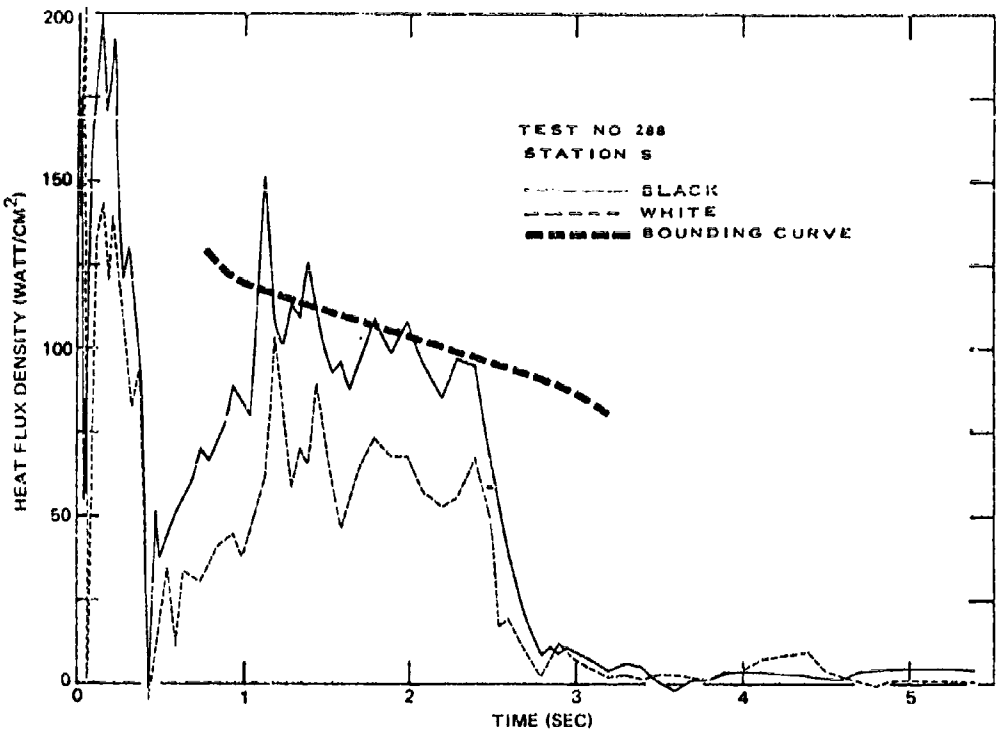

Fig. 4-5. Heat Flux Density at Station S from Test 288

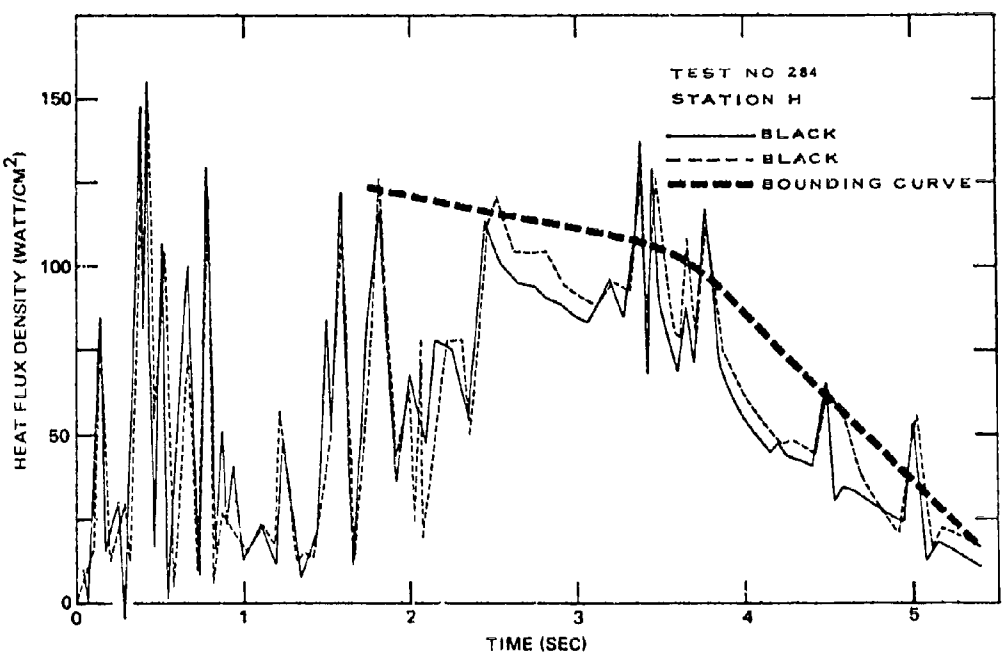

Fig. 4-6. Heat Flux Density at Station H from Test 284

5.5 sec. It is important to recognize that most of the energy transfer for these examples is associated with a single pulse, that the flux during these pulses is near the bounding curve, and that this is evidently not a rare event. This, coupled with the factors previously mentioned, suggests that the recommended curves should be as follows: that they should uninterruptedly superimpose the bounding curves and that their cumulative flux density should be reduced from that of the bounding curves to approximately 450 and 300 watt-sec/cm^2 for LO_2/RP-1 and LO_2/LH_2, respectively. Recommended curves as such are presented in Figs. 4-7 and 4-8, where the deletion of the cumulative flux density from that of the bounding curve is conservatively located at the late end of the heating period.

For some applications, the recommended curves may be slightly conservative, and the stringency may be reduced, for instance, by modifying from 0.01 the probability of exceeding the cumulative flux-density. Other possible means may be justified and suitable under given circumstances, as described in the following example. For purposes of illustration, the measured flux density for Test 275 is given in Fig. 4-9, and it can be seen that the flux is near the bounding curve from about 0.5 to 3 sec, although there is periodic but short-lived relief in the flux level during this time (at about 0.8, 1.75, and 2.1 sec). Intermittent relief such as this can significantly affect the response of some structures, and such flux density-time patterns are not uncommon. This relief, for instance, can afford an opportunity for energy to be conducted through the structure from high- to low-temperature regions, thus reducing the maximum temperature that the high-temperature regions of concern will sustain compared with that for an uninterrupted heat pulse having the same energy. If in applying the recommended curve, the structural response is found to reach, but not greatly exceed, damaging proportions, one may be justified in introducing an appropriate region of reduced flux. Justification of such a modification would, of course, require statistical analysis of the durations, magnitudes, and time distributions of the energy pulses, and such an analysis is not given here.

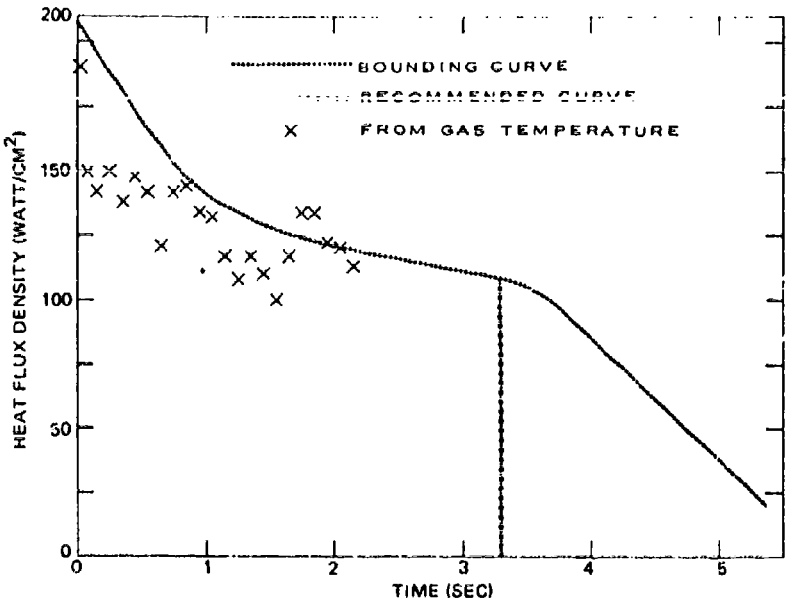

Fig. 4-7. Bounding and Recommended Heat Flux Density Curves for 25,000-lb LO_2/RP-1 Tests

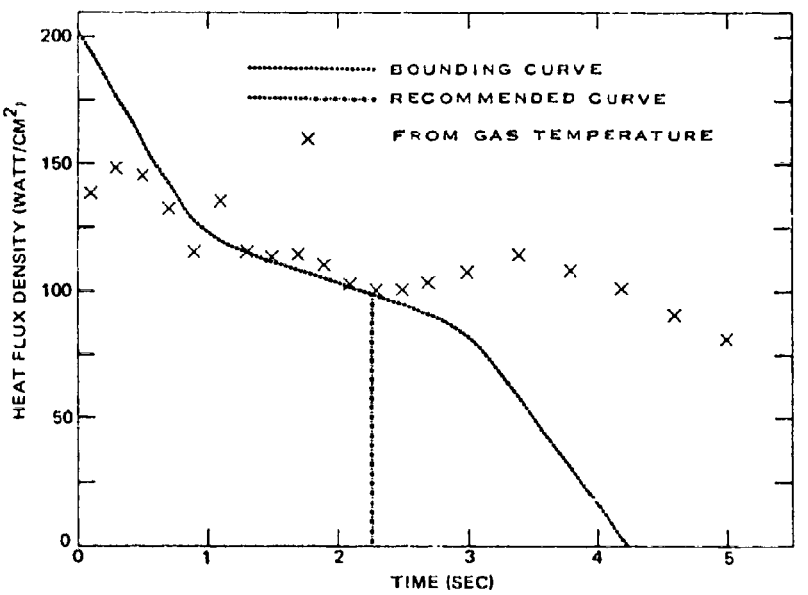

Fig. 4-8. Bounding and Recommended Heat Flux Density Curves for 25,000-lb LO_2/LH_2 Tests

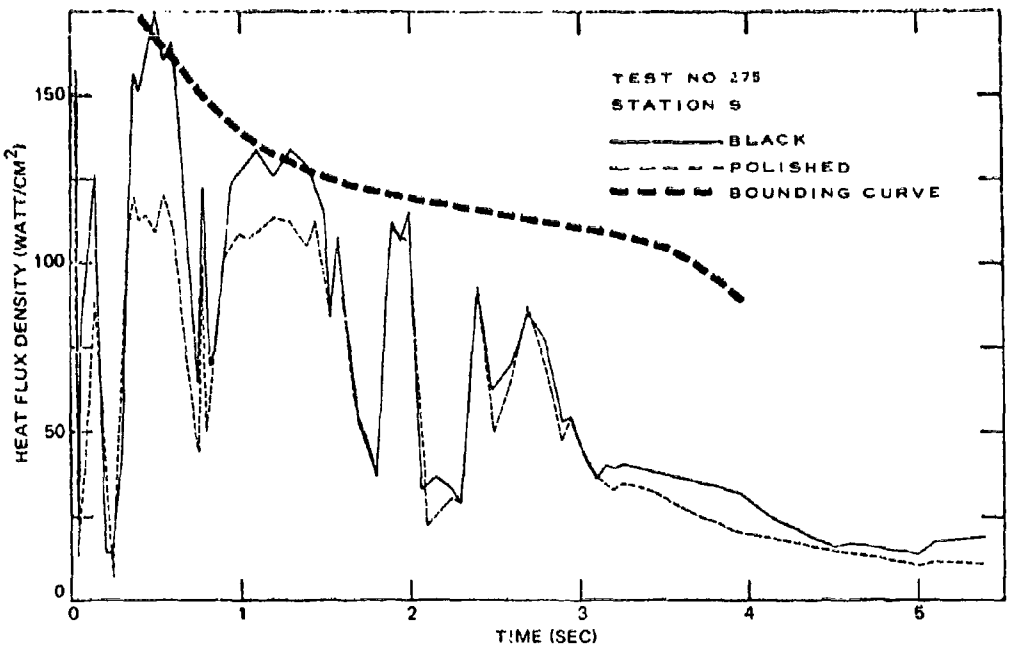

Fig. 4-9. Heat Flux Density at Station S from Test 275

Information computed from the pyrometric gas temperature measurements are included on Figs. 4-7 and 4-8 in order that the rather important comparison can be made between these measurements and the bounding curve. It has been previously mentioned that the gas temperature measurements are of the fireball region having the highest apparent temperature. It has also been implied above that the bounding flux curve approaches the flux that would be sustained in the region(s) of highest temperature. Thus, there should be a correlation between (not necessarily an equality of) the bounding flux curve and the flux implied by the gas temperature measurement. To this end, the radiant flux density values were computed from the gas temperature (on the assumption of a conservative emissivity of unity) and the results plotted (X's) on Figs. 4-7 and 4-8. The correlation is remarkable. Consider first the LO_2/LH_2 case in Fig. 4-8. During the early fireball stages, when the gas flow velocities can be sufficient for significant convective transfer to occur, it is reasonable to expect that the total heat flux measurements will exceed the radiant flux calculated from the remote gas

temperature measurements, since the latter account for radiative transfer alone, and Fig. 4-8 is compatible with this notion. As the more extreme velocities subside, it is reasonable to expect that the two curves will converge, with the radiative mode of energy transfer predominating; and the curves are also consistent with this supposition, at least to approximately 2.5 sec, where the two values commence to diverge, the "pyrometric" flux thereafter exceeding the directly measured values. This divergence is accounted for through film coverage of these tests. In particular, it is at this time that the fireball lifts from the ground surface or from the direct heat flux instruments. For the LO_2/RP-1 data given in Fig. 4-7, the pyrometric gas temperature measurements are restricted to about 2 sec, so that a comparison is possible only during this time.* It can be seen that the results are consistent with expectations in the same manner described for the LO_2/LH_2 case.

The results of this comparison are rather significant in that two totally independent means of evaluating heat transfer indicate similar magnitudes in the region where a similarity should exist. Moreover, in other regions, the comparative magnitudes of the two measurements are qualitatively correct.

A common feature of the heat flux data that is not indicated either in the data figures presented in this section or in those presented in Appendix B is the presence of a comparatively high-magnitude but very short-lived pulse at the beginning of the heating period. When this pulse occurs, it commences with a magnitude in the vicinity of 400 watts/cm^2 and decays to below 200 watts/cm^2 within, for the 25,000-lb tests, about 20 msec. It can be recalled that pulses of the same magnitude and duration were inferred from the pyrometric gas temperature measurements. The pulse was present in the heat flux measurements for Tests 278, 285, and 288; for the pyrometric measurements, it was present for Tests 275, 278, 282, 284, 285, and 288. A more detailed comparison will not be made for the following reason. In computing the heat flux from the slab temperature data, two comparatively large errors occur in the first few computational time intervals (that is, over the first 10 or 20 msec), and these

* This apparent difference in duration was discussed above, under the heading "Gas Temperature from the Photo-Recording Pyrometer."

errors become increasingly large as the time approaches the first (or earliest) computational interval. One of the errors is systematic and correctable, but a substantial effort is required. Since the pulse is of such small duration, the effort appeared to be clearly unjustified. It should be noted that the pulse was also present in the heat flux data from the Titan I test, although its duration was approximately 50 msec.

One further characteristic of the heat flux density data should be mentioned. The flux density data from instrument Stations S and H given in Appendix B are presented in pairs, one pair for each station, corresponding to the adjacent slab pairs of those stations. Usually the exposed surface of one of each pair was coated with a black deposit, and the companion slabs were either coated with a "white" deposit or the surface was polished. The comparative data trends for these companion slabs with dissimilar radiation absorption properties (as given approximately in Appendix A) are as follows. For the LO_2/LH_2 data, the ratios of the energy of the black slab to that of the white range from just over 1 to about 1.5, with the ratio for a given slab pair remaining approximately the same throughout the heating duration. For the LO_2/RP-1 tests, the data trends are somewhat different, with two patterns appearing. For some cases, the energy into each slab is essentially the same, while for others, the energy into the black slab is initially substantially larger than that into the white, but they become equal by about 1.5 sec. (See, for example, the data at Station S for Test 275 in Fig. 4-9 and Test 284 in Fig. B-6.) This combination of data trends for both propellant types suggests that modification of the radiation-absorbing properties of the slabs for LO_2/RP-1 tests through deposition of particulate carbon — always found in posttest examination and at thicknesses ranging to about 0.03 or 0.04 in. — occurs during the heating duration, and the deposition is, in some instances, immediate. It appears advisable, therefore, to use radiation absorptance values near unity for structural surfaces immersed in LO_2/RP-1 fireballs regardless of their initial value.

One of the primary reasons for the installation of instrument Station P (heat flux density measurements at locations distributed around the circumference of a vertically oriented cylinder) was to reveal any consistent, significant differences in the heat transfer at different locations on the surface of an

immersed object, with particular reference to the orientation and location of the instrument with respect to the gas flow direction of the initially expanding fireball. Data were obtained at the station from three 25,000-lb tests, and no marked trends with respect to instrument location were obtained. (Individual heat flux density records from these tests for this station are given in Figs. B-15 through B-17, B-20 through B-22, and B-26 through B-28 of Appendix B for Tests 288, 289, and 290, respectively.)

Radiant Flux Density Within the Fireball

Radiometer data within the fireball are presented in Figs. 4-10 through 4-12 for the 25,000-lb tests. (No equivalent Titan data were obtained.) These data are presented primarily to indicate the degree that they support the total heat flux density and gas temperature measurements above; and since the radiometers were always mounted near a slab heat-flux meter, as described in Appendix A, the radiant flux data are plotted with the heat flux curve that is evaluated from the adjacent slab which was coated black.

The variation among the radiometer data is somewhat larger than is desirable, although some of the scatter can be attributed to the difference in response time of the various instruments. For instance, during the sharp pulses that occur within the first second for Tests 284 and 289, the more rapidly responding radiometers at positions B and E more nearly follow the total flux. Large differences among the radiometer data were also obtained for Test 284, for instance, from about 1.5 to 4.5 sec, but this difference is not attributable to instrument response. Test 284 was a LO_2/RP-1 test (the only 25,000-lb LO_2/RP-1 test for which radiometer data within the fireball were obtained), which required purging of the radiometer windows to prevent deposition of the products of the explosion. Posttest examination indicated a clean window at position E and partially coated windows at positions B and C, and this appears to account for the differences. The flux for position B is significantly low throughout this time and, along with the flux from C, does not respond between 3.5 and 4 sec to the energy transfer that is indicated both by the radiometer at position E and by the total flux measurement.

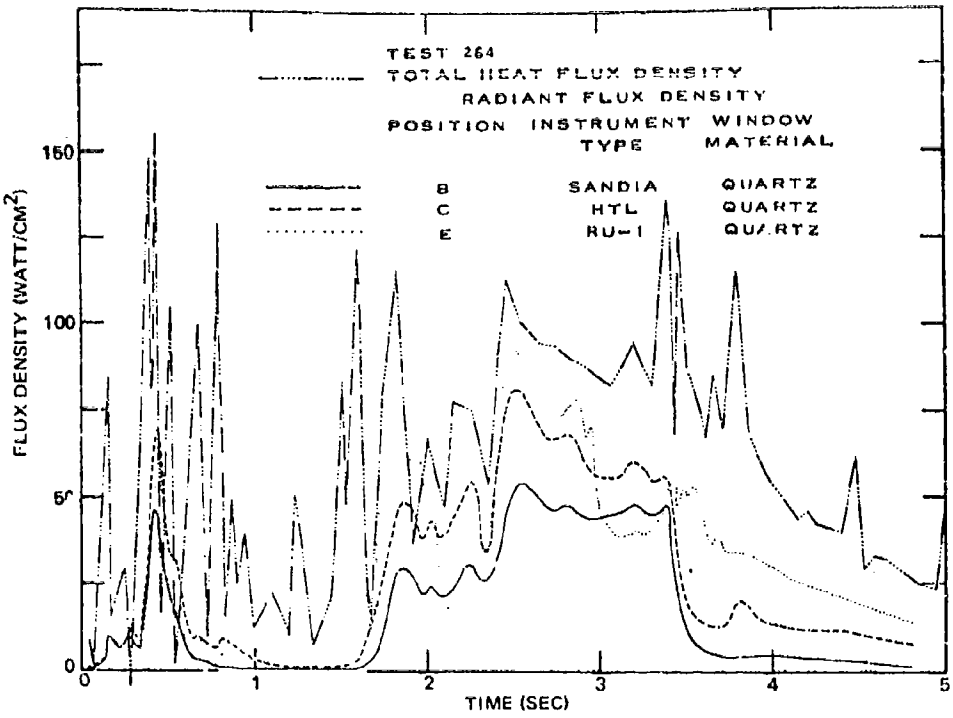

Fig. 4-10. Total and Radiant Flux Density for Test 284

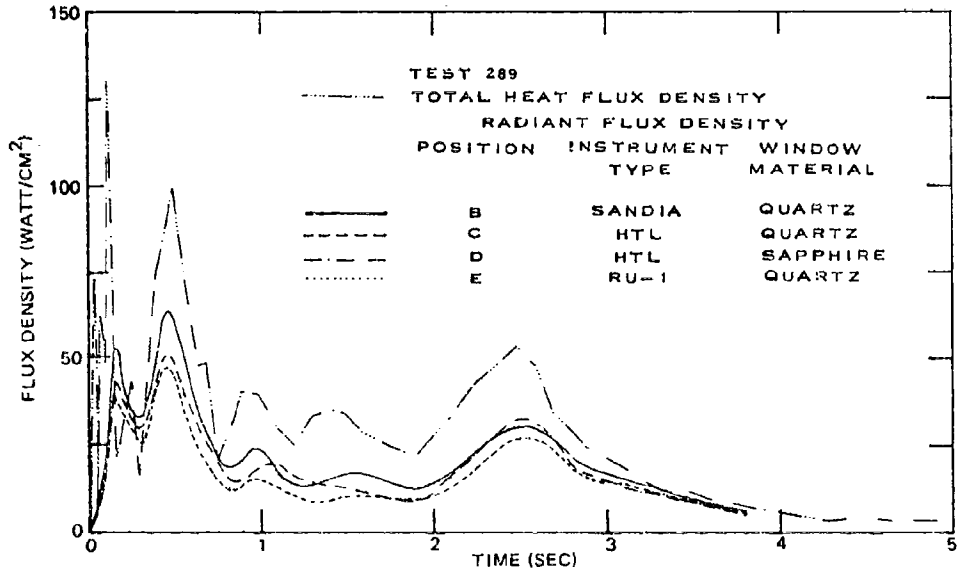

Fig. 4-11. Total and Radiant Flux Density for Test 289

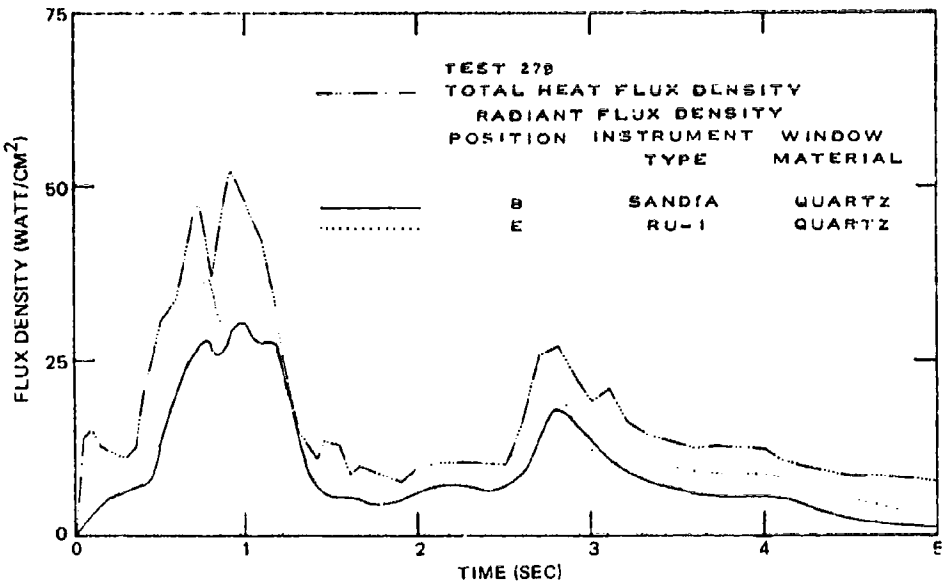

Fig. 4-12. Total and Radiant Flux Density for Test 279

In comparing the radiant with the total flux density, several factors should be considered. First, a correction factor has been applied to the radiometer data to account for energy losses by absorption within and reflection at the surfaces of the window, and, as indicated in Appendix A, the correction is based on a fireball at about 2200°K. Thus, only during times when there are indications of comparatively high-level energy transfer corresponding to such gas temperatures is the estimated correction applicable. For lower temperatures, the radiant flux density measurement will tend to be lower than the actual flux density. In addition, due to the comparatively slow response of the radiometers, the radiometer data are not expected to closely follow the total flux for "sharp" energy pulses, such as those during the early times of the three tests given in Figs. 4-10 through 4-12. Circumstances in which a reasonable comparison can be made are found between 2.5 and 4 sec for Test 284. In light of a relatively small convective component that should exist, the radiometer data, to the extent that their accuracy permits, clearly support or lend confidence to the total flux measurements.

Temperature of Thermocouple Probes

Measurements of gas temperature as indicated by thermocouple probes at one or two locations within the fireball were obtained by the Sandia Corporation throughout the program. The two measurements from Test 288 are given in Fig. 4-13, and example data from a few other tests are given in Appendix B.

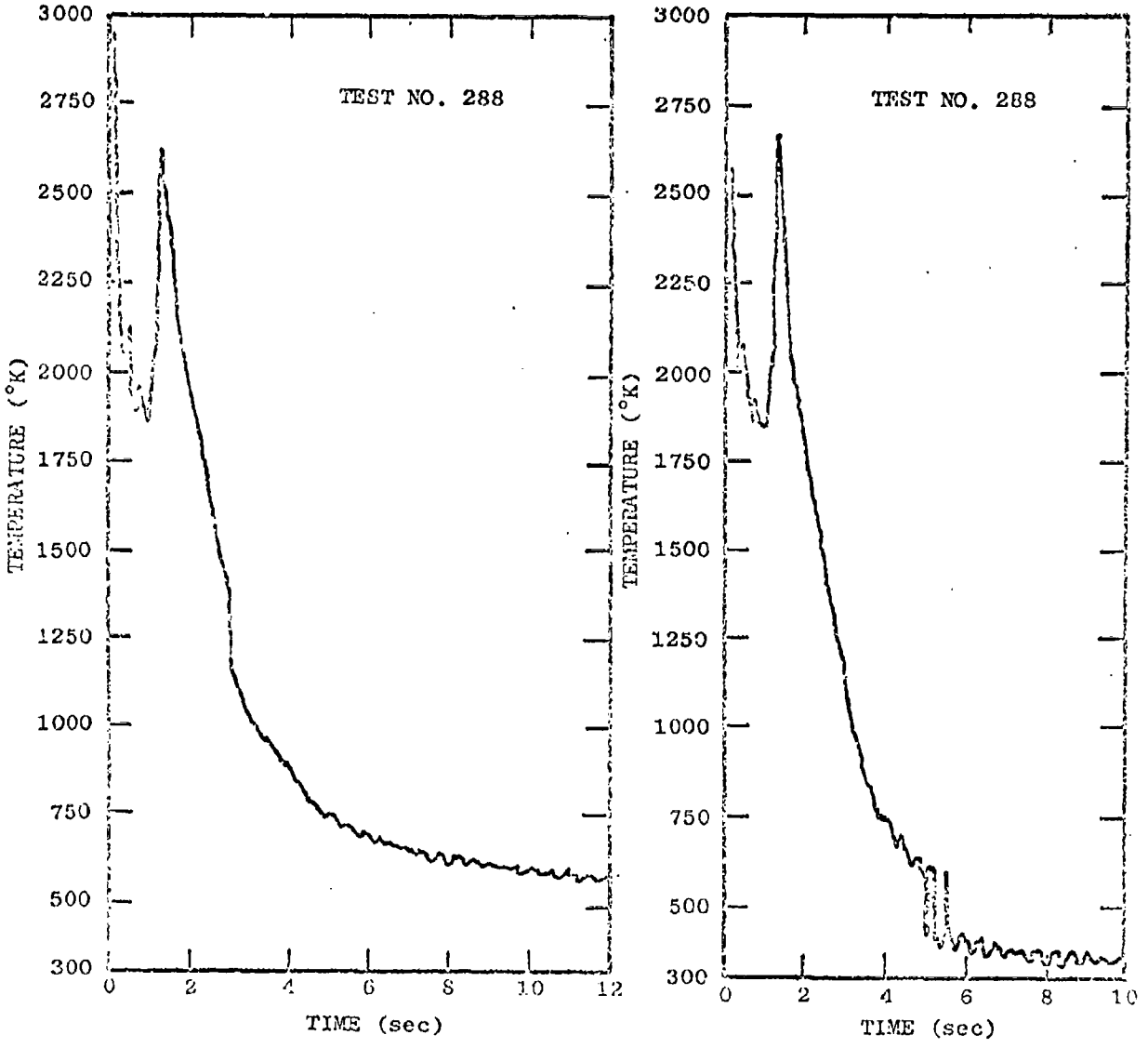

Fig. 4-13. Thermocouple Probe Temperatures from Test 288

The data of Fig. 4-13 may be compared with the gas temperatures for Test 288 from the remote photo-recording pyrometer given in Fig. 4-8. The "peak" values of the thermocouple temperatures are somewhat higher than the pyrometric temperatures. However, an error is not implied by this difference in temperature. Since the pyrometer measures a blackbody equivalent temperature and the thermocouple probe, with some reservation regarding its accuracy, measures the true gas temperature, the pyrometric temperature will, depending on the fireball emissivity, tend to be lower than, but at most equal to, the thermocouple temperature. Because of the uncertainty in the fireball emissivity, exact comparison between the measurements is not possible.

A crude comparison can also be made between the thermocouple data and the heat flux density data. For example, the thermocouple temperature in Fig. 4-13 can be compared with the heat flux density for the same test (Test 288) in Fig. 4-5. A similarity can be seen first with regard to the presence of first and second "peaks" at similar times. However, the radiant flux densities computed from the thermocouple temperature values (for an emissivity of 1) for both data traces are 380 and 250 watts/cm^2 for the first peaks and 250 and 280 watts/cm^2 for the second peaks, and this is substantially higher than the measured heat flux density at corresponding times in Fig. 4-5, which are in the vicinity of 200 and 150 watts/cm^2 for the first and second peaks, respectively. In this case, the direct heat flux density measurements should be equal to or higher than the flux computed from the pyrometric temperatures for any possible emissivity; thus the thermocouple probe measurements do not support the direct heat flux measurements.

HEAT FLUX AT "LARGE" PROPELLANT WEIGHT LEVELS

Heat flux data from explosions of propellant quantities in excess of 25,000 lb are available from only a single test – the Titan I test involving approximately 100,000 lb of the LO_2/RP-1 propellant combination – and reliable scaling relationships from which the bounding and recommended curves may be extended from the 25,000-lb level cannot therefore be obtained on the basis of heat flux data. Scaling relationships are described in the following paragraphs for curves that are instead based on fireball temperature data obtained

from the photo-recording pyrometer measurements and on heating duration data obtained from film coverage. This is followed by a comparison between the bounding curve scaled to the 100,000-lb level and the heat flux data from the Titan I test.

Scaling of Bounding and Recommended Curves

Fireball temperature measurements from the photo-recording pyrometer are available from more than 200 propellant tests, which range in propellant weight from 200 to 25,000 lb. (Only a summary of the 25,000-lb data is presented in this report.) It is found that the fireball temperature, for practical purposes, is invariant with propellant weight over this weight range. The weights of interest extend well above this range, however, and in the absence of experimental data on weights of interest or of suitable analytical relationships between temperature and weight, it is assumed that temperature remains invariant with weight. The uncertainty of this assumption in regard to weights of the order of a million pounds is clearly greater than is desirable. The assumption is, however, not entirely without support; the rough indications of temperature derived from the fireball "color" on the film coverage of comparatively large explosions suggests that the assumption is not grossly unrealistic.

In considering the effect of a temperature invariance on heat flux, it was seen in Figs. 4-7 and 4-8 that the bounding curve and radiant flux computed from the pyrometric gas temperature measurements were similar except at early times. An emissivity of 1 was used in this computation, which should be a close approximation, at least for the fireballs from LO_2/RP-1 explosions. The transfer of energy was therefore almost entirely through radiant transfer, and since the radiant transfer depends on the fireball temperature, the magnitude of the heat flux density should also be invariant with propellant weight.

The scaling relationships for the heating duration are based primarily on film coverage of tests that range to 100,000 lb of propellant. The heating duration as observed in the films is defined as the time from ignition for the fireball to rise from the ground surface, and this duration is nearly identical with the potential heating duration of the heat flux instruments. The heating

duration of a structure, of course, may easily be smaller because of its ejection from the fireball. While it may also be larger, it is difficult to hypothesize a set of circumstances which would cause a structure to follow the motion of the fireball. A heating duration given as the time to fireball "lift-off" is chosen because it is the longest that a structure is likely to experience.

It is found experimentally that for explosions of 200-lb quantities of propellant, the fireball temperature subsides before appreciable rising motion occurs, and the heating duration is thus synonymous with the fireball duration. For quantities of 25,000 lb and more, the fireball will rise substantially, and it appears that the ratio of the heating duration to the fireball duration may be some decreasing function of propellant weight. Since the bounding and recommended curves are based on 25,000-lb heat flux measurements and since most applications are for propellant quantities in excess of 25,000 lb, it is of particular interest to determine the dependence of heating duration on propellant weight for these larger quantities. Heating durations obtained from all the large-scale-test film available are given in Table 4-5, along with the fireball durations and the ratios of these two durations. In addition, estimates of heating durations from the heat flux measurements are included for data traces for the cases in which the duration can be readily identified. These latter durations, which are included to indicate the extent to which they support the film data, should be somewhat less than or equal to the heating durations derived from the film.

There are two uncertainties associated with the magnitudes of the heating duration that have been obtained from the film. First, events such as the fireball lift-off are not always distinct and are subject to interpretation. For tests where it is appropriate, therefore, qualifying remarks will be made. For instance, for several tests, and particularly for Tests 277, 281, and 284, a substantial region of burning remained near the ground after the original fireball lifted from ground surface. Lift-off time for these cases, however, was taken to be the time that the original fireball lifted from the ground surface. This time was chosen because the remaining region of burning was much less extensive than the original fireball, e.g., this region did not include the

Table 4-5

MEASURED HEATING DURATIONS

PROPELLANT TYPE	TEST NO.	FROM FILM COVERAGE			FLUX DENSITY HEATING DURATIONS (sec) FOR STATION		
		HEATING*** DURATION (sec)	FIREBALL DURATION (sec)	RATIO OF HEATING DURATION TO FIREBALL DURATION	H	S	P
LO_2/RP-1	275	4.7	5.7	0.82	4	4.5	-
	278	4.0	4.5	0.89	-	4.5	-
	282	5.2	6.1	0.85	-	-	-
	284	6.8	7.6	0.90	5.5	-	-
	285	3.4	4.8	0.71	-	-	-
	25,000-lb Average	4.8	5.7	0.83	-	-	-
	Titan I	6.7	8.2(12)*	0.82(0.56)*	-	-	-
LO_2/LH_2	281	3.7	9.5	0.39	-	-	-
	288	3.8	11.7	0.33	3	3	3
	290	3.5	6.7	0.52	-	3.5	3.5
	25,000-lb Average	3.7	9.3	0.41	-	-	-
	Saturn IV**	4.5	16	0.28	-	-	-

* There is some difficulty obtaining a distinct fireball duration for the Titan I Test. It may be as short as 8.2 sec, but probably extends to about 12 sec.

** About 92,000 lb of LO_2/LH_2 were involved in the Saturn IV test.

*** Time from propellant ignition to fireball lift-off from the ground surface.

points at which the instruments were located. The fireball for Test 285 was particularly lacking in definition, and the lift-off time is especially uncertain. Regarding the second uncertainty, while accurate timing marks were superimposed on the majority of films, for very few cases were adequate timing marks provided on films that were otherwise useful for evaluating the lift-off time. It was, consequently, necessary to evaluate most of the times on the basis of frame rate settings of the cameras, and this results in a larger error than is desirable. It was observed that the scatter tended to increase as the frame rate increased. Consequently the data were selected from the films with the slowest rates (usually 64 frames per second). Nevertheless, the standard deviation associated with the lift-off times (and total fireball durations), which are listed in Table 4-5, are probably of the order of 20 percent.

Consideration of the heating durations in Table 4-5 suggests that the heating duration does not increase as rapidly with weight as does the fireball duration, i.e., does not scale to the one-third power. With the one-third power law, the average heating duration of 4.9 seconds for LO_2/RP-1 at 25,000-lb would result in a heating duration of 7.8 seconds at 100,000-lb, while a value of 6.7 seconds was obtained for the Titan I test. Similarly for LO_2/LH_2, a heating duration of 4.5 seconds was obtained for the Saturn IV test, while a value of 5.7 seconds would be expected at 92,000-lb for an average of 3.7 seconds at 25,000-lb.

Consider next the ratios of the heating durations to the fireball durations given in Table 4-5. The errors that are contained in the durations which are due to the uncertainties in film speed mentioned above are not contained in these ratios. Once again, the evidence indicates that the heating duration has a somewhat weaker dependence on propellant weight than the fireball duration. For instance, the average ratio from the 25,000-lb LO_2/RP-1 tests is 0.85, while the ratio lies between 0.82 and 0.56 for the Titan I test. Similarly for LO_2/LH_2, the average ratio for the 25,000-lb tests is 0.39, while for the Saturn IV test, the ratio is 0.28. Since it was established in Ref. 3 that the fireball duration increases with the cube root of propellant weight, ratios which decrease with weight suggest a weaker dependence of heating duration on weight.

The conservative assumption that the heating duration increases with the cube root of the propellant weight for weights in excess of 25,000-lb is recommended even though the film data suggest a somewhat weaker dependence. The data are clearly too few and uncertain to recommend the reduction of durations from this rule at comparatively large propellant weights.

In summary, it has been assumed that the heat flux magnitudes will remain invariant with propellant weight, while the heating duration will increase with the cube root of propellant weight. In order to obtain a bounding or recommended curve at a scale in excess of 25,000 lb, it is recommended that the curves given in Figs. 4-7 or 4-8 be used, with the times given in these figures multiplied by $(W/25,000)^{1/3}$, where W is the propellant weight of interest in pounds.

In the section that follows, the heat flux data from the Titan I test are compared with the bounding curve scaled to the 100,000-lb level, with the above scaling rule applied.

Titan I Data

The instruments and their locations for the Titan I test, with one exception, were the same as for the 25,000-lb test series. The only modification was the replacement of copper slabs by iron slabs at Positions 1 and 5 of instrument Station P. In anticipation of the relatively long durations of this test, some of the copper slabs were replaced by iron slabs to avoid an error that would be encountered toward the end of the heating pulse if 1.4-in.-thick copper slabs were used. The flux curves from the copper slabs will gradually become larger than the correct value. It should also be noted that the thermocouple junction depth for the iron slabs is comparatively small (0.0002 in. compared with 0.005 in. for copper), with the consequence that slab temperature data and heat flux data will tend to be more erratic since the thermocouple junction can more readily sense minor and comparatively short-lived heating activity.

The heat flux density data are given in Figs. 4-14 through 4-16. Two of the data curves from Station P (Fig. 4-16) have somewhat larger than ordinary errors over certain time regions due to noise in the corresponding temperature

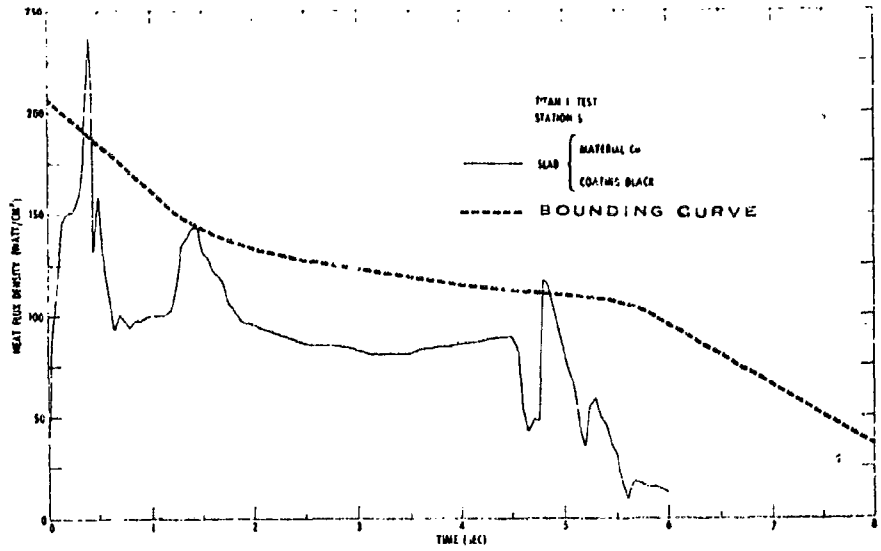

Fig. 4-14. Heat Flux Density at Station S for the Titan Test

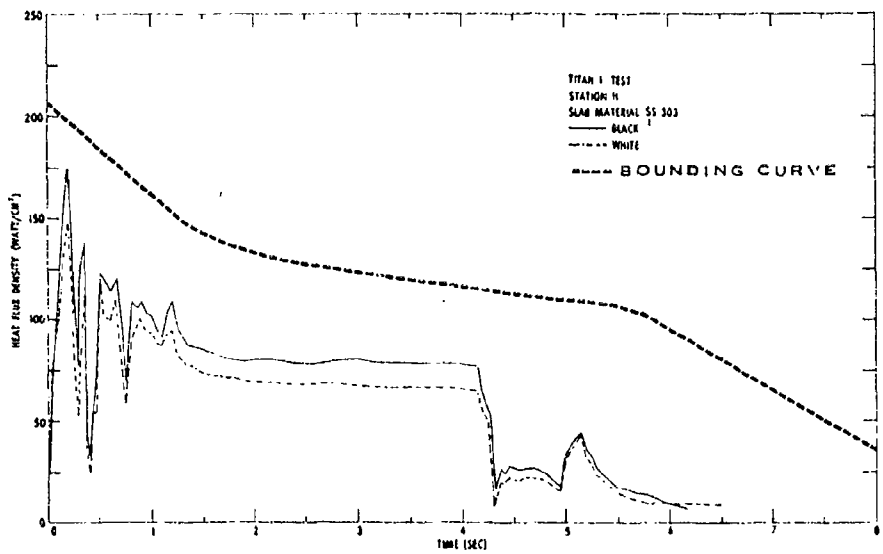

Fig. 4-15. Heat Flux Density at Station H for the Titan Test

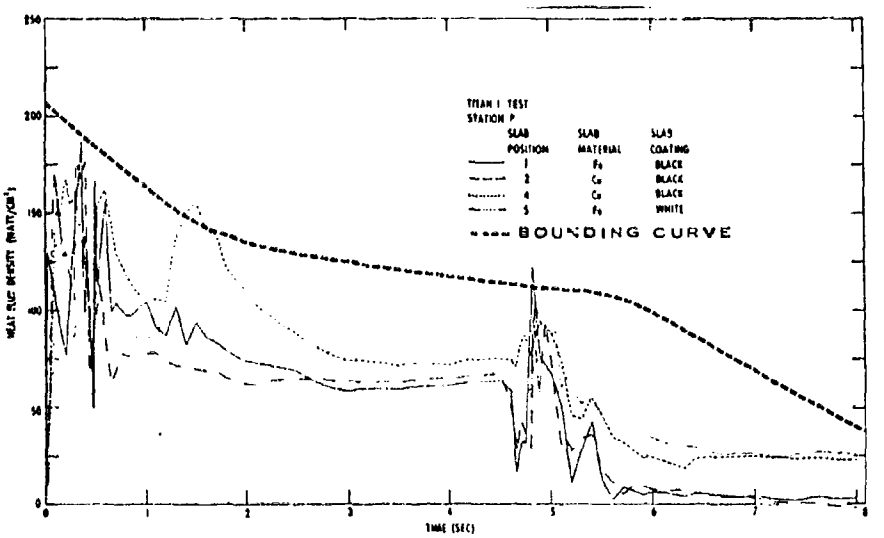

Fig. 4-16. Heat Flux Density at Station P for the Titan Test

records, and the details of these errors are noted in the data presentation section (Appendix B).

Included in Figs. 4-14 through 4-16 are scaled versions of the "bounding curve" that was given for the 25,000-lb LO_2/RP-1 test series in Fig. 4-3 in which the scaling rule described in the previous section has been applied.

Although the data from a single test can not validate the scaling that has been applied, it can be seen that the flux data are clearly not inconsistent with the scaled curve.

The cumulative or time-integrated flux to 8 sec for each flux curve is listed in Table 4-6, along with the ratio of each to the time-integrated flux of the scaled bounding curve, the latter being approximately 1075 watt-sec/cm^2.

The ratios of the measured cumulative flux density to that of the bounding curve are similar to those obtained throughout the 25,000-lb LO_2/RP-1 tests (Table 4-4). There is a similarity also between the ratios of cumulative flux

Table 4-6

CUMULATIVE FLUX DENSITY FROM THE TITAN I TEST

Instrument Station	Slab Material[1]	Surface Coating	Cumulative Flux Density ($watt\text{-}sec/cm^2$)	Fraction of the Scaled Bounding Curve
P	Fe	Black	416	.35
	Cu	Black	588[2]	.50[2]
	Fe	White	390	.33
	Cu	Black	535[2]	.45[2]
S	Cu	Black	555[2]	.47[2]
H	SS	Black	418	.36
	SS	White	371	.32

(1) SS refers to Stainless Steel 309.
(2) Cumulative Flux Value slightly larger than correct value.

density from black-coated slabs to those of white-coated slabs, suggesting again that there is a rapid deposition of explosive products. The actual deposit was not so thick as had been obtained for the 25,000-lb test, although it was sufficiently thick to be opaque both on upper horizontal surfaces and on side (vertical) and face-down surfaces.

HEAT FLUX DENSITY FROM THE 200- AND 1000-LB LO_2/RP-1 AND LO_2/LH_2 TESTS

There are two primary reasons for evaluating some of the heat flux data from the 200- and 1000-lb LO_2/RP-1 and LO_2/LH_2 tests. First, at the lower propellant weight levels, additional test conditions were introduced, and greater ranges of the values of given test conditions were obtained; and it is desirable to consider the effect of varying the test conditions on the heat flux. This has become important for the following reason. A theoretically based evaluation of the heat flux vs time for large quantities of the LO_2/RP-1 propellant combination resulted in flux magnitudes that were larger than the empirically obtained bounding curve by as much as a factor of two and in heating durations that are approximately one-half of that associated with the

bounding curve, although the cumulative or time-integrated flux compared within about 1 percent.* The theoretical curve is based on the following set of assumptions regarding test conditions and properties of the fireball:

(1) The propellants and air are added to the fireball at constant rates, and the propellants were added uniformly throughout the fireball

(2) The total amount of propellants available participate in the fireball reactions

(3) The fireball is an isothermal homogeneous radiating body in chemical equilibrium at 1 atmosphere pressure

(4) The fireball is spherical (hemispherical initially)

(5) The fireball emissivity is equal to 1.

While it is clear that, given these conditions, comparatively severe but short-lived flux curves would result, it is difficult to assess how realistic or probable some of them are. Since additional test conditions existed at the 200- and 1000-lb levels, and perhaps more importantly, since a comparatively wide range of values within some of the test condition categories existed for the small-scale tests, it is of particular interest to see if the flux data for any case exceeds the appropriate bounding curve, and this comparison is given below, along with a discussion of test conditions.

Regarding the second reason for considering the small-scale flux data, it is desirable to evaluate the effect of propellant weight alone on heat flux. This requires data whose test conditions otherwise match those of the 25,000-lb tests. A far less than desirable sampling of such data is available, and the question is pursued only to the extent that seems practical.

Before the data are examined, it is necessary to consider new test conditions. The 25,000-lb tests were described above in terms of the three test conditions of propellant type, propellant configuration, and ignition time. For the CBGS configuration, in which the propellant tankage was dropped from

* The fundamental analysis of this evaluation is given in Ref. 4, and an adaption of the results leading to heat flux within a particular fireball is given in Ref. 5.

a tower and the propellants allowed on impact to spread along the ground surface, it was not necessary to consider the impact velocity, i.e., the drop height, since it was identical for all tests. The impact velocity was about 44 ft/sec, and is referred to as the medium velocity. In addition, high and low velocities of 78 and 23 ft/sec were used for the 200- and 1000-lb tests. This is the only additional CBGS test condition for which heat flux data were evaluated. It might be expected that the flux from a given test would be similar to that for a second test having twice the velocity but half the ignition time, since the general shape and dimension of the propellant mixture would be similar in the two cases (for a time the propellants spread horizontally on impact at about the same speed as the impact velocity). However, it is more complex than this since the propellant mixing process is different in the two cases. Thus the magnitude of the explosion would be different, and this in turn may affect the heat transfer. Effects attributable to the magnitude of the explosion are discussed below.

For the CBM configuration, the other test conditions specified for the 25,000-lb tests were the propellant type and ignition time. The 200-lb tests were varied in two additional ways, although for reasons which are discussed below, we have evaluated data for a very limited number of tests having conditions different from the 25,000-lb tests.* One condition pertains to the length-to-diameter ratio (L/D) of the propellant tank. The 200-lb tests were conducted with an L/D of 1.8 or 5, although most tests, and all 1000- and 25,000-lb tests, were conducted with a value of 1.8. For the second condition, two-thirds of the normal weight of fuel and oxidizer of a 200-lb test was used with the normal 200-lb-capacity tank. This reduction of propellants resulted in explosions of larger magnitude.

For all CBM tests the propellants were confined to the tankage until the propellant mixture was ignited. Variations in the ignition time and the two

* A third test condition pertained to the size of the opening created in the diaphragm that initially separated the fuel and oxidizer. However, this condition was varied only during the early part of the test program, when the quality of the thermal data was poor, and these data have not been used.

conditions mentioned in the previous paragraph lead to variations in the magnitude of the explosion. Since the initial propellant mixture is confined to the comparatively small region of the tank, it would be expected that these test conditions do not markedly influence the flow velocities (or patterns) associated with the explosion, except insofar as they influence the magnitude of the explosion. That is, while the flow velocities depend on the magnitude of the explosion, a single number that quantifies the magnitude of the explosion should suffice as a number that collectively specifies these test conditions. For this reason, priority was given to obtaining flux data from tests having a wide range in their magnitudes of explosion rather than in their variety of these test conditions mentioned. For the CBGS propellant configuration, tests leading to a wide range of explosive magnitudes were evaluated, although some priority was given to impact velocity.

The basic blast data obtained from these tests were peak overpressure and positive-phase impulse, both as a function of distance from the propellant explosion. Equivalent explosive weights at each measurement distance were determined separately for peak overpressure and positive-phase impulse, using standard TNT surface burst reference curves. Characteristically the TNT equivalent weights computed from these data vary both as a function of the shock wave parameter used (peak overpressure or positive-phase impulse) and the distance from an explosion. At long distances, however, the equivalent weights tend to approach an equal and constant value, which has been defined as the terminal equivalent weight (when expressed in pounds of TNT) or terminal yield (when expressed as a percent of the total propellant weight).

The results of efforts to determine the effect of yield on heat transfer should be mentioned. To investigate the effect, plots were made of cumulative heat flux and of heat flux averaged over its duration vs yield for given conditions of propellant type, weight and configuration (plots not shown). No data trends were evident in the plots for any set of conditions, although the large data scatter would prevent any but pronounced trends from being revealed.

*Explosive yields are defined and discussed in Ref. 1.

All heat flux data that have been evaluated for the 200- and 1000-lb LO_2/RP-1 and LO_2/LH_2 tests are presented in Appendix B (Figs. B-39 through B-102). Data traces which tend to have the largest magnitudes were selected from among these data, and those traces are superimposed in Figs. 4-17 and 4-18 for the 1000-lb LO_2/RP-1 and LO_2/LH_2 tests, respectively, and in Fig. 4-19 for the 200-lb LO_2/RP-1 and LO_2/LH_2 tests. The bounding curves that have been scaled to the appropriate 200- or 1000-lb weight level by means of the scaling rules given above are also presented in the figures.

Temporarily disregarding the differences of duration between the bounding curves and the flux data, the flux data magnitudes, with one minor exception, tend to lie somewhat below the corresponding bounding curve. The exceptional case consists of a short pulse that exceeds the bounding curve for Test 248, as shown in Fig. 4-19. The test conditions for all the small-scale tests are listed in Table B-2. In summary, it is perhaps not misleading to say that the data are from tests which substantially cover the range of interest of ignition times for most propellant types, configurations, and weights; that the physically possible explosive yield range is well covered for most of these categories; and that the three impact velocities for the CBGS configuration are represented in addition. Moreover, the flowing of one propellant over another for these ranges of time and with this variety of relative velocities, and the mixing of propellants within the tankage for these ranges of time encompass many, although not all, of the physical circumstances that can or are likely to be encountered in an actual missile launch or aerospace vehicle mishap. At least for this range of conditions, the probability of significantly exceeding the bounding curve is evidently small.

Regarding the heating durations, from the discussion of the scaling of bounding curves above, we would expect the flux data to occasionally persist beyond the bounding curve scaled to the 1000-lb level. It was mentioned that for 1000-lb quantities or less, the fireball temperature subsides before an appreciable fireball rise occurs, and therefore that the heating and fireball durations are synonymous. Since the bounding curve is based on 25,000-lb tests, where there is a substantial rise, 1000-lb flux data durations should be potentially larger than for the (cube root) scaled bounding curve.

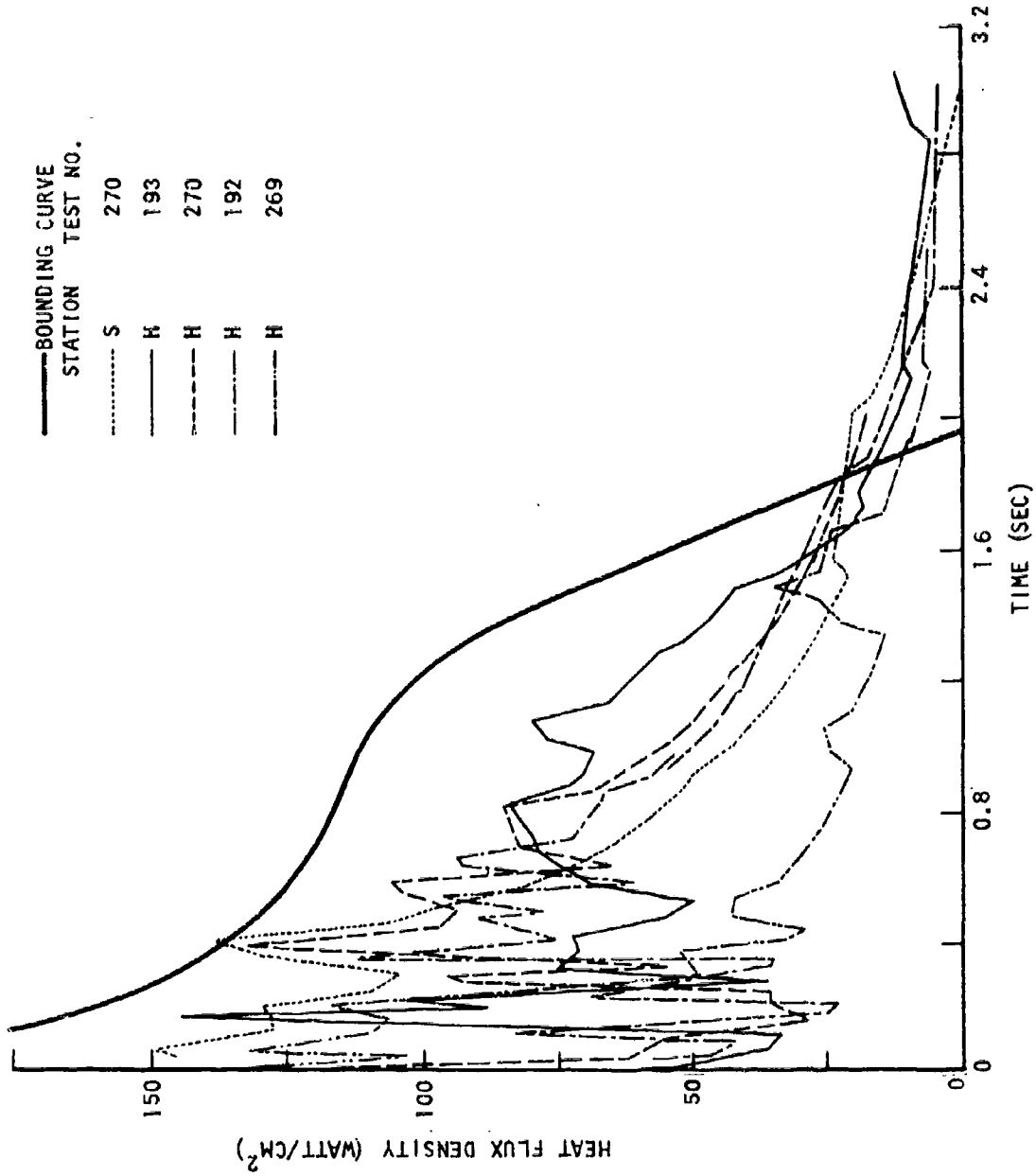

Fig. 4-17. Composite Heat Flux Graph for the 1000-lb LO_2/RP-1 Tests

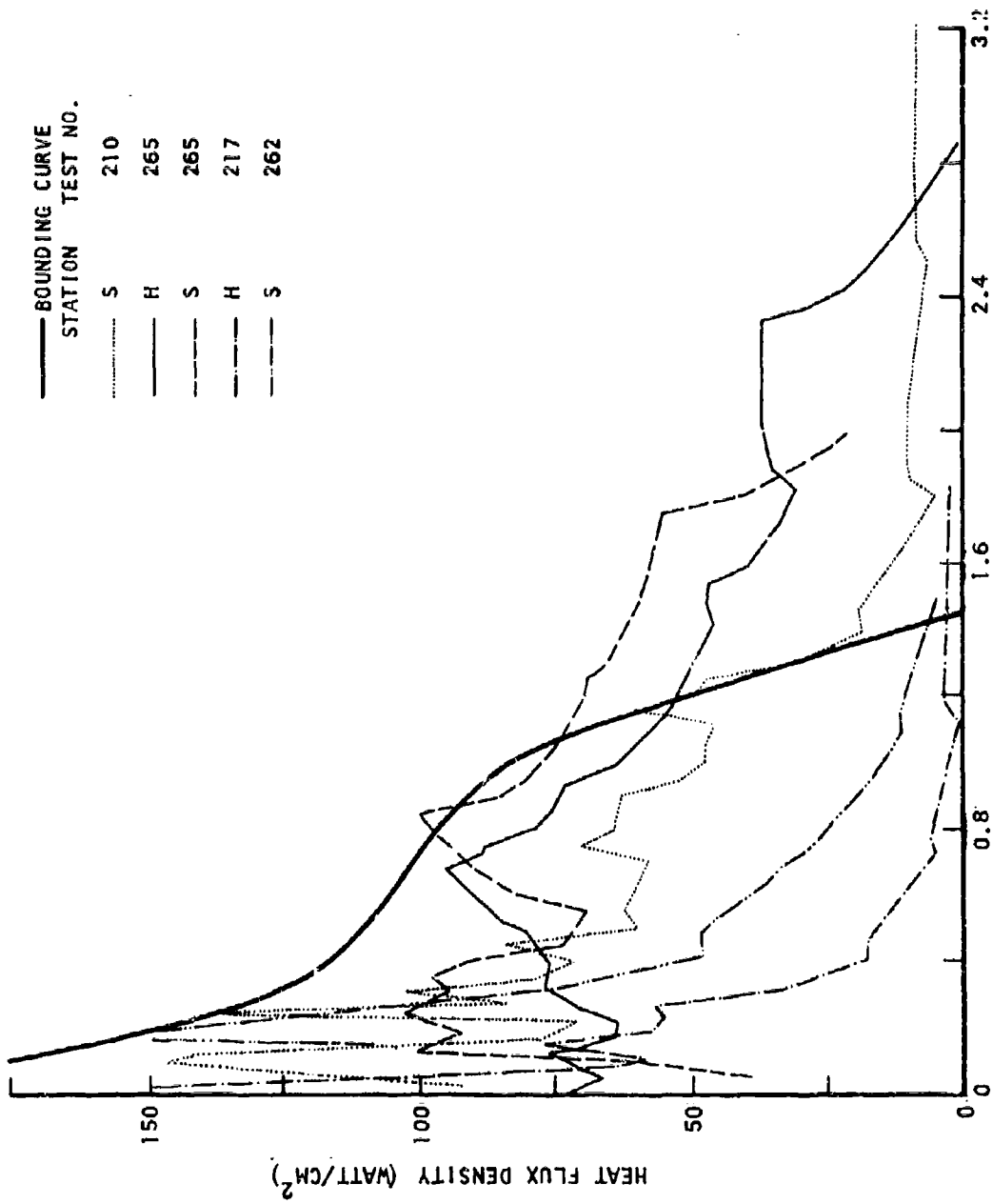

Fig. 4-18. Composite Heat Flux Graph for the 1000-lb LO_2/LH_2 Tests

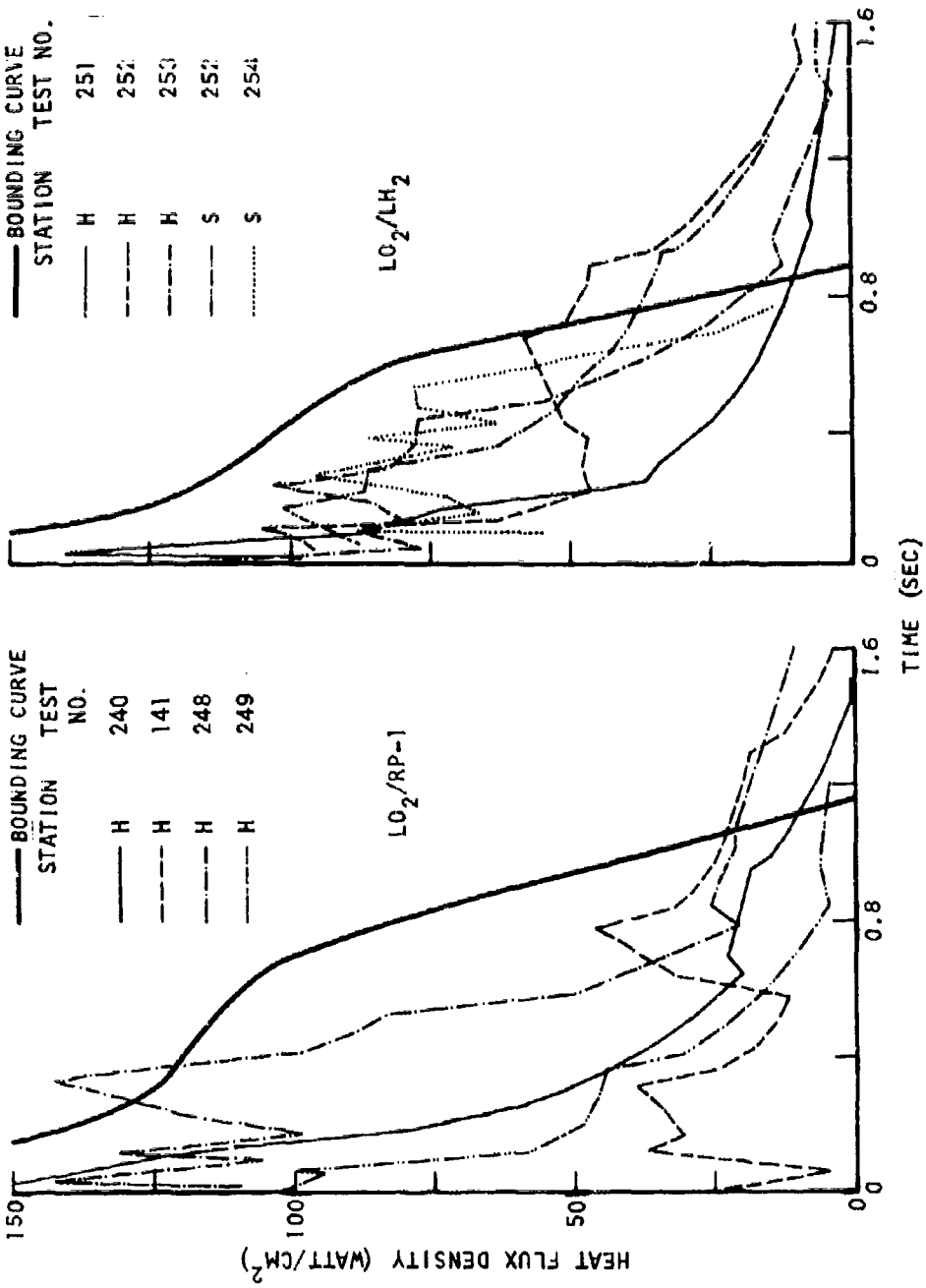

Fig. 4-19. Composite Heat Flux Graphs for the 200-lb LO_2/RP-1 and LO_2/LH_2 Tests

In order to compare these durations, flux data were selected from the 1000-lb tests whose magnitudes at appreciable levels persist the longest, and these data and the corresponding bounding curve are superimposed in Figs. 4-20 and 4-21 for LO_2/RP-1 and LO_2/LH_2, respectively. The figures illustrate, of course, that some of the data do extend well beyond the bounding curve. Thus, the scaling rule given above does not apply for weights significantly less than 25,000 lb, and another rule will be provided below. According to Eq. (2.2), for 1000-lb quantities the fireball duration, and therefore the heating duration, is approximately 2.2 sec for these propellants. While some of the durations in Figs. 4-20 and 4-21 extend beyond 2.2 sec, this is not surprising since the standard deviation given for Eq. (2.2) is approximately 85 percent. This percentage, of course, indicates how frequently durations of a given magnitude in excess of 2.2 sec would occur. The most meaningful comparison is between the 2.2 sec given by Eq. (2.2) and the average duration from the heat flux data traces. While the heating duration from the heat flux data is not always distinct, estimates from all 1000-lb data have been made (ignoring those traces in which it is indistinct), and the average calculated. From 34 tests, the durations ranged from 0.2 to 3.2 sec, with an average of 2.0 sec; and this average compares well with the 2.2 sec given by Eq. (2.2). It should be noted, also, that this average should be somewhat less than from the equation. During its final stages, the fireball consists of high-temperature regions of decreasing dimension, and the likelihood that the instruments will be in such a region decreases correspondingly. The heating of instruments will thus tend to cease somewhat before the fireball vanishes.

The similarity between fireball durations obtained from the flux data and that given by Eq. (2.2) tends to confirm that the latter is a good measure of the mean heating duration for propellant quantities of 1000 lb or less (and perhaps somewhat more), and this provides a firm basis for recommendations of heat flux vs time for this weight range. The recommended equations are given in Section 5.

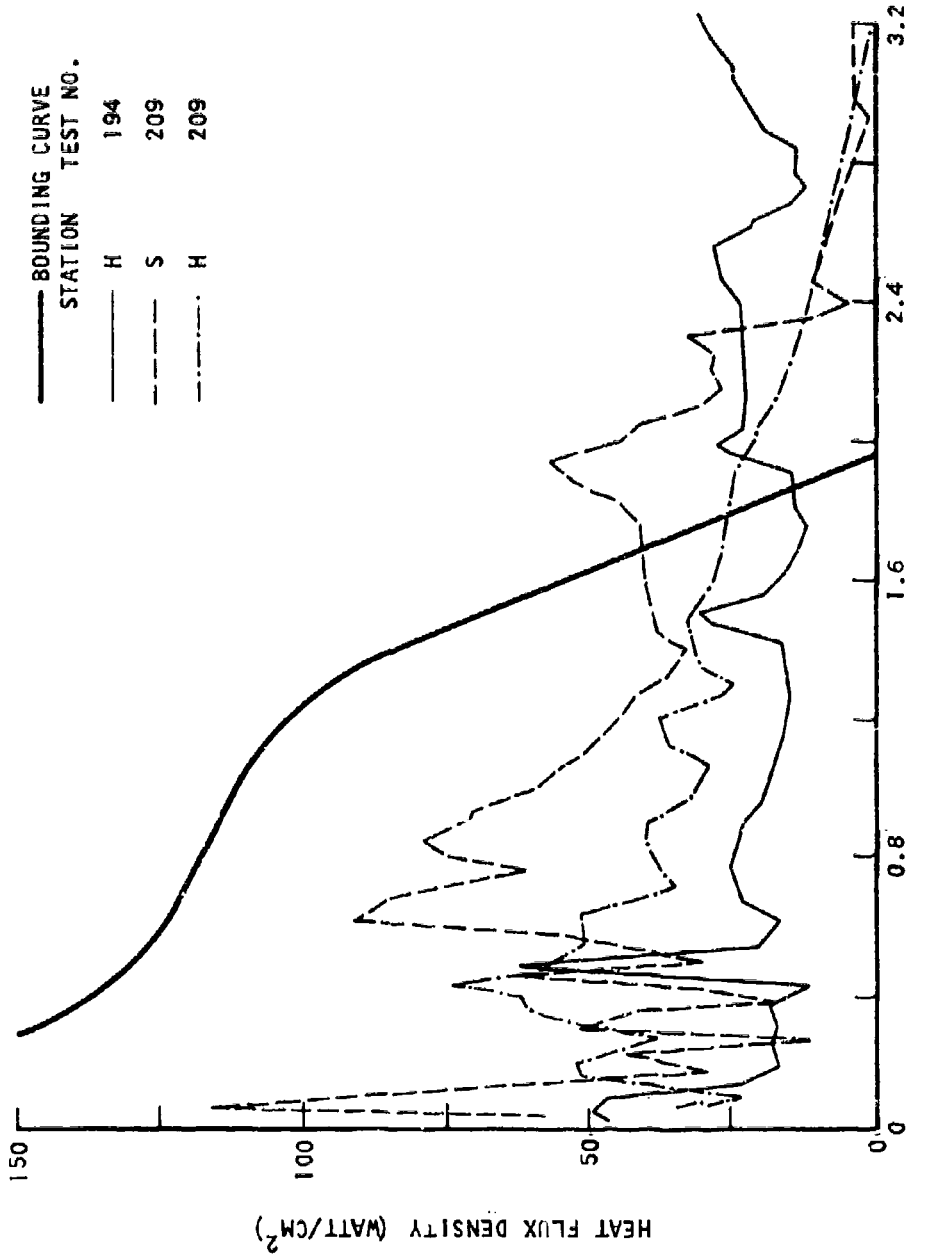

Fig. 4-20. Long Duration Heat Flux Traces for the 1,000-lb LO_2/RP-1 Tests

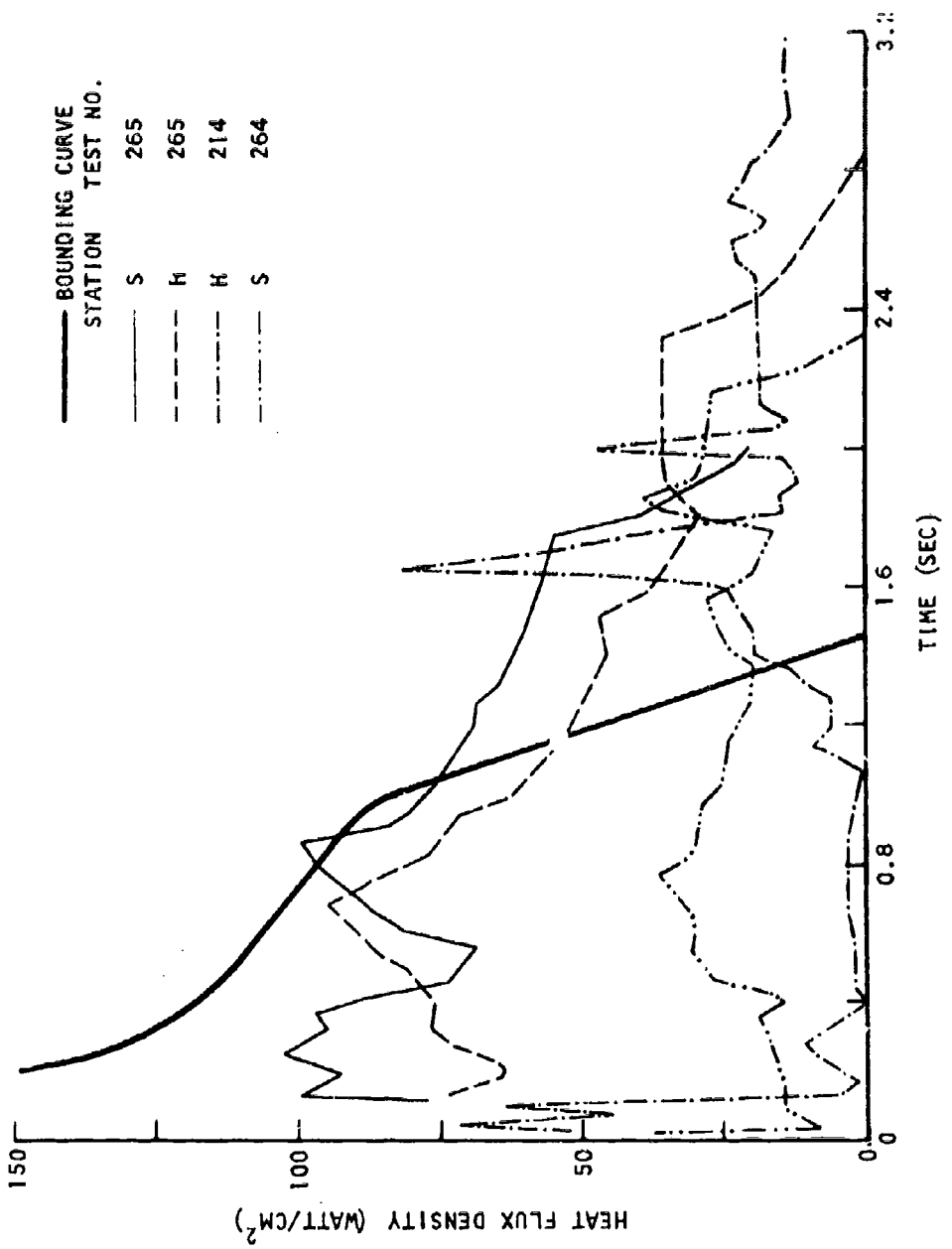

Fig. 4-21. Long Duration Heat Flux Traces for the 1,000-lb LO_2/LH_2 Tests

HEAT FLUX DENSITY FROM THE N_2O_4/50% UDMH-50% N_2H_4 TESTS

Thermal data were evaluated from six tests conducted with the hypergolic propellant combination of N_2O_4/50% UDMH-50% N_2H_4, three each at the 200- and 1000-lb levels. The test conditions for all the tests were identical. The propellant tankage was dropped from 100 ft, with the propellants being freed from the tankage just before their impact with the ground surface. In this case, ignition was, of course, at impact.

All available heat flux data are presented in Figs. B-101 through B-112 for the 200- and 1000-lb tests. All flux data for these tests from slabs whose surface was coated with a black deposit have been superimposed on a single graph for each propellant weight, and these plots are given in Fig. 4-22.

Perhaps the most striking aspect of the data is that the magnitudes are small compared with a large portion of the cryogenic (LO_2/RP-1 and LO_2/LH_2) data. Measurements of gas temperature from the photo-record pyrometer (data not included) indicate temperatures for the hypergolic tests are not sufficiently different from those for the cryogenic tests to account for the differences in flux.

The heating durations from the hypergolic tests do compare with those from the cryogenic tests. This is not surprising since fireball durations for both cases are similar according to data and analysis given in Ref. 3.

RADIANT FLUX DENSITY OUTSIDE THE FIREBALL

Summary plots of radiant flux measurements at locations outside of the fireball are presented in Figs. 4-23 and 4-24 for the 25,000-lb LO_2/RP-1 and LO_2/LH_2 tests, respectively. Information presented in these plots is limited to a curve representing the data mean for all tests (the measurements from each test rather than each measurement being weighted equally) along with an indication of the data range (shaded area). Other than adding a few qualifying remarks, the Presentation of Results subsection does not consider these

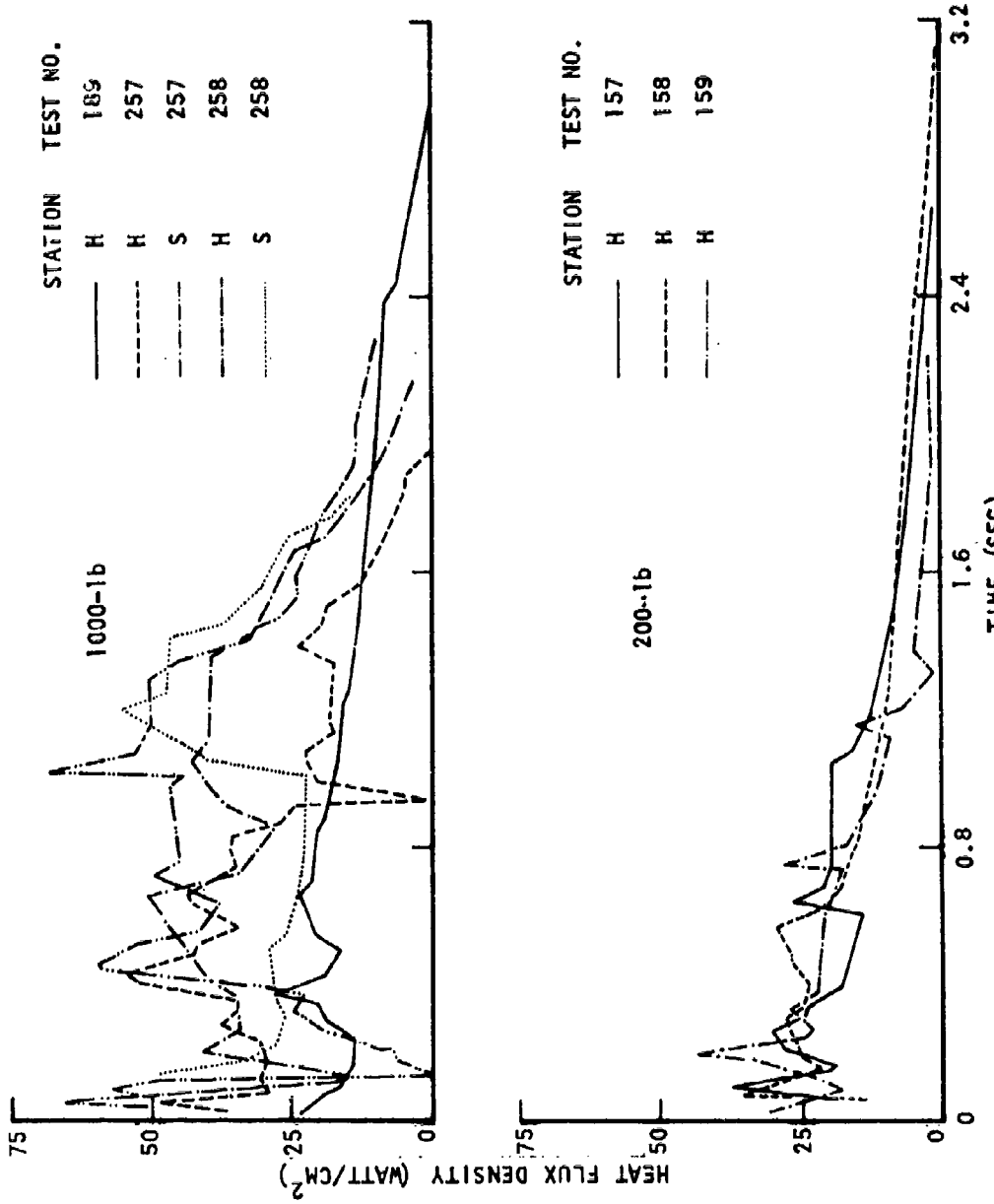

Fig. 4-22. Composite Heat Flux Graphs for the 200- and 1000-lb N_2O_4/50% UDMH-50% N_2H_4 Tests

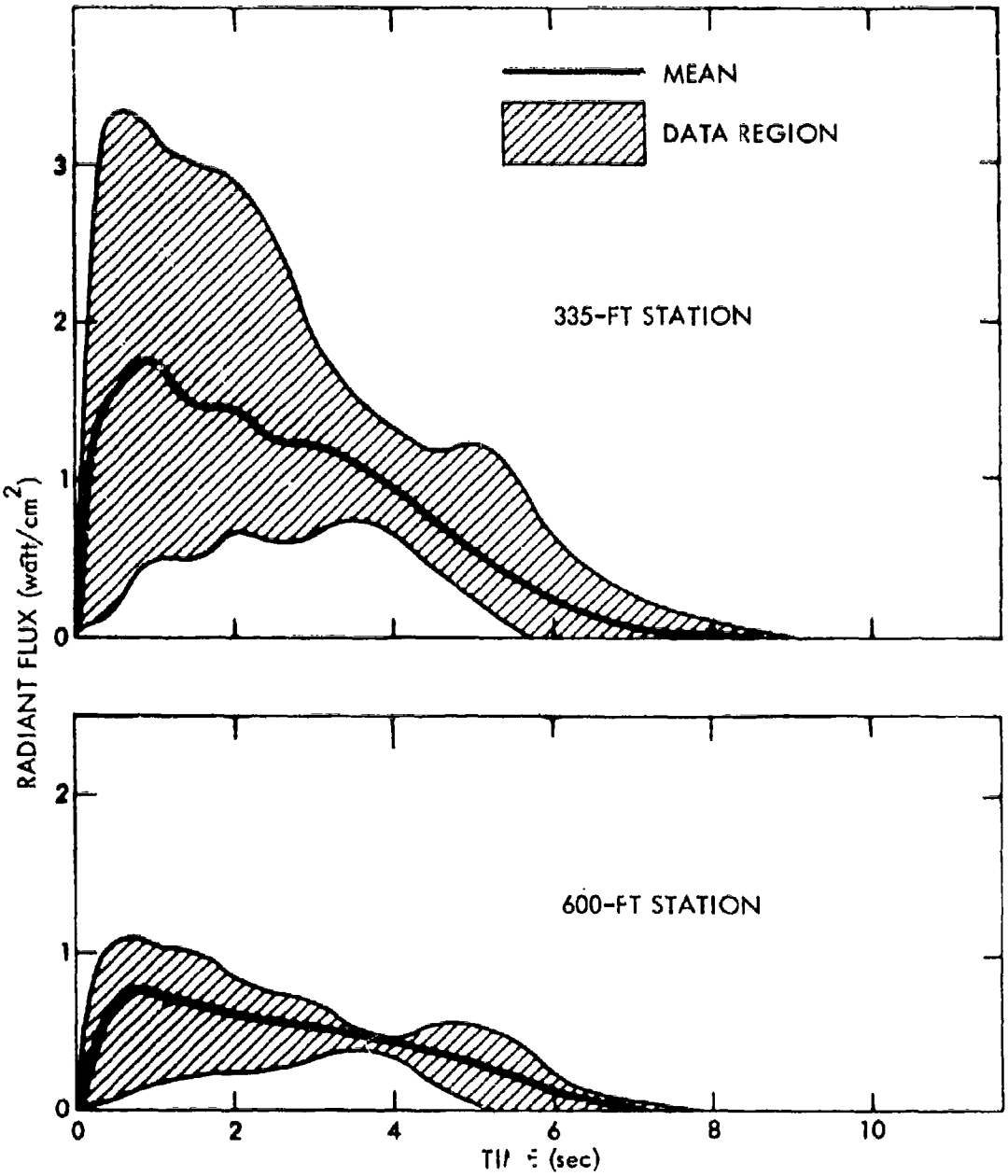

Fig. 4-23. Summary Plots of Radiant Flux Density Outside the Fireball for the 25,000-lb LO_2/RP-1 Tests

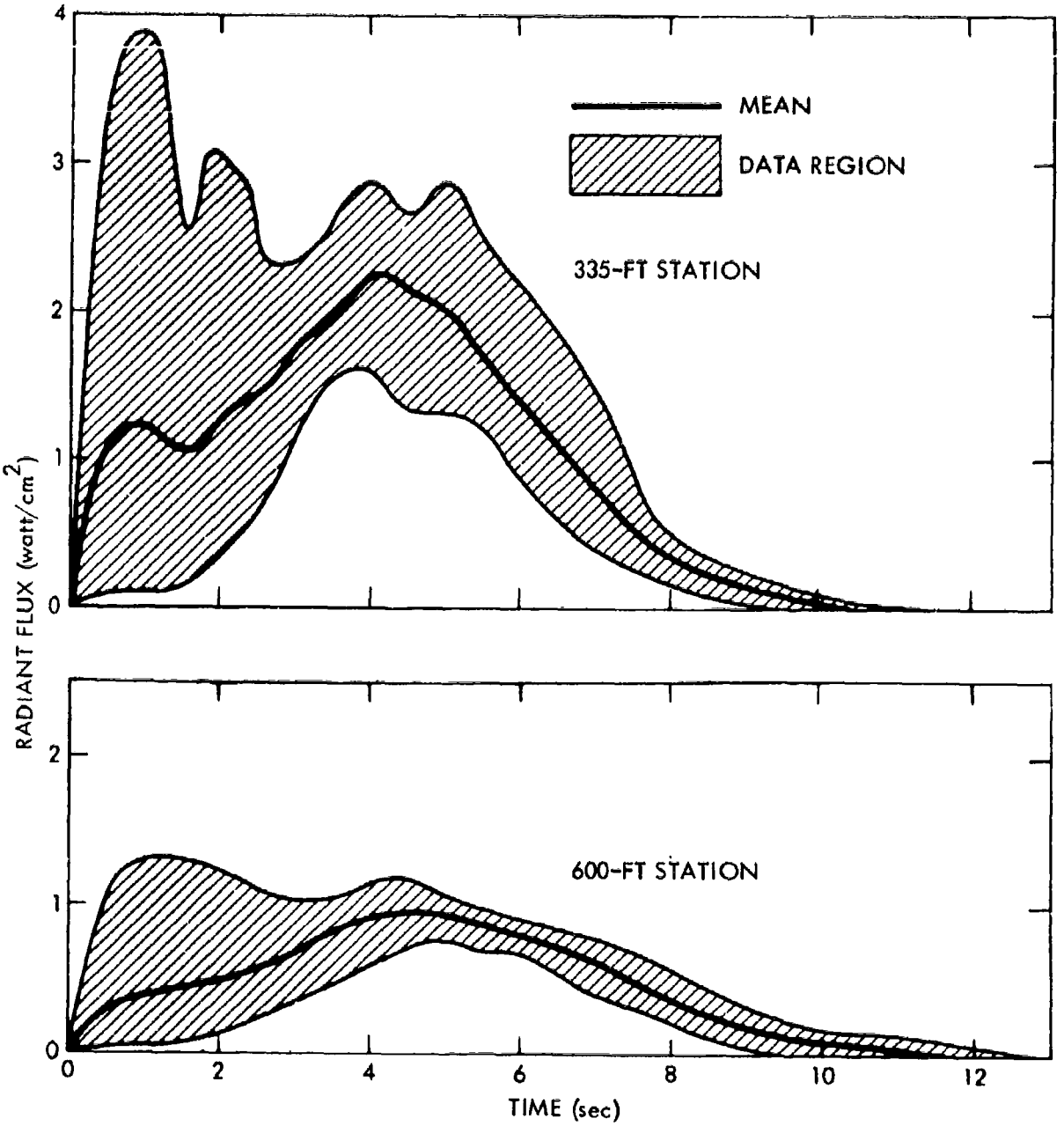

Fig. 4-24. Summary Plots of Radiant Flux Density Outside the Fireball for 25,000-lb LO_2/LH_2 Tests

data in any greater detail than is found in the summary plots. However, all of the available data (from both the 25,000-lb and Titan tests) are presented in Appendix B in order that the data may be examined in greater detail.

Generally, three radiometers were used per test, two at 335 ft from ground zero along radial gauge lines 120 deg from each other (gauge lines A and B), with the third at 600 ft from ground zero along one of these gauge lines (along gauge line A). For only two tests, however, were satisfactory data acquired from both radiometers at 335 ft. For one of these two tests, Test 278, the flux at 335 ft along gauge line B rose during the later stages of the heating pulse to a value significantly larger than that from the corresponding 335-ft gauge line A station, as seen in Fig. 4-25. Photographic coverage indicates that the fireball drifted toward the gauge line B station, thereby accounting for the inflated value. Gauge line B data from this test were consequently not used in the construction of the summary plot of Fig. 4-23. The data from gauge line A, even though somewhat deflated for the same reason, were used, however, since their deflation will tend to be less pronounced. This comparatively extreme example has been mentioned primarily to illustrate the "coarse nature" of these data, because such physical occurences, but of lesser degree, were present in the other tests. Moreover, these measurements are comparatively inaccurate, ranging, it is estimated, between 10 and 20 percent, depending on the quality of a given raw data trace; and as fireball temperatures subside, these errors tend to increase due to energy absorption within the radiometer window.

One further qualification of the data should be noted. The "field of view" of the external radiometers is inherently restricted to 90 deg (45 deg in any direction from the instrument "line of sight"), and the instruments are directed approximately 10 deg above the horizontal. It is thus possible for the fireball to rise sufficiently to escape view of the radiometers, first from those at 335 ft and later at 600 ft, before its temperature or radiant output has entirely subsided. This occurred noticeably for Test 288, as can be seen by comparing the 335 and 600 ft gauge line A flux traces in Fig. 4-26. During the early stages, the flux at 600 ft should be, and is to the first approximation, one-third of that at 335 ft, while at later stages this ratio changes,

and eventually the flux is greater from the 600-ft instrument. Whereas this has not occurred while any significant flux levels persisted, it cannot be concluded that the emitted energy from the fireball has subsided, since much of the decrease at the instrument is due to increase in distance between the fireball and the instrument produced by the elevation of the fireball. Thus fireball durations are not accurately reflected in the flux–time curves. It is of interest, however, to compare the duration for 25,000 lb as given by Eq. (2.2), which is approximately 6 sec, with the somewhat larger durations suggested by Figs. 4-23 and 4-24, the latter averaging approximately 7 and 11 sec for LO_2/RP-1 and LO_2/LH_2, respectively. While the difference in duration for LO_2/LH_2 is nearly a factor of two, it will be recalled that the estimated standard error of Eq. (2.2) is 84 percent.

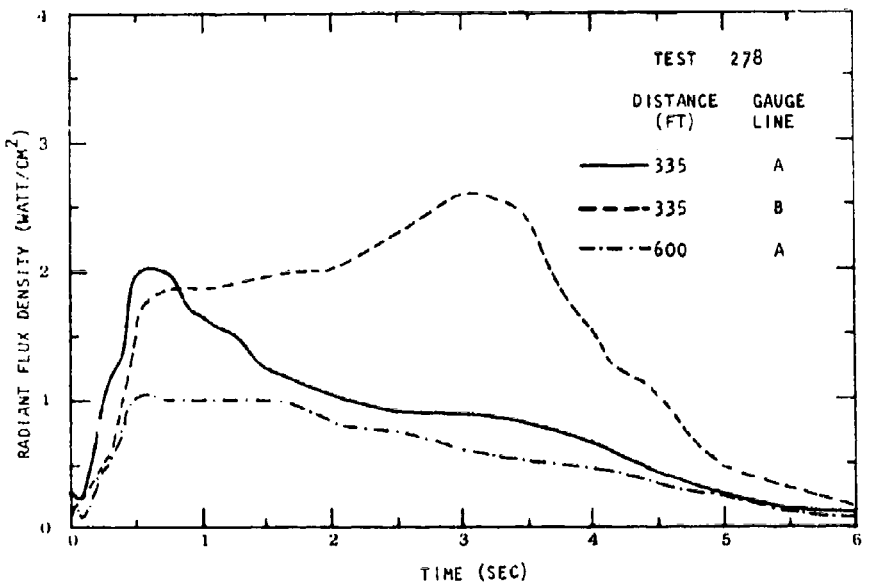

Fig. 4-25. Radiant Flux Density Outside the Fireball from Test 278

Radiant flux density at the 600-ft station for the Titan test is given in Fig. 4-27. The fireball dimensions and their uncertainty prevented interpretation of the radiometer data at the 335-ft stations; the fireball expanded beyond the field of view of all photographic coverage, but diameters along the horizontal near the ground surface were estimated to be from about 800 to 1000 ft. The uncertainty in diameter also prevents exact interpretation of the data at 600 ft.

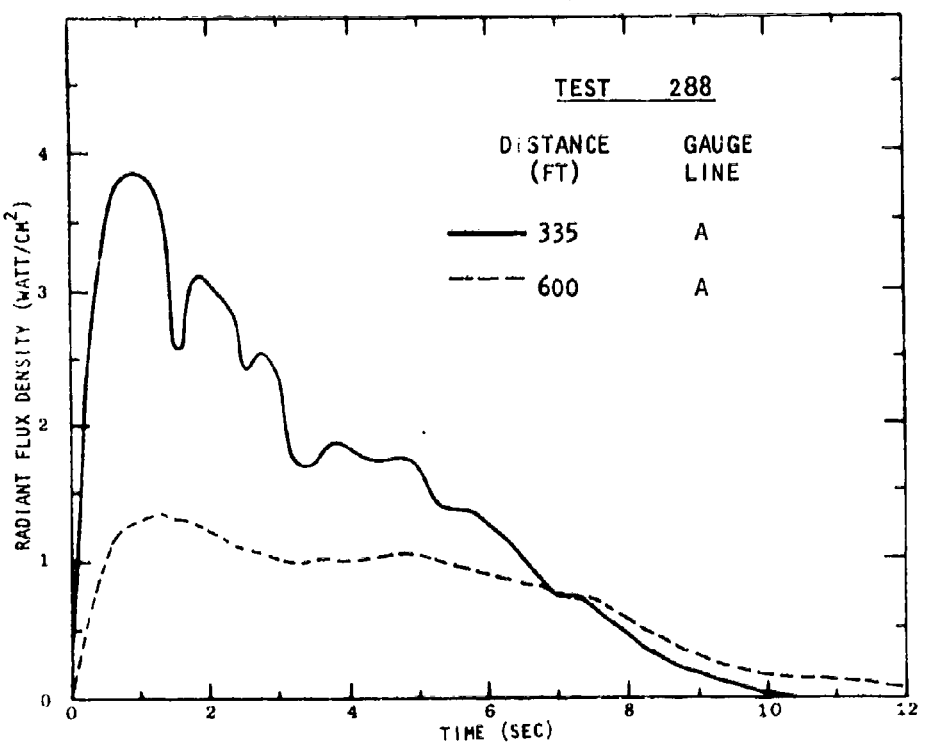

Fig. 4-26. Radiant Flux Density Outside the Fireball from Test 288

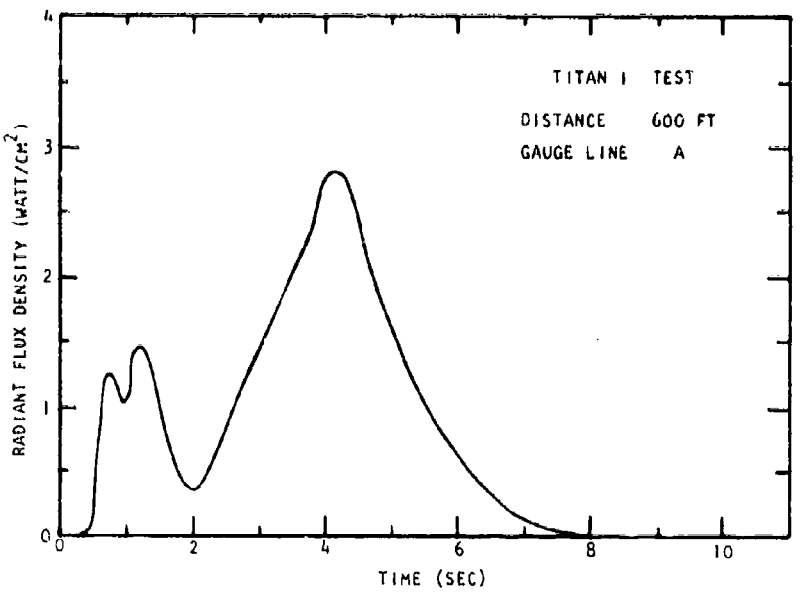

Fig. 4-27. Radiant Flux Density Outside the Fireball from the Titan I Test

Section 5
SUMMARY OF HEAT TRANSFER PREDICTION

This section is a summary describing the expected dimensions and duration of liquid propellant fireballs and of the heat flux density with time within them, each as a function of the quantity of propellants involved.* Remarks indicating the basis and limitations of each prediction are also included.

The dimensions of the fireball depend generally on the quantity of propellants. An empirically derived expression relating the fireball dimension in terms of an equivalent diameter D in feet to the total propellant (fuel and oxidant) weight W in pounds for the propellant combinations of LO_2/RP-1, LO_2/LH_2, RP-1/LH_2/LO_2, and N_2O_4/50% UDMH-50% N_2H_4 is given by**

$$D = 9.56\ W^{0.325} \qquad (5.1)$$

where the estimated standard error in the diameter is 30 percent. Equation (5.1) does not always provide an accurate indication of the maximum dimension(s) of the fireball since "in those instances where the fireballs were markedly asymmetrical, attempts were made to estimate equivalent spherical diameters."*** An indication of the departure from the diameter given in Eq. (5.1) of the maximum dimensions that can occur is provided, for instance, by the Titan test, which involved approximately 100,000 lb of LO_2/RP-1; the maximum horizontal fireball dimension from this test was estimated to be from 800 to 1000 ft, while Eq. (5.1) indicates diameters of approximately 400 ft.

---

* Information permitting the evaluation of thermal hazards external to th fireball through radiant energy transfer are given in Section 4.

** Equation (5.1), along with Eq. (5.2) below, have been extracted from J. B. Gayle and J. W. Bransford, Size and Duration of Fireballs from Propellant Explosions, NASA TM X-5314, August 4, 1965.

*** Ibid.

The fireball duration τ in seconds, that is, the time over which fireball temperatures persist at hazardous levels (excluding residual fires from propellants which tend to collect in ground surface depressions or structural confinements) is given by,

$$\tau = 0.196\ W^{0.349} \tag{5.2}$$

where the standard error in the duration is 84 percent.

Curves from which the heat flux density with time within the fireball can be obtained for a given propellant weight are given in Figs. 5-1 and 5-2 for the LO_2/RP-1 and LO_2/LH_2 propellant combinations, respectively. The time in these figures is given in seconds by,

$$\tau_o = C\ W^{1/3} \tag{5.3}$$

for a total propellant weight W in pounds, with a value of C of 0.113 for LO_2/RP-1 (Fig. 5-1) and of 0.077 for LO_2/LH_2 (Fig. 5-2). Two curves are presented in each figure. One is the "bounding curve," which is an estimate of the upper bound of the heat flux density and is primarily based on the analysis of heat flux density data that were obtained from eleven 25,000-lb propellant tests, five of LO_2/RP-1, and six of LO_2/LH_2. The remaining curve, designated the "recommended curve," is superimposed on the bounding curve until a time τ_o —given by Eq. (5.3)—where it abruptly decreases to zero. The recommended curves are also based primarily on analysis of the data from the eleven 25,000-lb tests mentioned above, and implicitly contain the constraint that the probability of exceeding the cumulative heat flux density associated with the recommended curves (the time integration of the heat flux density from time equal zero to τ_o) is 1 percent. The variation of the heating pulse with propellant weight, that is, the scaling implicitly contained in Figs. 5-1 and 5-2 and Eq. (5.3), assumes first, that the duration of the heating pulse will increase with the cube root of propellant weight, as implied by the empirical relation Eq. (5.2), and second, that the heat flux density at a scaled time, using this cube root time scaling, will be invariant with variation in propellant weight. The second statement is based on the invariance of fireball temperatures (measured) from scale to scale.

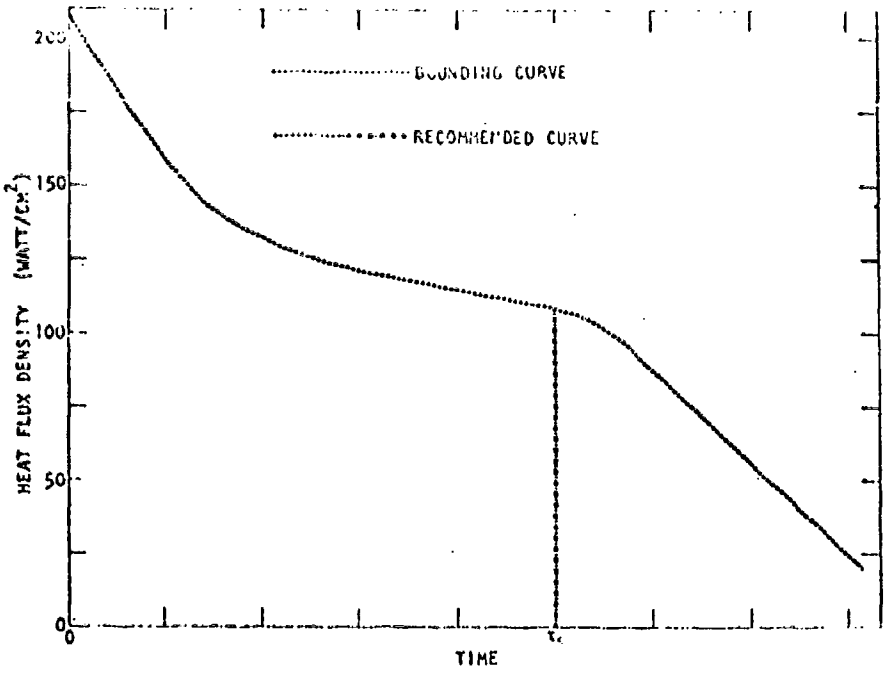

Fig. 5-1. Bounding and Recommended Heat Flux Density Curves for the LO_2/RP-1 Propellant Combination

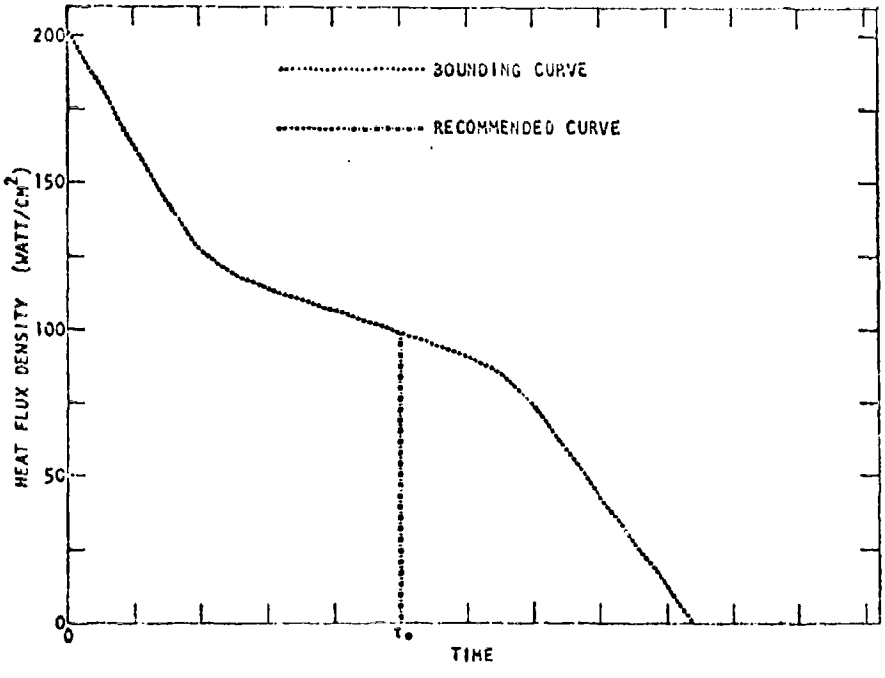

Fig. 5-2. Bounding and Recommended Heat Flux Density Curves for LO_2/LH_2 Propellant Combination

No account has been made in the bounding or recommended curves for the emission of radiant energy from the surface of an immersed object, and this emission can substantially reduce the transfer rates from those given in the curves as the surface temperature of the object becomes a significant fraction of the fireball temperature, the latter being typically of the order of 2300°K. A reduction occurs similarly for the convective component of transfer. Any corresponding modifications of heat transfer from the curves, however, depend on the details of the application and are not considered here.

Several other qualifications of the bounding and recommended curves should be noted. First, the heat flux density measurements upon which the curves are primarily based were obtained from instruments that were fixed in space; thus, a modified heat flux density may be appropriate for objects which, for example, become prematurely ejected from the fireball (due, for instance, to blast wave forces). For many circumstances, the modification would be a reduction of the total heat transfer, first, due to the tendency to reduce the time that an object is immersed, and second, due to a reduction in the convective heat transfer component, since the motion imparted to the object by the blast wave forces would tend to reduce the relative velocity between the object and the surrounding gas. Rotary motion imparted to the object, however, would generally result in an increased transfer rate at given locations on the object. Whether it is appropriate to consider these factors in greater detail depends again on the details of the particular application, and such factors are not discussed further here.

It can be seen from Eq. (5.3) that the heating durations of Figs. 5-1 and 5-2 (of either the bounding or recommended curves) increase with the cube root of propellant weight. This is an assumption that deserves some consideration. For comparatively small propellant quantities, say 1000 lb or less, the fireball duration is insufficient for appreciable motion (rise) of the fireball, and the fireball duration is then essentially synonymous with the heating duration of an object that is fixed in space. For larger propellant quantities, say for 25,000 lb and more, significant motion does occur and the heating duration of a fixed object is therefore less than the fireball duration. Thus,

the ratio of the heating duration of a fixed object to the total fireball duration is some function of the propellant weight. The curves of Figs. 5-1 and 5-2 are based on measurements fixed in space at the 25,000-lb level, and extrapolation to other propellant weight levels through Eq. (5.3) inherently assumes an invariance of this ratio of durations. For application to weights in excess of 25,000 lb, it is nevertheless recommended that Eq. (5.3) be used in conjunction with the curves of Figs. 5-1 and 5-2, although it is expected that the curves would be somewhat conservative. For extrapolation to significantly lesser weights, τ_o should be larger than given by Eq. (5.3); more specifically, at the 1000-lb (or less) level, τ_o as given by Eq. (5.3) should be increased by a multiplying factor of approximately 1.2 and 1.6 for LO_2/RP-1 and LO_2/LH_2, respectively.

It is possible that the heat transfer hazard can be intensified by the occurrence of chemical activity between the fireball constituents —notably the oxidants — and the surface of an object immersed in the fireball. Predictions of the rates (or existence) of the associated chemical reactions are not included in this section, in part, due to the heavy dependence of such reactions on the particular application, that is, on the molecular constituents of the object and the surface temperature attained. The latter, in turn, depends on the configuration and thermal properties of the object. (The reaction also depends critically of course, on the concentrations of various atomic and molecular species — and their excited and ionized states — present in the fireball.) Chemical activity is mentioned and should be considered in any application — particularly when comparatively large propellant quantities are involved — because the reactions can provide an energy contribution (not included in Figs. 5-1 and 5-2) to the object.

The heat flux density measurements upon which the curves of Figs. 5-1 and 5-2 are based were obtained at locations no closer to the "center of explosion" than about one-fifth of the radius of the fireball, and it would be expected that the heat transfer rates, at least during the initial "small" fraction of the fireball duration, could be somewhat more severe at or "very near" the center of explosion. Passive sensors capable of providing crude indications of

comparatively severe heat transfer were deployed in the central region (within a few feet of the planned ignition point) throughout most of the eleven 25,000-lb tests mentioned above, and a single positive indication was obtained. Specifically, from 0.1 to 0.2 in. was ablated from the surface of a solid aluminum structure in such a way as to suggest comparatively large heat flux densities over limited times, for instance, of the order of 1000 watt/cm^2 for 2 sec. (A thorough analytic evaluation of the possible ranges of heat transfer parameters resulting in the above ablation has not been performed. For details of the aluminum structure and its ablation, see Appendix A.) It is not clear if chemical activity, as mentioned in the previous paragraph, was an energy contributor.

Regarding the hypergolic propellant combination of N_2O_4/50% UDMH-50% N_2H_4, on the basis of data from three each 200- and 1000-lb tests, heating durations appear to be comparable to those given for the cryogenic propellants above, while the heat flux magnitudes are about one-half to two-thirds those given for the cryogenics.

Section 6
REFERENCES

1. Willoughby, A. B., et al., Liquid Propellant Blast Hazards, AFRPL-TR-68-92, URS 652-35, URS Research Company, Dec. 1968

2. Bader, B. E., Heat Transfer in Liquid Hydrocarbon Fuel Fires, Paper presented at the symposium on Shipment of Radioactive Materials, Fifty-seventh Annual Meeting, Boston, Massachusetts, Dec 6-10 1964

3. Gayle, J. B. and J. W. Bransford, Size and Duration of Fireballs from Propellant Explosions, NASA TM X-53314, George C. Marshall Space Flight Center, Huntsville, Alabama, 4 Aug 1965

4. Van Nice, L. J. and H. J. Carpenter, Thermal Radiation From Saturn Fireballs, NAS 9-4810, TRW Systems, 15 Dec 1965

5. Kite, F. D. and B. E. Bader, Pad-Abort Thermal Flux Model For Liquid Rocket Propellants, SC-RR-66-577, Sandia Corporation, Albuquerque, New Mexico, Nov 1966

Appendix A

THERMAL INSTRUMENTATION

Appendix A
Summary
THERMAL INSTRUMENTATION

Appendix A consists of discussions of the thermal instruments, the errors of the corresponding measurements, and the experimental arrangement and instrument mounting. The following list of measurements and the associated instruments are considered:

- Heat flux density computed from measurements of the surface temperature of slabs
- Fireball temperature from a photographic recording Pyrometer (a Sandia Corporation instrument)
- Radiant flux density within and external to the fireball from Gardon-type radiometers
- Gas temperature from thermocouple probes (Sandia Corporation instruments)

The general organization of Appendix A is given in the following paragraphs.

The measurement of heat flux density is considered first, starting with a description of the method of its evaluation from the surface temperature records. This is followed by an analysis of errors that are uniquely associated with this method and that are not related to the errors in heat flux density which are a consequence of errors in slab temperature measurements. The slab temperature transducers or instruments are then considered, and this is followed by a discussion of heat flux density errors that result from errors in the slab temperature measurements.

A brief description is then given of the photographic recording pyrometer. This instrument indicates blackbody equivalent temperatures through a radiation intensity comparison of an image of the fireball with corresponding images of several tungsten filaments, each of which is at a different temperature.

The radiometers are next described, and this is followed by an analysis of radiometer data correction factors, including an indication of their uncertainties, which are required in conjunction with intrafireball measurements.

A brief description of the thermocouple probes is then given. Finally, the experimental arrangement and instrument mounting is described.

Appendix A

THERMAL INSTRUMENTATION

HEAT FLUX DENSITY: METHOD OF EVALUATION, INSTRUMENTS, AND ERRORS

Computational Method of Evaluating Heat Flux Density from Surface-Temperature Data

The basic relationship from which the heat flux density history at the surface of a slab is evaluated from the slab surface-temperature history is*

$$q(t) = K' \int_0^t \frac{\frac{\partial T_s(\tau)}{\partial \tau}}{\sqrt{t - \tau}} \, d\tau \qquad (A.1)$$

where q is the heat flux density; $K' = (K\rho c/\pi)^{1/2}$; K, ρ, and c are the conductivity, density, and specific heat, respectively, of the slabs; T_s is the slab surface temperature; and t is time. This relationship is valid provided the heat flux density is uniform over the surface of the slab, the thermal properties, K, ρ, and c, are constant, and the slab is semi-infinite, that is, it occupies, or effectively occupies, half of space.

The evaluation of q(t) from the surface temperature in data-trace form through application of Eq. (A.1) may be accomplished by any of numerous procedures. For convenience, we have chosen to modify Eq. (A.1) to a form which particularly accommodates temperature data in digital form, and this modification is described in the following paragraph.

Integration of Eq. (A.1) over the time range t = o to t = t is first divided into arbitrary intervals, so that for t in the interval $t_{i-1} \leq t \leq t_i$, q(t) is given by

* A derivation of Eq. (A.1) is given starting p. 132 in Ref. A-1.

$$\frac{q(t)}{K'} = \sum_{n=1}^{n=i-1} \int_{t_{n-1}}^{t_n} \frac{\frac{\partial T_s(\tau)}{\partial \tau}}{(t-\tau)^{1/2}} d\tau + \int_{t_{i-1}}^{t} \frac{\frac{\partial T_s(\tau)}{\partial \tau}}{(t-\tau)^{1/2}} d\tau, \quad (t_o = 0) \qquad (A.2)$$

Then an expression representing the temperature in the n^{th} interval $t_{n-1} \le t \le t_n$ is assumed and substituted into Eq. (A.2); in particular, the linear expression $T_{ns}(t) = a_n + b_n t$ has been chosen. Equation (A.2) then reduces to

$$\frac{q(t)}{K'} = 2\left[b_1 t^{1/2} + \sum_{n=1}^{n=i-1} (b_{n+1} - b_n)(t - t_n)^{1/2} \right] \quad \text{for } t_{i-1} \le t \le t_i \qquad (A.3)$$

Eq. (A.3) is further modified by writing the constants b_n in terms of the temperatures and corresponding times at the ends of the time intervals, that is, by $b_n = (T_n - T_{n-1})/(t_n - t_{n-1})$, giving

$$\frac{q(t)}{K'} = 2\left[\frac{T_1}{t_1} t^{1/2} + \sum_{n=1}^{n=i-1} \left(\frac{T_{n+1} - T_n}{t_{n+1} - t_n} - \frac{T_n - T_{n-1}}{t_n - t_{n-1}} \right) \left(t - t_n \right)^{1/2} \right] \qquad (A.4)$$

$$\text{for } t_{i-1} \le t \le t_i$$

Eq. (A.4) is, finally, the working equation, that is, q is evaluated at t by the substitution of appropriate temperature values (T_{n+1}, T_n, ..., T_1) and corresponding times (t_{n+1}, t_n, ..., t_1) that are evaluated from the data records.

Errors Associated with the Heat Flux Density Computational Method

Errors that are encountered in evaluating the heat flux density are, for convenience, separated into those associated with the instrumentation (that is, those due to errors in the thermal properties of the slabs [K' in Eq. (A.1)] and to errors in the surface temperature–time record due to the transducer, amplifier,

and recording system) and into those that are not associated with the instruments. Those related to the instruments are considered later. The remaining errors, which concern the application of Eq. (A.4), are considered in the present section. This discussion commences with the assumption that a true or correct surface temperature–time record (trace form) is available. Under this circumstance, there are two types of errors encountered in the evaluation of the heat flux.

The first error type is that which results from the misrepresentation of the true surface temperature–time curve which occurs when this curve is replaced, in effect, by a sequence of line segments. By itself, this error can, of course, be minimized to any desired degree by decreasing the time interval over which the temperatures are evaluated; however, its elimination is precluded by the fact that errors of the second type tend to increase with decreasing interval sizes.

Errors of the second type result from the inability to exactly evaluate the "true" temperatures at the ends of the intervals, there being the natural tendency for the measured values to scatter above and below the true values. The effect of these temperature errors on the computed heat flux density is illustrated on Fig. A-1. On Fig. A-1a is a portion of a true temperature curve

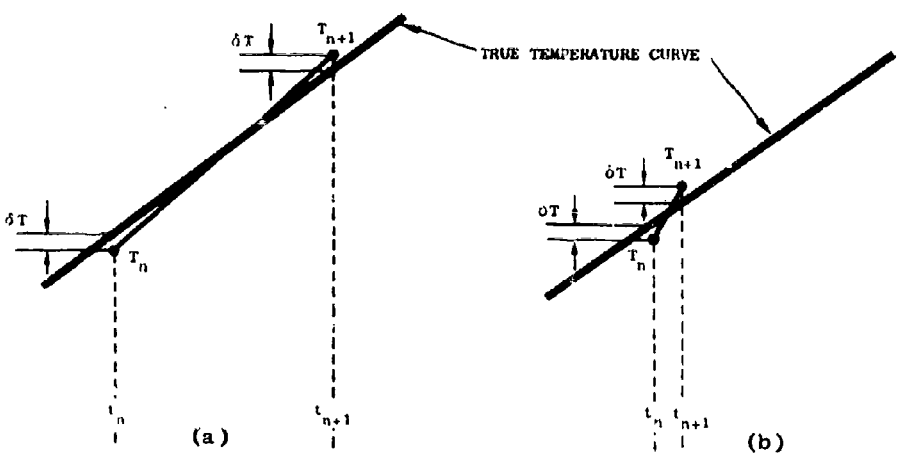

Fig. A-1. Illustration of Origin of Errors of Second Type

along with a line segment representing the curve over a single interval, where there is a temperature error, indicated as δT, at both ends of the interval, the evaluation being less than the true value at the early end and greater at the late end. For the same set of temperature errors over a smaller interval, as shown in Fig. A-1b, the error in the slope of the temperature–time curve is larger. From Eq. (A.4), the heat flux density is seen to depend on the slope over the interval (and all preceding intervals), and thus the flux density error due to temperature errors of this type will tend to increase as the size of the interval is decreased, as implied above.

Thus, with the first type error decreasing and the second type increasing with decreasing interval size, there is an optimum interval length, although the optimum length will vary along a given temperature curve, for instance, as the curvature of the temperature curve varies. A more complicating circumstance, however, is that an error in the heat flux evaluated within a given interval depends not only on the temperature–time slope error in the interval, but in all preceding intervals, as examination of Eq. (A.4) indicates. Because of this latter circumstance and the fact that there is a great variation in the temperature–time records obtained, a general and analytical error analysis is prohibitive and, in light of the objectives, unnecessary. In consequence, the analysis is confined to the evaluation of errors for temperature curves that resemble typical temperature data forms that have been obtained. In addition, because the maximum values of the heat flux that are obtained during heat transfer surges are given relative importance in the presentation of results, errors of the maximum values are emphasized in the error analysis.

The method of evaluating errors consists of comparing an exact heat flux density–time solution for a given surface–temperature–time function (equation) with the solution when Eq. (A.4) is applied to the same temperature function but with, in some cases, the insertion of deliberate and likely temperature errors in Eq. (A.4). The exact solutions are obtained in two ways, the first being simply to utilize existing solutions that are appropriate. When suitable solutions are not available, they are obtained by applying the basic relationship, Eq. (A.1), to temperature–time functions which both resemble typical data forms and which render Eq. (A.1) readily integrable. Examples of the heat flux

errors of both kinds that are encountered for various temperature curves are presented in the following paragraphs.

An example of a temperature–time function which is representative of "early time" data that are obtained is presented in Fig. A-2, along with the "true" flux density–time curve corresponding to that temperature for a K' [Eq. (A.1)] of 0.455 watt/°C-cm^2-sec$^{1/2}$, corresponding approximately to some of the stainless steels. The heat flux was evaluated "exactly" through Eq. (A.1), and the flux computed numerically by applying Eq. (A.4). This example is presented primarily as an illustration of concepts and certain features of the two error types, but the associated magnitudes are also useful since the temperature curve is representative of data obtained.

It is convenient to introduce a "psuedo-curvature," hereafter referred to simply as the curvature, which is defined as

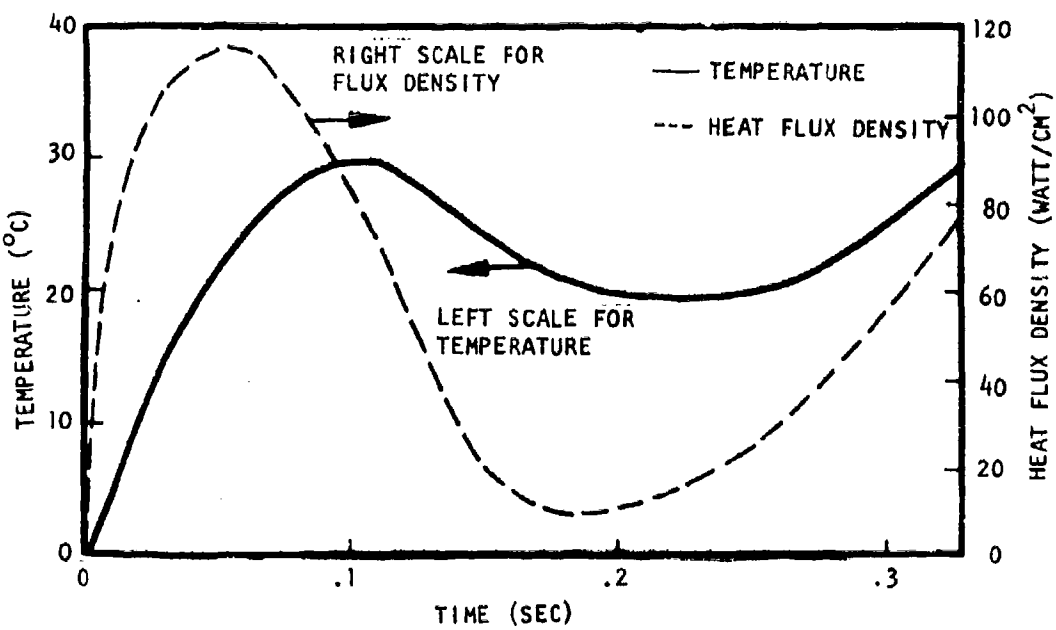

Fig. A-2. Heat Flux Density from Example Temperature–Time Trace

$$C = \frac{d^2T}{dt^2} \Big/ \left[1 + \left(\frac{dT}{dt}\right)^2\right]^{3/2} \qquad (A.5)$$

where C is the curvature, T is the temperature, and t is time. This is an extension of the ordinary or geometric curvature in that space or dimension variables have been replaced by those representing temperature and time.

Errors of the first type have been evaluated for this temperature curve by applying Eq. (A.4) with a specific and uniform time interval for each computation, with the correct values of the temperature being used. This computation has been done for various computational time intervals, and the resultant error is plotted with the time interval on Fig. A-3 (continuous curve). Errors of this type tend to increase with increasing curvature of the temperature curve, and errors for other ranges of curvature will be presented later.

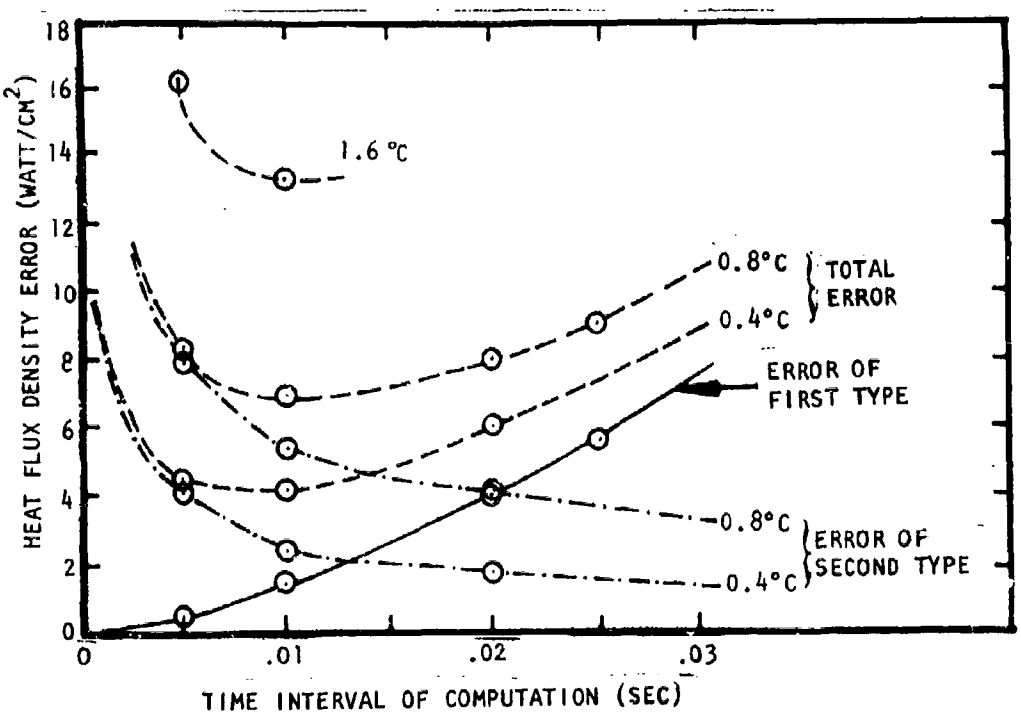

Fig. A-3. Heat Flux Density Errors for a Representative Temperature—Time Curve

Equation (A.4) was subsequently applied to the same temperature curve using the same time intervals, but with deliberate sequences of errors in the temperature values, thereby revealing the total flux error, that is, the error which includes errors of both types.* The temperature errors used correspond to those that are likely to have occurred with the data processing procedures that have been used. The temperature error distribution used consists of temperatures at the ends of time intervals that are alternately above and below the correct value by a fixed magnitude. Thus, the slope of the temperature curve over a time interval is alternately (from time interval to time interval) above and below the correct slope, and while this particular distribution of errors is highly improbable, it is diagnostically useful. Total errors obtained from this computation are plotted on Fig. A-3 (dashed line) for a range of time intervals of computation and for various magnitudes of temperature errors. A temperature of 0.4, 0.8, or 1.6 °C is listed adjacent to a curve to indicate the total temperature error inserted at the ends of each interval, that is, the magnitude that the temperature is above the true value at one end of a given time interval plus the magnitude that it is below at the other end. As before, the curves are plotted for errors obtained at 0.1 sec, and also as before, the error is for practical purposes invariant for the range of curvatures present in the temperature curve of Fig. A-2. It can be seen that the total error curves reach minimum values for time intervals in the vicinity of 10 msec, with least total errors of about 4, 7, and 13 watts/cm^2 for temperature errors of 0.4, 0.8, and 1.6 °C, respectively. At the peak of the flux curve, where the magnitude is approximately 114 watts/cm^2 (at about 0.05 sec on Fig. A-2), errors of 4, 7, and 13 watts/cm^2 correspond to 3.5, 6, and 10 percent. From estimates of the standard deviation of the temperature evaluation, the error curve that most nearly corresponds to actual errors is the curve labeled "0.8 °C," thus indicating that a flux error of about 6 percent can be expected for this circumstance. It should be noted, however that this will vary somewhat with the quality of the temperature data. More

* Errors of the second type may be isolated through certain applications of Eq. (A.1). However, the effort is more extensive than is felt to be justified.

importantly, it should be understood that the value of 0.8 °C for a typical temperature error is the result of both the techniques used for measuring the displacement (or height) of the data trace and the particular scale of the data trace. Regarding the latter, a temperature - time trace with a different number of degrees (temperature) per inch on the paper would result in typical temperature errors other than 0.8 °C, and perhaps well outside the 0.4 to 1.6 °C range mentioned above. For a given scale, improving the accuracy of the trace displacement measurement would of course decrease the temperature error. The value of 0.8 °C is an estimate for the methods of displacement measurement used with the data at the graphical scale that was available. Referring once again to the typical flux error of 7 watts/cm^2, for periods during which the flux is comparatively low, the percentage error can be exceedingly large; for instance, in the vicinity of 0.2 sec where the flux is approximately 12 watts/cm^2, the error is about 60 percent. It is not correct, however, that all relatively small flux values have percentage errors of this order. Roughly speaking, low but steady flux magnitudes will be comparatively accurate, and the larger errors in flux (on a percentage basis) are associated with the minimum value of a sharp depression or trough in a flux curve.

Estimates and trends of errors of the second type are also given on Fig. A-3 (dash-dot curve), which were obtained by subtraction of the error of the first type (continuous curve) from the errors which are due to errors of both types (dashed curve)*. With this additional curve, Fig. A-3 serves as a useful guide. It is known, for instance, that for temperature curves having less curvature than the curve of Fig. A-2 at 0.1 sec, the errors of the first kind will not increase as rapidly with time interval as the curve presented

* For convenience, the errors of the first and second type are treated as though their sum always represents the total error. For approximately one-half of the intervals, however, the first and second error types are in opposing directions, that is, the error of one type tends to negate the error of the other type. Thus, the plots indicate worst or bounding case errors.

on Fig. A-3, and therefore, the flux error for a given temperature error can be greatly reduced by increasing the time interval of the computation from 10 msec. If, however, it is necessary to maintain or improve the accuracy for conditions of greater curvature, the only recourse is to improve the temperature-data-evaluating procedure.

The effect of variation in the curvature of the temperature curves on errors of the first type is given to a limited extent in Fig. A-4, where the error is plotted vs time interval of computation for three values of

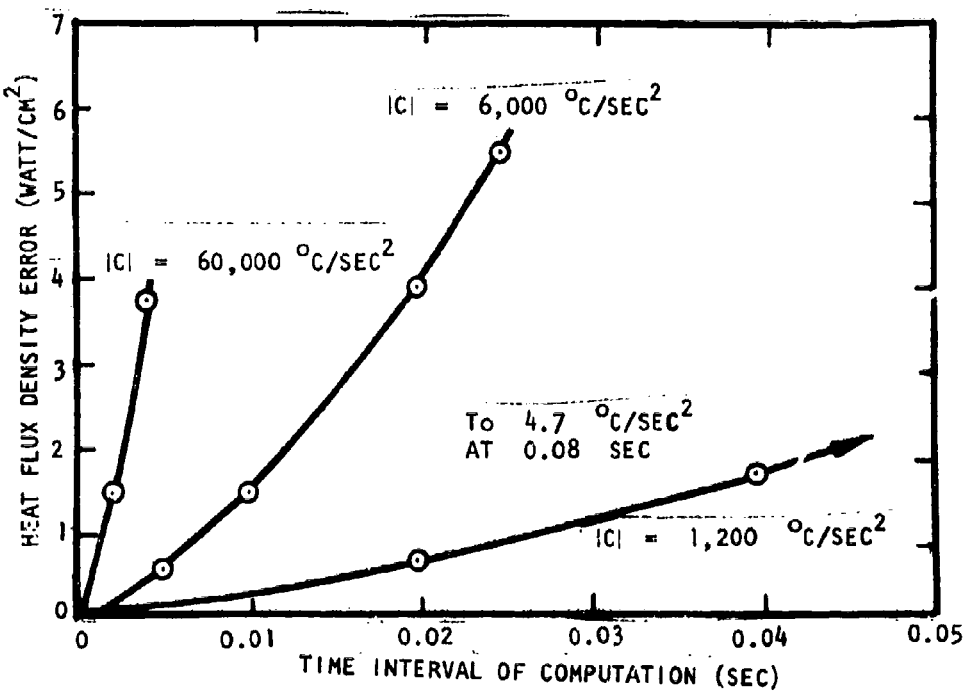

Fig. A-4. Heat Flux Density Errors of the First Type

curvature. Since errors of the second type depend only on the time interval of computation and temperature evaluation error, that is, they are independent of curvature*, the curves for errors of the second type on Fig. A-3 and those for the first type on Fig. A-4 may be combined so as to reveal curves representing the total error for a range of curvatures. A family of curves obtained from this process for the anticipated temperature errors of 0.8 °C are given on Fig. A-5.** These curves provide guidance in selecting the computational interval that will minimize the errors, and provide an indication of the errors that can be expected for a given set of conditions.

It should be recognized that the error within a given interval depends not only on the error in the slope of the temperature curve for that interval but in the corresponding errors for all preceding intervals, and that the sequence of temperature errors that has thus far been considered has consisted of errors of a fixed magnitude that are alternately (from interval to interval) above and below the true value. The error curves that have been presented are, then, representative of this particular distribution of temperature errors, while the actual distributions are, of course, infinite in their variety. The effect of modifying the distribution was investigated by imposing several different and intuitively probable temperature error distributions on the same temperature function. The variation in the errors for a given interval from among the various distributions was never in excess

---

* The independence of errors of the second type with curvature can be proven analytically by applying Eq. (A.4) to two dissimilar but mathematically arbitrary temperature functions which have identical but arbitrary temperature error distributions imposed on them.

** Since the values of the errors of the second type on Fig. A-3 are very uncertain at times less than 0.04 sec and these values are required over this time range for the construction of total error curves for curvatures of 60,000 °C/sec^2, an estimate of the error curve of the first type for a curvature of 12,000 °C/sec^2 was obtained and the total error curve corresponding to this curvature is given in Fig. A-5.

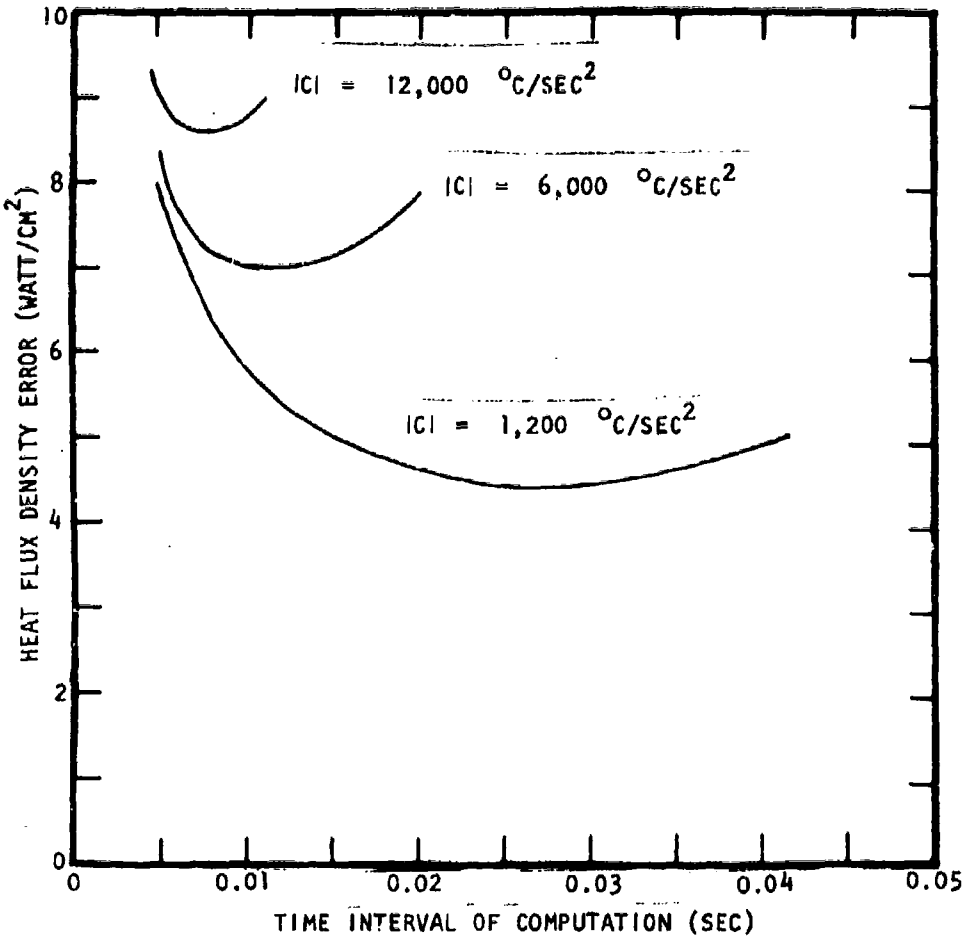

Fig. A-5. Heat Flux Density Error with Curvature and Time Interval of Computation

of 5 percent, and the error curves given for the special-case distribution in the figures above are representative of the errors for these distributions. The distributions that were considered by no means represent a thorough sampling, however, and distributions which result in variations in excess of 5 percent may occur.

The general errors as illustrated on Fig. A-5 have been generally verified for numerous conditions, and the results from a further example are presented primarily in the interest of illustrating certain points. One of the conditions of error that is of particular interest is that associated with the peak values for comparatively short-duration heating pulses. This was investigated by analytically imposing various short-duration heating pulses at various times on an otherwise constant and comparatively low-magnitude heating cycle. In the usual way, exact solutions were obtained and compared with numerical evaluations for which various appropriate errors had been introduced into the temperature values. For the example presented, a heating pulse of 40 msec duration centered about 0.1 sec* was superimposed on a constant heat flux density of 40 watts/cm^2, with the pulse maximum reaching approximately 132 watts/cm^2. Temperature errors covering their expected range were introduced at approximately the time corresponding to the peak of the heating pulse. The errors for this case are presented (in terms of percentage) on Fig. A-6. For a temperature error of 0.8°C corresponding to the most likely magnitude, the error from Fig. A-6 is about 15 percent, which corresponds to an error of about 20 watts/cm^2. This error is substantially greater than the minimal error (about 8.6 watts/cm^2) given for this curvature [about 12,000 °C/sec^2] on Fig. A-5 because a time interval of computation of 0.004 sec rather than the optimum interval of approximately 0.007 sec was used. However, since the 'dip or trough' in the total error curves of Fig. A-5 is comparatively 'sharp' for curvatures of this and larger magnitudes, this minimal error (cited above) is perhaps common for this curvature unless inordinately refined data analysis procedures are

* Precisely, the corresponding temperature 'pulse' rather the heating pulse was centered about 0.1 sec, the peak of the heating pulse slightly preceding this time.

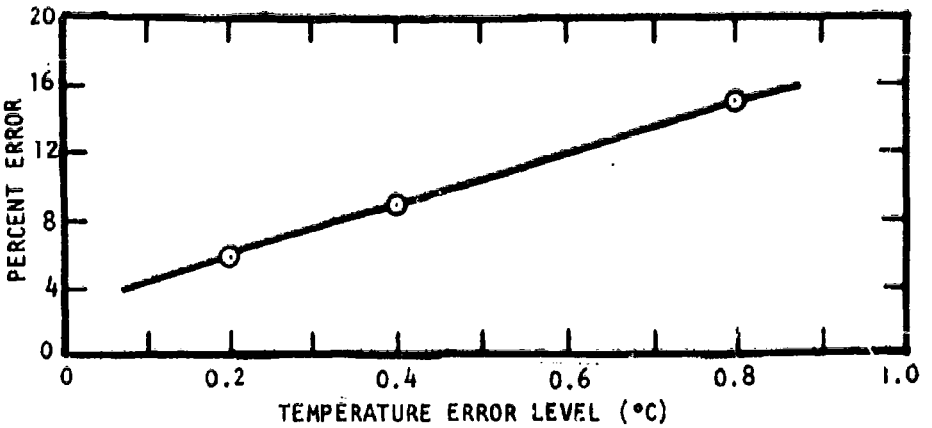

Fig. A-6. Error at the Peak of Heat Flux Density Pulse

adhered to. Moreover, misjudgments of a given magnitude would tend to more substantially inflate the error in this case compared to cases where the curvature of the temperature curve is smaller.

Finally, it is important to recognize that the errors presented above are representative of those associated with a single computational interval, and that they will tend to scatter from interval to interval above and below the true value by such magnitudes. In the case above, ten computational intervals would be associated with the 40-msec pulse. An erroneously high value over a given interval will tend to be compensated by a correspondingly low value in the subsequent interval. Thus, a smooth curve through the computed values over the 40-msec pulse will be substantially more certain than indicated by the errors plotted on Fig. A-5 above. By way of illustration, the exact and computed cumulative flux density values over, say, 20 to 30 computational intervals for typical temperature curves and errors, never differ by more than 0.5 percent.

Surface-Temperature Transducers

The method employed to measure the temperature within a solid material, hereafter referred to as the parent material, is standard and described or referred to in several articles, for example in Refs. A-2, A-3, and A-4. Briefly, the transducer, illustrated in Fig. A-7, consists of a fine wire which is contained within a cavity in the parent material and which is electrically insulated from the walls of the cavity except at an end, where it is joined (welded) to form a thermocouple junction just below one exterior surface of the parent material. Thus, any change of temperature of the junction will introduce a corresponding change in the electrical potential difference between the wire and parent material.

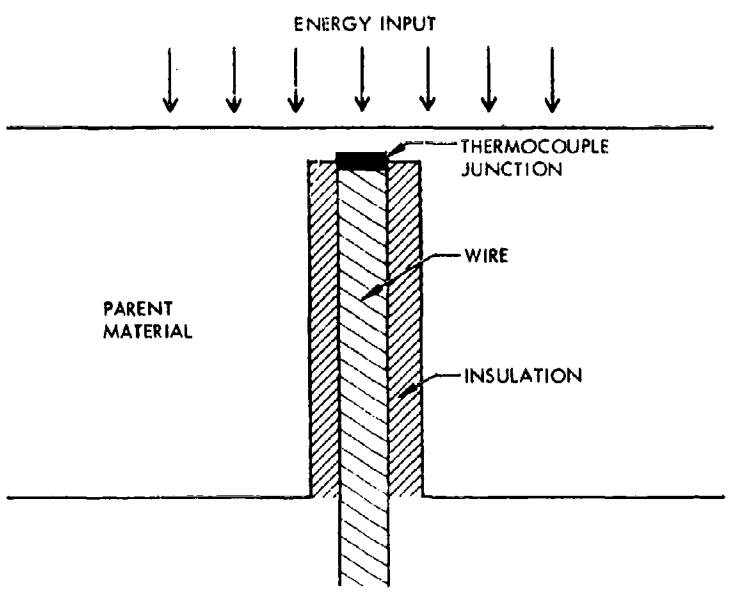

Fig. A-7. Generalized Configuration of a Surface-Temperature Transducer

Instruments of two somewhat different designs are used. The details of the first type,* the transducer that was predominantly employed, are presented in a cross-sectional cutaway view, along with an enlargement of the thermocouple junction region, in Fig. A-8.** This transducer incorporates two wires so that only the molecular composition of the wires, not the parent material, enters into the electromotive force per unit temperature rise characteristic of the transducer.

Three slightly different versions of the transducer type shown on Fig. A-8 were used, differing only in the parent material and a single dimension. The parent material of the instrument presented in Fig. A-8 is copper, and the depths of the thermocouple junctions are 0.005 in. For the other two, the parent material is stainless steel 303 and 309, with junction depths for each of 0.002 in. The three versions are otherwise identical, including the thermocouple wire combination of chromel and alumel.

The important features of the second type of transducer*** are presented on Fig. A-9, which is a cross-sectional view of just the thermocouple junction region, analogous to the region that was enlarged on Fig. A-8. This is a single-cavity (and wire) system, so that the parent material, in this case iron, enters into the electromotive force per unit temperature change characteristic. The depth of the thermocouple junction is 0.0002 in., and unlike the previous example. the material between the junction and the exposed surface does not match the parent material, the thin exposed layer being a copper deposit on an iron surface, as illustrated on Fig. A-9. The particular application planned for this transducer called for the parent material to be a comparatively poor heat conductor, more specifically, that the thermal diffusivity be low, in order to minimize the distance that a spatial non-uniformity in heat input along the surface of the parent material can effect

---

* Manufactured by Advanced Technology Laboratories, Mountain View, California.

** Unless tolerances are noted on the figures, the distances shown were obtained by measurement of one transducer that has been cross-sectionally sliced and are uncertain to perhaps 0.003 in.

*** Manufactured by Heat Technology Laboratories, Huntsville, Alabama.

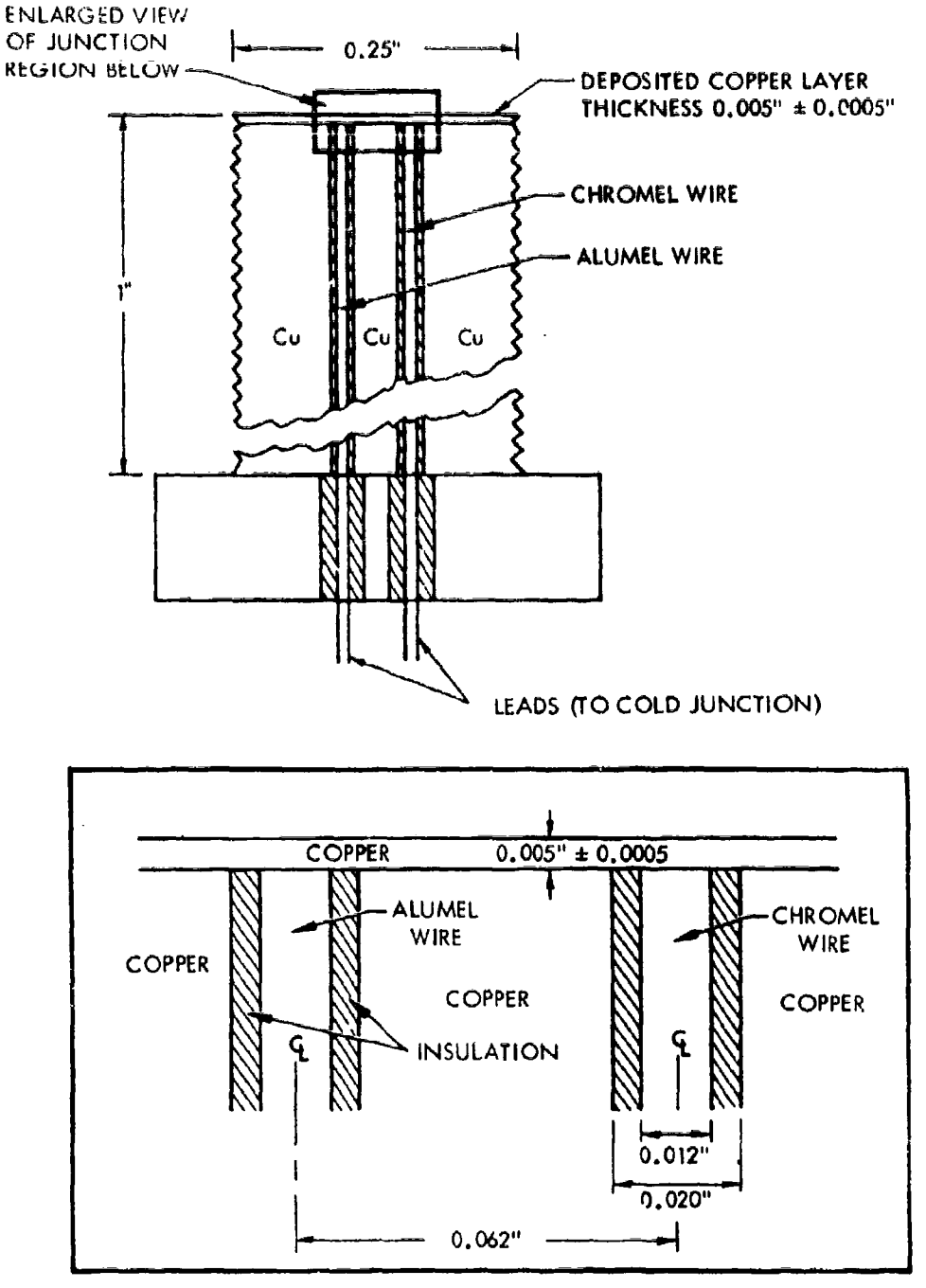

Fig. A-8. ATL Surface-Temperature Transducer

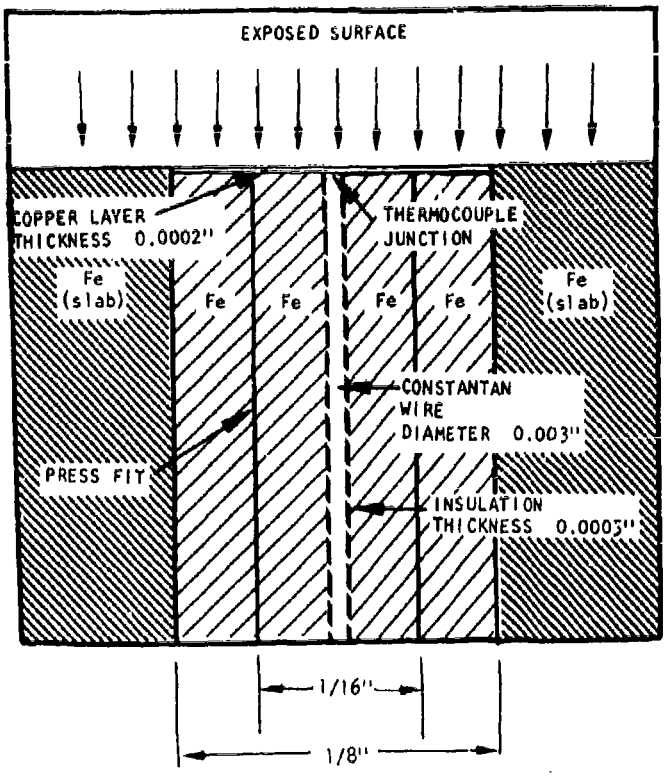

Fig. A-9. Thermocouple Junction Region of HTL Surface-Temperature Transducer

the temperature of the thermocouple junction in a given time interval. Of the materials immediately available at that time, iron had the best thermal properties. Because of the pronounced tendency of pure iron to oxidize in a high temperature oxidant atmosphere, thereby changing the thermal properties, the layer was made of copper. The replacement of this thin iron region with a copper layer, however, does not for practical purposes, alter the temperature measurement for a given energy input.

The surface temperature instruments as thus far described are inserted into larger objects, hereafter called slabs since for a time period they are thermally representative of semi-infinite slabs, which match the parent material of the given transducer. The surface of the transducer that is exposed to the

fireball, the surface nearest the thermocouple junction, is always flush with the surface of the slab it is inserted into. The exposed surface of the slab in most instances is planar, with the exception of a few measurements, described in more detail below, taken on a surface having some curvature, e.g., a radius of curvature of 6 in.

The thickness and lateral dimensions of the slabs are given below in the section on Instrument Mounting. These dimensions are of importance in that they govern the length of time that the slabs are thermally representative of semi-infinite slabs, or consequently, the time throughout which Eq. (A.1) may be properly applied.

The thermal properties of the slabs that have been applied in evaluating the heat flux are given in Table A-1 below, where the column on the extreme right is the value of the constant, $K' = (K\rho c/\pi)^{1/2}$, required in Eq. (A.1). These values were obtained from several sources including, for instance, Ref. A-5. The values listed for copper and iron are comparatively accurate since pure grades were used (see error analysis) whereas lot to lot variations can be expected for the stainless steels.

Table A-1

SLAB THERMAL PROPERTIES USED IN HEAT FLUX COMPUTATION

Slab Material	Conductivity (watt/cm-°C)	Mass Density (gm/cm^3)	Specific Heat (watt-sec/gm-°C)	K' of Eq. (A.1) ($watt\text{-}sec^{1/2}/cm^2\text{-}°C$)
Copper	3.81	8.94	0.389	2.05
Iron	0.652	7.85	0.418	0.825
Stainless Steel 303	0.147	7.8	0.503	0.437
Stainless Steel 309	0.155	7.8	0.586	0.475

The heat flux data and slab surface temperature data given in Appendix B and the Presentation of Results section are labeled black, white, or polished, according to the condition of the exposed surface of the corresponding slab. The designations of black or white indicates that the slab was coated with a 0.001 in. thick deposit of "Nextel Velvet Coating" 101-C10 black or 101-A10 white, respectively.*

Heat Flux Density Errors That Are Due to Instrument Errors

Heat flux density errors associated with the method of its computation from the surface-temperature of slabs were discussed above, starting with the assumption that a true temperature curve was available. There are, of course, errors in the temperature-time traces, and errors that are propagated to the heat flux density evaluation from these temperature errors are considered in this section, along with the error that depends on the error in the properties of the slab, i.e., on K' of Eq. (A.1). Consideration is given first to the four sources of systematic errors, that is, errors that can be corrected, and then to random errors

The equation through which the heat flux density is evaluated from the slab temperature [Eq. (A.4)] is applicable to the surface temperature, while the slab thermocouple junctions are slightly below the surface. In order to evaluate the effect of this on heat flux density, temperature-time functions were first evaluated at the surface and then at depths corresponding to the thermocouples for various heating pulses applied to the surface of the slabs, and a comparison was then made of the heat flux densities from the two temperature functions. The heating pulses or the slab boundary conditions applied to both copper and stainless steel slabs were the so-called radiation boundary conditions using a gas temperature of 2,000°K and heat transfer coefficients of both 0.34 and 0.042 watt/cm^2-°K. The resultant fractional errors are presented on Fig. A-10. The curves indicate that large initial errors rapidly converge to tractable values. The curves are somewhat misleading in the following manner. Roughly speaking,

* 3M Company, Reflective Products Division, St. Paul, Minnesota.

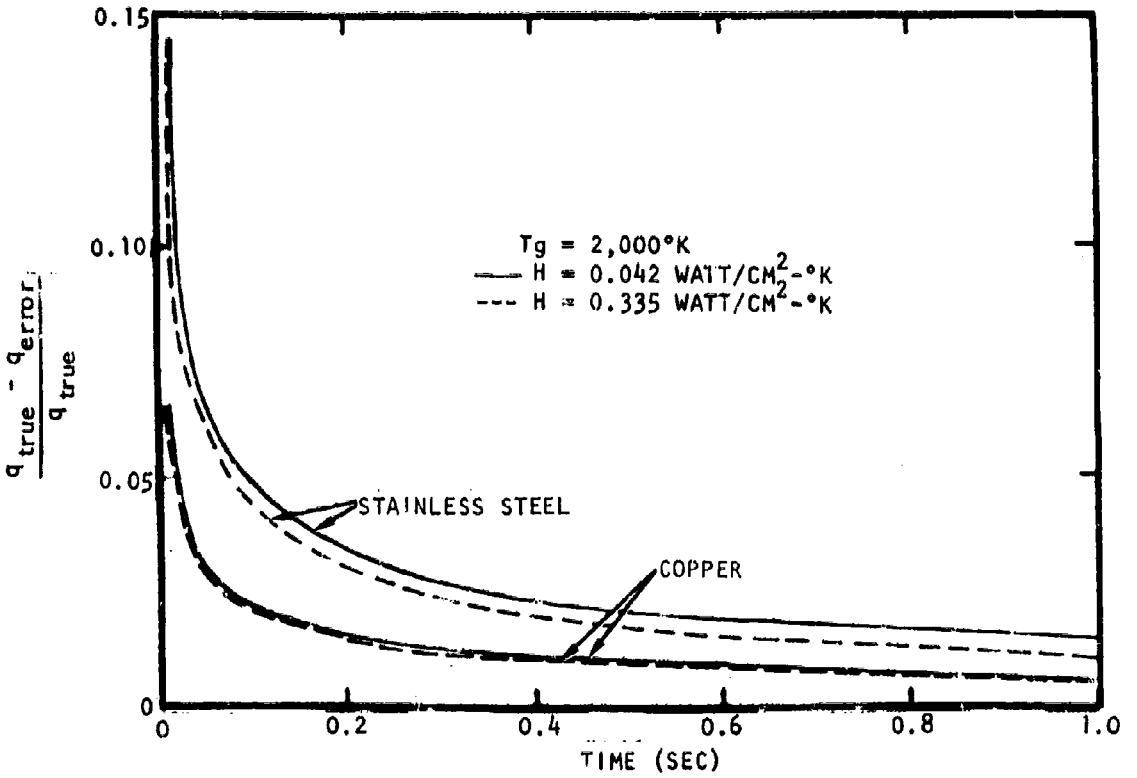

Fig. A-10. Heat Flux Density Errors which Result from Using Temperatures at Depths which Correspond to Those of the Thermocouple Junctions

the temperature slightly below the surface tends to follow the surface temperature but with a small time delay. Thus, in the analysis, there is a time period when the embedded temperature is essentially zero while the surface temperature is rising appreciably, with the consequence that infinitely large fractional errors are indicated at early times. In actuality, zero time for an embedded measurement would be designated as the instant the temperature commences to rise, thus tending to minimize the magnitude of the initial error. The curves of Fig. A-10 tend, in this sense, to bound the errors. However, the curves are also misleading in another sense. The heating pulses applied to obtain these curves vary gradually with time, while the corresponding pulses for propellant tests are often comparatively erratic. Consequently, erratic behavior in the heating pulse can occur before the errors indicated in Fig. A-10 have decreased sufficiently. The effect here is perhaps best summarized as follows. Sharp or erratic behavior of a surface temperature will tend to "smooth" slightly at the thermocouple depth, with the result that the measured heat flux density is also a slightly "smoothed" version of the true input. To an extent, this is desirable. Extremely high resolution is not required, and the expense of the heat flux computation for precise representations of the surface temperature would be unjustifiably increased.

The second systematic error pertains to the effect on the temperature within the slab due to the presence of the thermocouple (including leads) and the cavity which contains the thermocouple. The analysis of this error is extremely involved, and evidently as a consequence few thorough analyses appear in the literature even though this is a standard instrument. While the ultimate errors in heat flux density are not expected to be of particular concern, it is difficult to numerically specify the uncertainty for a given circumstance. A series of analytical studies* for slab and transducer conditions, i.e., depth to thermocouple, cavity dimensions, properties of both the slab and thermocouple leads, etc., that differ in some respects from the cases of interest suggest minor errors can be expected. For instance, the effect of heat conduction down the thermocouple lead for comparatively large diameter leads and for lead to slab

* A relevant part of this study is given in Ref. A-4.

conductivity ratios of ten indicate corrections of the order of 25 percent. With comparatively high conducting leads, it is not surprising that errors of this magnitude would be attained. For the instruments used, however, the conductivity ratios were no greater than 20 percent, and the errors from this effect would be substantially less. An experimental study* in which known heat pulses were applied to slabs with very similar instruments was conducted and a comparison made between the measured temperature and that which should result from the heating pulse. In such a study, the effects of all the systematic errors are inherently in the temperature differences observed, and it is not clear which individual error(s) are predominantly responsible. Yet the systematic error in question is the only one that cannot be readily estimated, so that conclusions can be drawn with regard to this error. In any case, errors obtained were of the order of 5 percent or less, thereby suggesting that the effect of the systematic error in question was not grossly in excess of this figure.

While it does not appear that the effects of the presence of the cavity and thermocouple leads are of serious concern, being perhaps no larger than a few percent, these effects are the least certain of the systematic errors leading to errors in heat flux density measurements.

The third and fourth types of systematic errors result from the nonlinearity of the amplifying and recording systems and the nonlinearity between the thermocouple emf and the temperature of the junction. These errors are similar and relatively simple to estimate or correct.

The deviation from linearity of the amplifying and recording systems was determined by applying a sequence of step voltages to the amplifier, where the ratios of steps are accurately known (0.5 percent), and measuring the magnitudes of the corresponding step deflections on the final data record. Such measurements were taken for all thermal data channels over several tests. Then for each channel, fractions of various step deflections to the highest step deflection on the final data record were obtained and compared with the corresponding

* Ref. A-4.

fractions of the input step voltages. The deviation, in each case, of the fraction on the final record from the fraction of the input is equal to the deviation, or error, of the temperature evaluation along the trace from zero to maximum temperature. An erroneous temperature curve that is representative of the error indicated by the fractions was constructed, and the heat flux was computed for the erroneous curve and a corresponding true temperature curve. The representative erroneous temperature curve was constructed using the criterion that, at each step, two-thirds of the deviations from linearity mentioned above were between the true and erroneous curves, with the remaining one-third outside this range. The resultant fractional error in heat flux density is presented on Fig. A-11, and as can be noted, the effect of nonlinearity in the amplifying and recording system tends to be minor.

Consideration of the nonlinearity of the appropriate emf vs temperature curves indicates that the associated errors are negligible over typical temperature ranges of the slabs (50 and 200°C for copper and stainless steel, respectively).

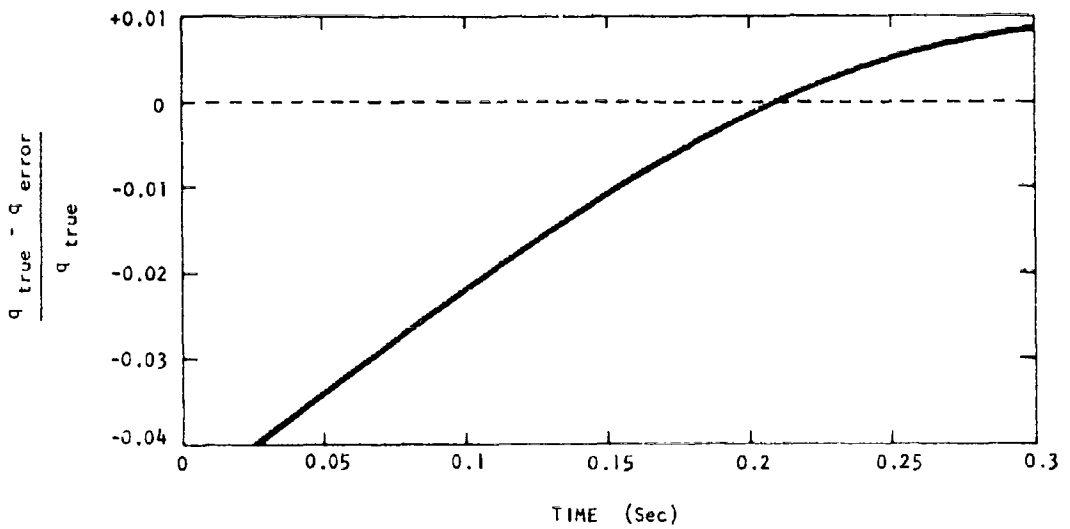

Fig. A-11. Heat Flux Density Error Due to the Nonlinearity of the Amplifying and Recording System

Random errors in the slab temperature measurements will be separated into two different types. The first type has a fixed value for a given data trace, while the second type fluctuates with time over the course of acquiring a data trace. Errors of the first type are considered first.

The slab temperatures are, in effect, evaluated using the equation

$$T(t) = \frac{Vd(t)}{EG} \tag{A.6}$$

where T is the temperatue above ambient at any time t, E is the emf (volts) generated by the temperature transducer per unit temperature rise, G is the amplifier gain, V is the voltage applied to the recording system per unit deflection on the final data record, and d is the trace deflection on the final record. The uncertainty in E is specified by the manufacturer to be 0.5 percent, and G is periodically measured to within an accuracy of 1 percent. V is obtained by measuring the step calibration voltage applied to the recording system immediately before each test and dividing this voltage by the measurement of the corresponding deflection on the final record. It is estimated that the step deflection, preset to approximately match the maximum expected trace deflection, can be evaluated to about 0.5 percent, while the voltage is evaluated to about 5 percent; the uncertainty in the quotient V is then approximately 5 percent. This error, or its component errors, remain constant over the entire data trace for a given channel. It can be seen from Eq. (A.4) that the error in heat flux due to a particular error in temperature of this kind is equal to the temperature error, so that the flux and temperature uncertainties are about 5 percent.

Fluctuations of the measured temperature about the true value that occur throughout the duration of the data traces (noise) are introduced by the transducer, amplifier, recording system, playback system, and so on. Some of these fluctuations are cyclic, while others vary in a randomlike fashion with time. The cyclic fluctuations can be readily identified as

noise because of their presence on the constant value voltage input to each data channel immediately prior to each test. The random fluctuations are evidently comparatively negligible; they are imperceptible during the constant-value voltage input (due account being made for the superimposed cyclic fluctuations).

Regarding the uncertainty in K', the uncertainty in measurements of the dependent parameters K and c (assuming the uncertainty in ρ is relatively small) is typically 5 percent, so that the uncertainty in a measurement of K' would be

$$\frac{\Delta K'}{K'} = \frac{\sqrt{2}}{2} \times 0.05 = 0.035$$

Since the copper and iron slabs are of comparatively pure grade material (99.9-percent pure for copper), the uncertainty in the properties specified for these materials should be about equal to the typical measurement uncertainty. It is likely to be somewhat higher for the stainless steel slabs (specified as stainless steel 303 and 309) since there is a greater lot-to-lot variability in the constituents of stainless steels.

A further but temporary source of error occasionally arises due to a somewhat sinusoidal high-frequency oscillation in the initial portion of the surface temperature—time data trace, which evidently results from passage of the shock wave and/or the impact of high-speed fragments of the tankage hardware on the instrument or its mounting. This signal attenuates rapidly with time and generally decays to negligible proportions in less than 0.1 sec, and the amplitude for the most extreme and rare cases is about 25 percent of the true signal. Since the period of vibration is usually orders of magnitude smaller than the period of typical changes of the true signal, "smoothing" the initial portion of the trace to eliminate the vibration induced noise can usually be accomplished with reasonable accuracy.

One additional systematic error should also be considered. The relationship from which the heat flux density is computed from the slab surface temperatures [Eq. (A.1)] assumes that the slab is effecitvely semi-infinite (occupies

half of space), while the instrumented slabs are finite. The surface temperature-time curve from a finite slab will eventually commence to diverge from that of a corresponding semi-infinite slab, and thus, an error will be introduced into the computed heat flux unless Eq. (A.1) is modified to accommodate a finite slab. This modification is somewhat involved, however, and the alternate approach was taken of selecting the slab materials and dimensions such that the errors in applying Eq. (A.1) are minor. The worst case was in connection with copper slabs having thicknesses of about 1-1/2 in. (detailed slab dimensions are given below in the discussion of instrument mounting). Comparative examination of first time derivatives of the temperature – time curves for copper slabs of this thickness and corresponding semi-infinite slabs indicate, for instance, that errors in heat flux density as large as 10 percent can occur at 5 sec, but that they are negligible at 2.5 sec. Iron slabs of similar thickness and stainless steel slabs 1 in. thick were also used, and the corresponding errors are comparatively small.

PHOTO-RECORD PYROMETER

Blackbody equivalent temperature measurements using a photographic recording pyrometer at a remote location were made by the Sandia Corporation. This instrument is shown in Fig. A-12. Basically, the measurement consists of matching in the visible spectrum the intensity of an image of a region of the fireball with the intensity of a similar image of one of four tungsten filaments, each of which is at a known and preset temperature. Since the intensity of the tungsten in the optical spectrum approximates that of a blackbody, the measured fireball temperature is near the blackbody equivalent temperature.

A more specific description is as follows. A camera is positioned to photograph a region of the fireball to be measured. A lamp box containing four tungsten lamps is placed so that the lamp filaments are in the lower portion of the camera field of view and are in focus at the film plane. The lamps are then adjusted to temperatures bracketing the expected temperature of the fireball. The lamp temperatures are read with an optical pyrometer. A Wratten 29 filter

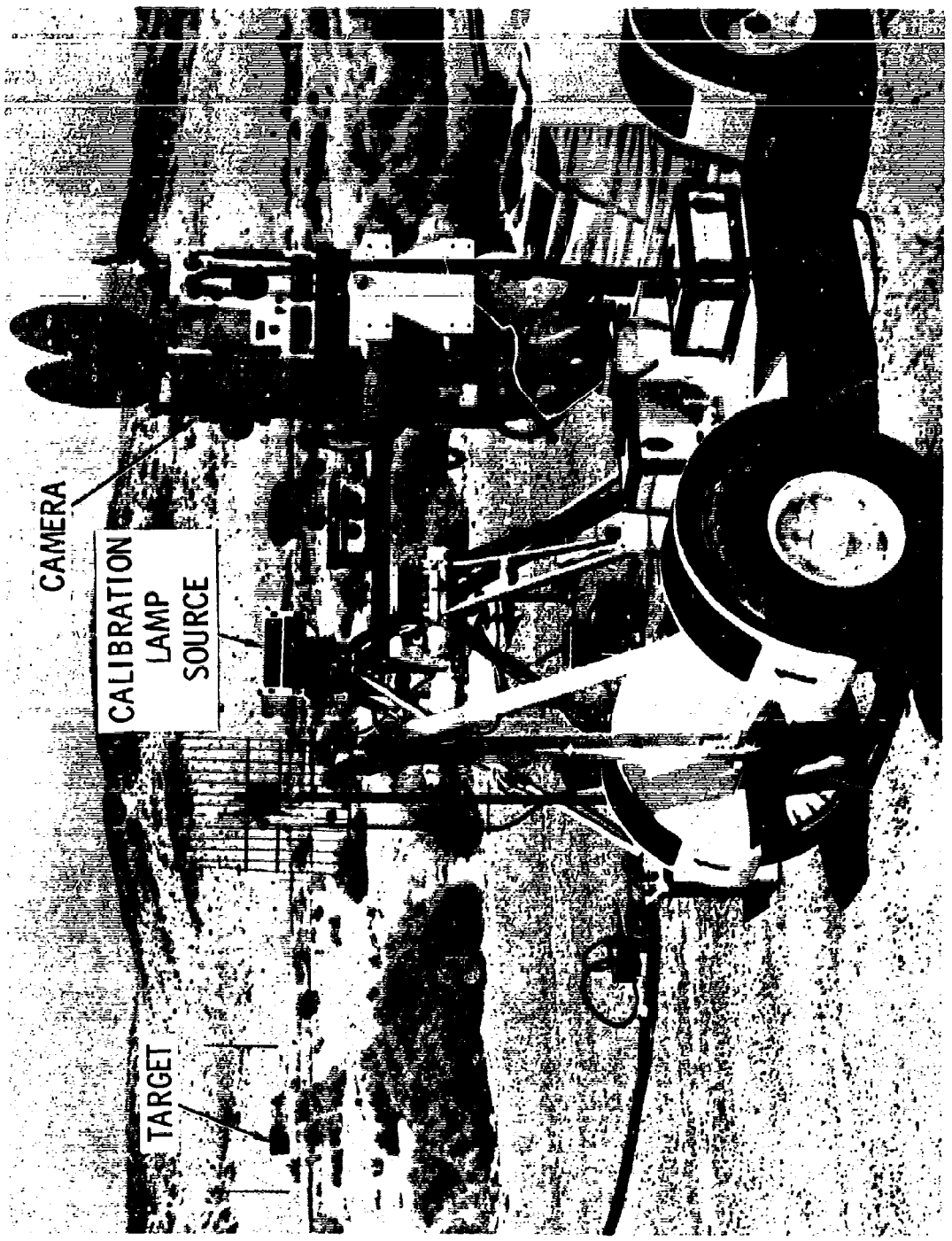

Fig. A-12. Photographic Recording Pyrometer

is placed in front of the camera lens, and the exposure set so that the lamp filament images will give a maximum density on the film of about 1.8. The lamps are burning during the operation, so that each data frame, when processed, contains an image of the fireball, and the images of the lamp filaments, each of the latter at a different calibrated temperature. The density of the calibration lamps is plotted against temperature, and the temperature of the fireball taken from this curve.

RADIANT FLUX: INSTRUMENTS, CORRECTION FACTORS AND ERROR ANALYSIS

Basic Description of Radiometers

The radiant flux measurements are made with an instrument ordinarily referred to as the Gardon-type radiometer. Detailed descriptions of the principles of operation of this instrument are given in Refs. A-7 and A-8. The following is a brief summary from these references.

The basic radiant-energy-receiving element of the instrument is a circular metallic foil, as illustrated in Fig. A-13. If energy is absorbed at a constant rate uniformly* over the surface of a sufficiently thin circular foil (or heat is generated at a constant rate uniformly within the foil) whose circumferential edge is maintained at its initial temperature, a steady-state temperature field is such that the temperature differential between the center and circumferential edge of the foil is, to an approximation, proportional to the rate of radiant energy absorption by the foil** (or rate of heat generation within the foil). Specifically, an approximate equation relating the temperature differential to the constant heat flux (watt/cm^2) is

$$q = 4K\delta\ \Delta T/R^2 \qquad (A.7)$$

* Uniform irradiance of the foil may not be a necessary condition for the flux to be proportional to the temperature differential upon reaching steady state, but it is known to be a sufficient condition, and thus we have made efforts to maintain uniform irradiance.

** Some of these statements are subject to conditions too complex to consider in this brief summary.

where K, δ, and R are the thermal conductivity, thickness and radius of the foil, q is the heat flux, and ΔT is the temperature difference between the center and edge of the foil.

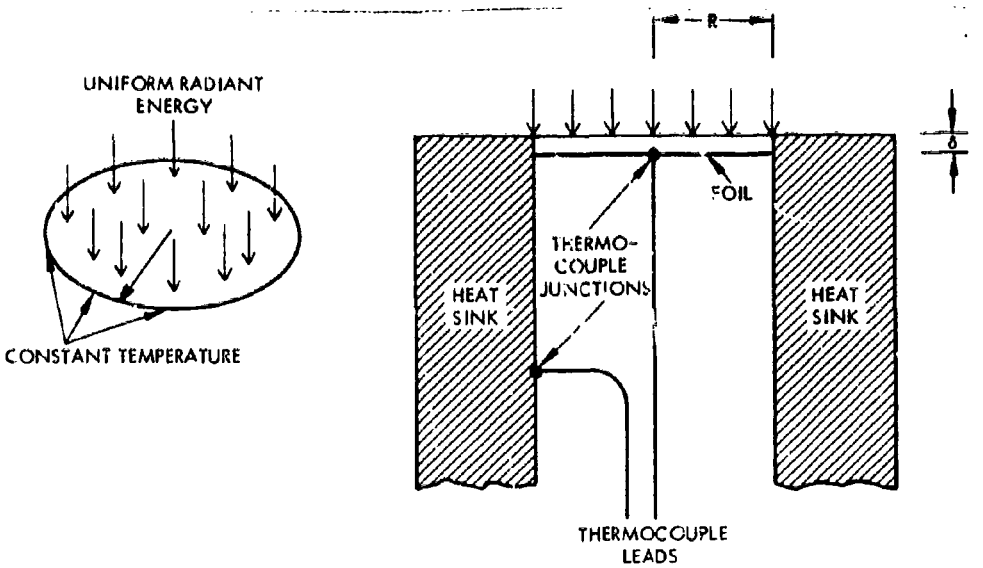

Fig. A-13. Configuration of Gardon-Type Radiometer

In practice, the condition that the temperature at the edge of the foil be maintained constant is approximately met by welding the foil to a highly conducting heat sink, as illustrated in cross section in Fig. A-13. Finally a differential thermocouple, whose voltage output is proportional to ΔT, is made by welding wires of the same material (but different from that of the foil) to the center and edge of the foil (the latter wire may be joined at any region of the heat sink). Then in terms of the electrical potential difference ΔV across the thermocouple leads, Eq. (A.7) becomes

$$q = 4Ke\delta\ \Delta V/R^2 \qquad (A.8)$$

where e is the voltage difference per unit temperature difference across the thermocouple junctions.

An order of time τ for steady state to be approached after initiating the constant flux is given by

$$\tau = R^2/4\kappa \qquad (A.9)$$

where κ is the thermal diffusivity of the foil.

Description of Radiometers

Radiometers of three slightly different types were used for measurements within the fireball designated as the Sandia, RU-1, and HTL* radiometers, and a fourth type for all remote measurements, designated the external radiometer. All four, however, are Gardon-type radiometers and function as in the basic description above. The differences are primarily in the materials used, for instance, for the sensitive foil and heat sink, and in dimensions, such as the foil diameter and thickness and the thickness of the windows.

A cross-sectional sketch of the HTL radiometer is given in Fig. A-14, with an enlargement of the aperture and foil region in the lower portion of the figure. The foil for this particular radiometer is 0.001-in.-thick constantan with a diameter of 0.89 in. The thermocouple junction wires are copper, and with this combination of materials and dimensions, the instrument has a time response of 50 msec and a sensitivity of 10 watts/cm^2/mV.

A feature of the HTL instrument that is not present in the other intrafireball radiometers is an annular disc which restricts the aperture to approximately the diameter of the foil, as illustrated in the lower portion of Fig. A-14. The upper surface of the disc is coated with a thin, light-absorbing layer to minimize reflection, and energy that is absorbed by the disc is conducted to a region of the heat sink that is remote from the foil. This disc, along with an external annular ring illustrated on the upper sketch of Fig. A-14,

* The basic energy-sensing element of this radiometer was manufactured by Heat Technology Laboratories, Huntsville, Alabama. Fabrication of the supplementary hardware and assembly was done at the AFRPL shop, Edwards Air Force Base, California.

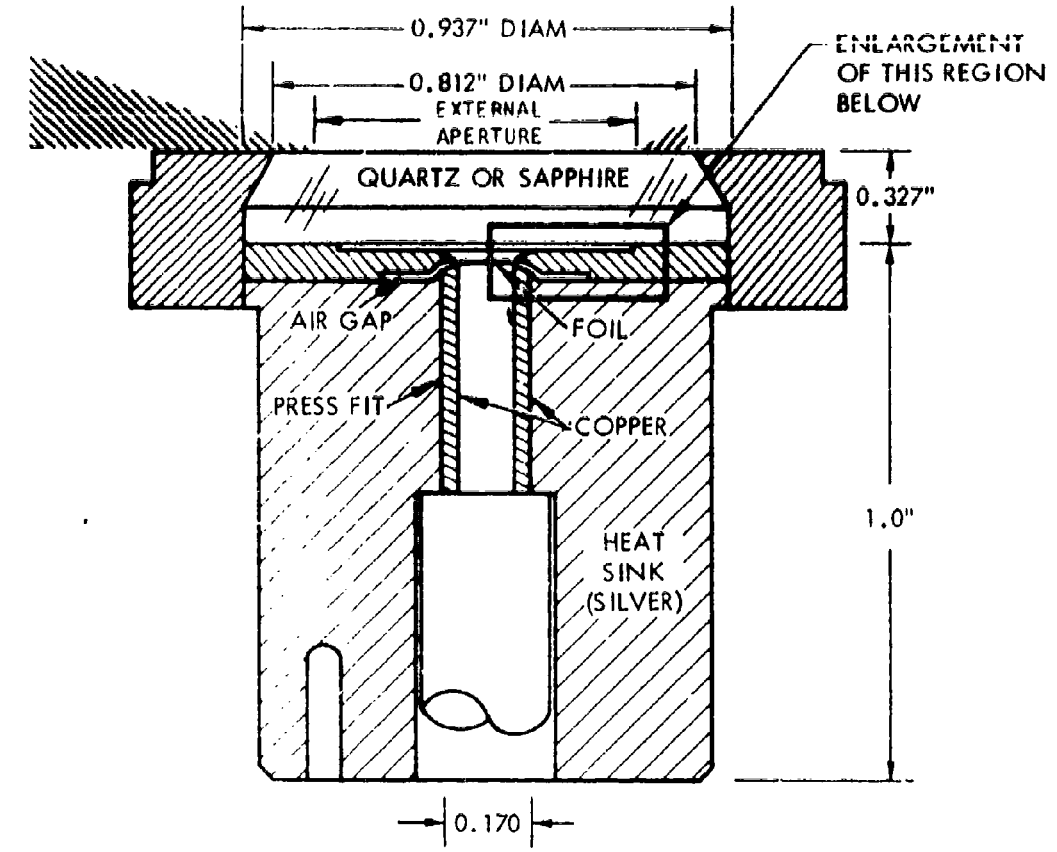

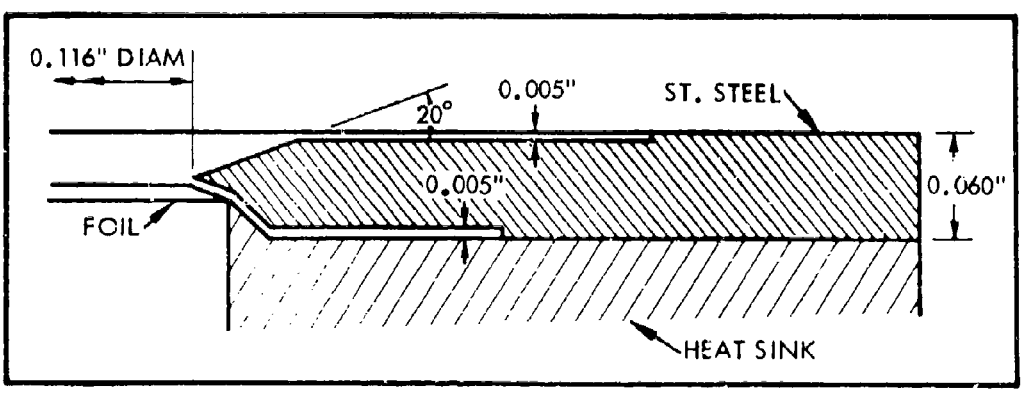

Fig. A-14. HTL Radiometer

restricts energy having angles of incidence between 70 and 90 deg from arriving at the foil. The diameter of the external aperture is just sufficient, accounting for refraction at the window surfaces, to restrict energy incident between 70 and 90 deg from arriving at the foil. No such restriction, either internally or externally, existed for the remaining two intrafireball radiometers.

The relevant data and characteristics of all four radiometers are listed in Table A-2.

Table A-2
DIMENSIONS AND CHARACTERISTICS OF THE RADIOMETERS

		HTL	SANDIA	RU-1	EXTERNAL
FOIL	Thickness (in.)	0.001	0.005	0.001	0.001
	Diameter (in.)	0.089	0.25	0.25	0.25
	Material	Constantan	Silver	Silver	Silver
Thermocouple Junction Wire Material		Copper	Constantan	Constantan	Constantan
WINDOW	Thickness (in.)	3/16	3/8	3/16	1/4
	Diameter (in.)	0.94	3.2	0.94	1.75
	Material	Quartz or Sapphire	Quartz	Quartz or Sapphire	Quartz
Field-of-View (deg)		70	90	90	45
Time Response (msec)		50	60	60	60
Sensitivity (watt/cm^2/mV)		10	50	8	10

Correction Factors for Radiometer Measurements Within the Fireball

Questions for interpreting radiometer data that are obtained within the fireball arise, and a correction factor permitting proper interpretation must be obtained. Evaluation of the correction factor is necessary because the intention is to evaluate the radiant energy incident on an immersed object

while the energy-detecting element of the radiometers is behind a window. Energy is lost enroute to the element by reflection at both surfaces of the window and by absorption within the window, and adjustment of the measured flux requires knowledge of the relationship between the flux at an exposed surface to that at the sensitive elements.

As will be described below, rather significant uncertainties exist regarding two properties of the fireball that are used in evaluating the radiometer-data correction factor. While these properties can be measured, a rather substantial effort is required, and in light of the secondary nature of the measurements, as mentioned in the general discussion, an effort to lessen these uncertainties did not appear to be warranted, nor was any made. In addition, no thorough analysis which would indicate the level of the uncertainty has been performed, although limited consideration suggests uncertainties of perhaps 20 or 30 percent. The data, however, are considered of value in supporting, at this level of uncertainty, the general magnitudes of other measurements, and consequently estimates of the correction factors based on the best available information have been evaluated. The origin and nature of the uncertainties will become more evident in the following paragraphs, which describe the process of evaluating the correction factors. The correction factor consists of the ratio of the radiant energy incident on an exposed surface area to that on the same area which is separated from the gas by a window, and the discussion commences with the evaluation of the energy on the exposed area.

Consider in Fig. A-15 the energy emitted from an elemental volume ΔV of gas which intersects the elemental area ΔA. Letting the energy emitted per unit volume of gas be e_1, the energy emitted from ΔV in all directions is $e_1 \Delta V$, and the fraction emitted in a direction so as to intersect the area ΔA is $(\Delta A \cos \Theta)/4\pi r^2$, where r is the distance between ΔA and ΔV and Θ is the angle between the line intersecting ΔV and ΔA and the normal to ΔA. Some of this energy is absorbed by the gas. In particular, the fraction of the energy not absorbed is e^{-kr}, where k is an absorption coefficient. The energy emitted by ΔV that arrives on ΔA then is

$$\frac{e_1 \Delta A}{4\pi} \sin \theta \cos \theta \, e^{-kr} \, d\theta dr d\phi \qquad (A.10)$$

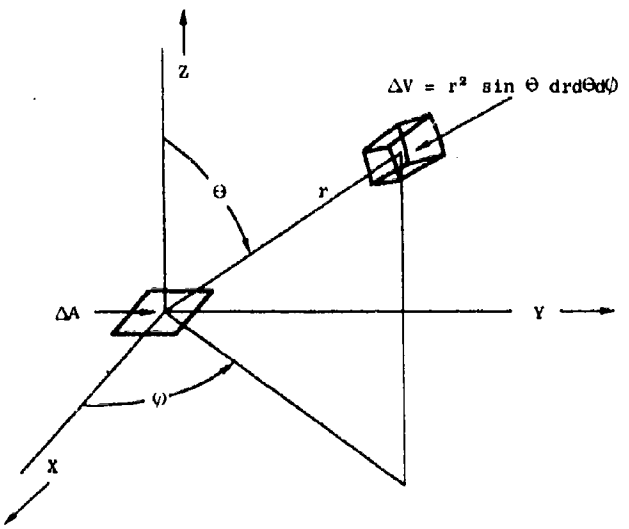

Fig. A-15. Basic Geometry for Computation of Radiant Flux Density Correction Factor

In summing the contributions of energy from the entire gas, where it is assumed that the gas extends indefinitely in both the lateral (X and Y) and vertical (Z) directions, it is convenient to identify for later use the angular energy distribution on ΔA by summing first over the ranges of the variables r and ϕ giving

$$e_\theta = \frac{e_1 \theta A}{2k} \sin \theta \cos \theta \, d\theta \qquad (A.11)$$

Thus e_O is the total energy arriving at ΔA with an angle of incidence between Θ and $\Theta+d\Theta$. Continuing the summation over the range of the angle Θ, the total energy arriving on ΔA is

$$e = \frac{e_1 \Delta A}{4k} \tag{A.12}$$

It is this quantity that must be compared with the energy on ΔA when a window is inserted between the radiating gas and ΔA.

For the case where a window separates ΔA from the radiating gas, it is convenient to first evaluate the energy incident on ΔA for a window having infinite lateral dimensions and to subsequently show that the energy is approximately the same for windows that are appropriately finite laterally.

Commencing with the assumed laterally infinite window and assuming that the radiating gas occupies all of the space on one side of the window, the angular distribution of energy on the upper exposed surface of the window is given by Eq. (A.11) (now interpreting the angle Θ as simply the angle of incidence) and the energy is uniformly distributed over this surface since the gas extends indefinitely. Since the irradiance of the upper surface is uniform, the energy emerging from the lower surface of the windows is also uniform, although the angular distribution of the emerging energy will not be described by Eq. (A.11) since energy is lost by reflection at both the upper and lower surface of the window (absorption within the window is momentarily ignored) and the fraction of the energy reflected depends on the angle of incidence. However, since the radiant energy emerging from the lower surface of the window is uniform, evaluating the emergent radiant flux density (or the energy on ΔA below the window) is simply a matter of evaluating the energy that is transmitted through the window for an angular distribution of incident energy given by Eq. (A.11). That is, the complexities of computation that arise for cases where the emergent energy is not uniform can be avoided. The reflected energy at the exposed window surface depends on the angular distribution of energy at that surface and on the index of refraction of the window material relative to the radiating gas.

(The fundamental relationships permitting evaluation of reflected energy are given, for instance, in Chapter 1 of Ref. A-9 and Chapter 25 of Ref. A-10). At the lower or unexposed surface, the reflected energy depends on the index of refraction of the window material relative to air and on the angular distribution of energy at the lower surface. This distribution is different from the above distribution due both to refraction (or bending) at the upper surface and to the different quantities of energy that were reflected at each angle at the upper surface. The index of refraction associated with the upper surface is comparatively uncertain due to the uncertainty that exists in the properties of the radiating gas, and this lack of knowledge represents one of two significant weaknesses of the intrafireball radiometer measurements. In order to provide an approximation to the correction factor, however, computations were made for the single case where the index of refraction of the window relative to the radiating gas is the same as that of the window relative to air (the same as the index associated with the lower window surface). For this case, the fraction of energy with an angle of incidence of Θ that is transmitted through both surfaces, ignoring multiple reflections at a given surface, is given by

$$T(\Theta) = 8(n \cos \Theta \cos \Theta')^2 \left\{ \frac{1}{(\cos \Theta + n \cos \Theta')^4} + \frac{1}{(n \cos \Theta + \cos \Theta')^4} \right\} \qquad (A.13)$$

where n is index refraction of window relative to surrounding gas and Θ is related to Θ' by $\sin \Theta = n \sin \Theta'$. The angular distribution of energy on ΔA beneath the window is then

$$e_\Theta = \frac{e_1 \Delta A}{2k} T(\Theta) \sin \Theta \cos \Theta \, d\Theta \qquad (A.14)$$

The summation of Eq. (A.14) gives the energy on ΔA and, as will be shown below, has been computed for quartz and sapphire over various appropriate ranges of Θ. Finally, the data correction factor (thus far excluding the correction for absorbed energy) is given by

$$F = \frac{e_1 \Delta A}{4k} \Big/ \frac{c_1 \Delta A}{2k} \cdot \int_0^{\theta_1} T(\theta) \sin\theta \cos\theta \, d\theta \qquad (A.15)$$

$$= 1/2 \cdot \int_0^{\theta_1} T(\theta) \sin\theta \cos\theta \, d\theta$$

where θ_1 is the maximum angle of incidence permitted in the particular instrument. Eq. (A.15) is the ratio of energy incident on ΔA without a window [Eq. (A.12)] to that with a window, so that the measured radiant flux density should be multiplied by F in order to determine the radiant flux density on an exposed surface. For the RU-1 and Sandia radiometers, θ_1 was 90 deg. whereas it was usually 70 deg for the HTL radiometer due to presence of an aperture arrangement b th on the exposed and underneath side of the window.

Thus far, a laterally infinite window has been assumed. Consideration of the path of light "beams" which arrive on ΔA from any possible direction, as illustrated in cross section with incident beams at 0, 45, 90 deg on Fig. A-16a, indicates that because of refraction, only a window section of finite diameter D is involved. That is, the window, except for the disk of diameter D, could be removed without any effect on the energy at ΔA. For the radiometers, ΔA, the sensitive element of the radiometer, is slightly below the lower window surface, and for radiation at a given angle, the diameter must be increased, as

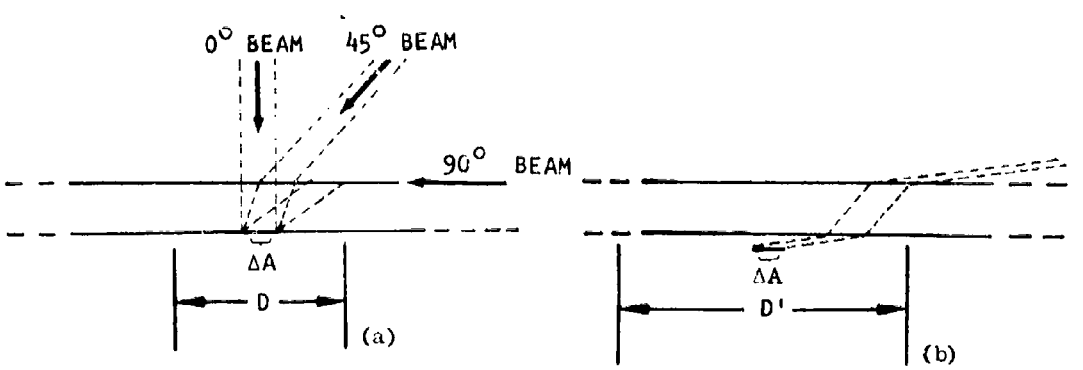

Fig. A-16. Illustration of the Useful Dimensions of Radiometer Windows

illustrated in Fig. A-16b, to D'. In addition, energy incident at and approaching 90 deg is restricted from arriving at ΔA for a finite window. For the radiometer dimensions used, however, this energy loss is negligible; for instance, for the HTL radiometers where 3/16-in.-thick windows with an effective diameter of 0.81 in. were used and the sensitive element was 0.003 in. below the window surface, the fraction of the energy lost due to its finite diameter is estimated to be about 1/10,000 for quartz, and similar numbers occur for other materials and radiometers.

Evaluating the energy absorbed within the window requires knowledge of the wavelength and angular distribution of the incident radiant energy and the absorption coefficient of the window material as a function of wavelength. The wavelength distribution is not precisely known, although the general form for black or grey bodies is known, given the temperature. The distribution for fireballs from LO_2/RP-1 explosions probably reasonably approximates that from a blackbody. This uncertain wavelength distribution, however, does create an uncertainty in the evaluation of the absorbed energy, although it is not particularly serious at the expected temperature levels. The window materials have been chosen so that for temperatures obtained, the absorbed energy will be minor for any probable wavelength distribution. For instance, special grades of fuzed quartz* are used which are excellant transmitters beyond (at greater wavelength than) the 2.7-μ water band region to about 3.5 μ, along with sapphire,** which transmits to the 4.5-μ region. To illustrate, the fraction of the energy from a blackbody at 2300°K that is beyond 3.5 and 4.5 μ is about 14 and 8 percent, respectively. This percentage can be somewhat higher for probable wavelength distributions of the fireball, however. In addition, as the gas temperature decreases, the fraction of the energy that is in the wavelength region beyond the transmission cutoff increases, that is, the fraction absorbed increases, and the error in the estimated energy loss tends to have a more serious effect on

* A grade referred to as "Infrasil" from Englehard Industries, Inc., Amerisil Quartz Division, Hillsdale, N.Y., and grade G-106 from General Electric Comp., Lamp Glass Dept., Cleveland, Ohio.

** Optical grade synthetic sapphire from Linde Division, Union Carbide Corp., Torrance, California.

the total correction factor. In addition to the energy absorbed that is beyond transmission cutoff at 3.5 and 4.5 μ, some energy is also absorbed in the transmission region of quartz and sapphire. For the window thicknesses involved, this represents a small fraction of the energy, and evaluating the energy in this case does not depend critically on the wavelength distribution since the absorption properties of quartz and sapphire are for practical purposes constant over this portion of the spectrum. The absorption properties are more uncertain here and increase in uncertainty as the absorption coefficients become negligibly small; however, since this entails a large error of the negligible energy loss, the correction factor is not seriously effected by the error.

An estimate of the fraction of the energy absorbed for the various window thicknesses and materials and radiometer fields-of-view was obtained, and the corresponding correction factors associated with absorption alone (as well as those associated with the combined effect of reflection and absorption) are presented below. For the absorption estimate, the wavelength distribution from a 2200°K blackbody was assumed, and the absorption properties used were those specified by the manufacturer of the windows, supplemented by data from the technical literature.* Also, while the distance a given beam of energy traverses through the window varies with the angle of incidence, the estimate was based on an averaged distance. The absorption losses should properly have been evaluated in conjunction with reflection losses. However, the error resulting from their separate treatment is comparatively insignificant.

The final correction factors are listed in Table A-3. In order to indicate the relative influence of reflection and absorption, the factors due to reflection alone and absorption alone have been included along with the results from their combined effect. It should be noted that these factors will tend to become larger as the gas temperature decreases from 2200°K.

* Absorption properties of sapphire are given in Refs. A-11 and A-12. The properties of fuzed quartz (silica; SiO_2) are available in numerous handbooks and infrared reference books.

Table A-3

RADIOMETER CORRECTION FACTORS

INSTRUMENT DESIGNATION	WINDOW MATERIAL	FIELD-OF-VIEW (deg)	CORRECTION FACTOR		
			DUE TO REFLECTION ONLY	DUE TO ABSORPTION ONLY	DUE TO REFLECTION AND ABSORPTION
Sandia	Quartz	90	1.19	1.19	1.43
RU-1	Quartz	90	1.19	1.18	1.41
HTL	Quartz	70	1.28*	1.18	1.51
HTL	Sapphire	70	1.37*	1.18	1.60

THERMOCOUPLE PROBE

Measurements of the fireball gas temperature at instrument locations within the fireball were made by the Sandia Corporation with a metallically sheathed thermocouple junction, or thermocouple probe. The probe consists of a 1-mil-wire-thickness tungsten/tungsten 26% rhenium thermocouple sheathed with 16-mil-O.D. molybdenum disulfate-coated tantulum. The thermocouple wires are insulated from the sheath and, except at the junction, from each other by beryllium oxide.

While the thermocouple probe is a standard instrument, for the temperatures and molecular constituents that occur in the fireball, a comparatively large uncertainty in the indicated temperature of its environment occurs. Upon immersion in the fireball, the temperature of the instrument commences to increase rapidly toward that of its environment, and at temperatures well below the melting temperature of the sheath, a chemical reaction between the sheath material and the nearby oxidants of the fireball gas commences. The energy from the reaction can contribute substantially to the temperature elevation of the probe and its ultimate temperature can exceed that of its environment. The rate of

* Includes loss due to field-of-view restriction.

reaction depends, of course, on the type and concentration of available oxidants, the flow velocities, and the sheath material, and it is difficult to establish whether the reaction is or is not inducing a false indication of significance. The resultant data, however, should be used with caution.

Passive Sensor

A piece of test hardware inadvertently became a passive thermal sensor for Test 285. This sensor consists of a solid aluminum cone, as illustrated in Fig. A-17. At the time of ignition, it was located at or within a few feet of the point of initial propellant ignition, and after the test was located within a few feet of its initial location. Approximately 0.1 to 0.2 in. of material had been uniformly ablated from the surface of the sensor. No thorough analysis of the possible heating pulses that could have induced such an ablation has been performed, nor is it clear if chemical reaction was involved in the process of ablating the surface.

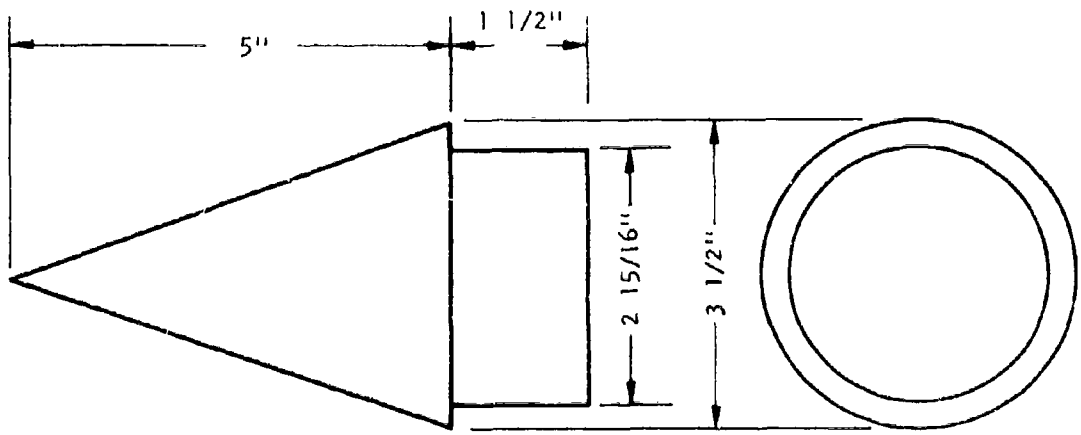

SCALE = 1/2
MATERIAL = 6061 - T6 Aluminum

Fig. A-17. Dimensions of Aluminum Cone

INSTRUMENT MOUNTING

Within the Fireball (25,000-lb Tests and Titan Test)

There are four intrafireball instrument mounts which are designated as the H, S, P, and Sandia Stations. This section contains a description of these stations, their location, and the position of the instruments on the stations.

A sketch of station "H" is given in Fig. A-18, showing the location of two slabs and four radiometer positions along the upper surface of the mount. Also along the upper surface is a "wing-like" projection (or wing), which extends beyond the main body of the mount both laterally and toward the center of the explosion. The wing is 1 in. thick (steel), with two adjacent slabs (3- by 3- by 1-in.-thick stainless steel 303) mounted with their exposed surface flush with the upper surface of the wing. The upper wing surface is entirely planar, and the leading edge and wing tips are tapered in toward the main body from the perimeter of the upper surface at an angle of 30 deg from the horizontal. The function of the wing is to induce similarity of gas flow along the surface of the two slabs even though the flow direction may be somewhat askew of the vertical plane of symmetry of the mount and/or of the horizontal plane.

Positions for four radiometers were included in order that gross differences could be detected between simultaneous measurements from dissimilar instruments, similar instruments with dissimilar window materials, etc., although differences exceeding the measurement uncertainty were not obtained. The radiometers of this station are provided, starting with test No. 279, with a helium purge (apparatus not included in sketch) along the exposed surface of their windows, the purpose being to minimize particle deposition and window heating, the latter because it tends to alter the reflection and absorption properties of the window. Through appropriate shaping of the purge-gas orifice and control of the velocity of the purge gas at the orifice, the purge-gas flow along the upper surface of the window was confined to a thickness of about a millimeter, and thus did not tend to repel the fireball gas from the window surface to an undesirable extent. The

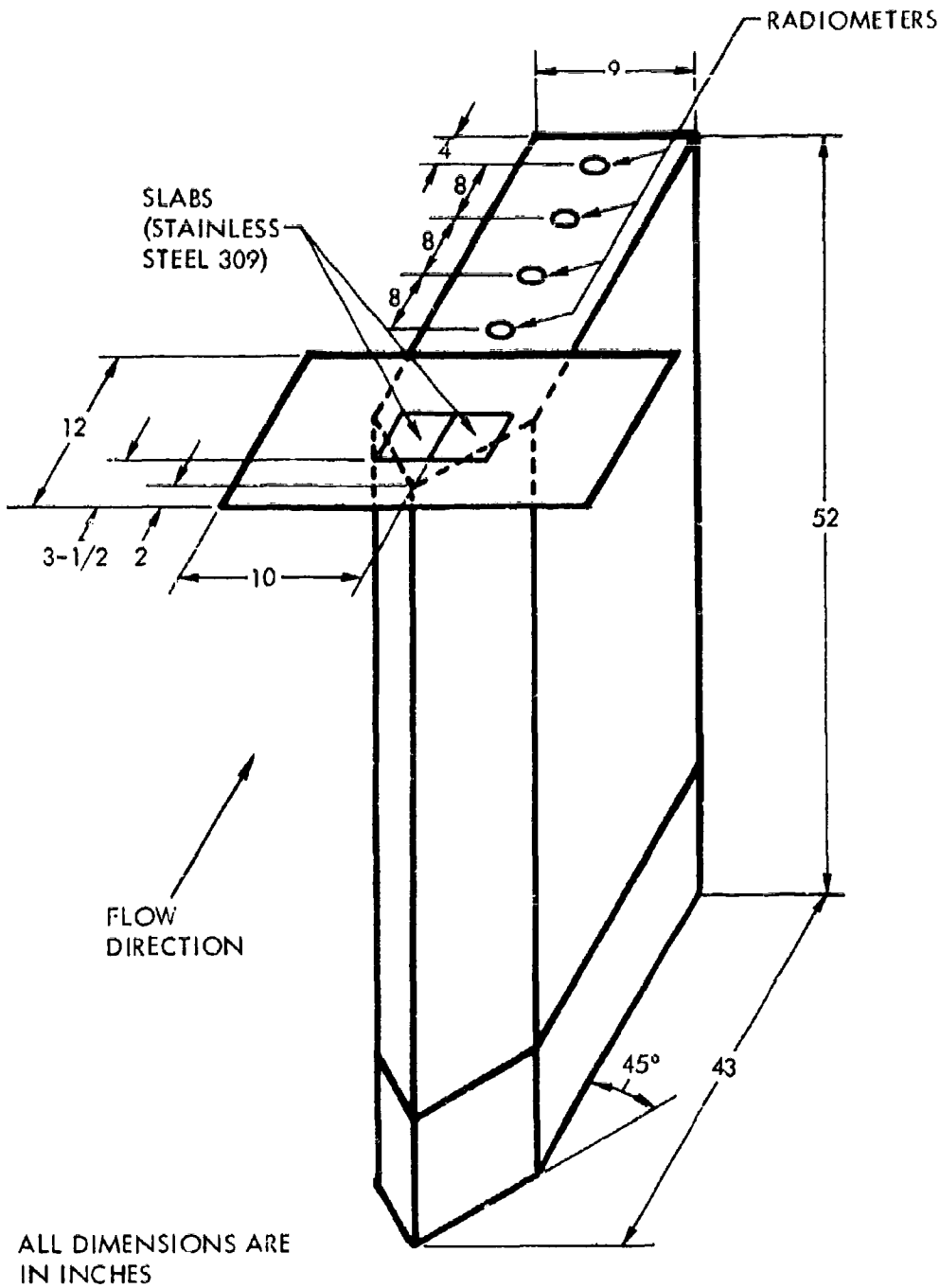

Fig. A-18. Intrafireball Thermal Instrument Station H

purge, however, did successfully eliminate deposition, although difficulty was experienced in maintaining the required purge-orifice alignment.

A sketch of station S is given on Fig. A-19, showing locations of two slabs, two thermocouple probes, and a radiometer, although no radiometer data were successfully acquired at this station. Station S was generally located approximately 13 ft above the ground surface and as near to the center of the explosion as practical. During Tests 275 through 285 it was located at a ground distance from the center of the test pad of about 23 ft approximately along gauge line A. Due to the difficulty of maintaining the station at this distance, it was relocated for the remaining tests to a ground distance of 32 ft along a radial line about half way between gauge lines A and B. A sketch of the station and its final support structure is given in Fig. A-20.

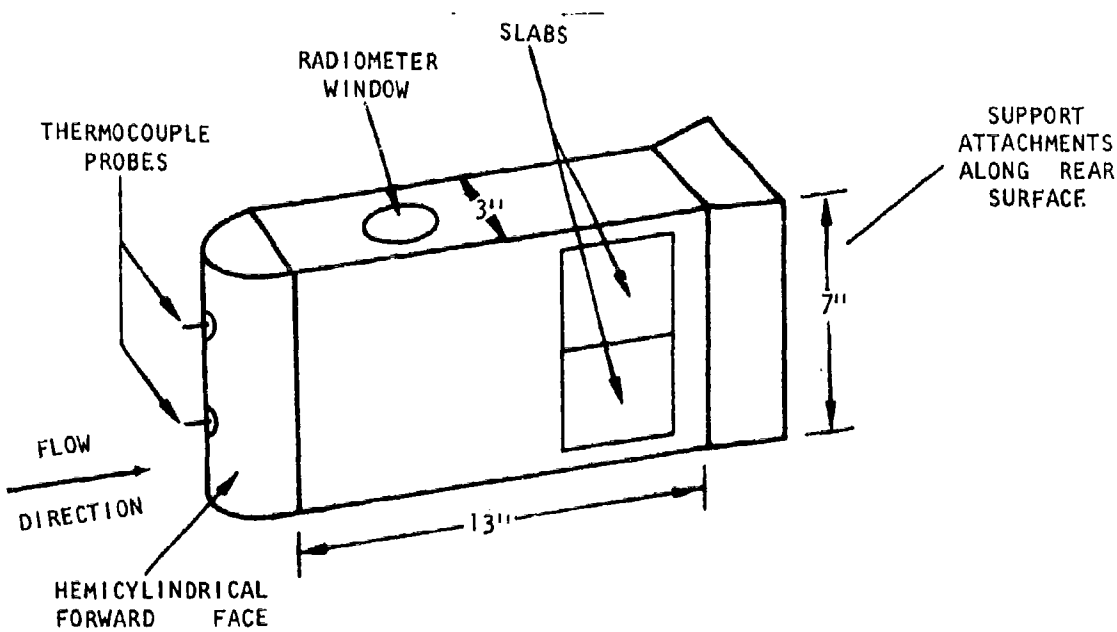

Fig. A-19. Intrafireball Thermal Instrument Station S

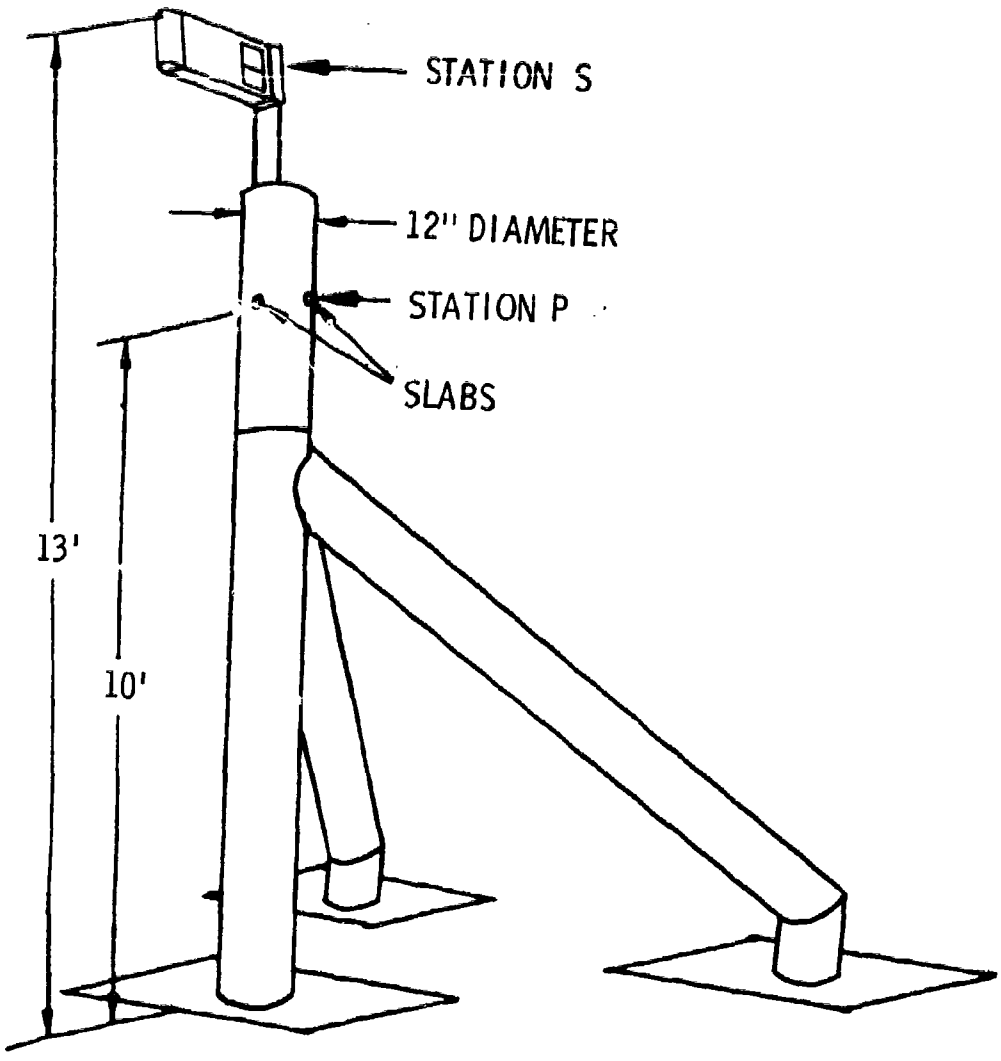

Fig. A-20. Thermal Instrument Stations P and S

The slabs on the S station from Tests 275 through 279 were 3- by 3- by 1-in.-thick stainless steel 309. While slabs having comparatively small thermal diffusivities such as stainless steel are preferable for the longer duration tests, the loss of several temperature transducers during the first few 25,000-lb tests required their replacement with transducers and slabs of copper. In order to increase the time during which negligible errors occur in the evaluation of heat flux, slabs having a thickness of 1-1/2 in. were installed, where as usual, the exposed slab surface was flush with the external surface of the mount.

The location of station P is shown in Fig. A-20 just below station S, station P being actually part of the support structure for station S. Station P, installed after Test 285, consists of a series of instrumented slabs distributed at 60-deg-angle intervals along the circumference of a 12-in.-diameter, vertically oriented pipe. A more detailed cross-sectional cutaway view showing the slab arrangement is given in Fig. A-21, along with a dimensional sketch of an individual slab in the lower right hand corner of the figure. The primary purpose of the station was to determine if there are pronounced and consistent variations of flux density with position on such an object.

It was planned to use iron transducers and slabs in station P. However, iron transducers were not available until the Titan I test (Test 301) and copper transducers and slabs were substituted. The use of copper with these comparatively small slab dimensions will result in small errors in the evaluation of heat flux toward the end of the heating pulse as noted in the discussion of errors above. Iron slabs were installed for the Titan I test at station P positions 1, 3, and 5 (position is designated by numbers in parentheses on Fig. A-21.

The Sandia station was elevated above the ground surface approximately 13 ft and supported by a structure similar to that for station S shown on Fig. A-20. It was located about 30 ft from the test pad center at a point approximately intersecting gauge lines A and C.

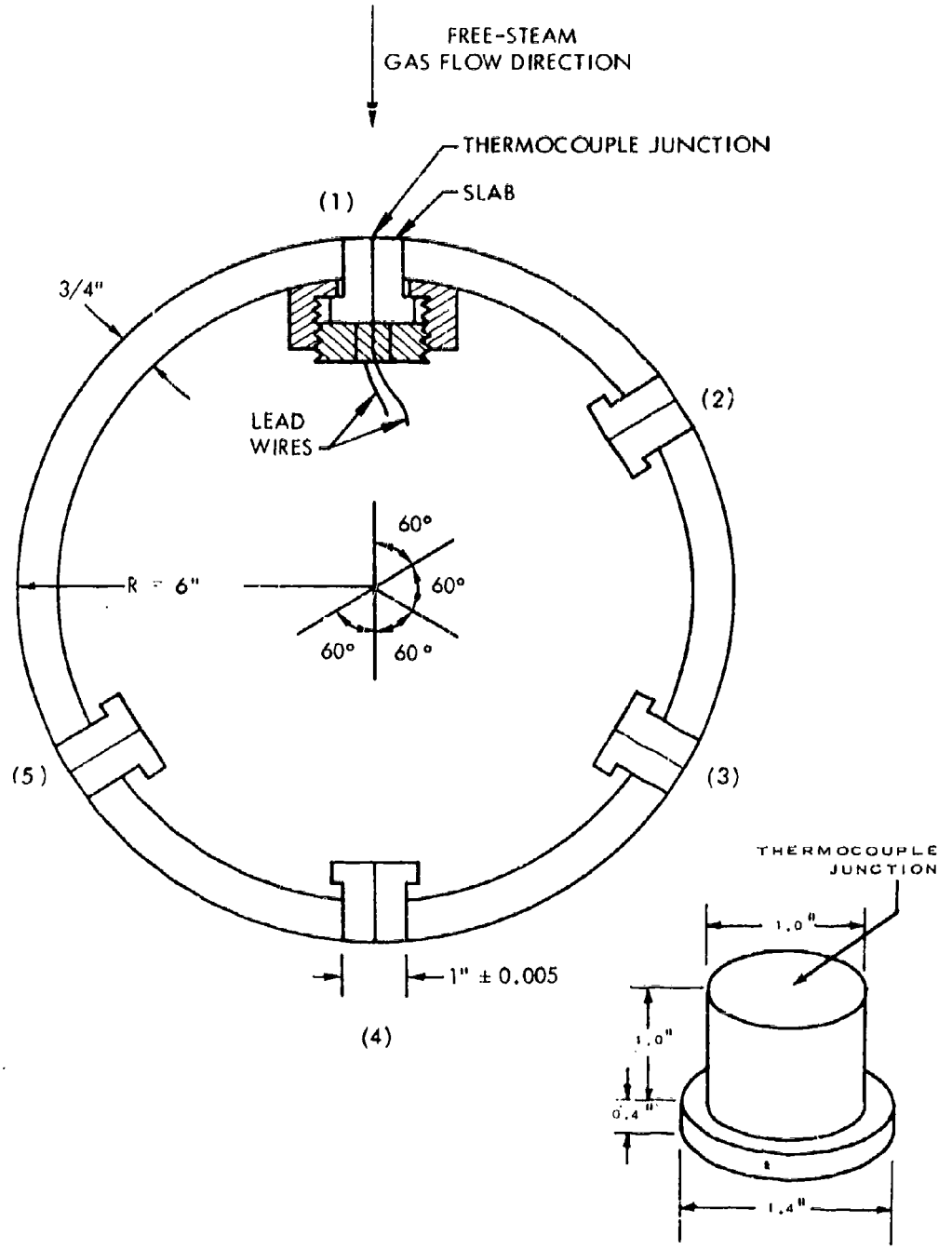

Fig. A-21. Cross-Sectional Cutaway View of Thermal Instrument Station P and a Perspective View of the Associated Slabs

Within the Fireball (200- and 1000-lb Tests)

Station H

Instrument station H as it existed for the 25,000-lb tests and the Titan test was described starting on page A-42 and illustrated in Fig. A-18. A slightly modified version of the station was used for the 200- and 1000-lb tests as follows. The wing-like projection shown in Fig. A-18 was absent, and the upper surface of the mount was instrumented with two 6- by 6- by 1-in.-thick slabs, in tandem with respect to a line through the center of the test area (center of explosion). It was located approximately 13 ft from the center of the test area along gauge line A.

Station S

Instrument station S is described starting on page A-44 and is illustrated in Fig. A-19. This station (as shown in the figure) was located about directly above the center of the test area at a height of approximately 13 ft (attached to a propellant tank drop tower). Its orientation with respect to the expanding fireball gas was as indicated in Fig. A-19.

Outside the Fireball (25,000-lb Tests and Titan Test)

Measurements of radiant flux density and fireball temperature are made from remote locations. Generally three radiometers were used per test, two at the same distance (335 ft) from ground zero along radial gauge lines (A and B) 120 deg from each other, with the third more remotely located (600 ft) along gauge line A. These distances are such that with the existing field-of-view of the instruments, radiant energy originating in any region of the fireball prior to its rise is not restricted from falling incident on the sensitive foil of the instrument.

The photo-recording pyrometer (a Sandia Corporation instrument) was located about 450 ft from the test pad along gauge line A.

REFERENCES, APPENDIX A

A-1. Churchill, R. V., Operational Mathematics, McGraw-Hill Book Company, Inc., New York, New York, 1958

A-2. Kendall, D. N. and W. P. Dixon, Heat Transfer Measurements in a Hot Shot Wind Tunnel, IEEE Aerospace Systems Conference, Seattle, Washington, 11-15 July 1966

A-3. Robertson, S. J., Theory and Application of Long Duration Heat Flux Sensors, HTL-TR-18, Contract NAS 8-11558, Heat Technology Laboratory, Inc., Huntsville, Alabama, 21 September 1964

A-4. RAD, Beck, J. V., Correction of Transient Thermocouple Temperature Measurements in Heat-Conducting Solids, Part I, Procedures of Thermocouple Temperature Correction in Solids Possessing Constant Thermal Properties, Technical Report, RAD-TR-60-38, Contract AF04(647)-258, 8 February 1961, (AD 269354)

A-5. Goldsmith, A., T. E. Waterman, and H. J. Hirschhorn, Handbook of Thermo-Physical Properties of Solid Materials, The Macmillan Company, New York, New York, 1961

A-6. Marchi, Vito V., Advanced Technology Division of American-Standard, Mountain View, California, Private Communication, 29 November 1965

A-7. Gardon, R., "An Instrument for the Direct Measurement of Intense Thermal Radiation," The Review of Scientific Instruments, Vol. 24, No. 5, May 1953

A-8. Ferris, H. G., Theoretical Analysis of Radiometer Performance, R & D Technical Report USNRDL-TR-311, AFSWP-1119, U.S. Naval Radiological Defense Laboratory, San Francisco, California, 13 January 1959

A-9. Born, M. and E. Wolf, Principles of Optics - Electromagnetic Theory of Propagation, Interference and Diffraction of Light, Pergamon Press, New York, New York, 1959

A-10. Jenkins, F. A. and H. E. White, Fundamentals of Optics, McGraw-Hill Book Company, Inc., New York, New York, 1957

A-11. Oppenheim, U. P. and U. Even, "Infrared Properties of Sapphire at Elevated Temperatures," Journal Optical Society of America, Vol. 52, No. 9, September 1962, pp. 1078-1079

A-12. Gryvnak, D. A. and D. E. Burch, "Optical and Infrared Properties of Al_2O_3 at Elevated Temperatures," Journal Optical Society of America, Vol. 55, No. 6, June 1965, pp. 625-630

Appendix B
BASIC DATA

Appendix B
BASIC DATA

This section consists of a presentation of the basic thermal data. The following data are included:

- Heat flux density computed from measurements of the surface temperature of slabs, and a selected sample of the corresponding slab surface temperatures. (All available flux density data from the 25,000-lb and Titan I tests are included. However, data from Tests 277, 281, and 282 are not presented; substantial winds in an unfavorable direction prevented significant instrument response. Some flux data from all 1000-lb LO_2/RP-1 and LO_2/LH_2 tests are presented, this consisting of 13 tests for each propellant type. At the 200-lb level, data are presented from seven LO_2/RP-1 tests and five LO_2/LH_2 tests, this representing only a fraction of the tests conducted. For the hypergolic propellant combination of N_2O_4/50% UDMH – 50% N_2H_4, data are presented from three each 200- and 1000-lb tests, these six tests being the only hypergolic tests for which flux data were obtained.)

- Radiant flux density within the fireball. (All useful data from the 25,000-lb tests are included. However, a limited quantity of reliable data was obtained due primarily to transducer failure and failure of the window purge system. o Titan I data were obtained, and no 200- or 1000-lb data are given.)

- Radiant flux density outside the fireball. (All available data from the 25,000-lb tests and the Titan I test are included.)

- Gas temperature as indicated by the thermocouple probes—Sandia Corporation instruments. (Only a sample selection of data from the 25,000-lb tests is presented.)

Gas temperatures as indicated by the photographic recording pyrometer – a Sandia Corporation instrument – are not included. However, a graphic summary of these data from the 25,000-lb tests is given in Section 4.

The data are organized as indicated in Table B-1. The order in which the data are presented follows the order that the data were considered in Section 4.

For the 25,000-lb tests and the Titan I test, the heat flux density data for stations H and S are presented in pairs, one pair for each station, corresponding to the adjacent slab pairs that existed for these two stations as described

Table B-1

ORGANIZATION OF THERMAL DATA

FIGURE NUMBER	THROUGH	FIGURE NUMBER	DATA DESCRIPTION
B-1		B-9	Heat flux density and selected slab surface temperatures for 25,000-lb LO_2/RP-1 tests.
B-10		B-28	Heat flux density and selected slab surface temperatures for 25,000-lb LO_2/LH_2 tests.
B-29		B-30	Radiant flux density within the fireball for 25,000-lb tests.
B-31		B-33	Temperature of thermocouple probes for 25,000-lb tests.
B-34		B-36	Heat flux density for Titan I test.
B-37		B-59	Heat flux density for 1000-lb LO_2/RP-1 tests.
B-60		B-82	Heat flux density for 1000-lb LO_2/LH_2 tests.
B-83		B-91	Heat flux density for 200-lb LO_2/RP-1 tests.
B-92		B-100	Heat flux density for 200-lb LO_2/LH_2 tests.
B-101		B-112	Heat flux density for 200- and 1000-lb N_2O_4/50% UDMH - 50% N_2H_4 tests.
B-113		B-119	Radiant flux density outside the fireball for the 25,000-lb tests and the Titan I test.

in Appendix A. Usually, the exposed surface of one of each pair was coated with a black deposit, and their companion slabs were either coated with a "white" deposit or the surface was polished. In order that the degree of similarity under identical instrument conditions could be revealed, both slabs at Station H for Test 284 were coated black. These deposits are identified in Appendix A, and the surface condition and slab material for each measurement is indicated on the data figure. Since slight differences in the instruments of a given pair of slabs are inevitable, the associated bias was minimized by frequently transposing the sequence or order of the coating arrangement for a given pair. For Station P (which existed only for Tests 288 through 290 and the Titan I test), the slabs at positions 1 through 4 were coated black, while Position 5, the conjugate of Position 3 with respect to gas flow, was coated white. Stations H and S were always instrumented with a pair of slabs, and Station P always with five slabs. Any omission of the corresponding heat flux data from this arrangement is due, with one exception, to instrument destruction during the test. The measurement at Position 3 of Station P for the Titan I test is not presented due to an inordinately noisy temperature record.

The heat flux density of Station S for Test 284 (Fig. B-6) is not valid beyond about 3 sec, this time being indicated by a vertical line on the data figure. The support structure for this station failed at some time during the test. No data discrepancies are evident until a simultaneous increase and decrease in the flux for companion slabs commences at the above time, followed soon thereafter by a decrease for both slabs to physically unrealistic negative magnitudes.

For the Titan I test, uncertainties in the flux density that are somewhat larger than ordinary are encountered temporarily for some of the measurements at Station P due to noise in the temperature – time records. Specifically, noisy signals were obtained from zero to 0.4 sec for instrument Position 2, and from 1.2 to 1.4 sec for Positions 2 and 4. This will cause flux density uncertainties throughout these time periods and for a comparatively short time thereafter.

For the 200- and 1000-lb tests, the heat flux data from the slab of a companion pair of slabs that was coated black are always presented; occasionally the flux from both the black and polished companion slabs are given although they are presented on consecutive figures rather than in superposition on a single figure as they are for the 25,000-lb tests. No data from slabs coated with a white deposit were obtained.

The accuracy of the data is thoroughly described in Appendix A.

The test conditions of propellant type, propellant configuration, ignition time, and impact velocity are described briefly in Section 4. (A detailed description of test conditions is given in Ref. B-1.) These test conditions are specified for each propellant test discussed or used in this report in Table B-2. Heat flux data are presented for all tests listed in Table B-2 except for Tests 281 and 282 and the Saturn S-IV test. Also listed in Table B-2 are so-called "terminal yield" values. Very roughly speaking, terminal yield is a measure of quantity of propellants that entered the explosion.

Regarding the measurements of radiant flux density within the fireball, correction factors as specified in Appendix A have been applied to the data presented in Figs. B-29 and B-30. For Test 284 (Fig. B-30), the window purge system did not successfully function for the measurement labeled "HTL, quartz", and was only partially successful, i.e., there was an opaque deposit over about one-half of the window, for the measurement labeled "Sandia, quartz."

Table B-2

SUMMARY OF TEST CONDITIONS

PROPELLANT TYPE	PROPELLANT WEIGHT (lb)	PROPELLANT CONFIGURATION	TEST* NO.	IGNITION TIME (msec)	TERMINAL YIELD (%)
LO_2/RP-1	100,000	CBM	Titan I	840	4
	25,000	CBM	275	515	4
			278	530	13
			282	540	13
		CBGS	284(M)*	0	2
			285(M)	465	37
	1,000	CBM	192	215	14
			193	220	20
			194	5000	5
			209	120	10
			270	225	13
		CBGS	190(H)	570	96
			191(M)	0	13
			218(M)	0	4
			219(M)	1835	14
			220(M)	525	96
			267(M)	1770	64
			268(M)	340	70
			269(H)	80	44
	200	CBM	238	85	19
			240**	155	60
		CBGS	141(H)	0	5
			206(H)	350	85
			248(L)	210	25
			249(M)	710	50
			250(M)	200	52

* Letters L, M, and H in parentheses signify low, medium, and high impact velocity, respectively.

** Two-thirds of the normal weight of both fuel and oxidizer of a 200-lb test were used with the normal 200-lb-capacity tank, however, yield for these tests were computed on basis of full tank.

Table B-2, cont.

PROPELLANT TYPE	PROPELLANT WEIGHT (lb)	PROPELLANT CONFIGURATION	TEST NO.	IGNITION TIME (msec)	TERMINAL YIELD (%)
LO_2/LH_2	92,000	CBM	Saturn IV	185	5
	25,000	CBM	277	31	0.2
			279	33	0.2
			281	-	0.1
		CBGS	288(M)	365	13
			289(M)	165	4
			290(M)	105	4
	1,000	CBM	210	20	7
			212	1365	27
			213	710	35
			265	750	10
		CBGS	211(M)	0	12
			214(H)	-	-
			215(M)	20	20
			216(H)	0	9
			217(M)	1490	33
			262(M)	900	42
			263(M)	-	-
			264(M)	21	22
			266(M)	0	14
	200	CBM	138*	100	17
		CBGS	251(M)	775	64
			252(M)	325	38
			253(H)	110	-
			254(M)	535	32
N_2O_4/ 50% UDMH- 50% N_2H_4	200	CBGS	157(H)	0	0.3
			158(H)	0	0.2
			159(H)	0	0.3
	1,000		189(H)	0	0.4
			257(H)	0	0.3
			258(H)	0	0.3

* The tank length to diameter ratio for Test 238 was 5 as opposed to 1.8 for the other 200-, 1000-, and 25,000-lb tests listed.

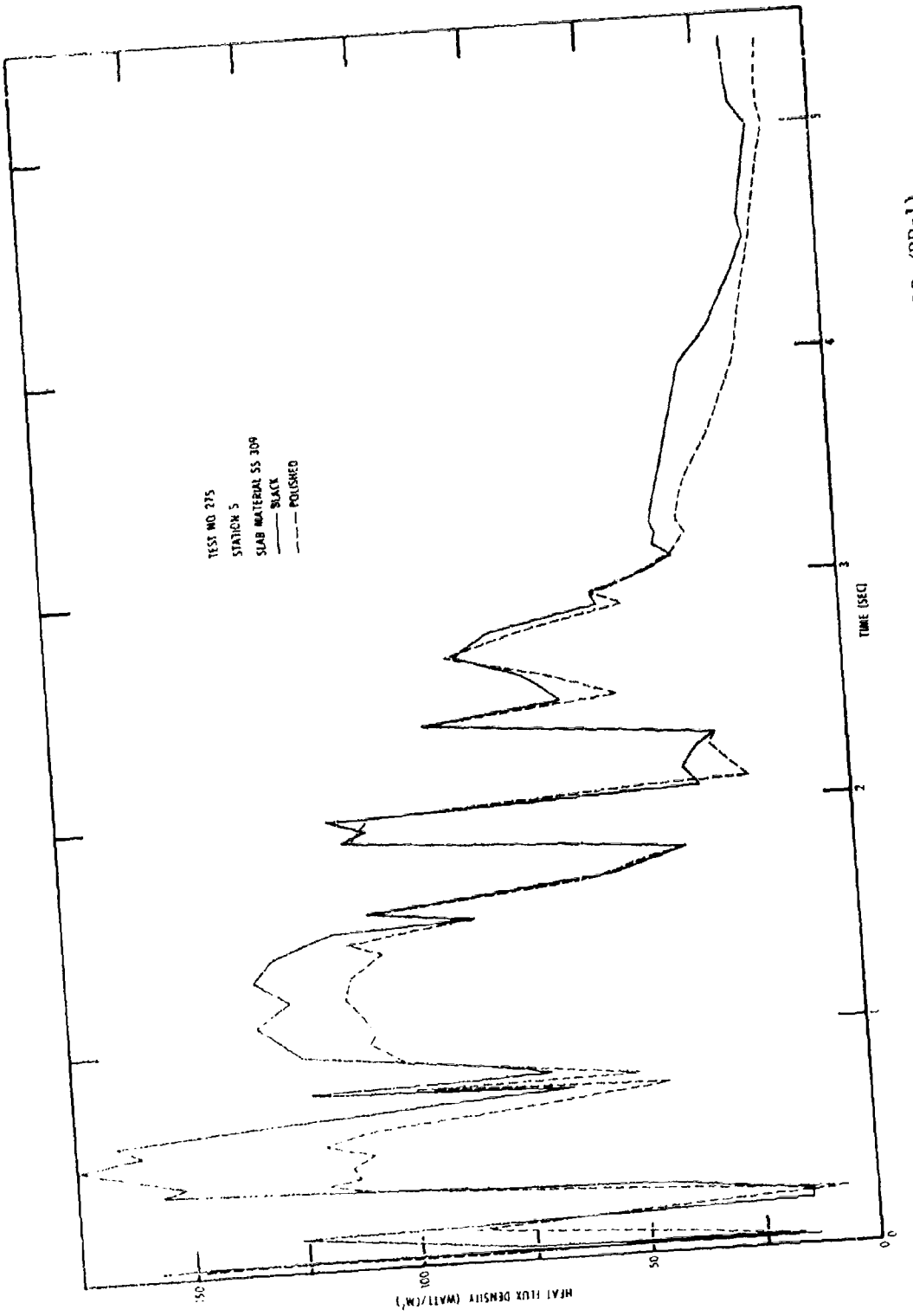

Fig. B-1. Heat Flux Density at Station S from Test 275 (25,000-lb LO_2/RP-1)

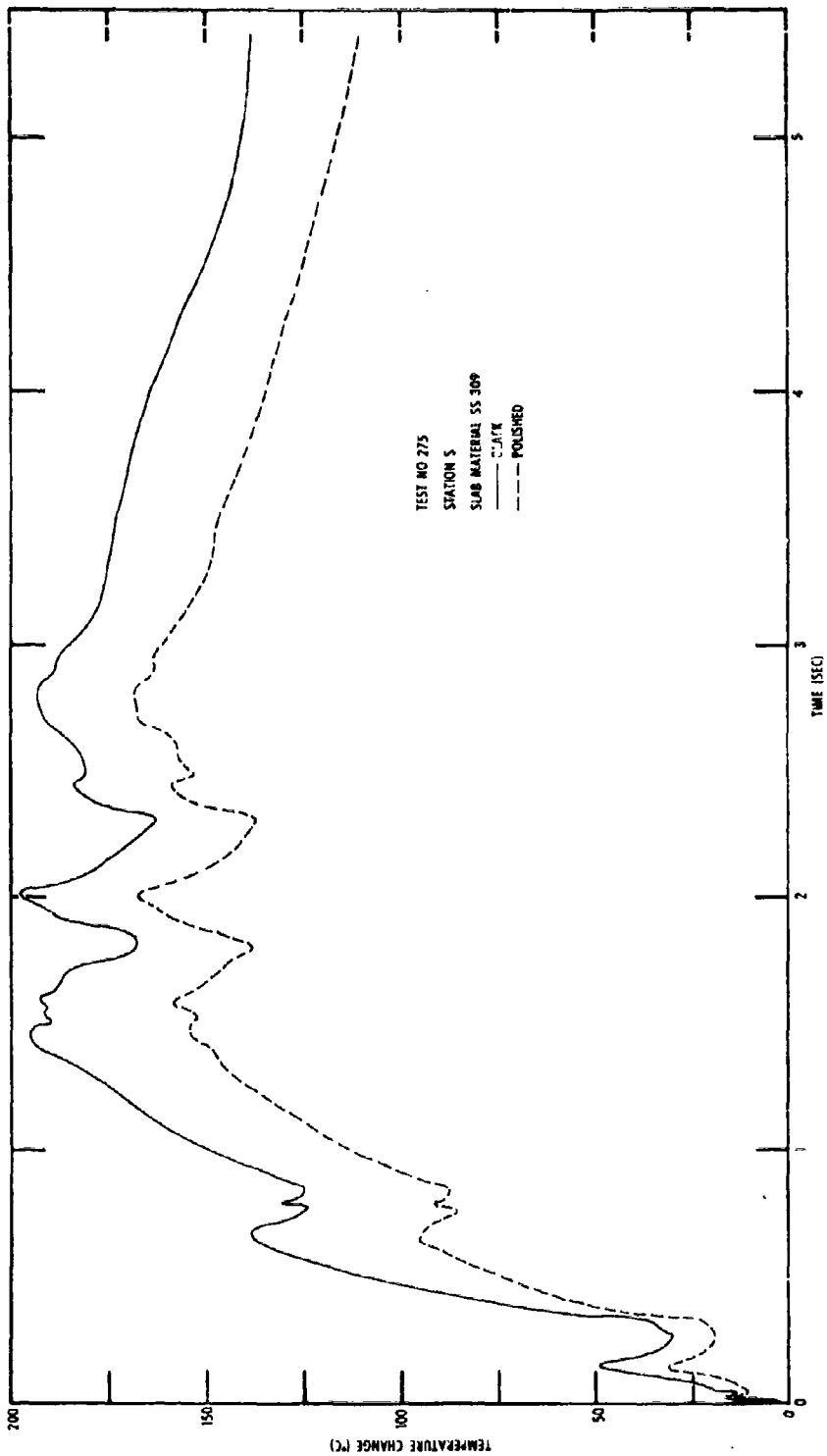

Fig. B-2. Slab Surface Temperature at Station S for Test 275

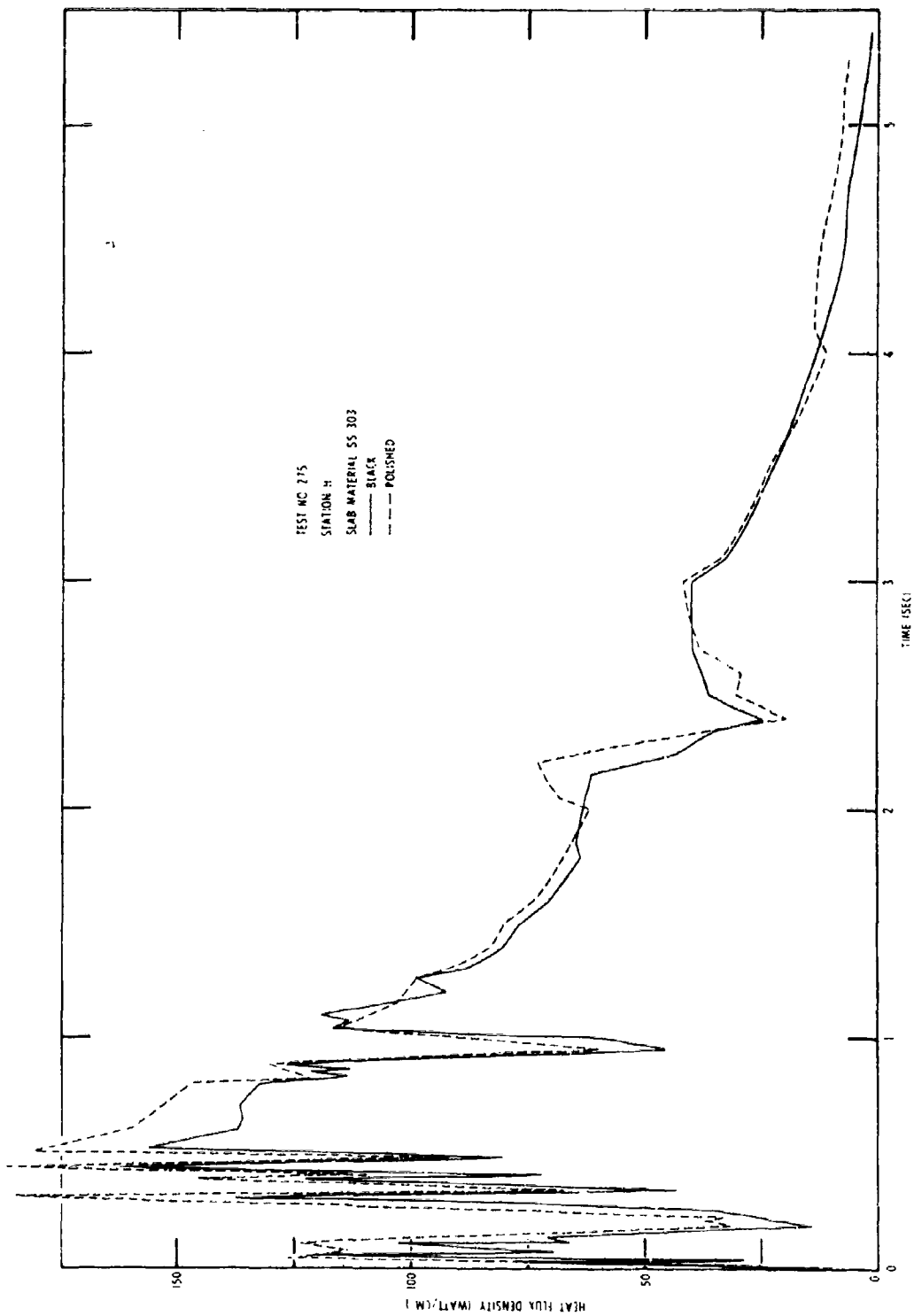

Fig. B-3. Heat Flux Density at Station H from Test 275 (25,000-lb LO_2/RP-1)

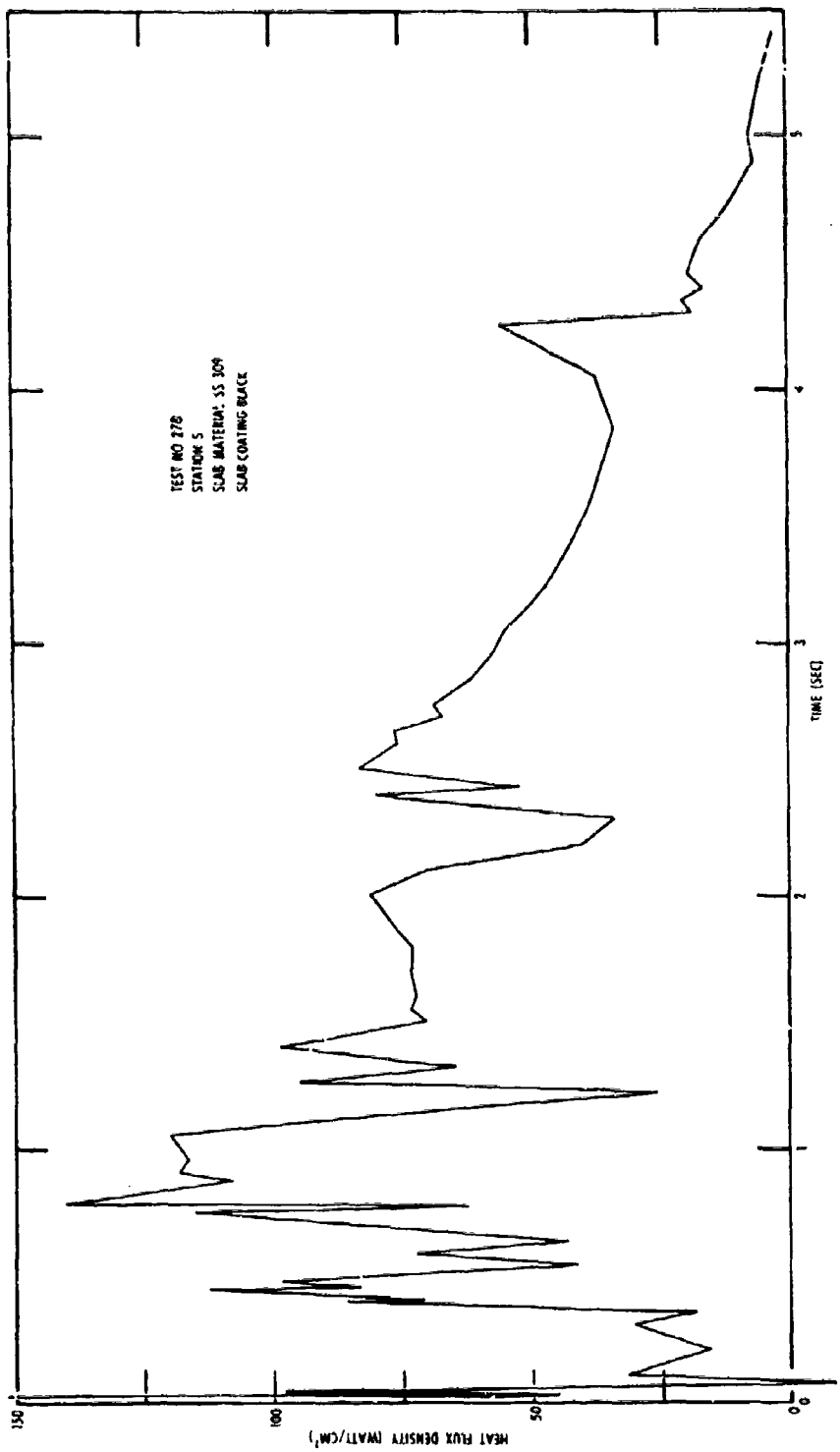

B-4. Heat Flux Density at Station S from Test 278 (25,000-lb LO_2/RP-1)

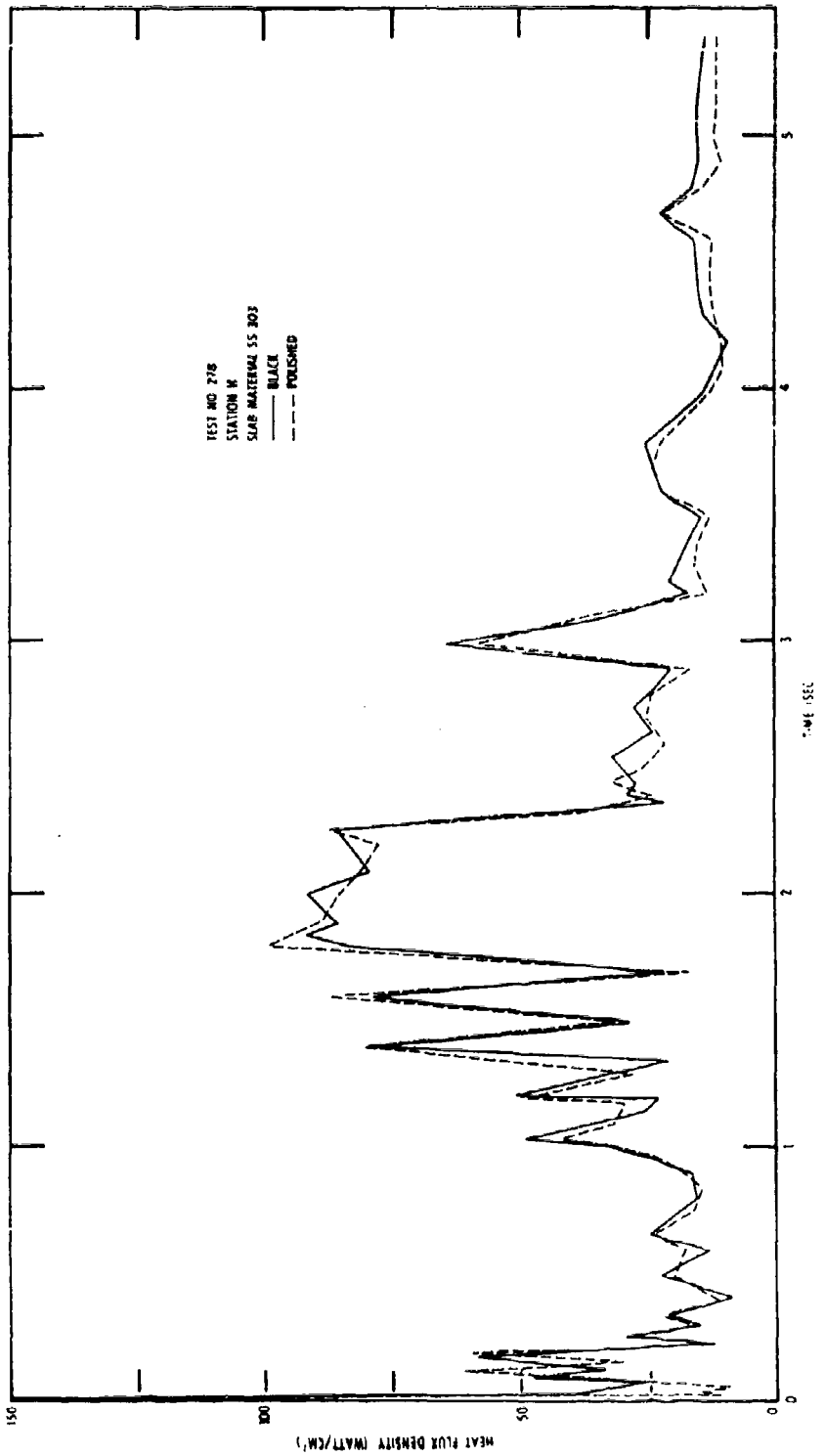

Fig. B-5. Heat Flux Density at Station H from Test 278 (25,000-lb LO_2/RP-1)

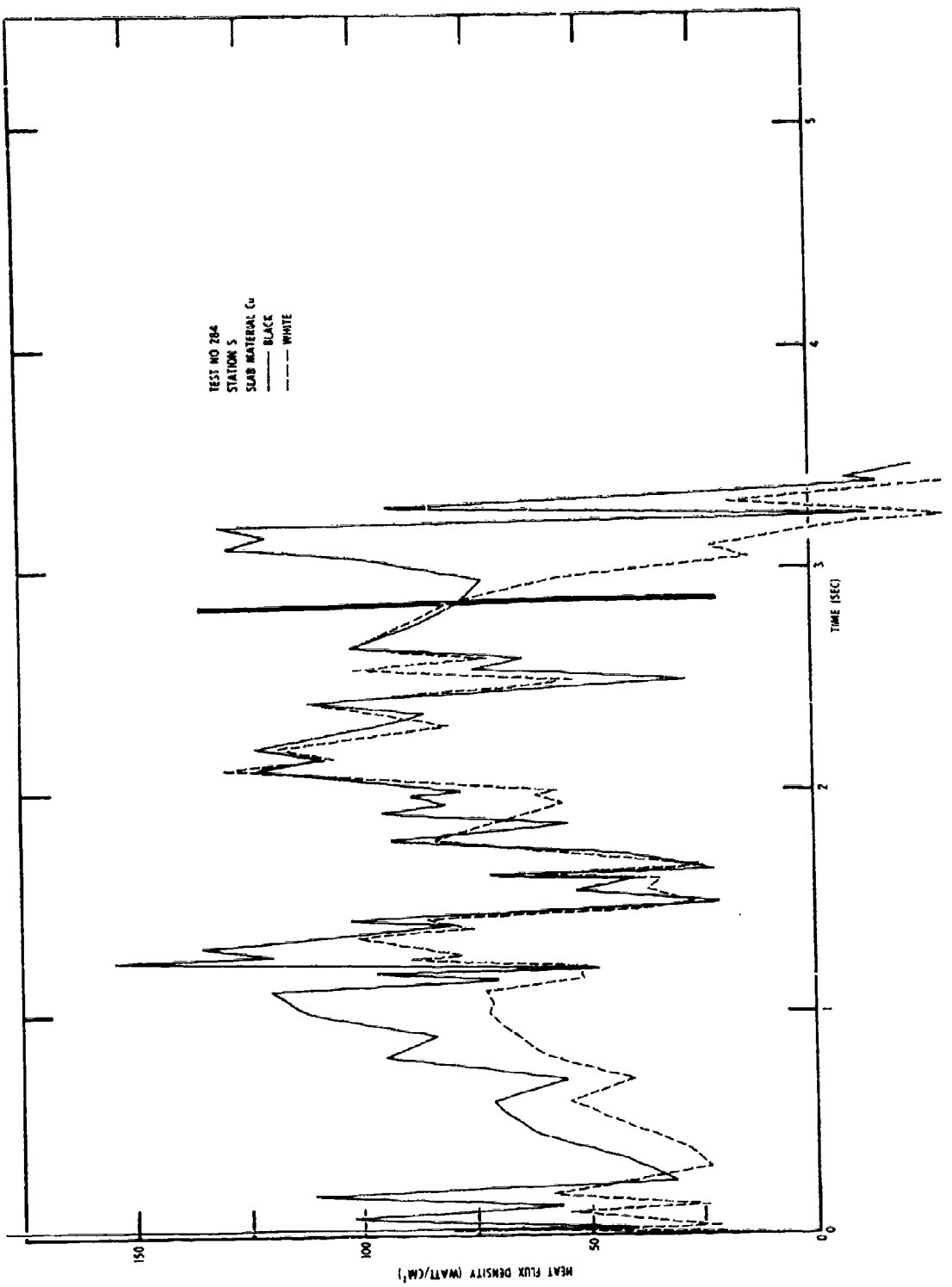

Fig. B-6. Heat Flux Density at Station S from Test 284 (25,000-lb LO_2/RP-1)

Fig. B-7. Heat Flux Density at Station H from Test 284 (25,000-lb LO_2/RP-1)

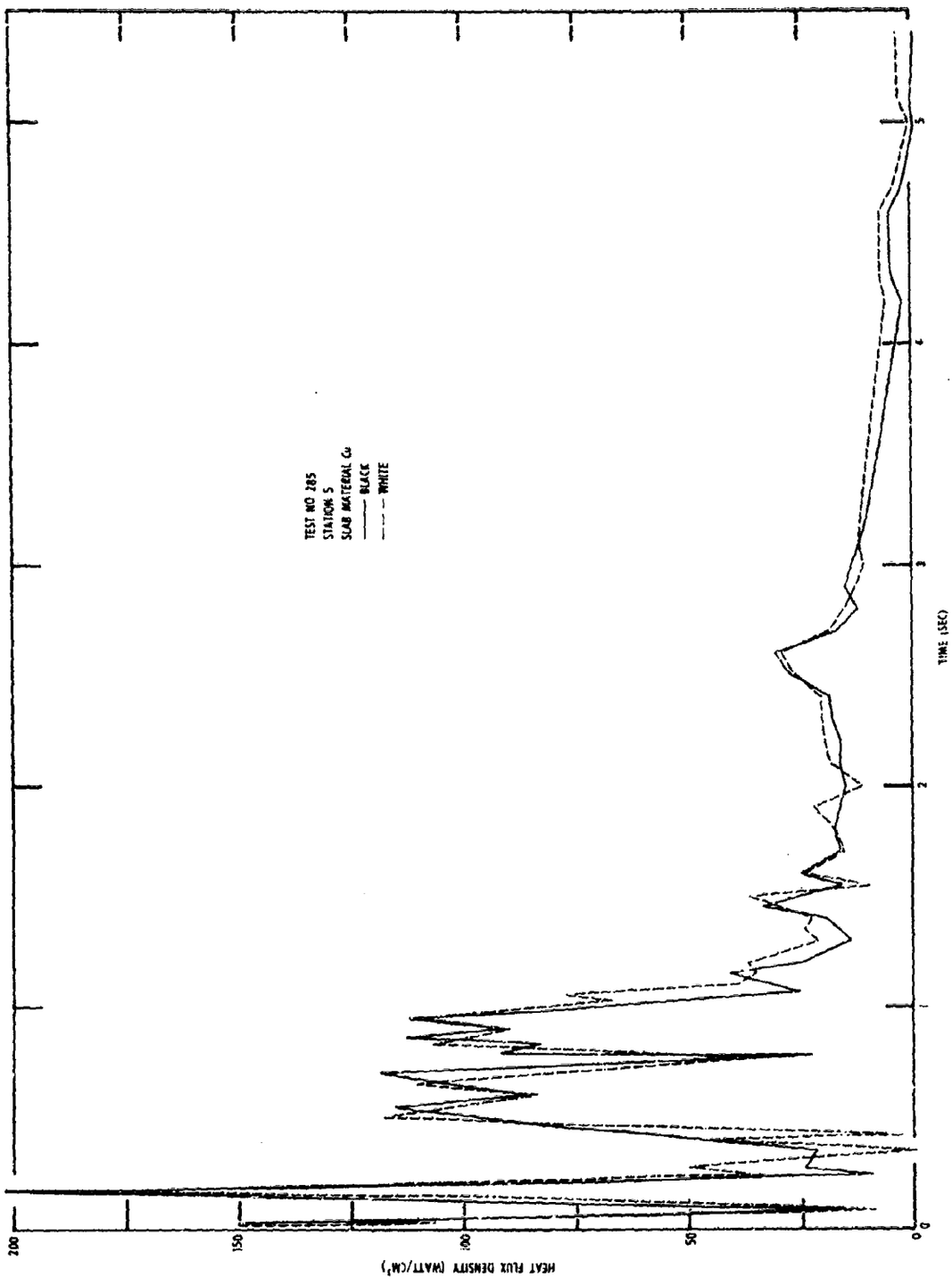

Fig. B-8. Heat Flux Density at Station 5 from Test 285 (25,000-lb LO_2/RP-1)

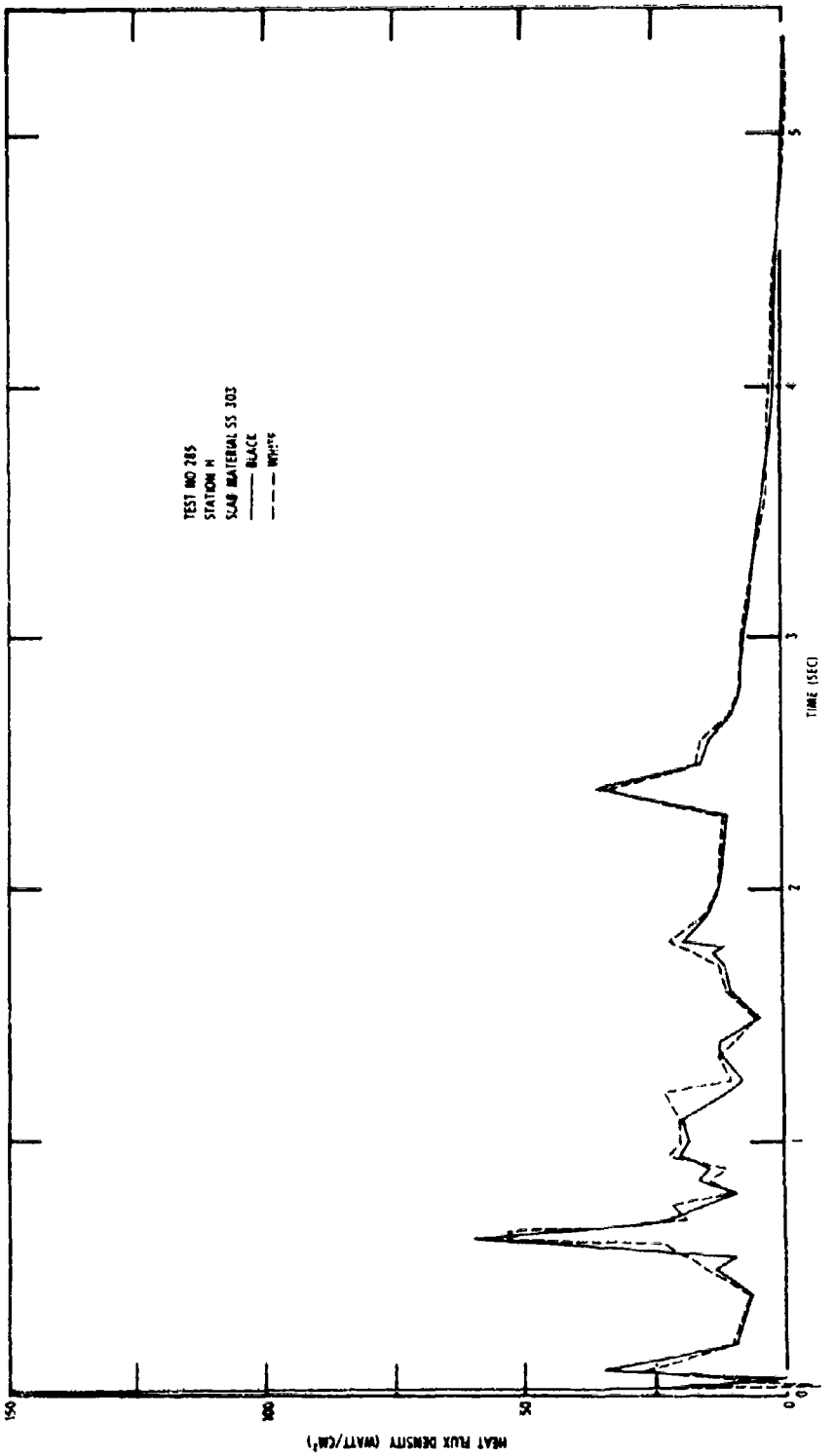

Fig. B-9. Heat Flux Density at Station H from Test 285 (25,000-lb LO_2/RP-1)

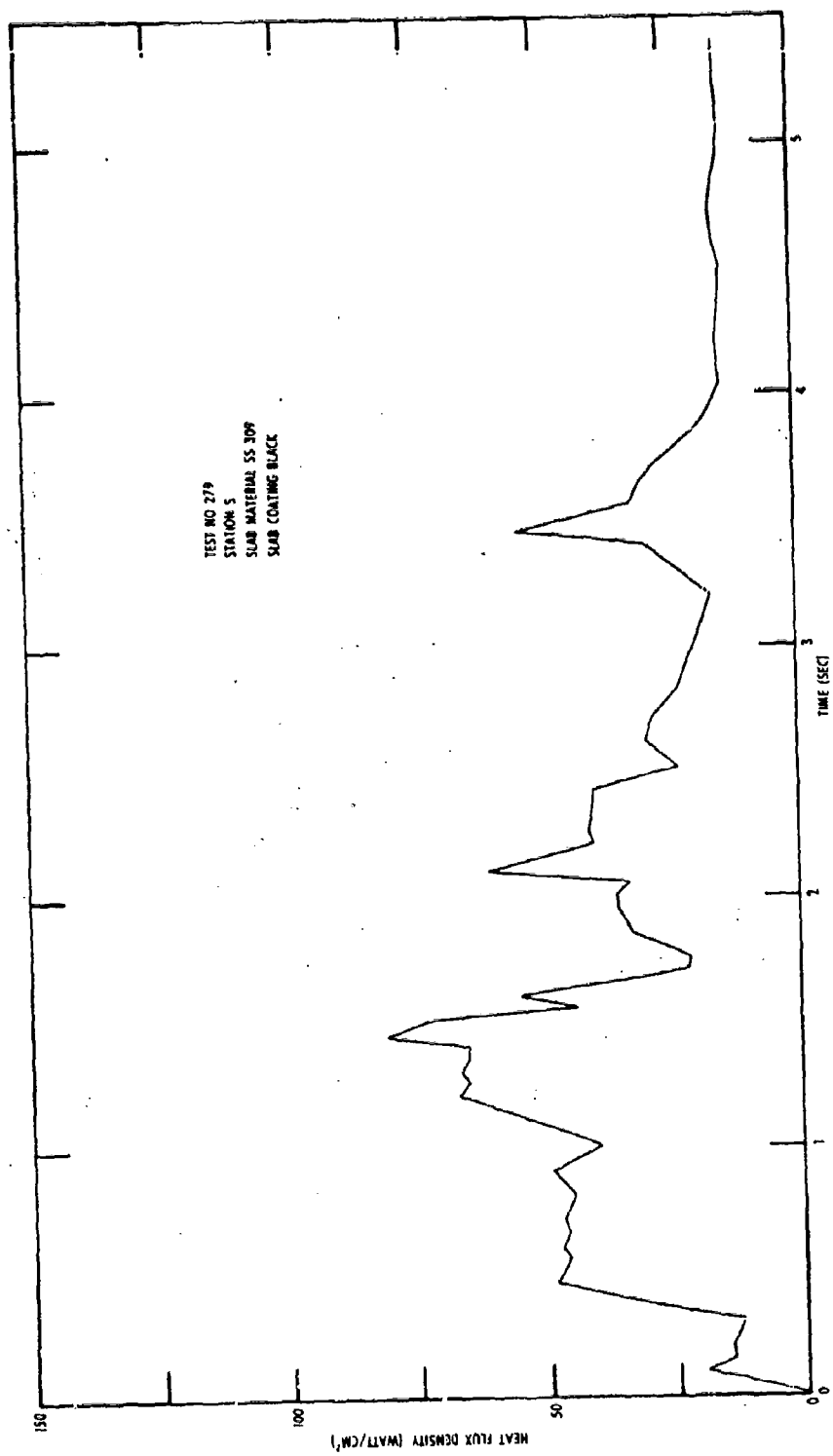

Fig. B-10. Heat Flux Density at Station S from Test 279 (25,000-lb LO_2/LH_2)

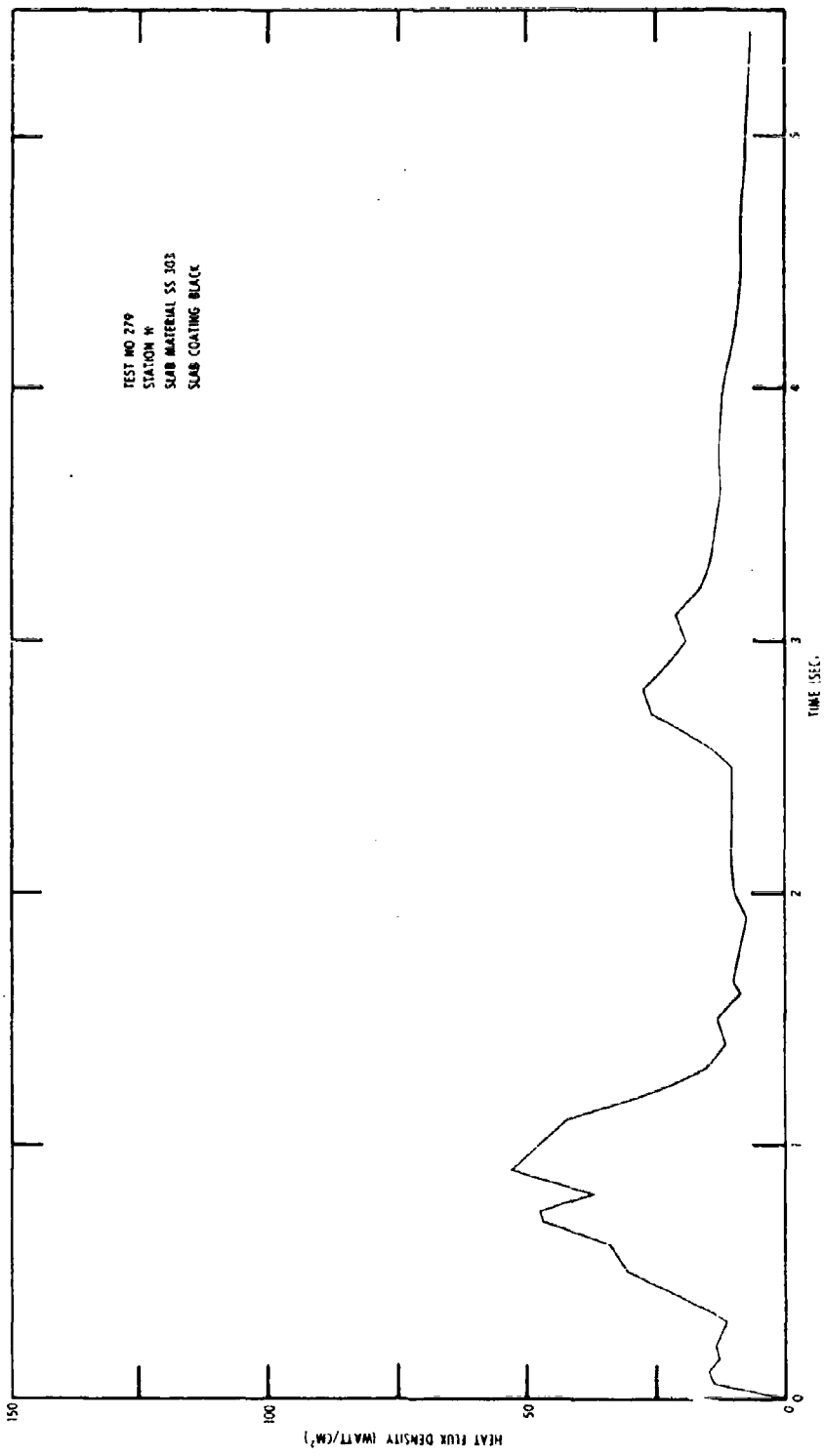

Fig. B-11. Heat Flux Density at Station H from Test 279 (25,000-lb LO_2/LH_2)

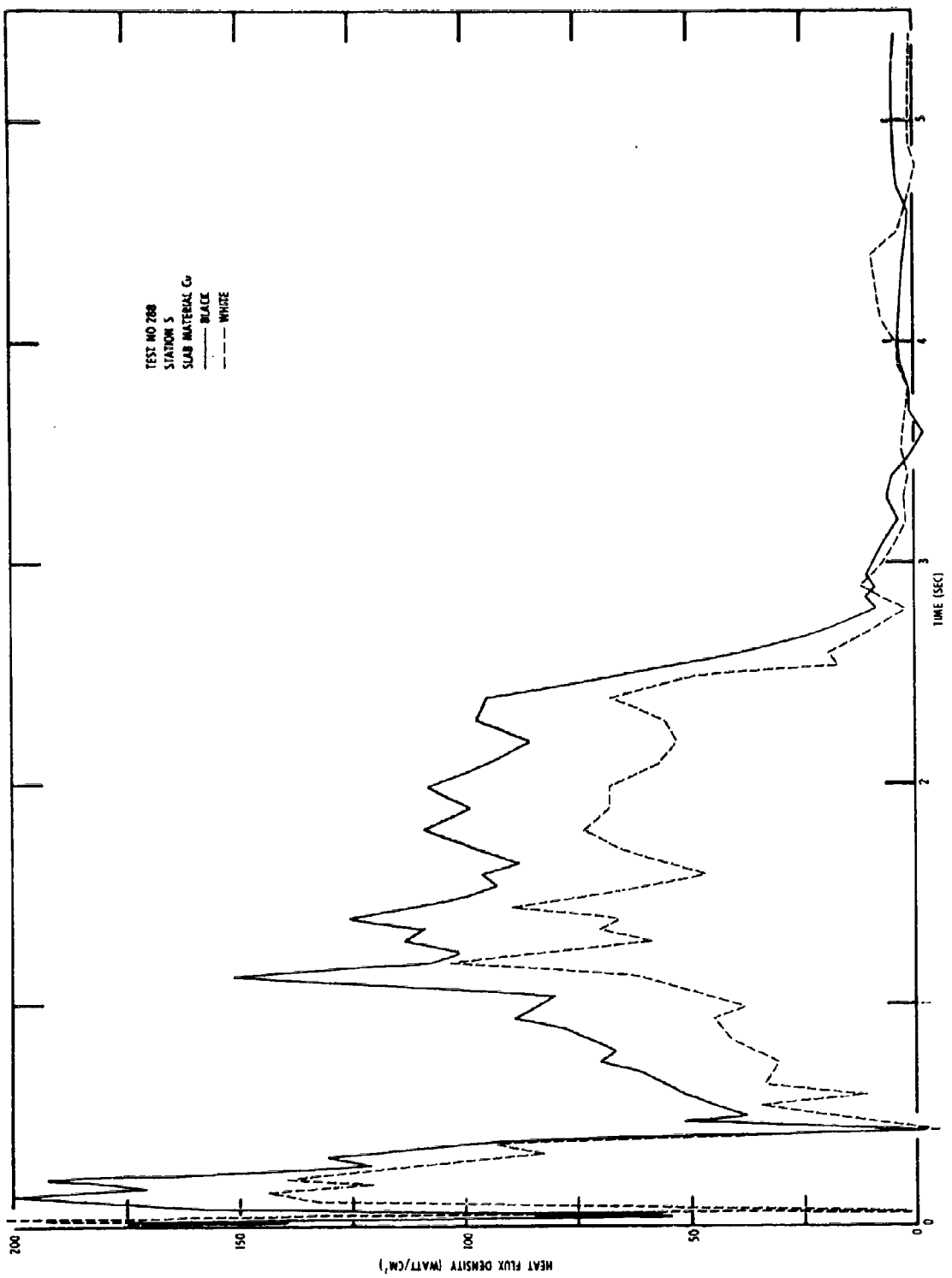

Fig. B-12. Heat Flux Density at Station S from Test 288 (25,000-lb LO_2/LH_2)

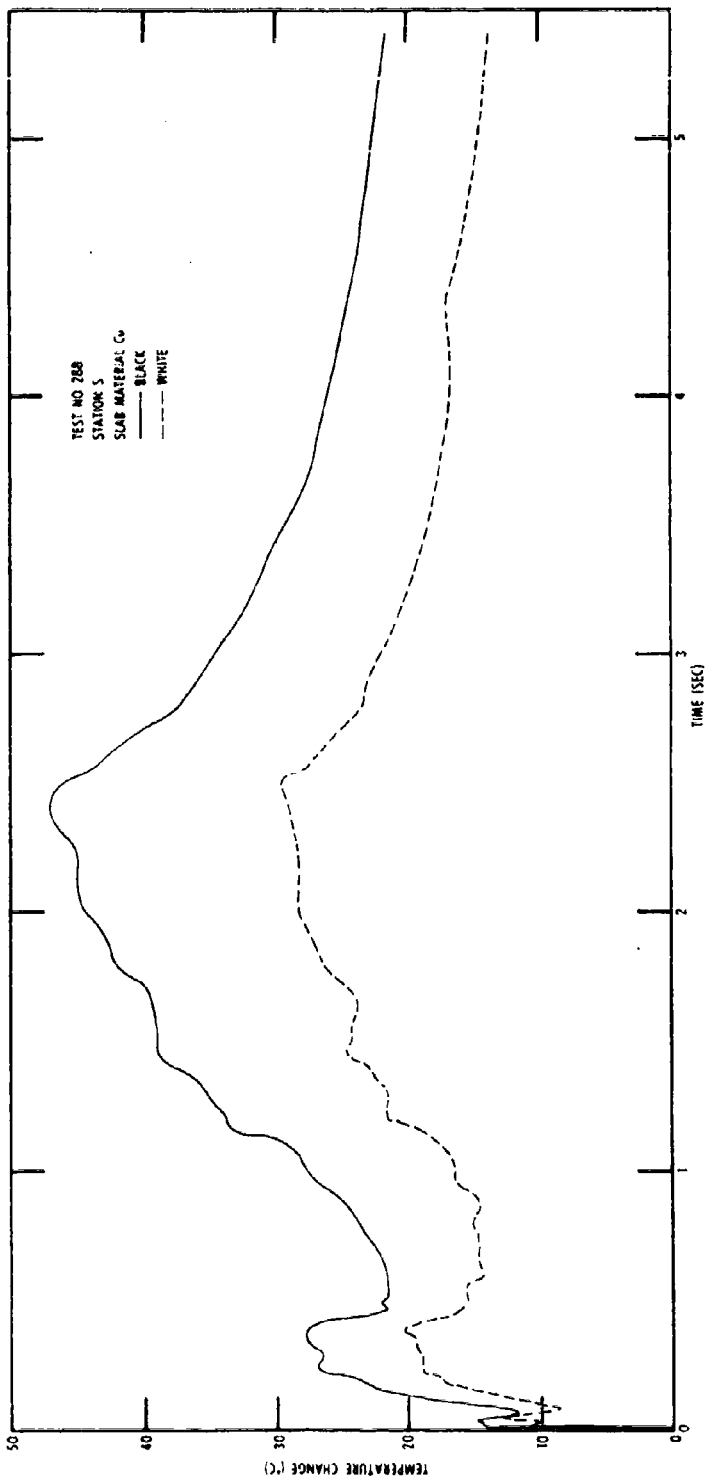

Fig. B-13. Slab Surface Temperature at Station S from Test 288 (25,000-lb LO_2 LH_2)

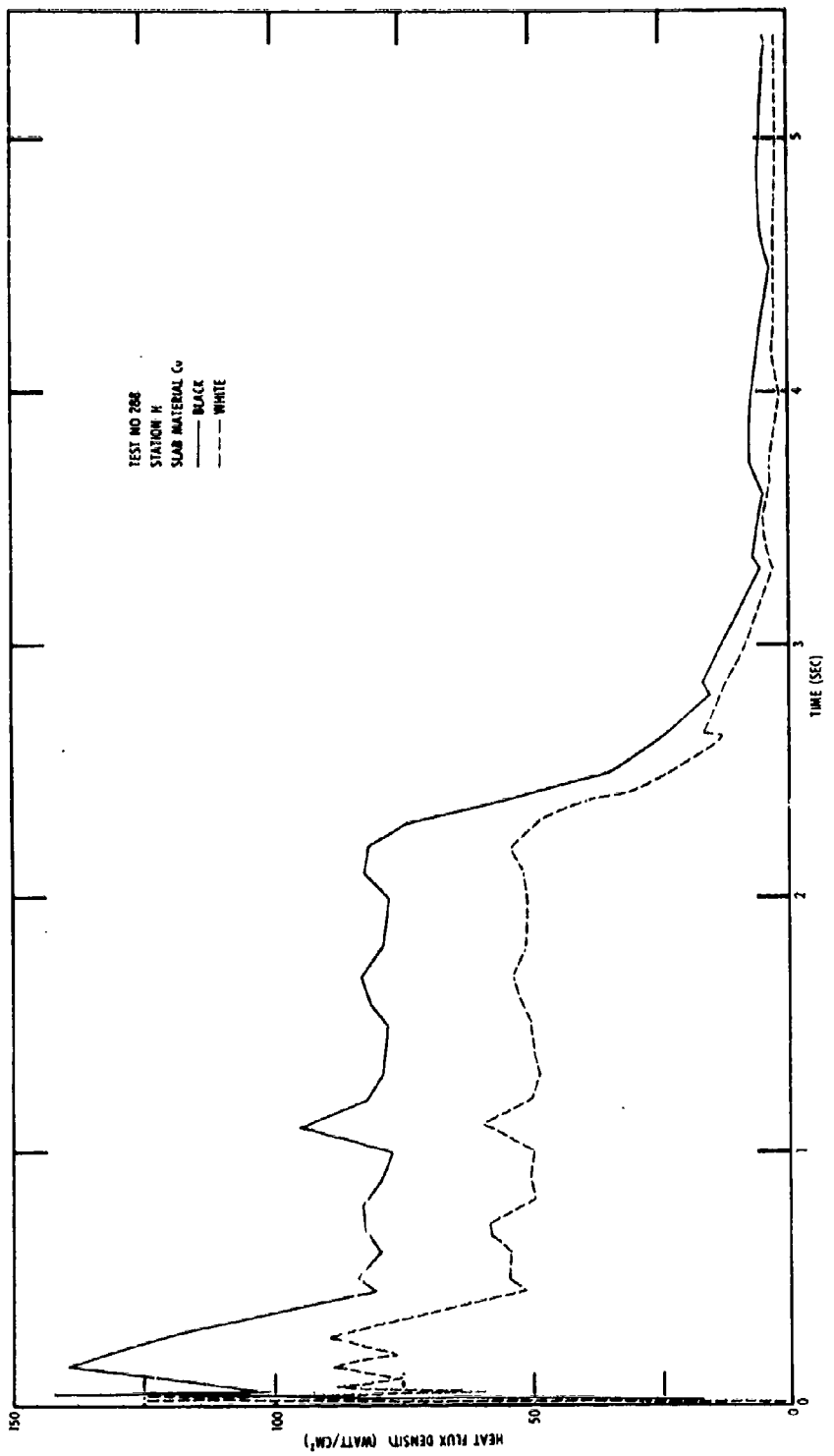

Fig. B-14. Heat Flux Density at Station H from Test 288 (25,000-lb LO_2/LH_2)

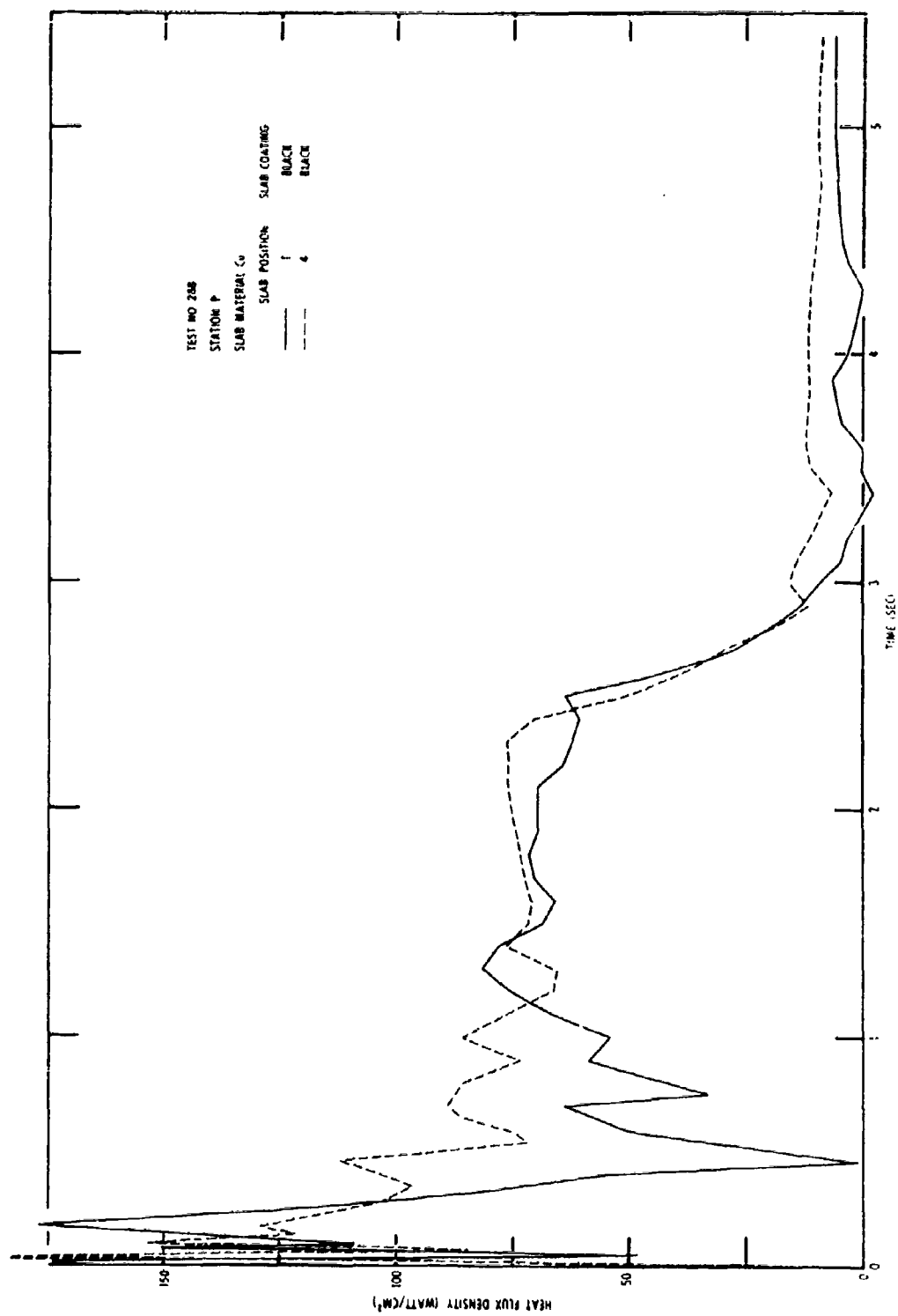

Fig. B-15. Heat Flux Density at Positions 1 and 4 of Station P from Test 288 (25,000-lb LO_2 LH_2)

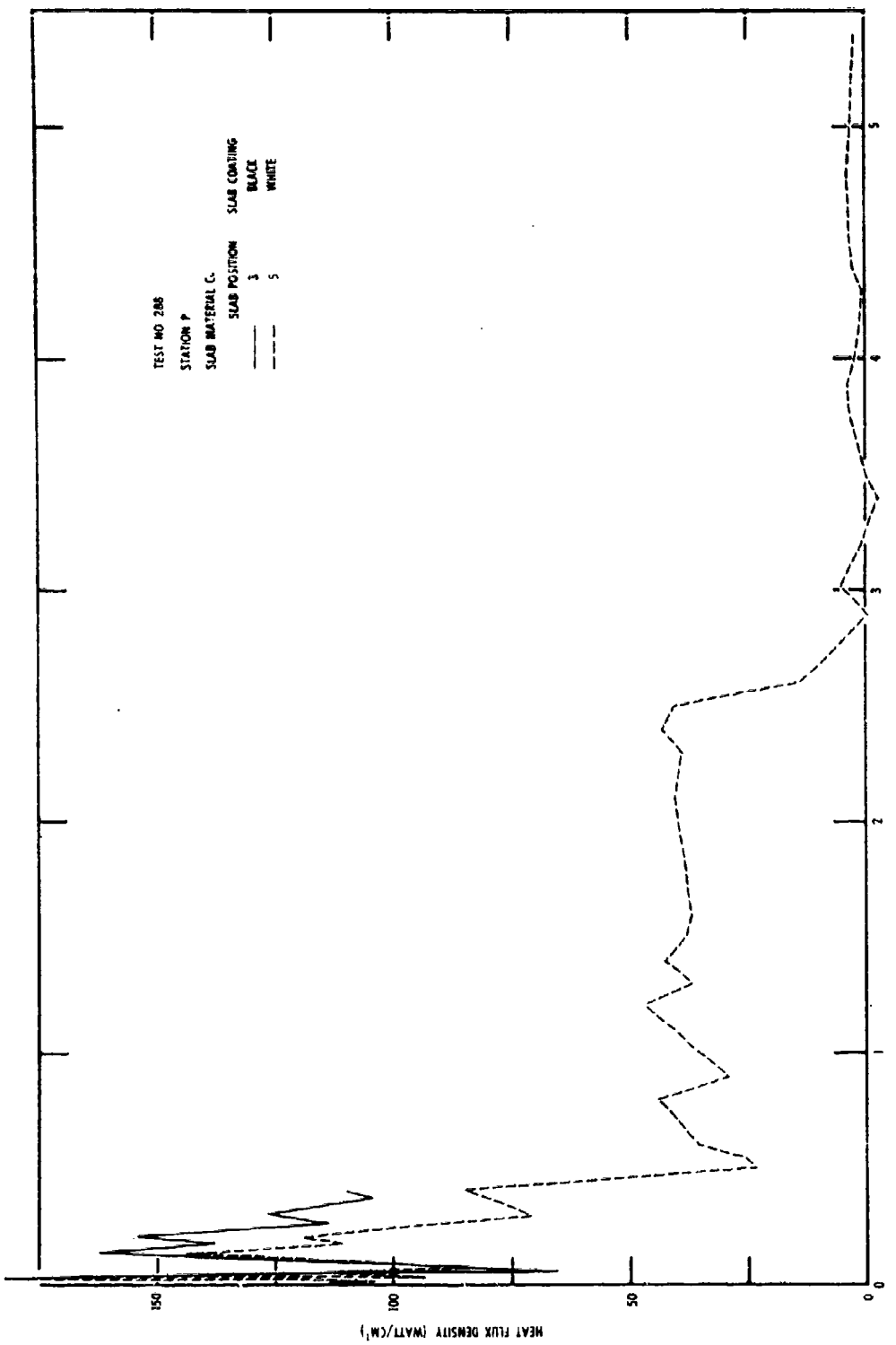

Fig. B-16. Heat Flux Density at Positions 3 and 5 of Station P from Test 288 (25,000-lb LO_2/LH_2)

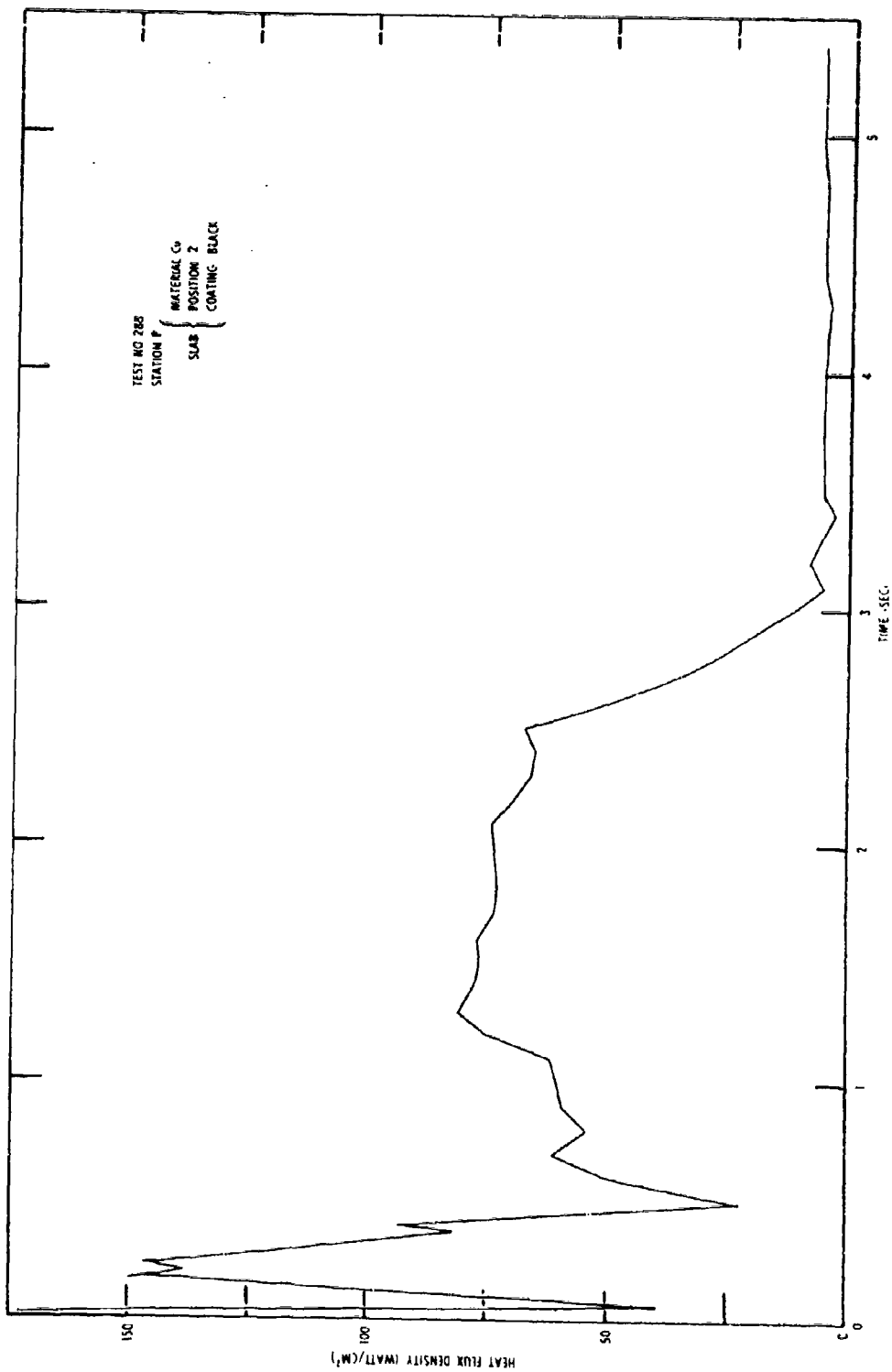

Fig. B-17. Heat Flux Density at Position 2 of Station P from Test 288 (25,000-lb LO_2/LH_2)

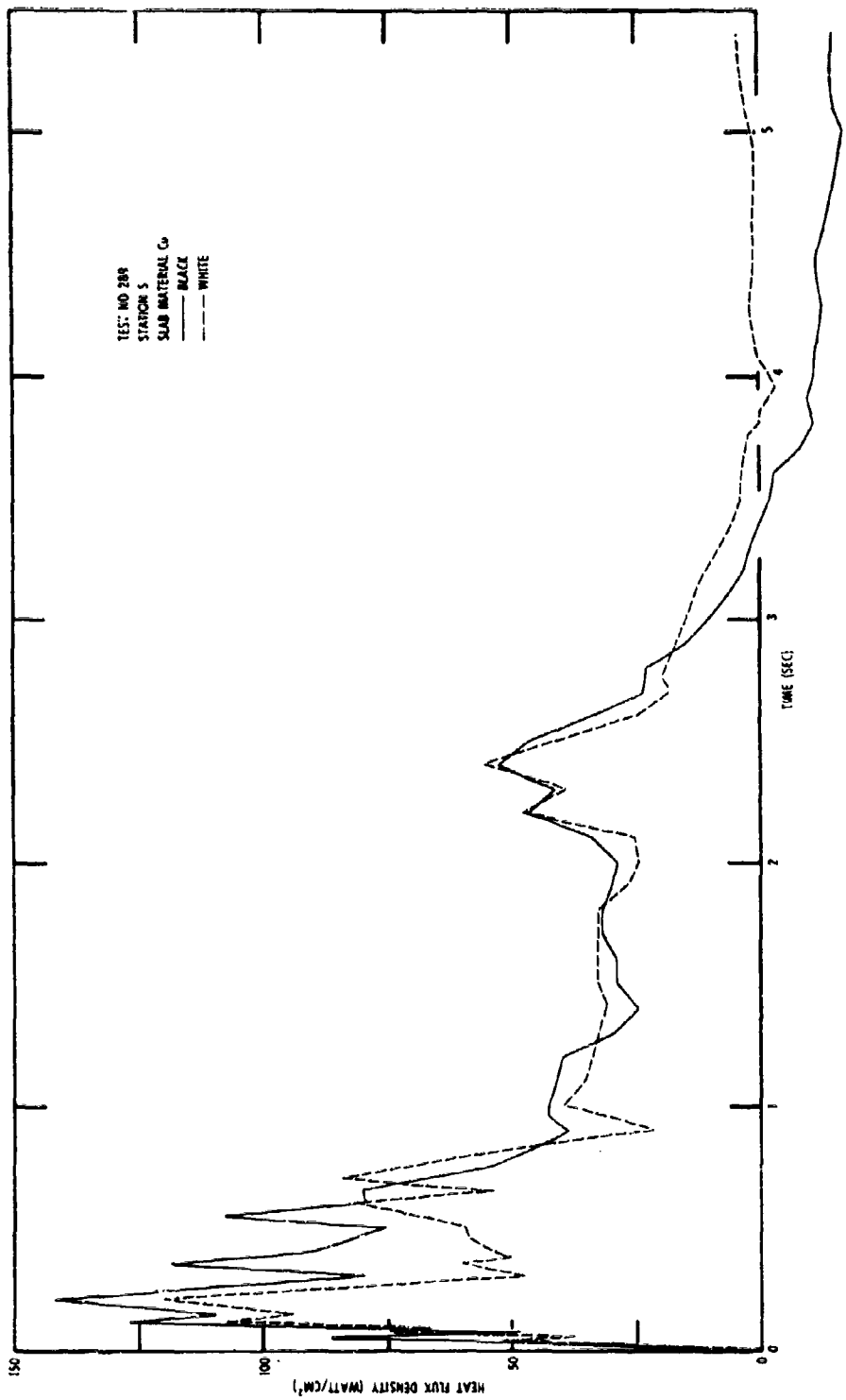

Fig. B-18. Heat Flux Density at Station S from Test 289 (25,000-lb LO_2/LH_2)

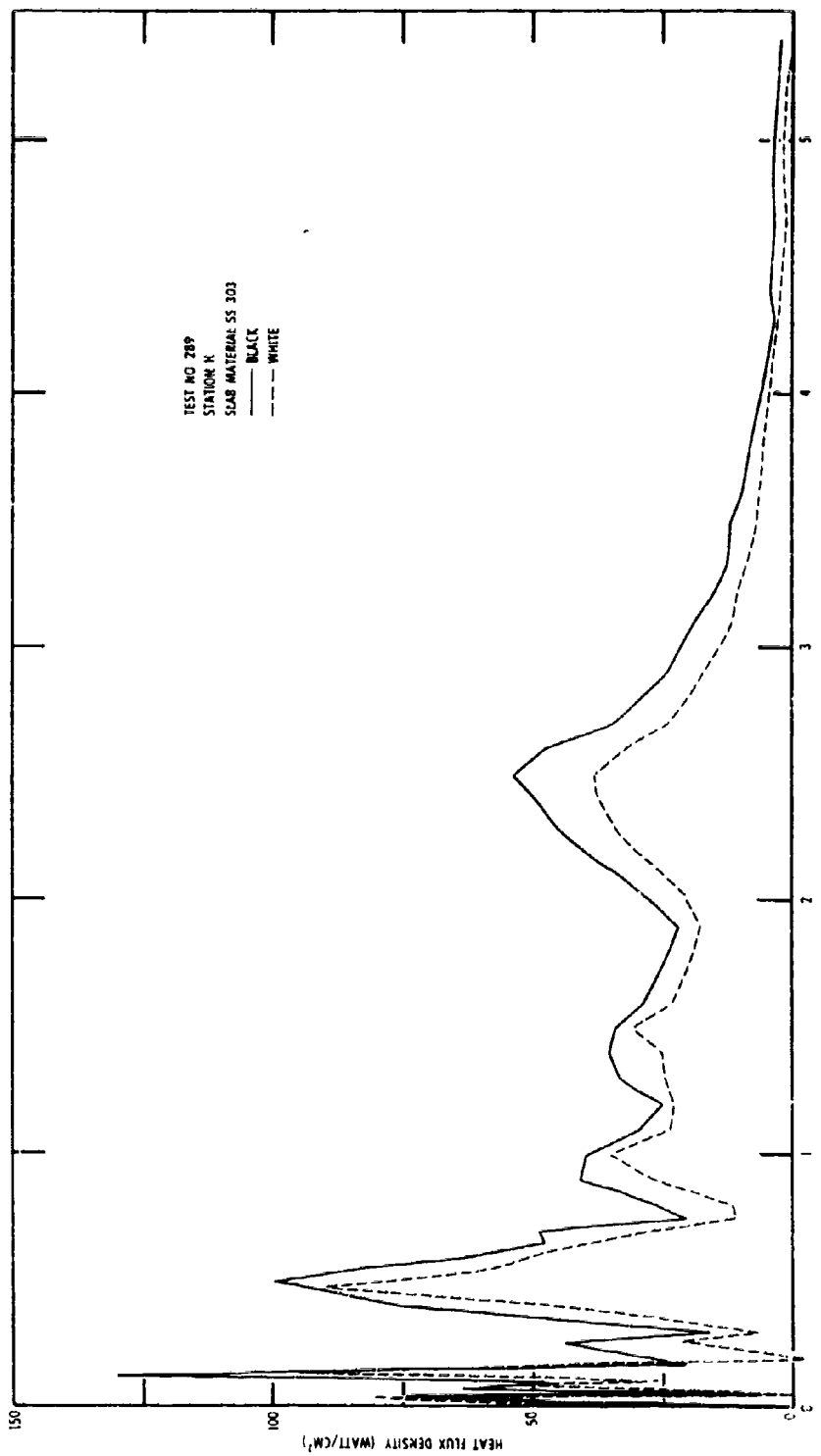

Fig. B-19. Heat Flux Density at Station H from Test 289 (25,000-lb LO_2/LH_2)

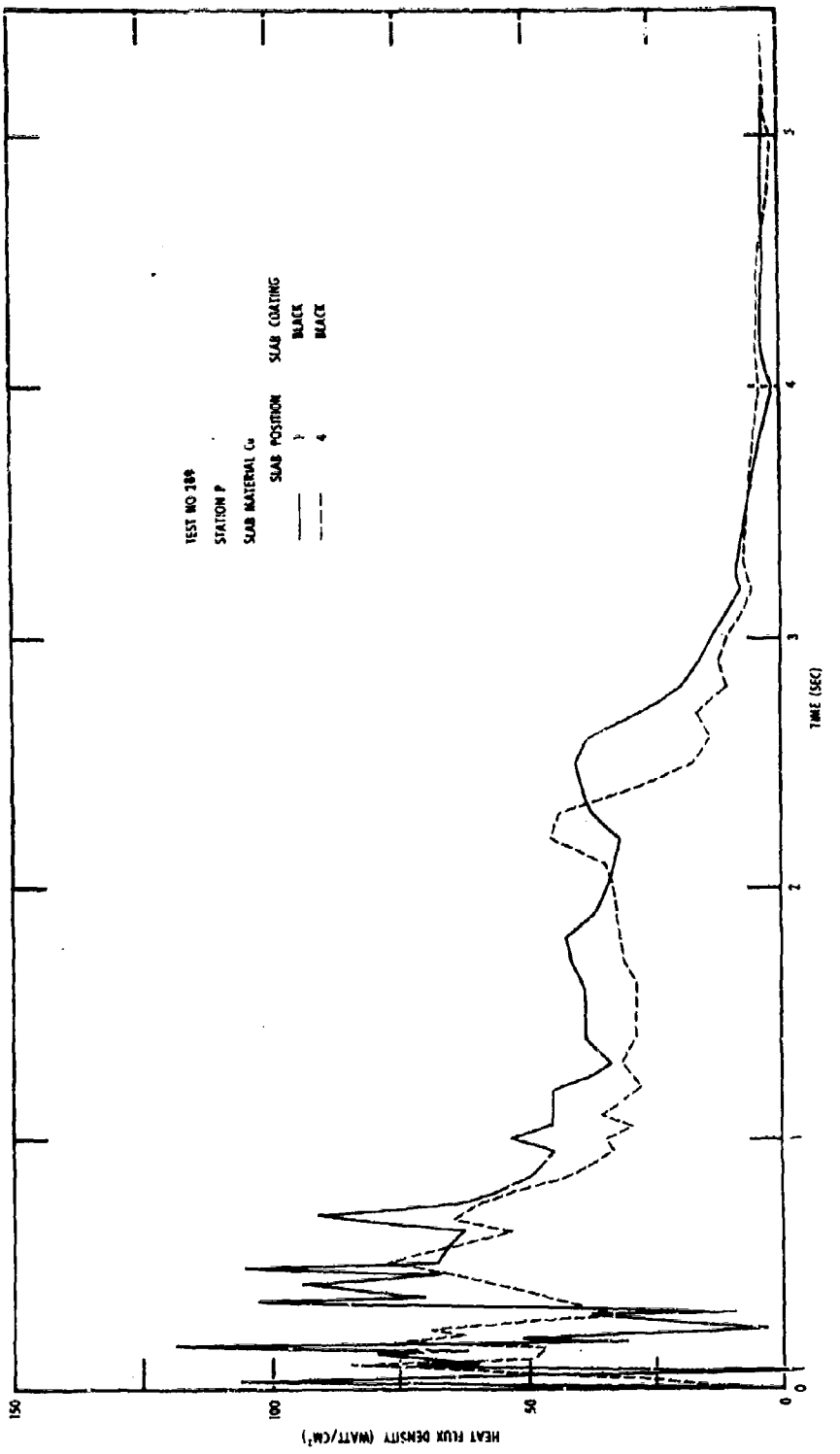

Fig. B-20. Heat Flux Density at Positions 1 and 4 of Station P from Test 289 (25,000-lb LO_2/LH_2)

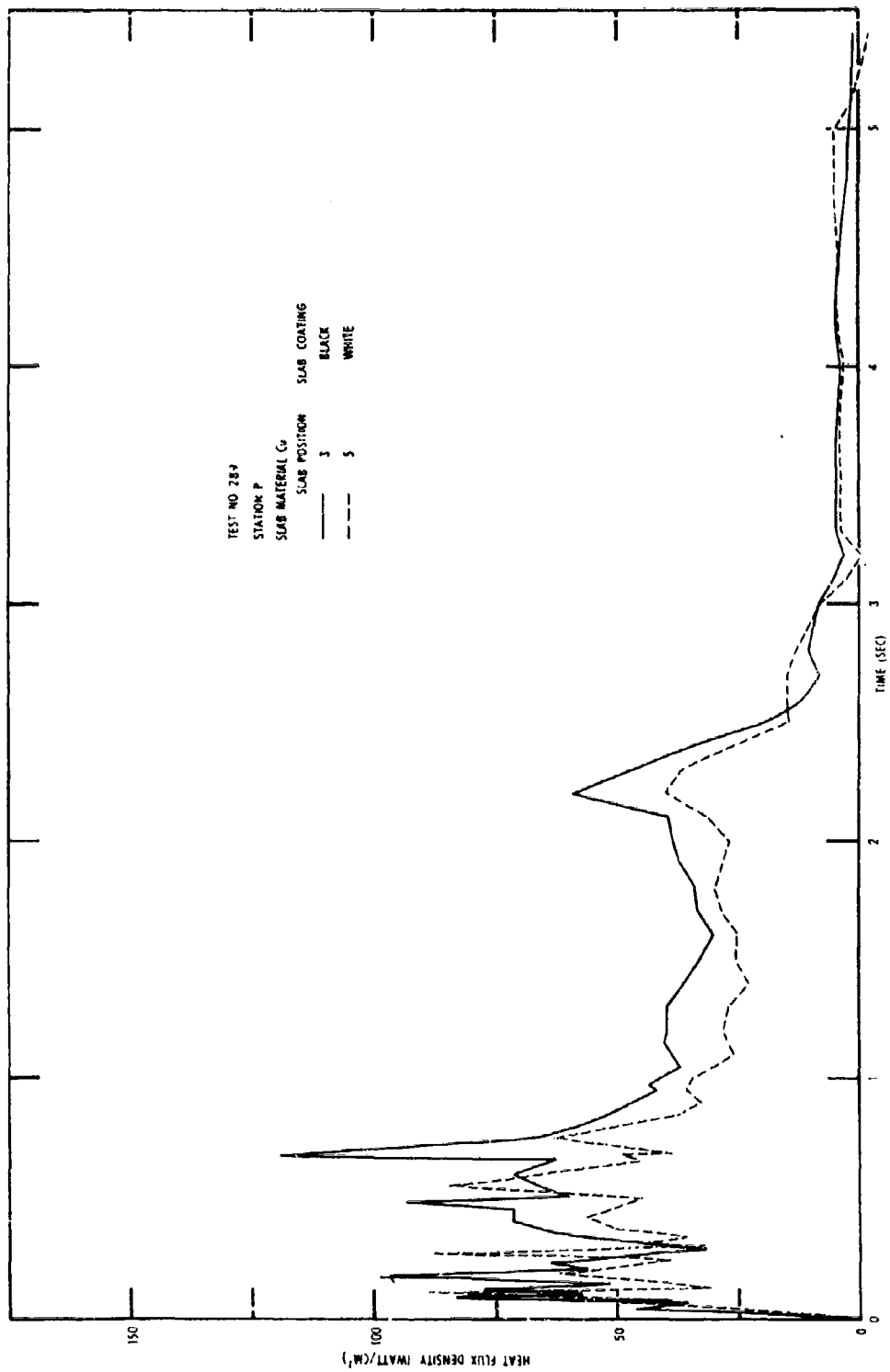

Fig. B-21. Heat Flux Density at Positions 3 and 5 of Station P from Test 289 (25,000-lb LO_2/LH_2)

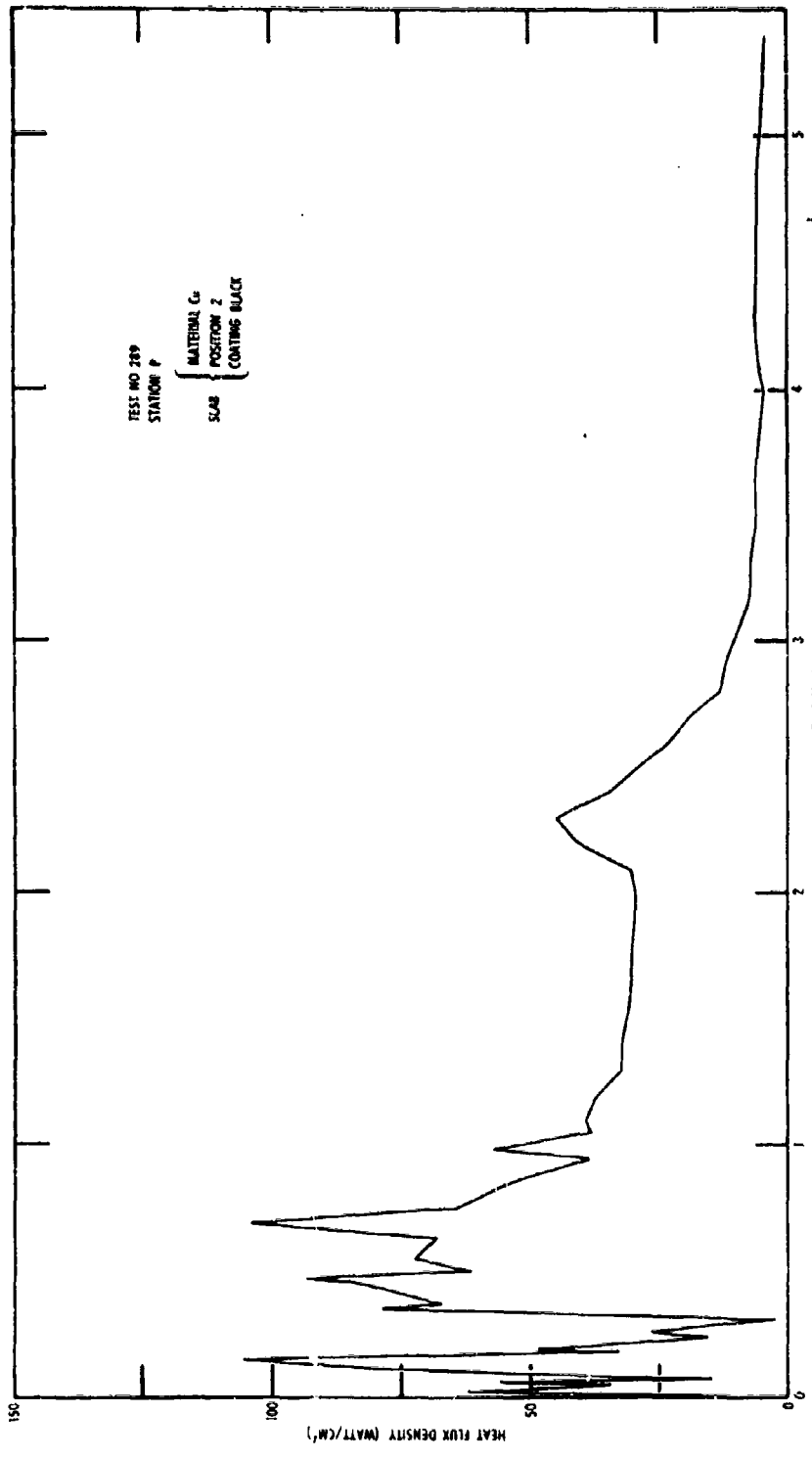

Fig. B-22. Heat Flux Density at Position 2 of Station P from Test 289 (25,000-lb LO_2/LH_2)

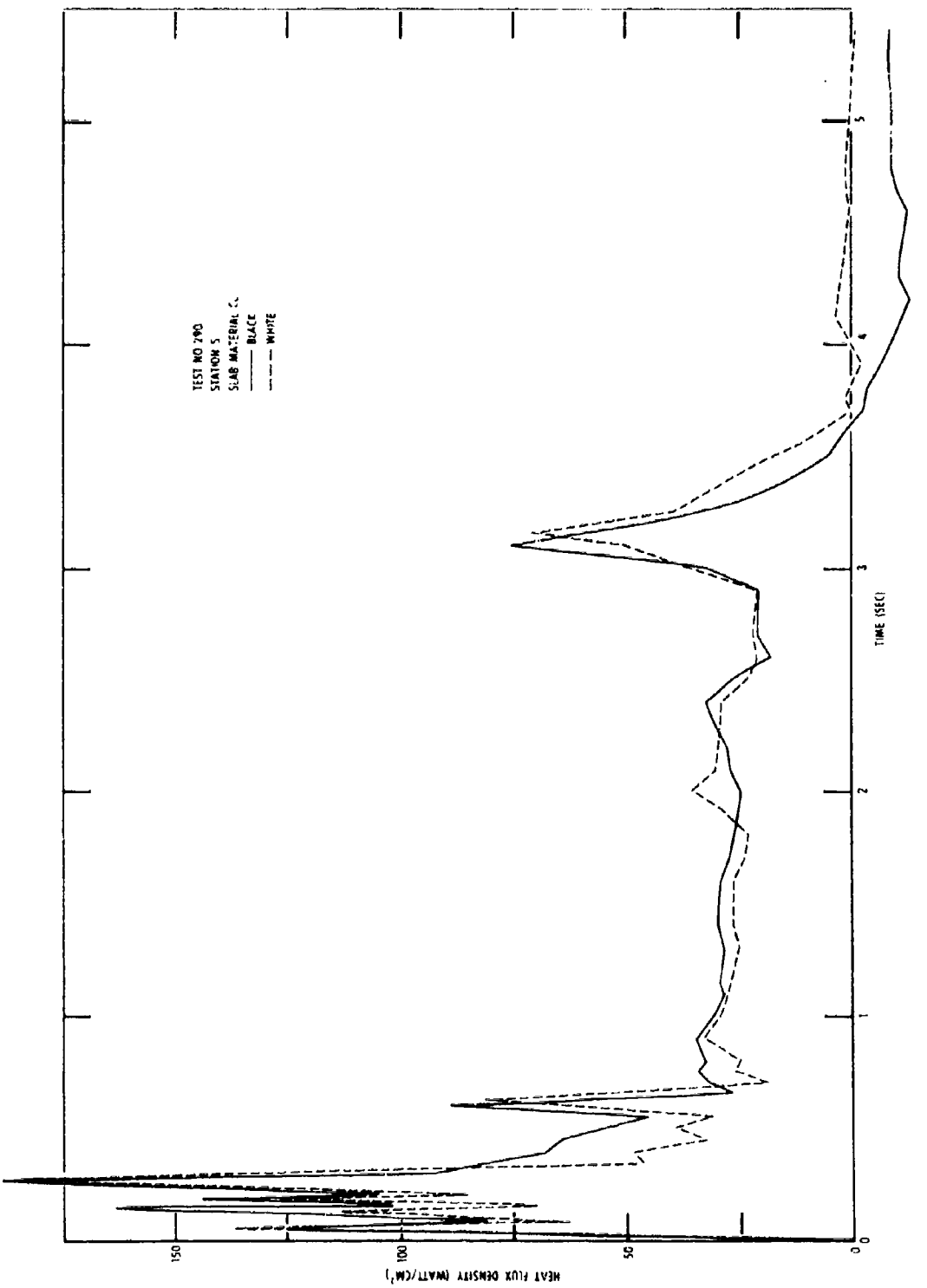

Fig. B-23. Heat Flux Density at Station S from Test 290 (25,000-lb LO_2/LH_2)

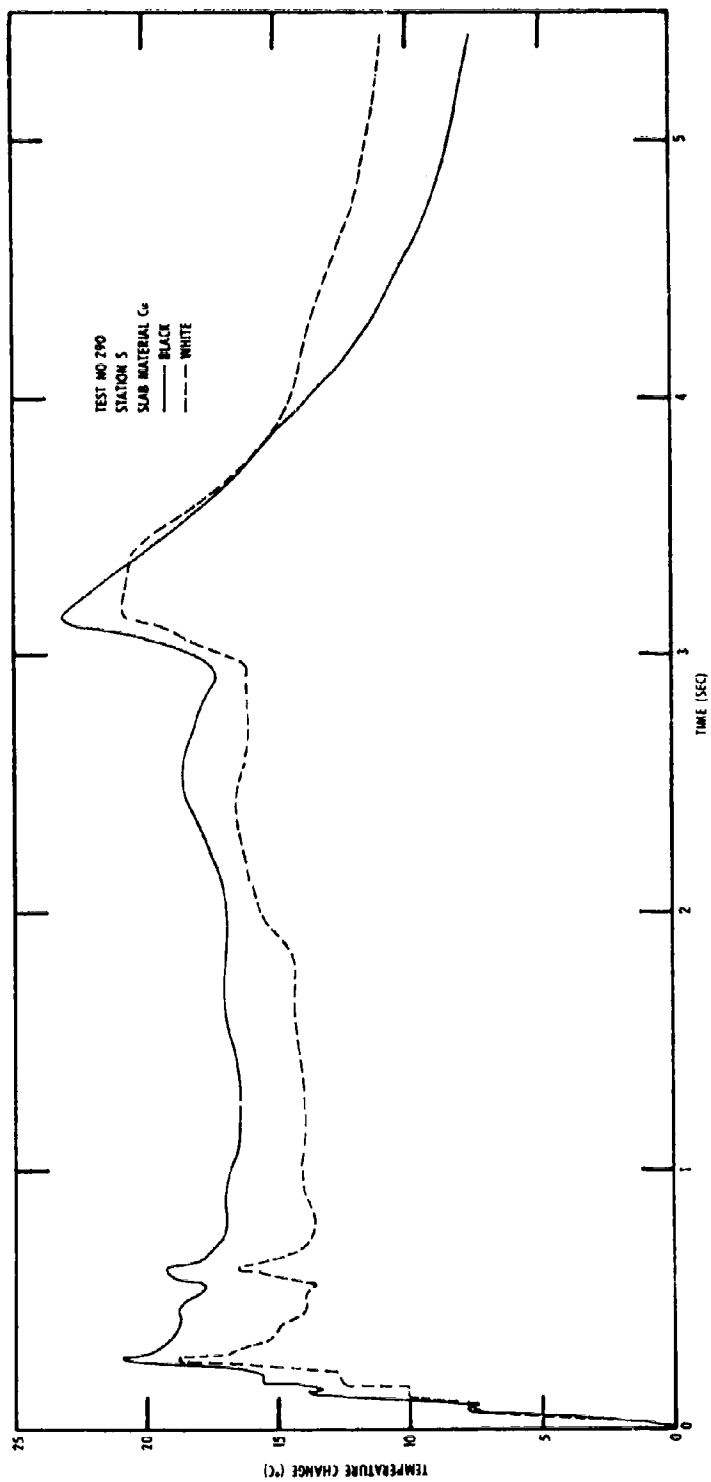

Fig. B-24. Slab Surface Temperature at Station S from Test 290 (25,000-lb LO_2/LH_2)

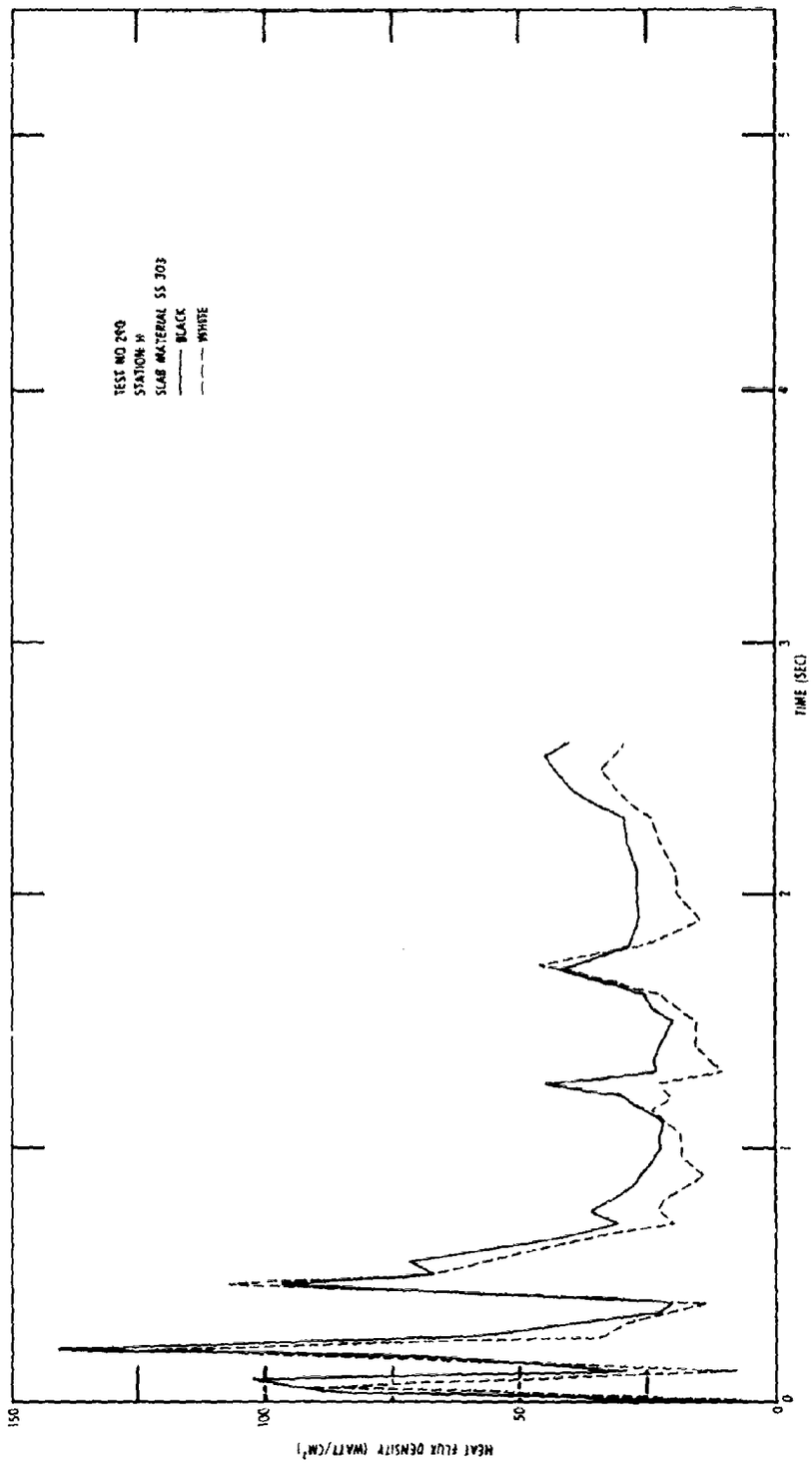

Fig. B-25. Heat Flux Density at Station H from Test 290 (25,000-lb LO_2 LH_2)

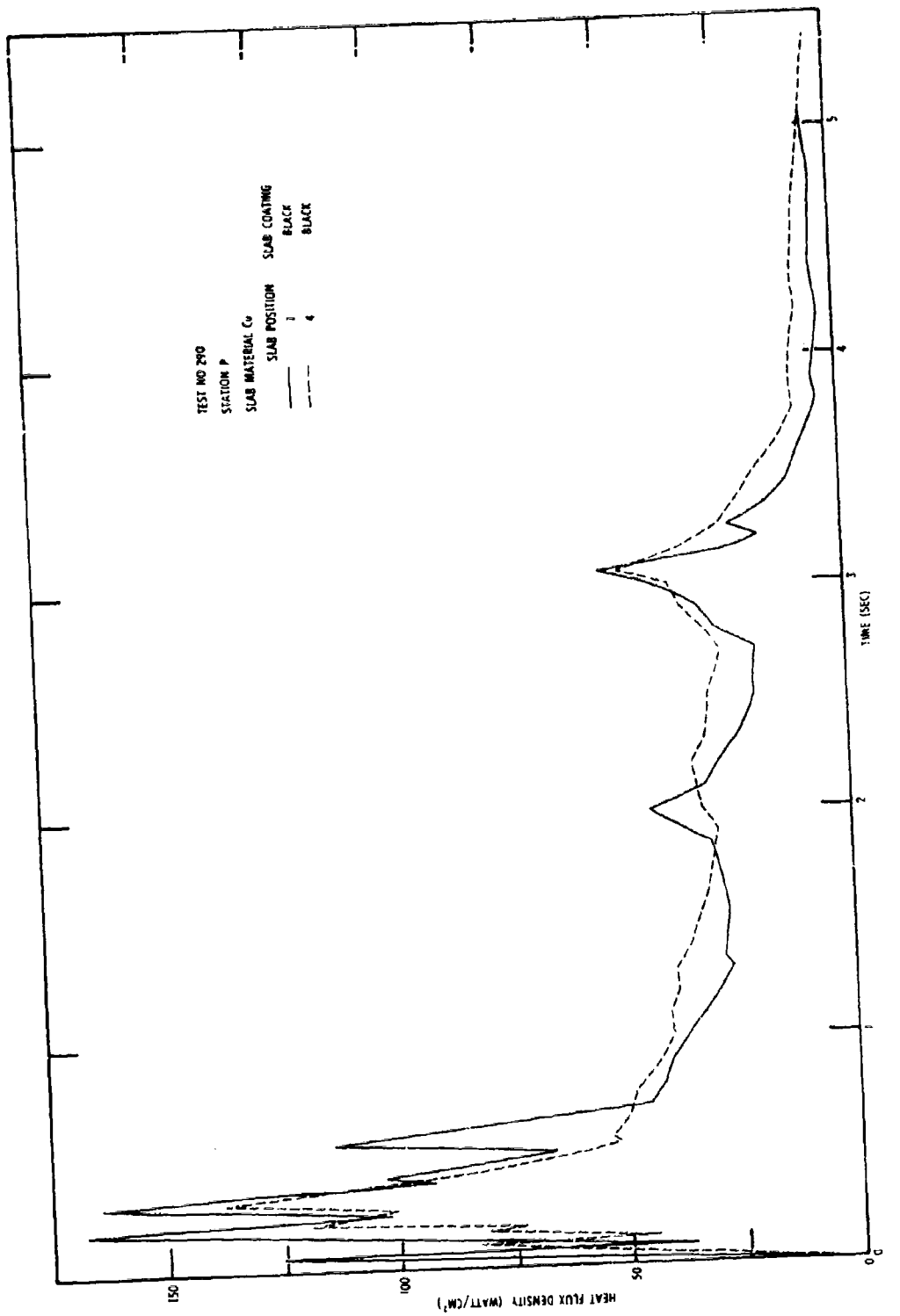

Fig. B-26. Heat Flux Density at Positions 1 and 4 of Station P from Test 290 (25,000-lb LO_2 LH_2)

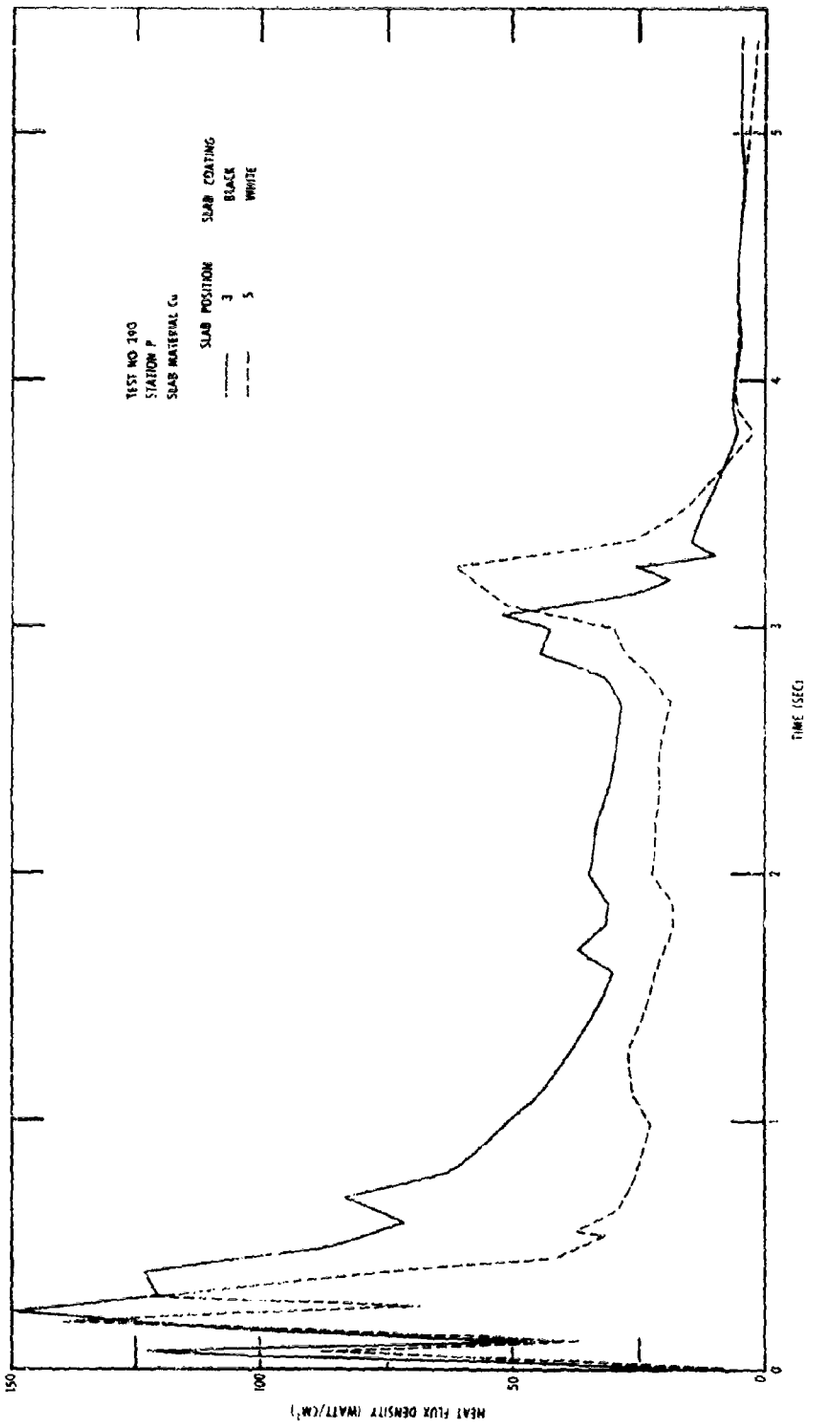

Fig. B-27. Heat Flux Density at Positions 3 and 5 of Station P from Test 290 (25,000-lb LO_2 LH_2)

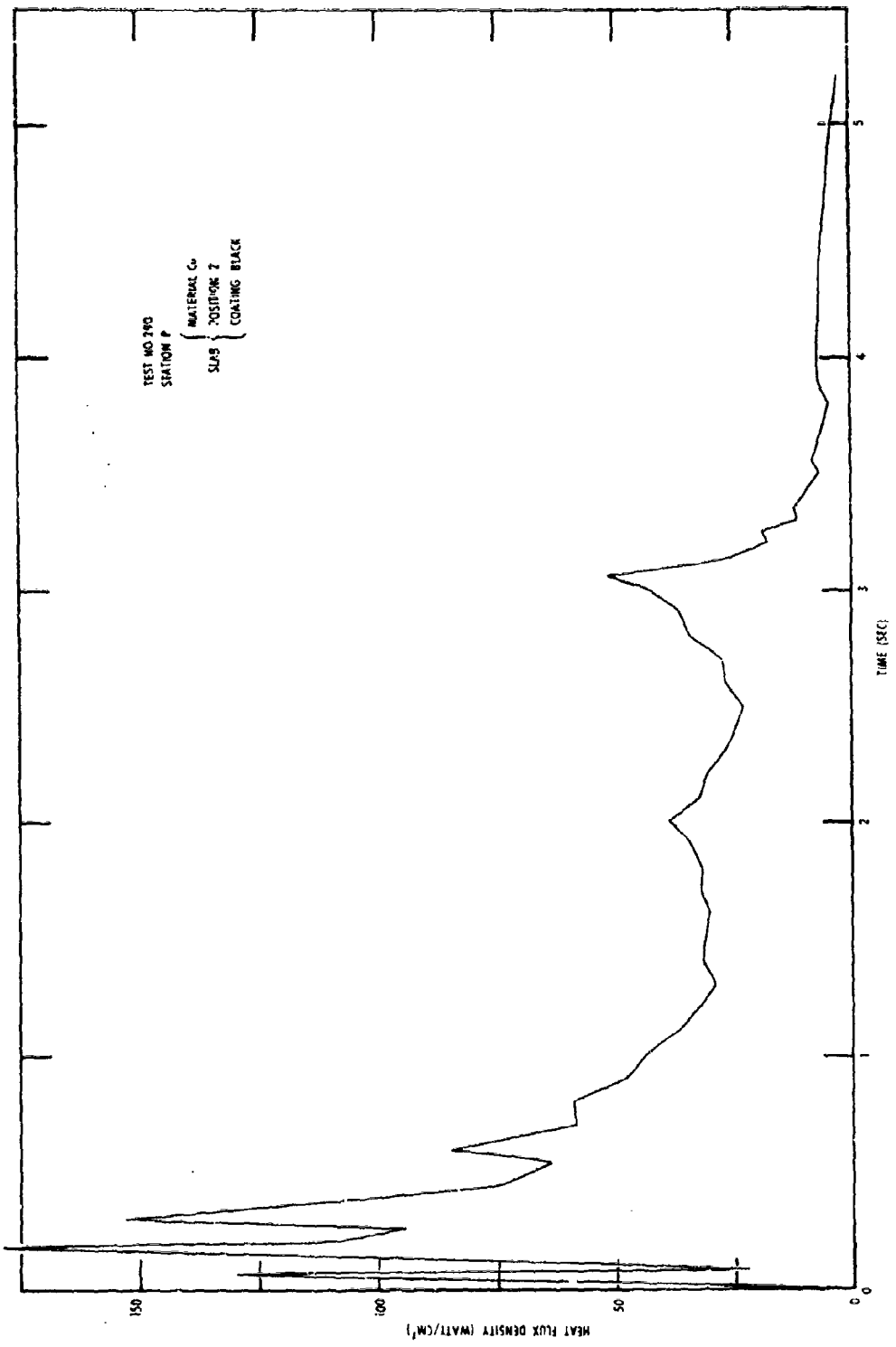

Fig. B-28. Heat Flux Density at Position 2 of Station P from Test 290 (25,000-lb LO_2 LH_2)

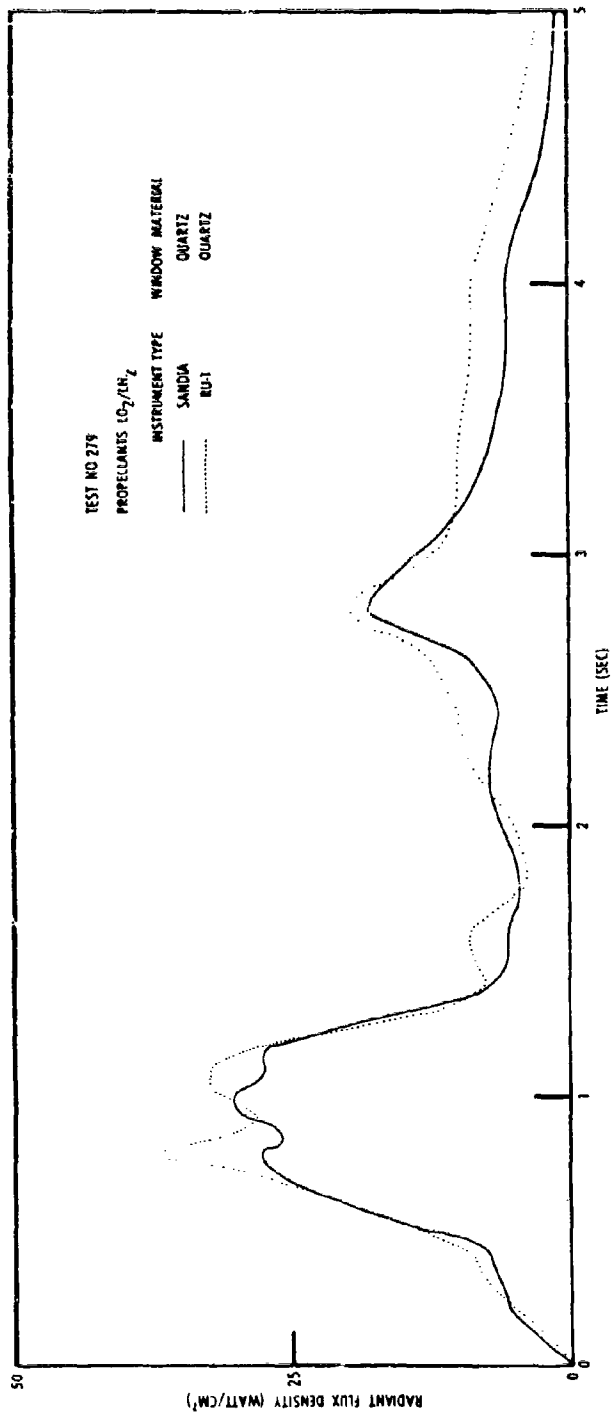

Fig. B-29. Radiant Flux Density Within the Fireball from Test 279 (25,000-lb LO_2/LH_2)

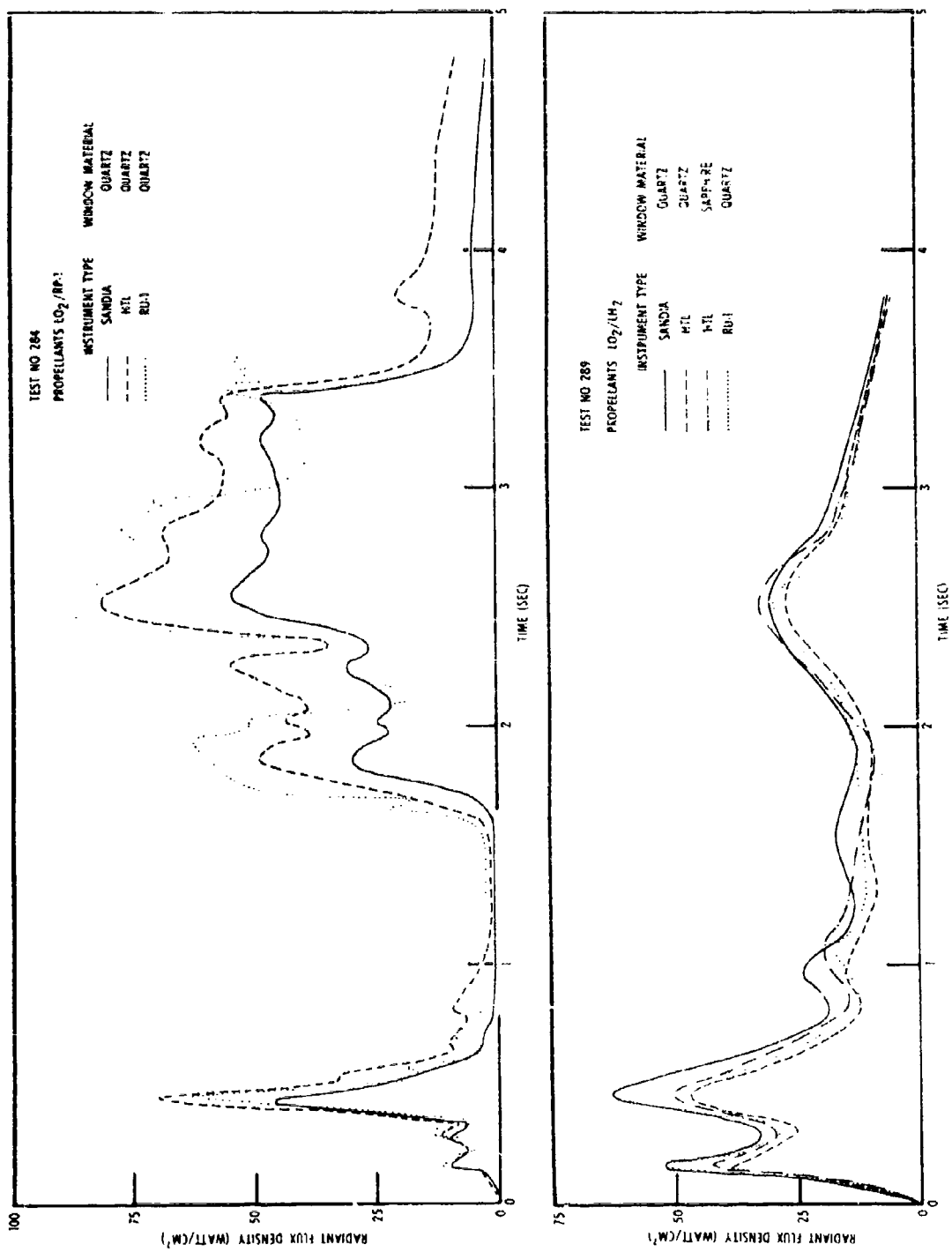

Fig. B-30. Radiant Flux Density Within the Fireball from Tests 284 and 289 (25,000-lb)

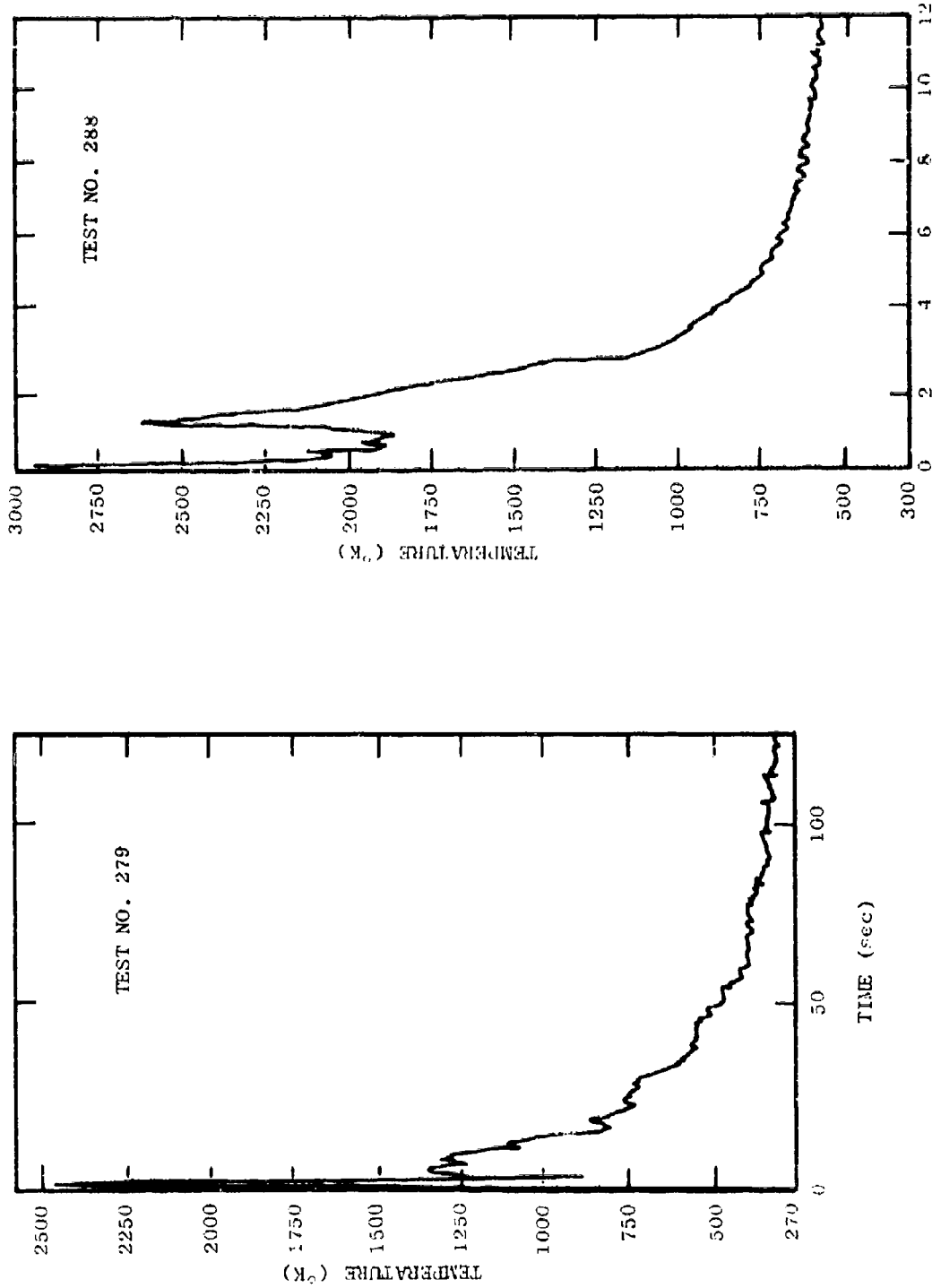

Fig. B-31. Temperature of Thermocouple Probes for Tests 279 and 288 (25,000-lb LO_2/LH_2)

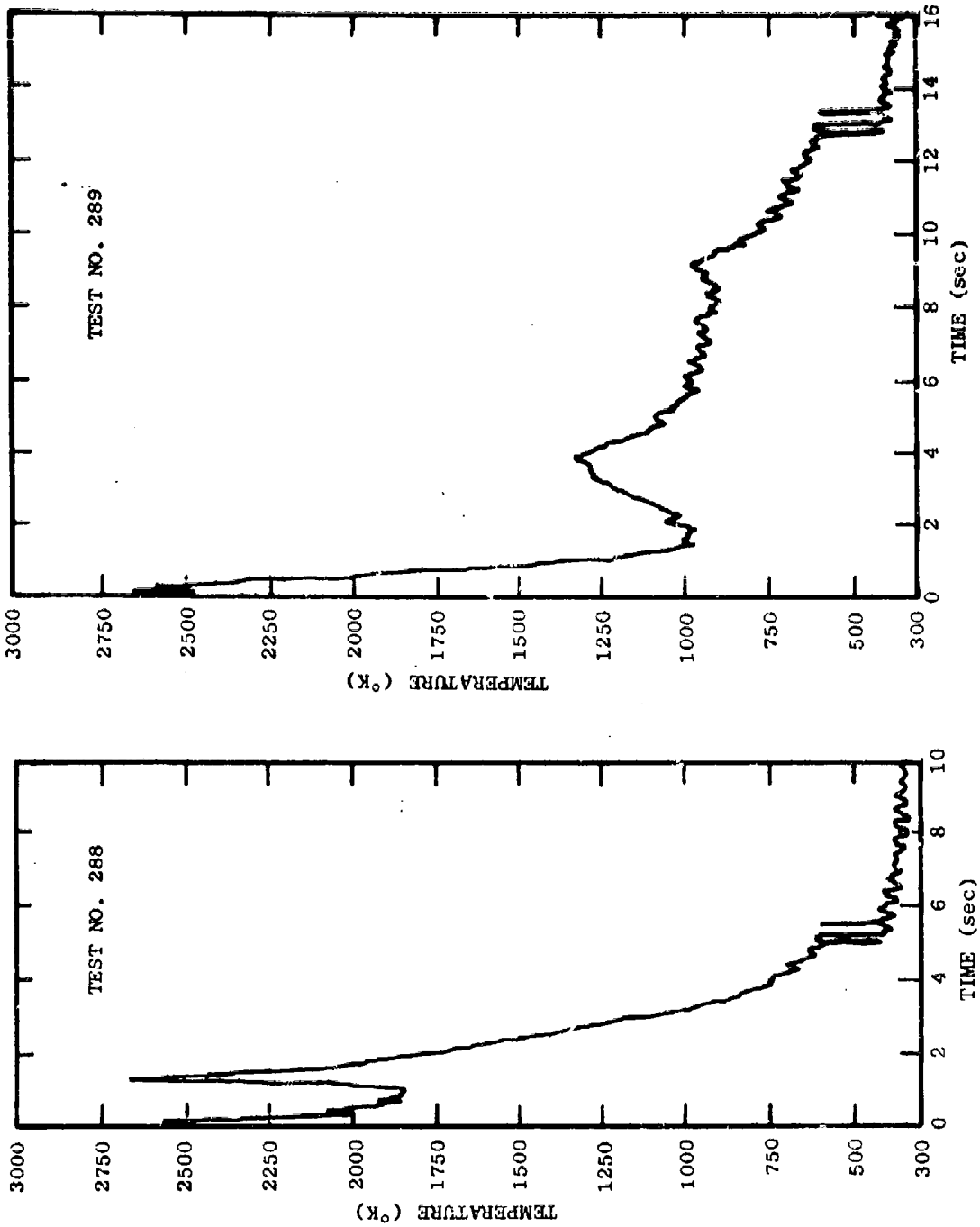

Fig. B-32. Temperature of Thermocouple Probes for Tests 288 and 289 (25,000-lb LO_2/LH_2)

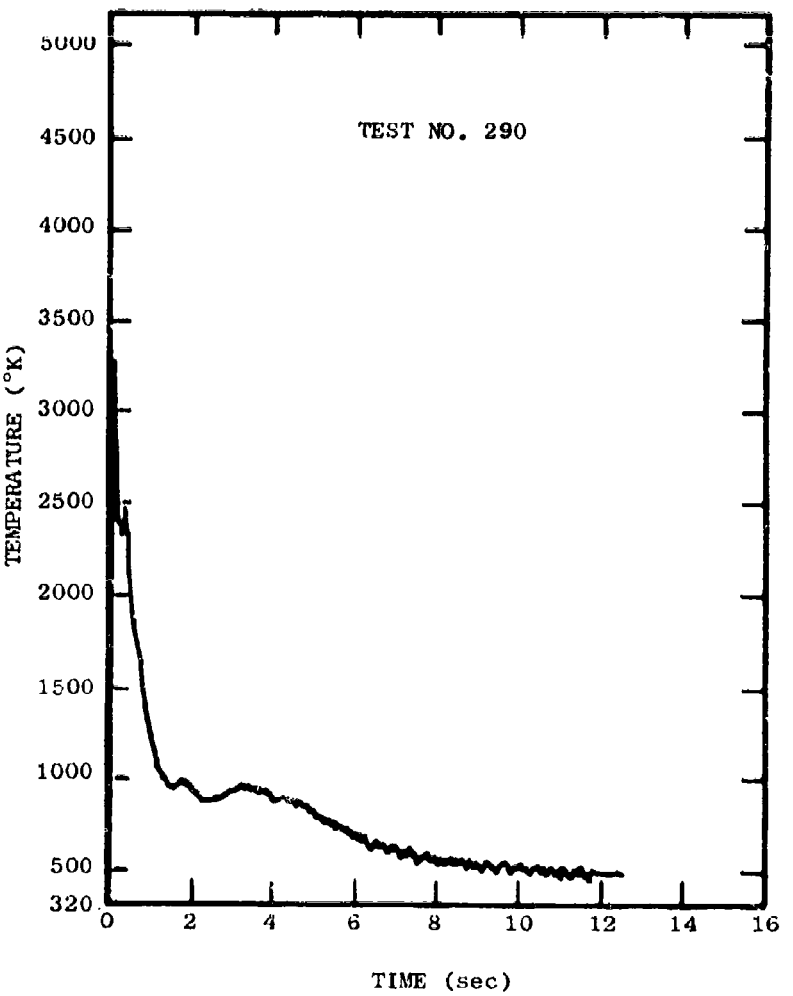

Fig. B-33. Temperature of Thermocouple Probe for Test 290 (25,000-lb LO_2/LH_2)

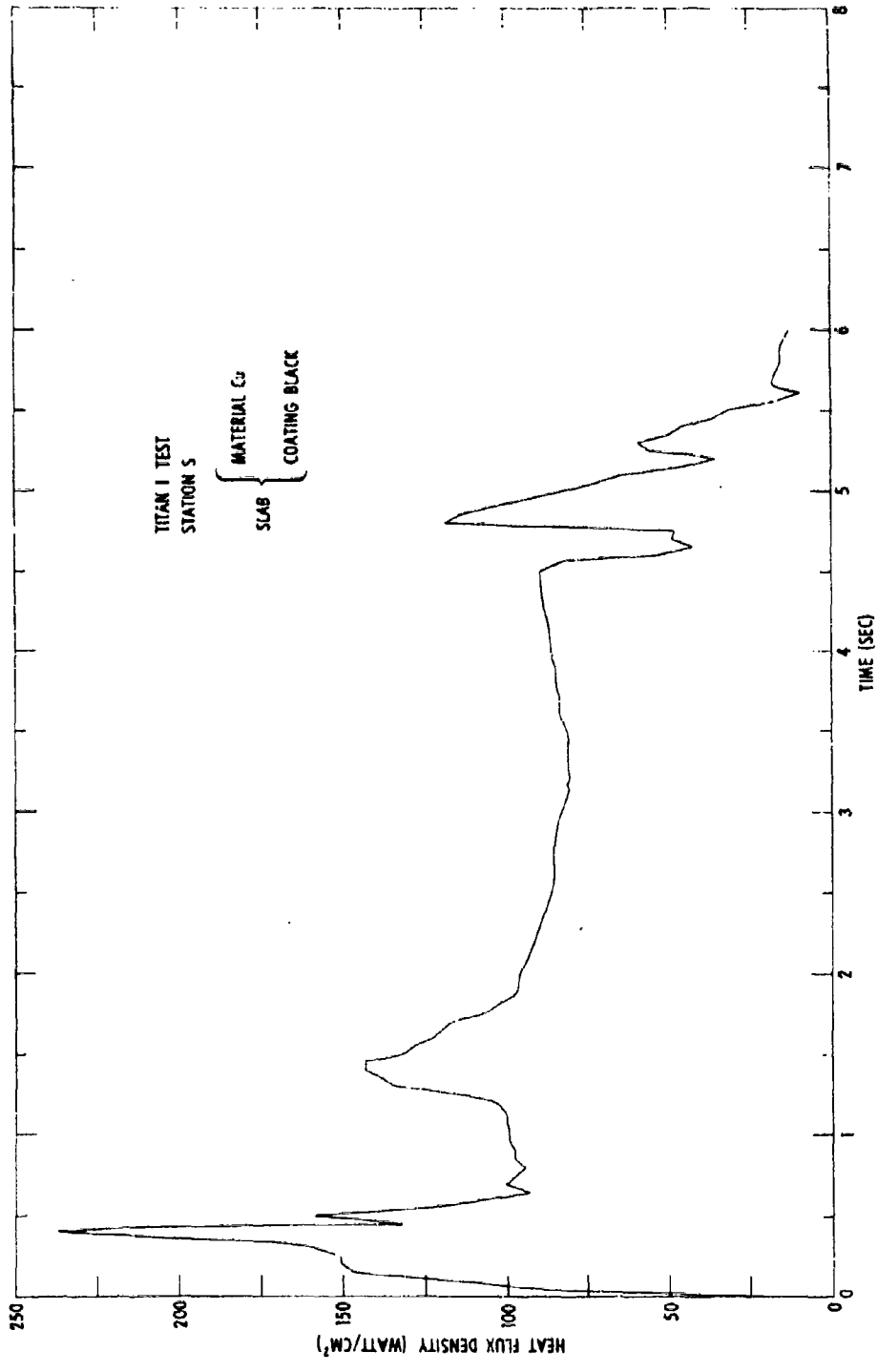

Fig. B-34. Heat Flux Density at Station S from the Titan I Test

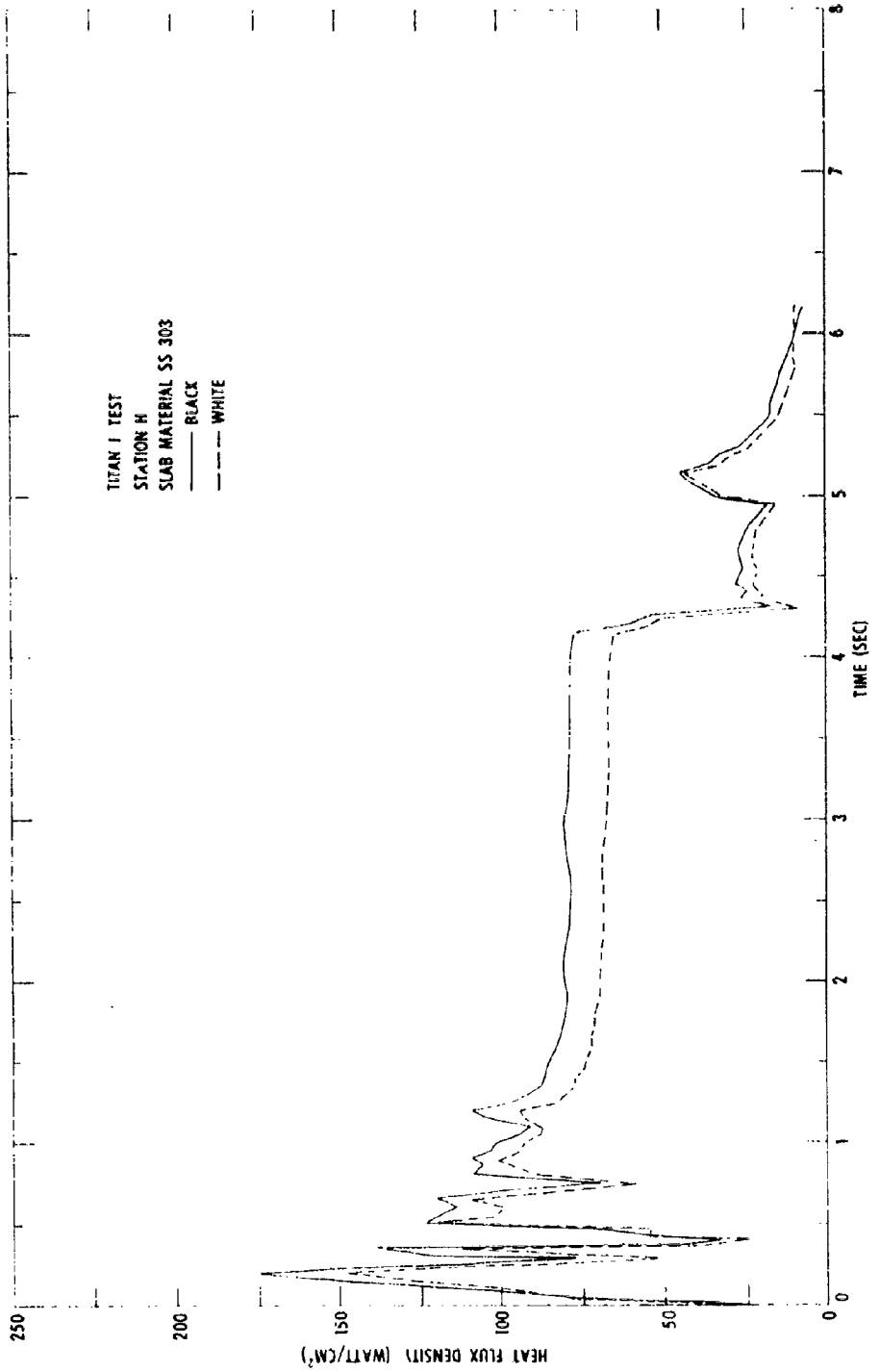

Fig. B-35. Heat Flux Density at Station H from the Titan I Test

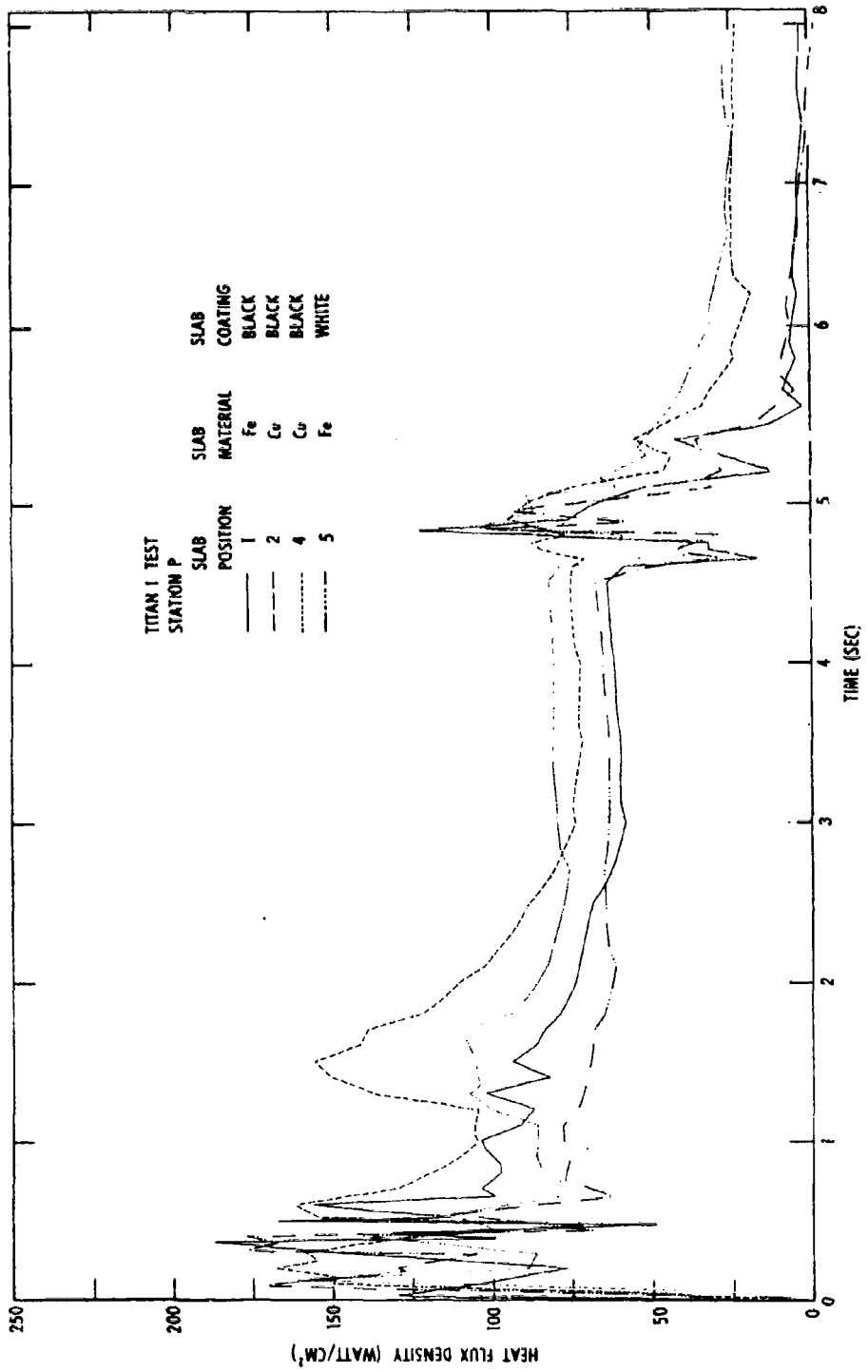

Fig. B-36. Heat Flux Density at Station P from the Titan I Test

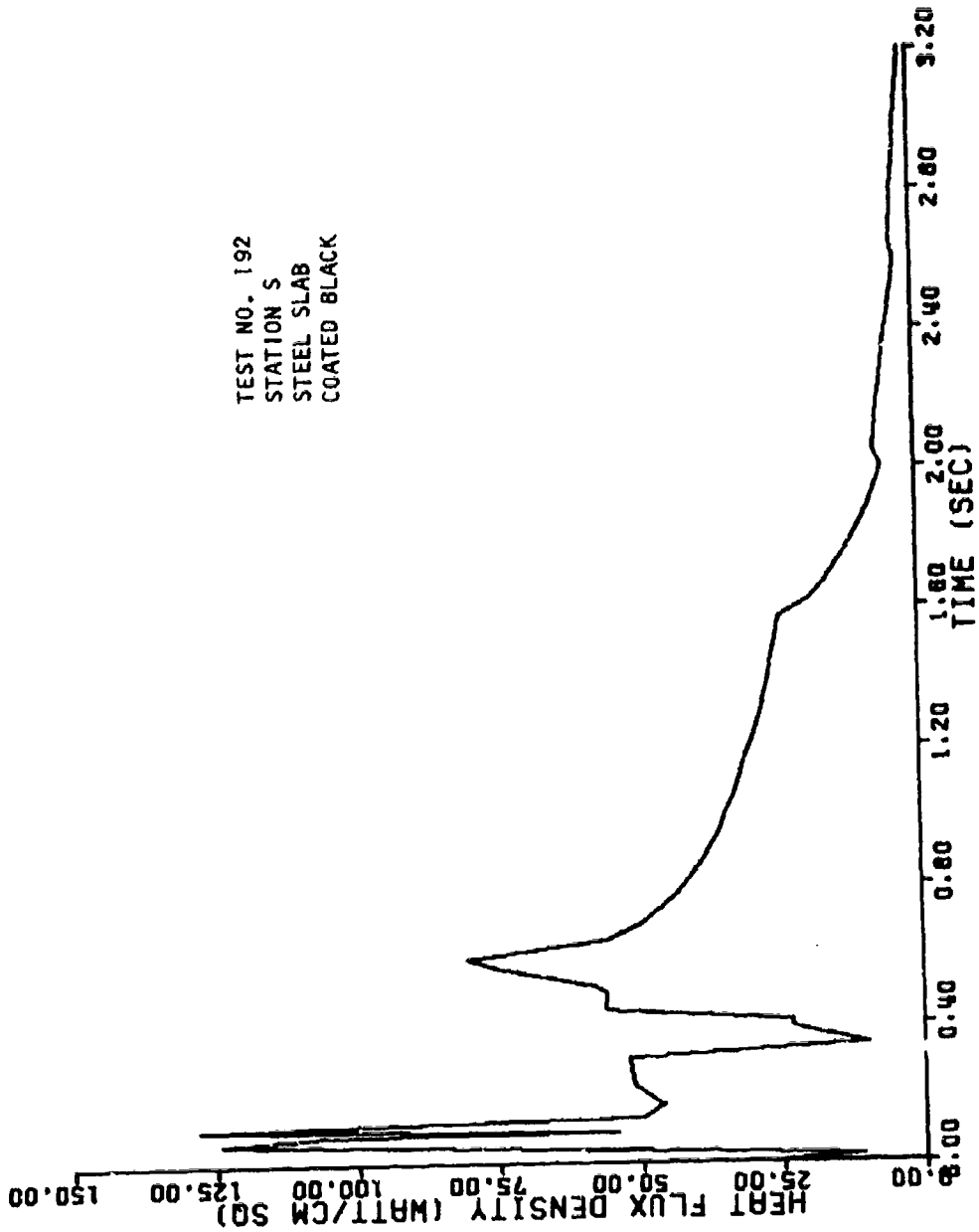

Figure B-37. Heat Flux Density at Station S for Test 192 (1000-lb LO_2/RP-1)

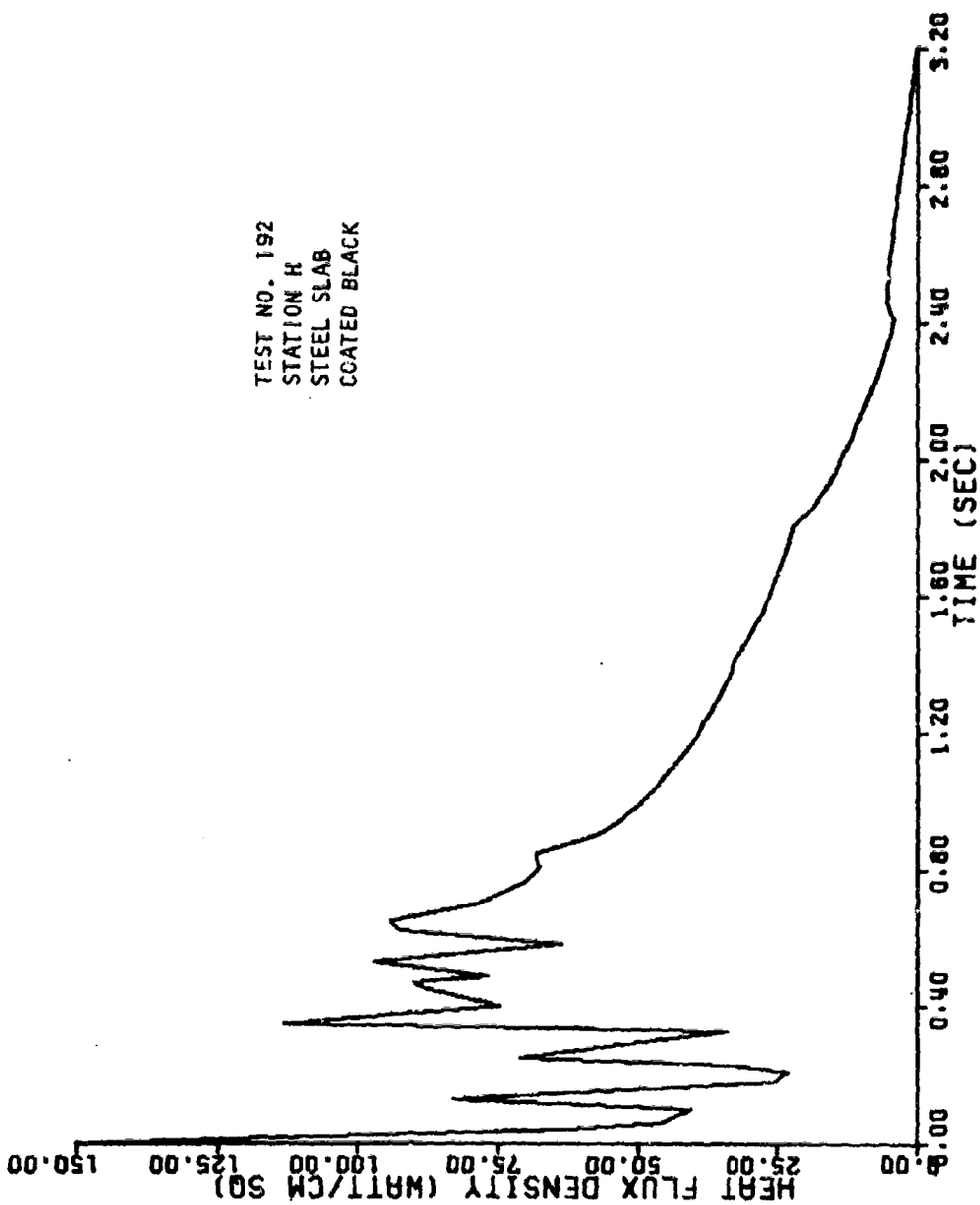

Figure B-38. Heat Flux Density at Station H for Test 192 (1000-lb LO_2 RP-1)

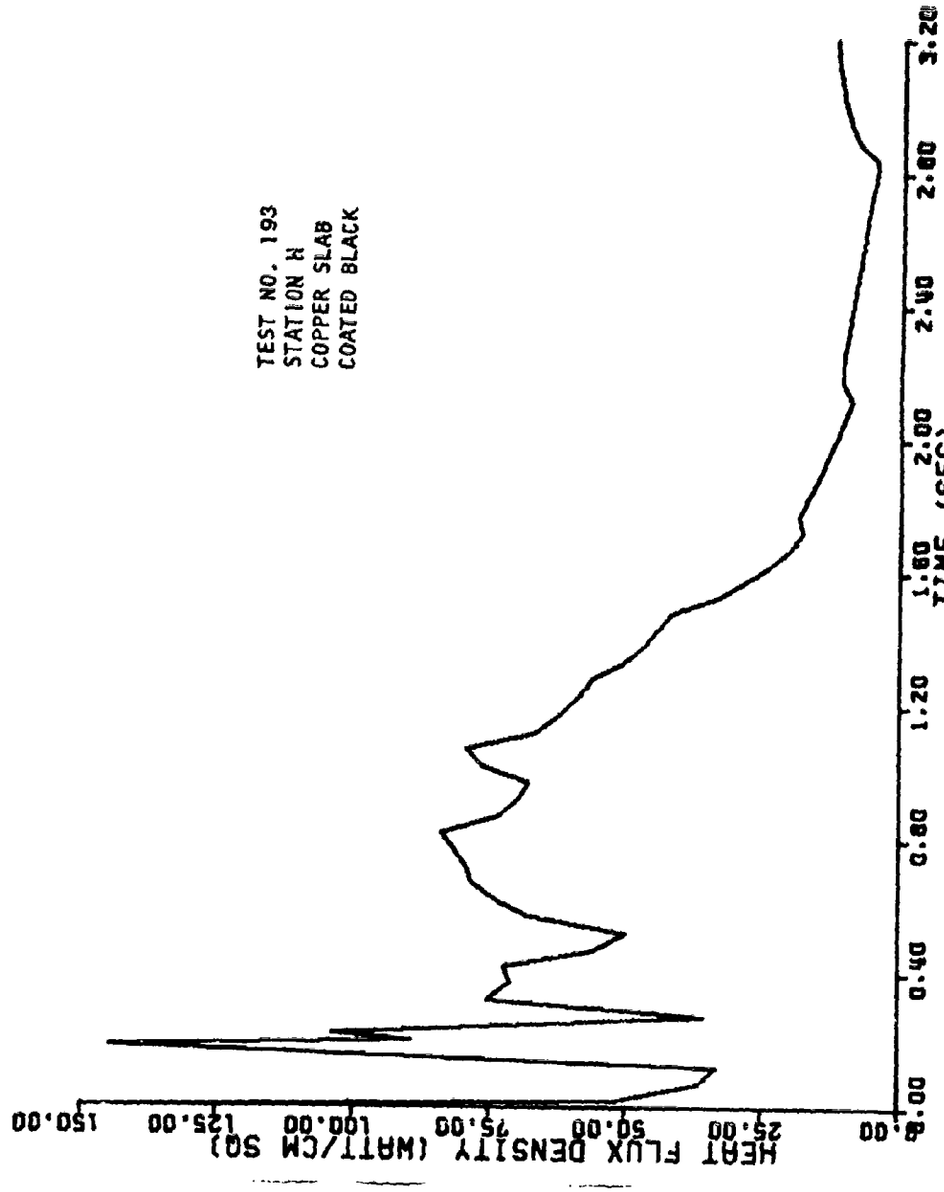

Figure B-39. Heat Flux Density at Station H for Test 193 (1000-lb LO_2/RP-1)

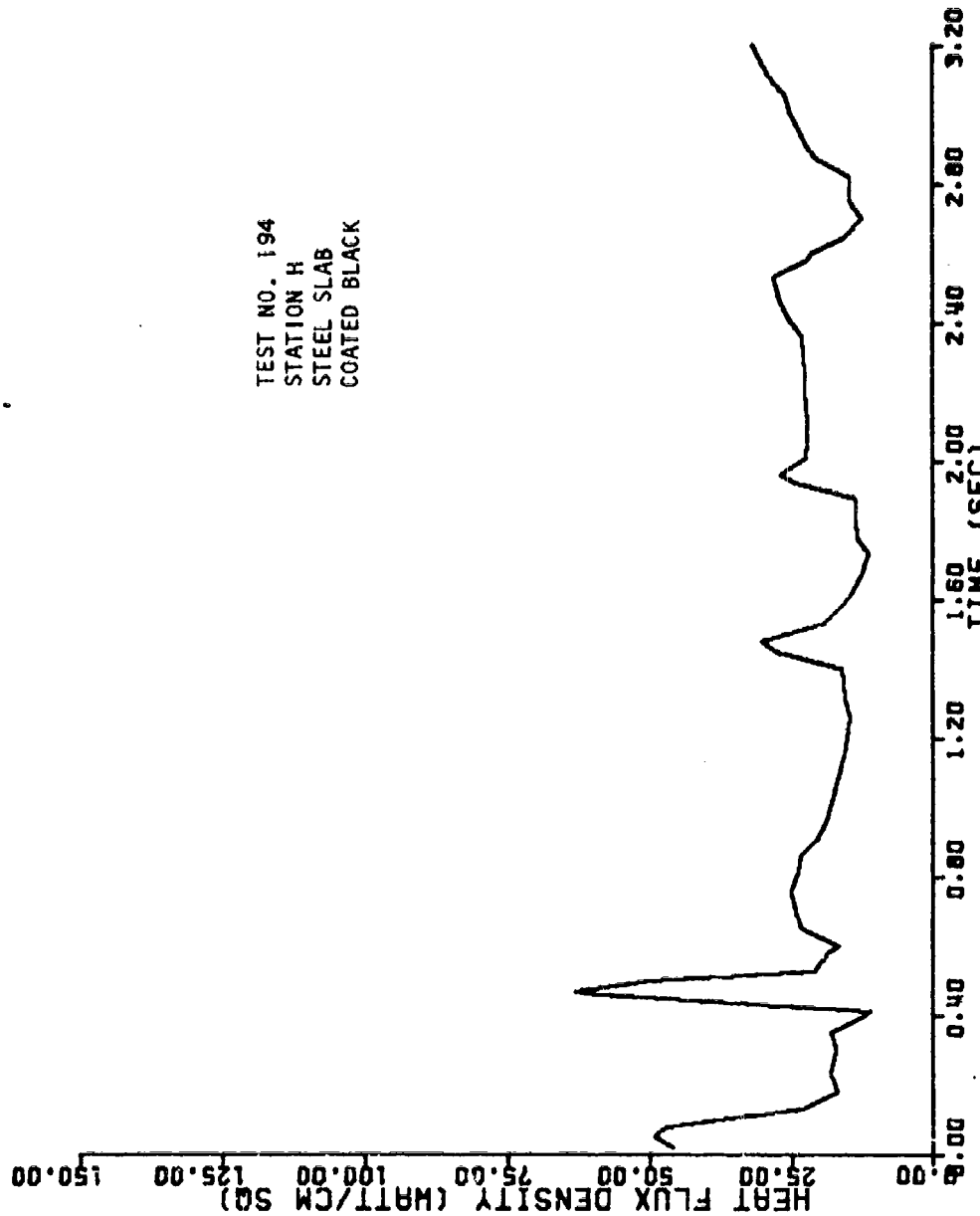

Figure B-40. Heat Flux Density at Station H for Test 194 (1000-lb LO_2/RP-1)

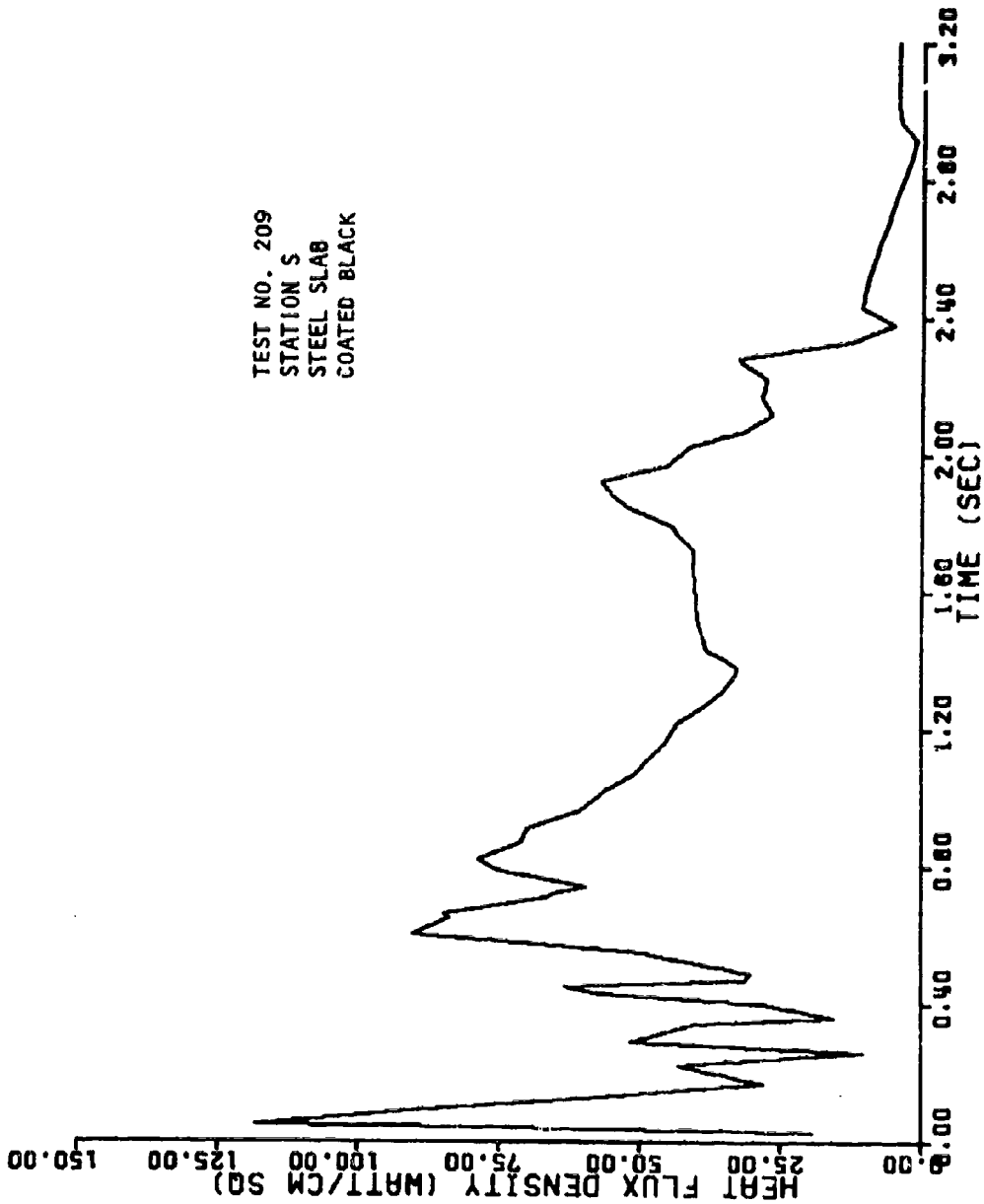

Figure B-41. Heat Flux Density at Station S for Test 209 (1000-lb LO_2/RP-1)

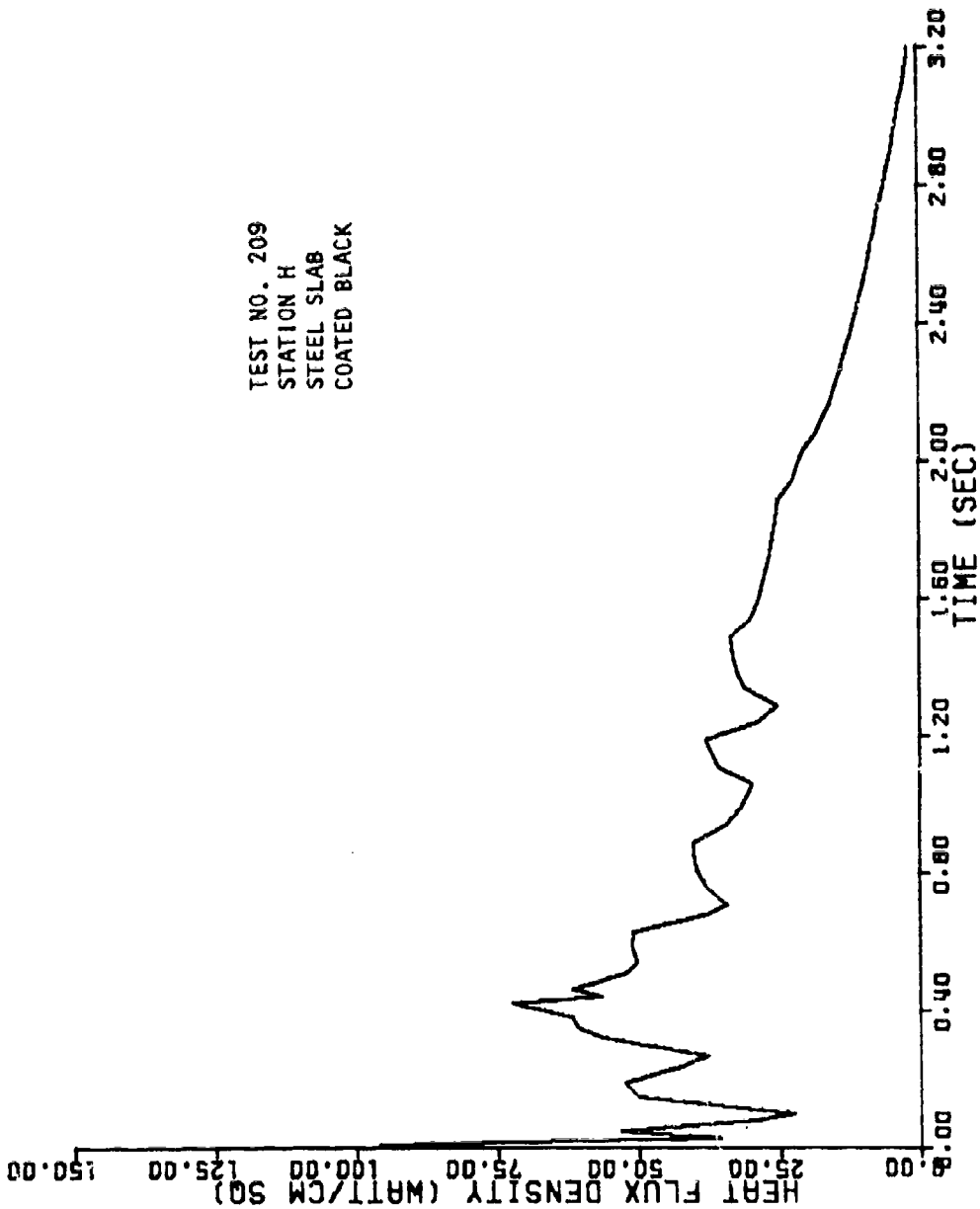

Figure B-42. Heat Flux Density at Station H for Test 209 (1000-lb LO_2/RP-1)

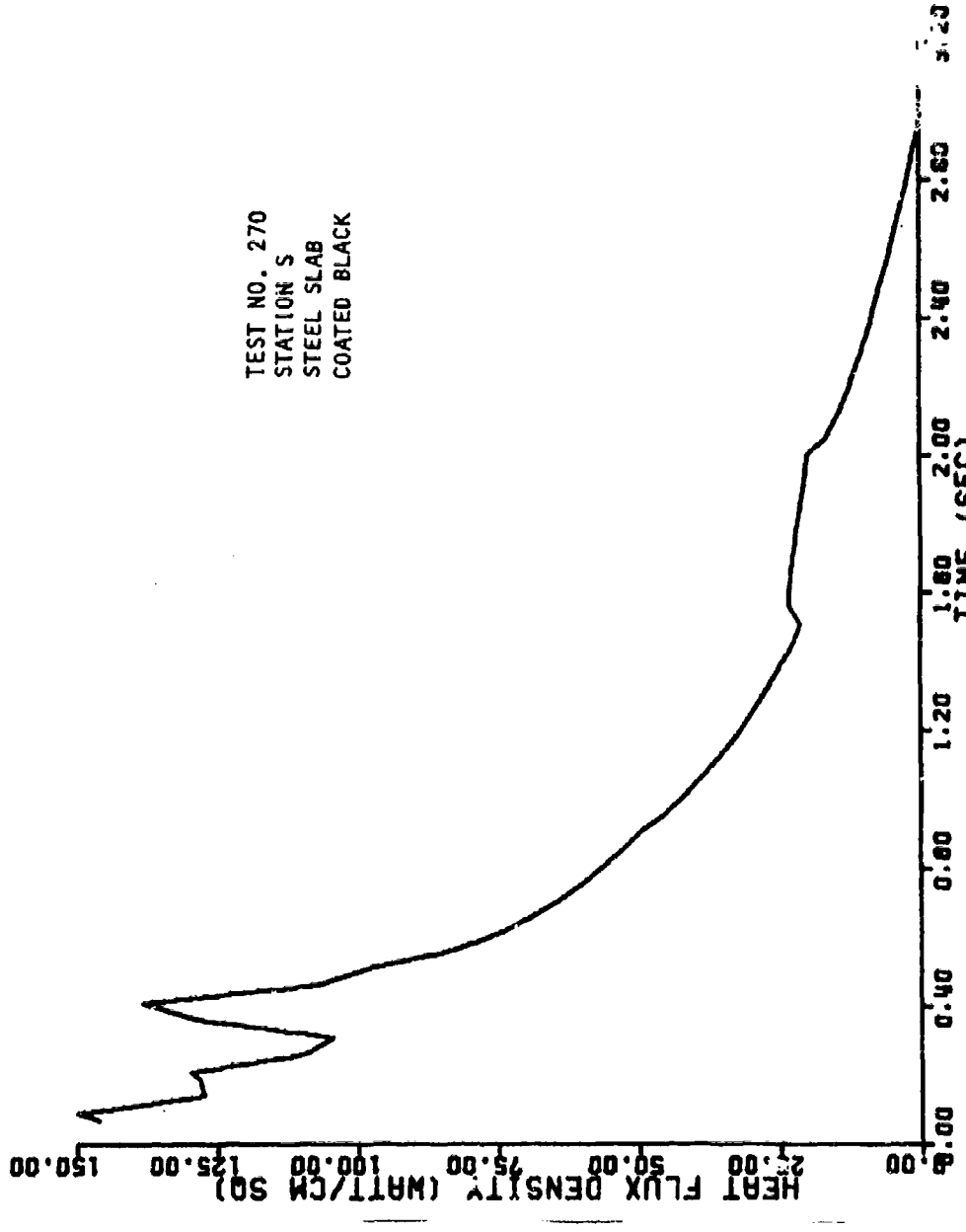

Figure B-43. Heat Flux Density at Station S for Test 270 (1000-lb LO_2/RP-1)

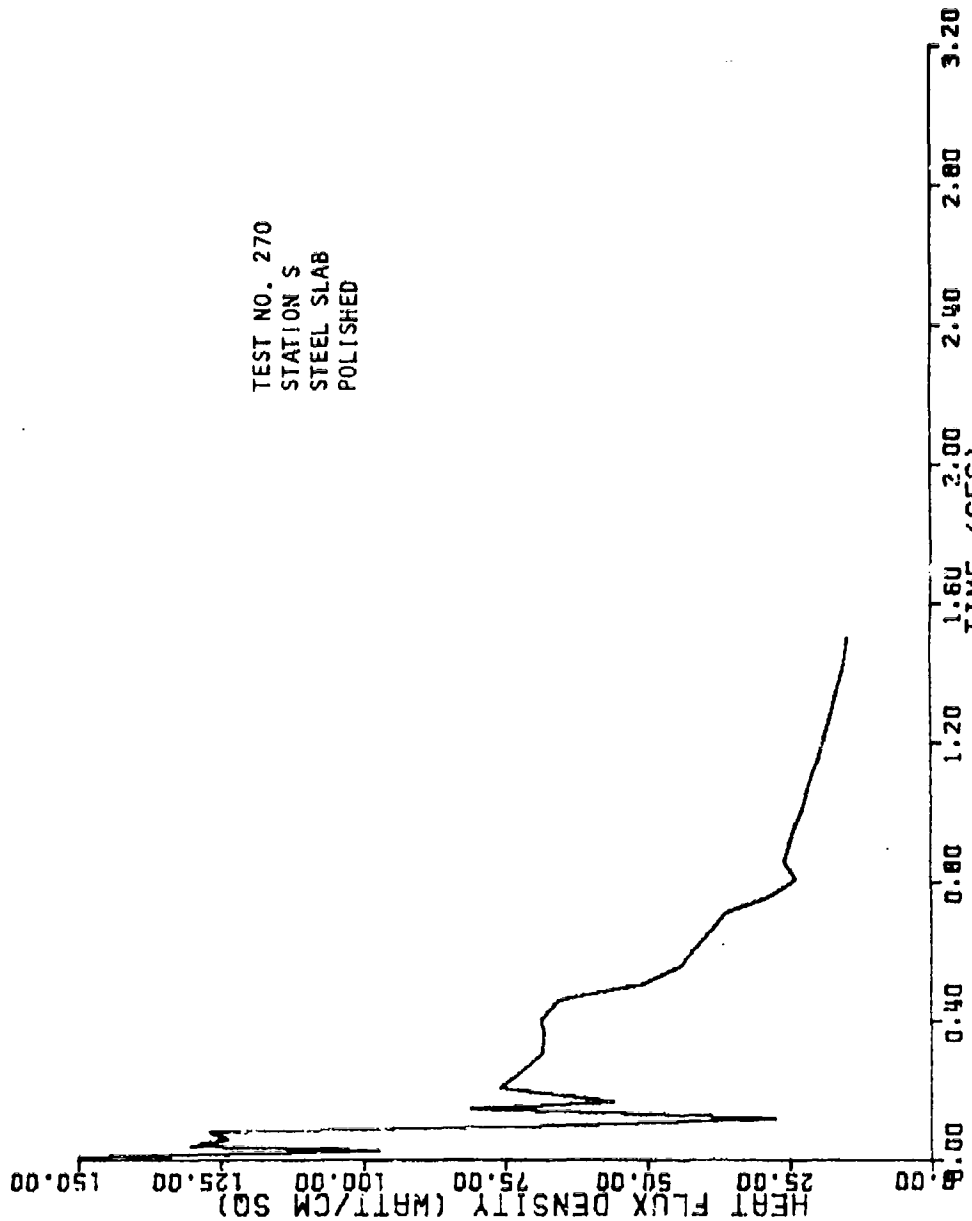

Figure B-44. Heat Flux Density at Station S for Test 270 (1000-lb LO_2/RP-1)

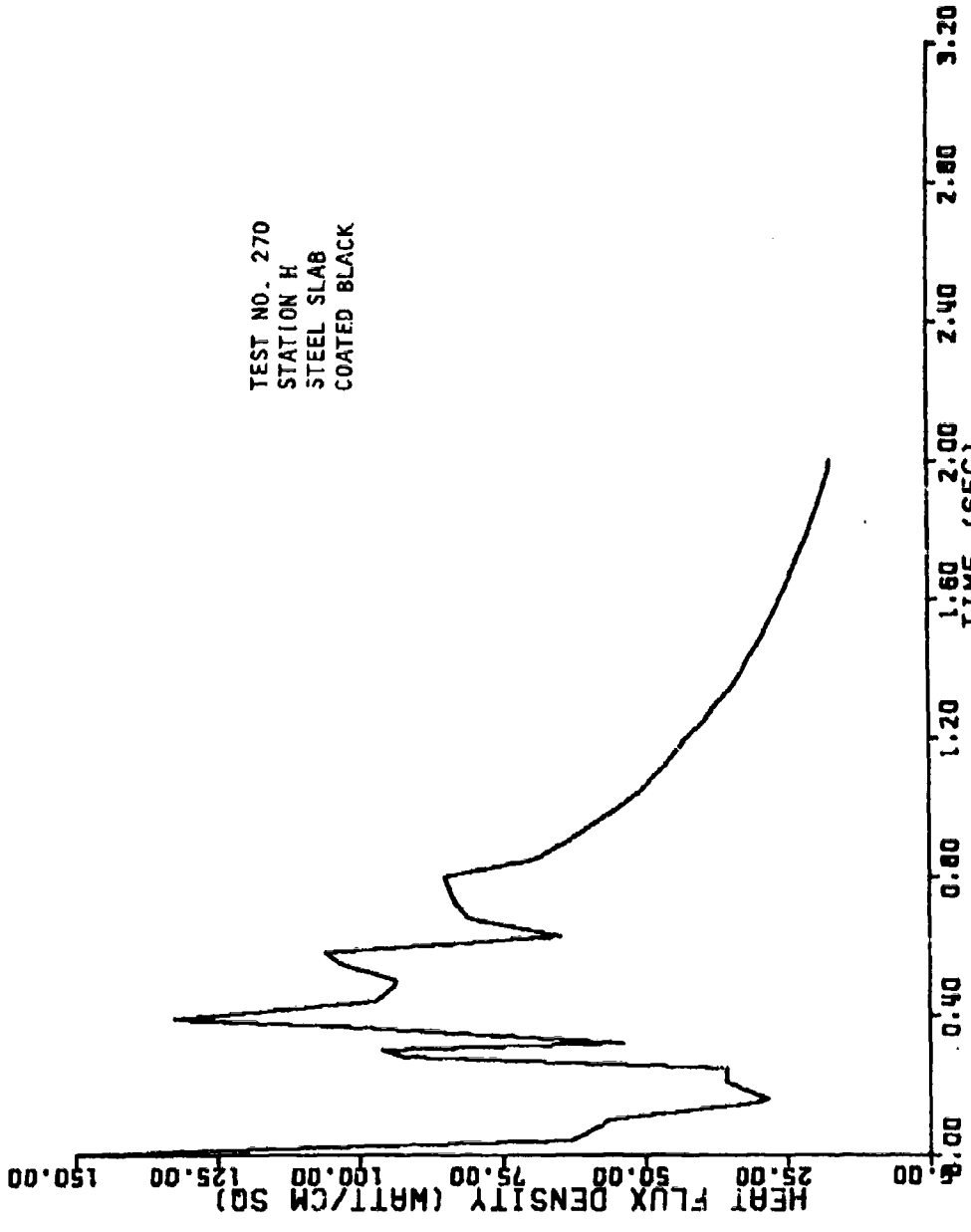

Figure B-45. Heat Flux Density at Station H for Test 270 (1000-lb LO_2/RP-1)

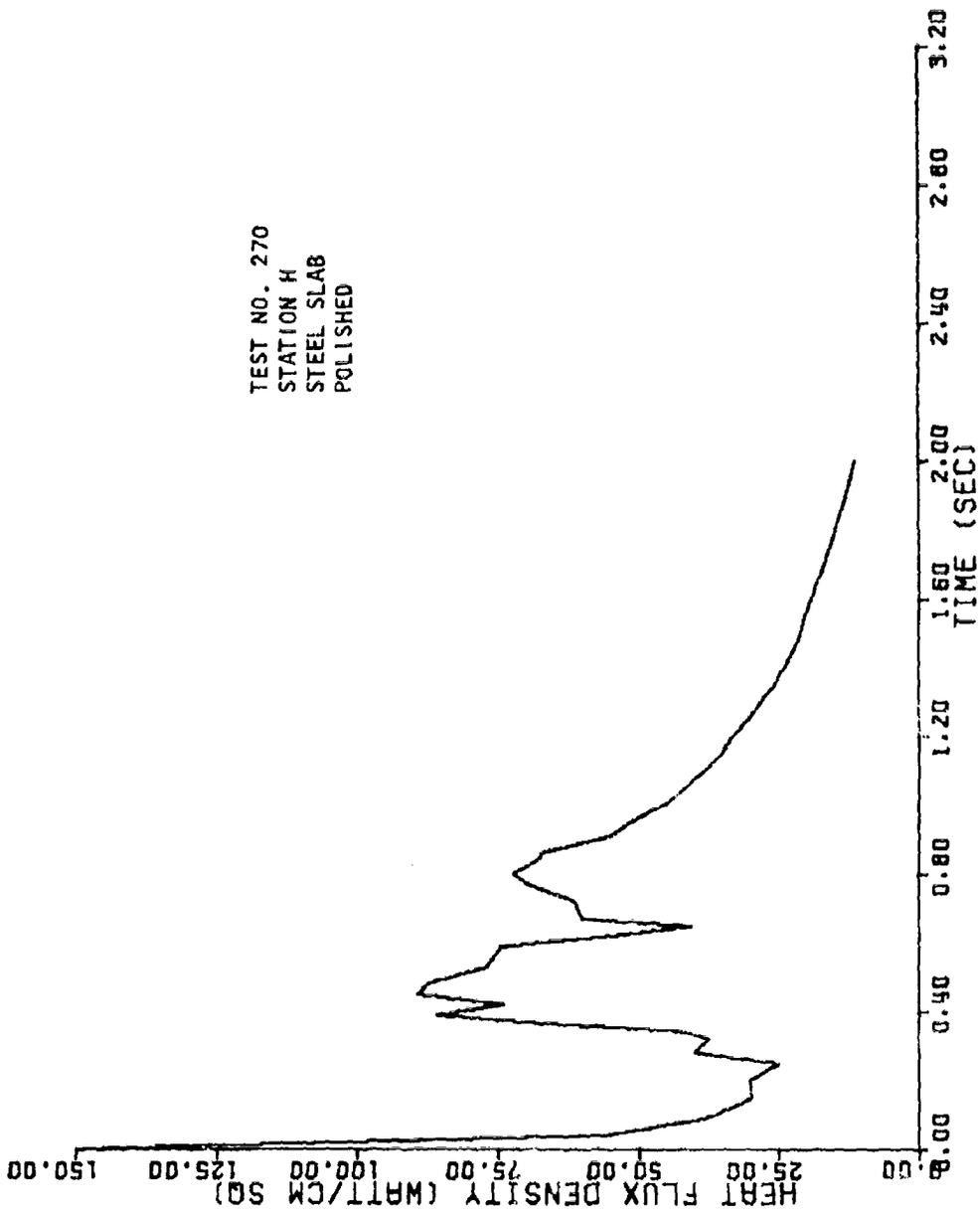

Figure B-46. Heat Flux Density at Station H for Test 270 (1000-lb LO_2/RP-1)

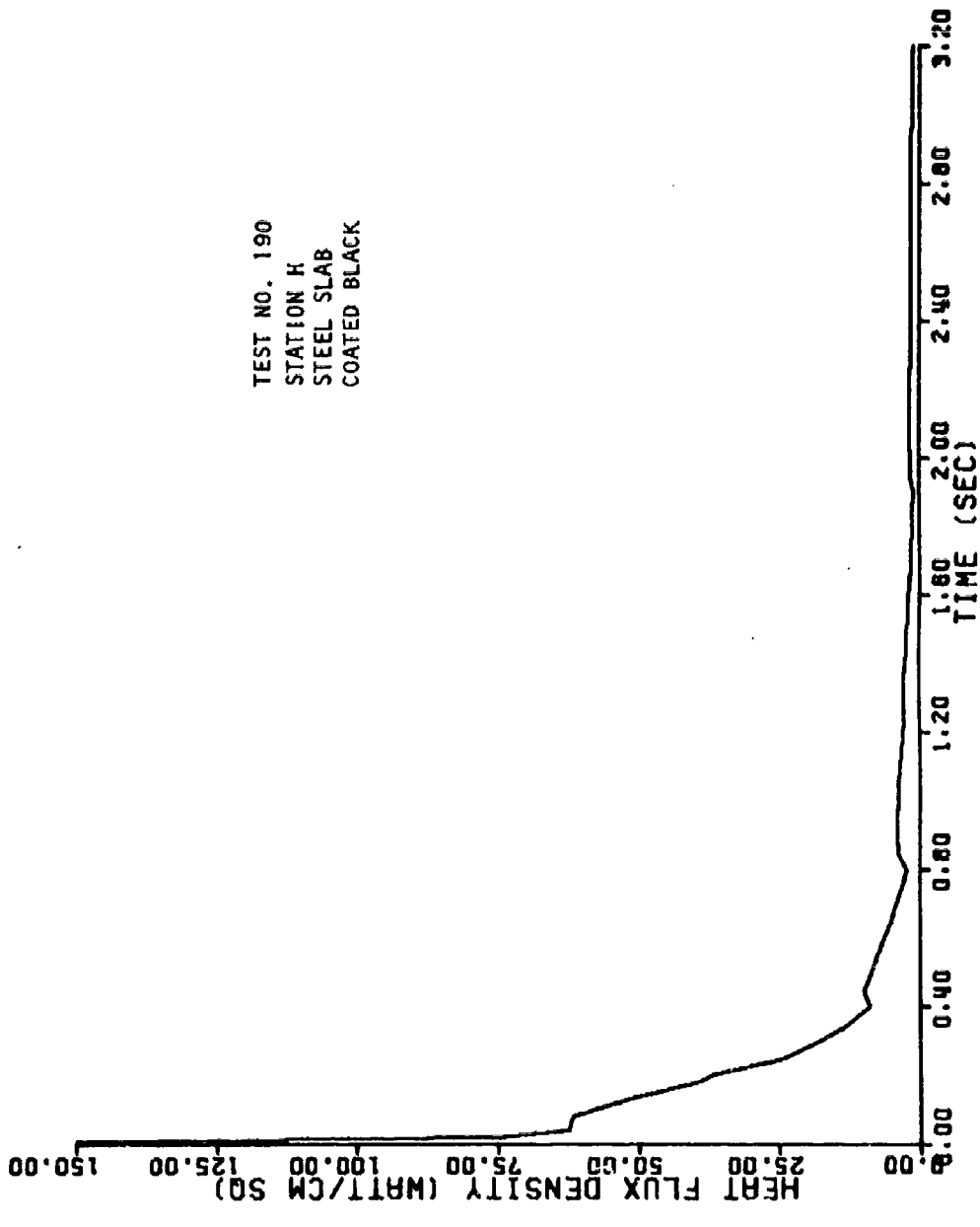

Figure B-47. Heat Flux Density at Station H for Test 190 (1000-lb LO_2/RP-1)

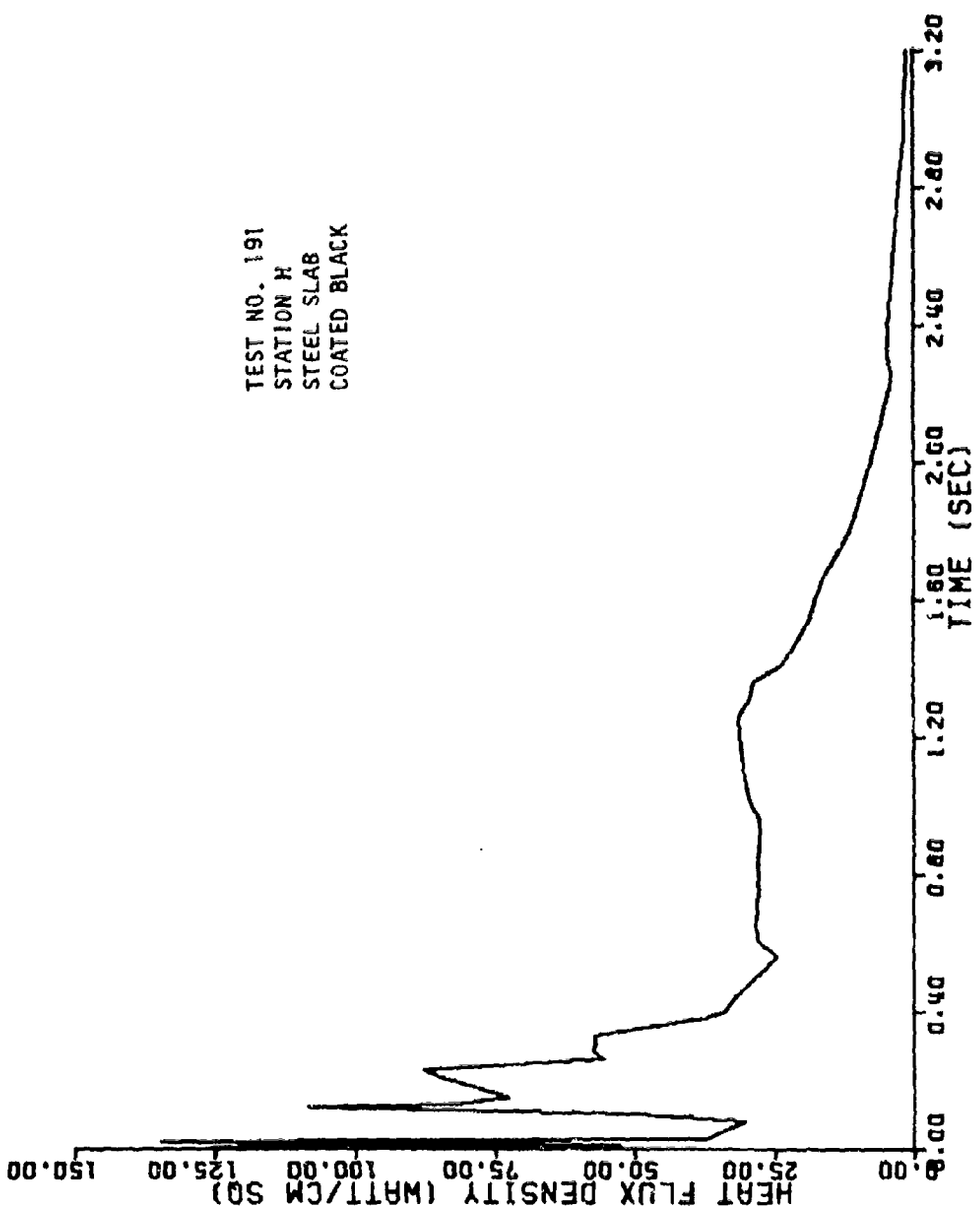

Figure B-48. Heat Flux Density at Station H for Test 191 (1000-lb LO_2/RP-1)

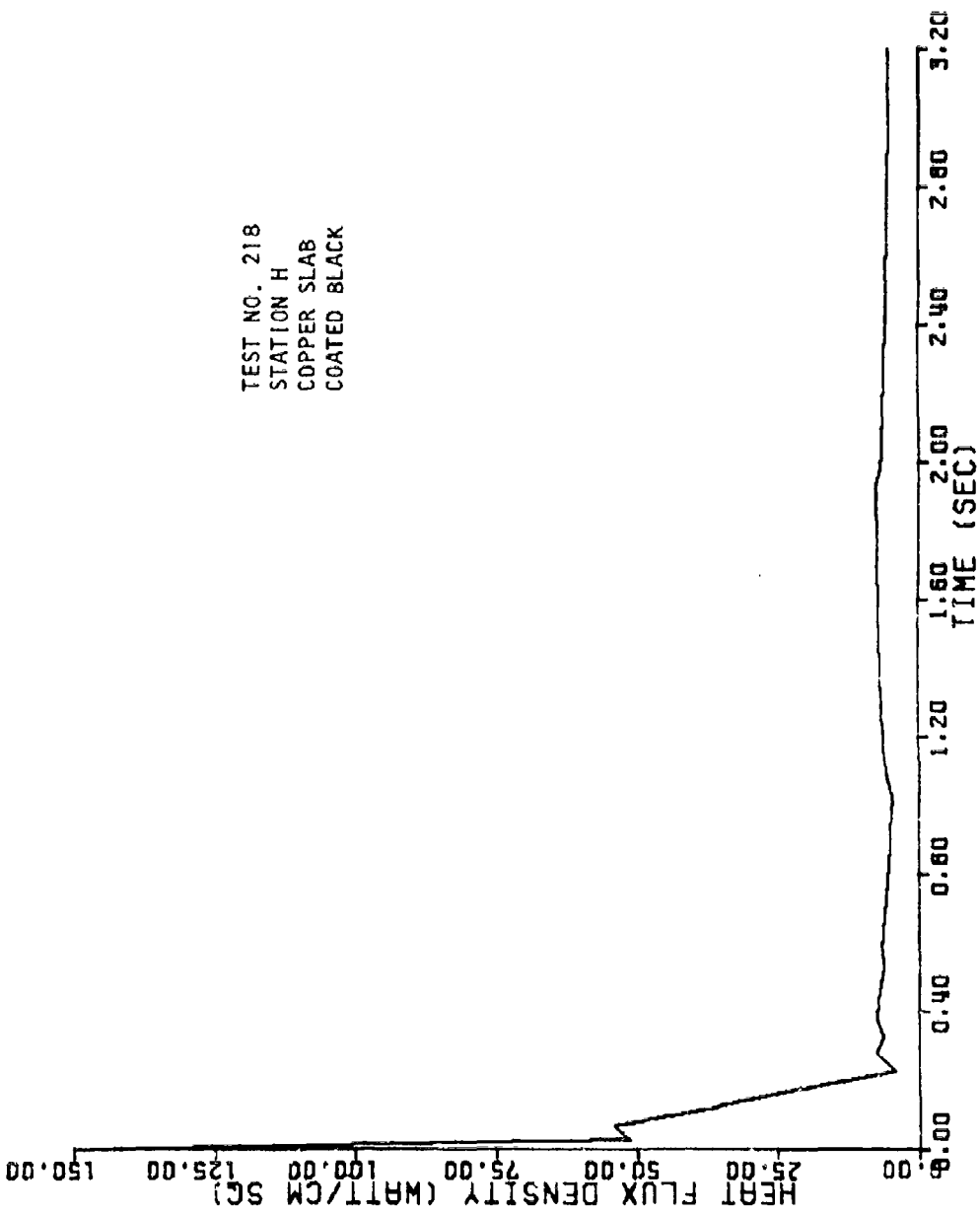

Figure B-49. Heat Flux Density at Station H for Test 218 (1600-lb LO_2/RP-1)

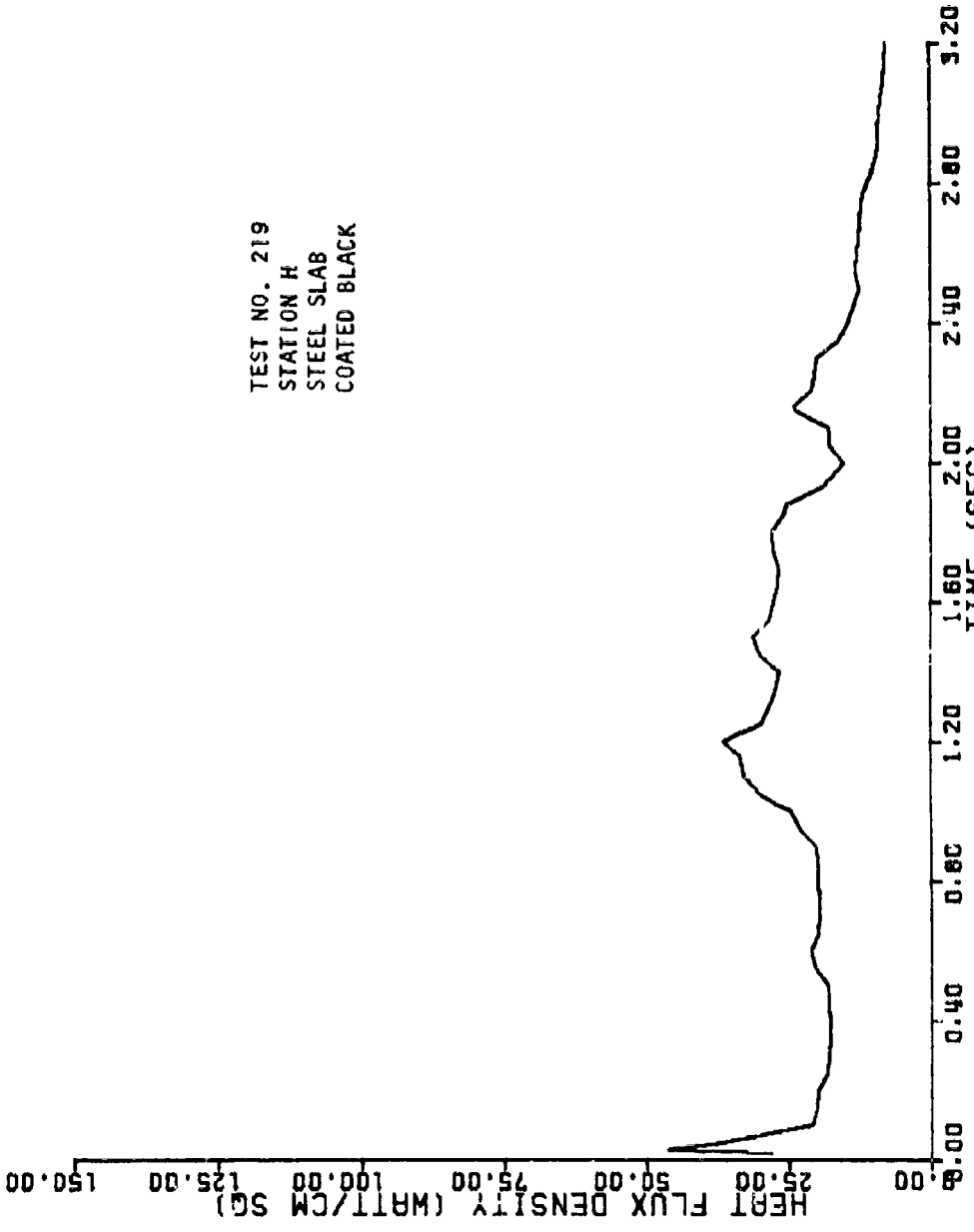

Figure B-50. Heat Flux Density at Station H for Test 219 (1000-lb LO_2/RP-1)

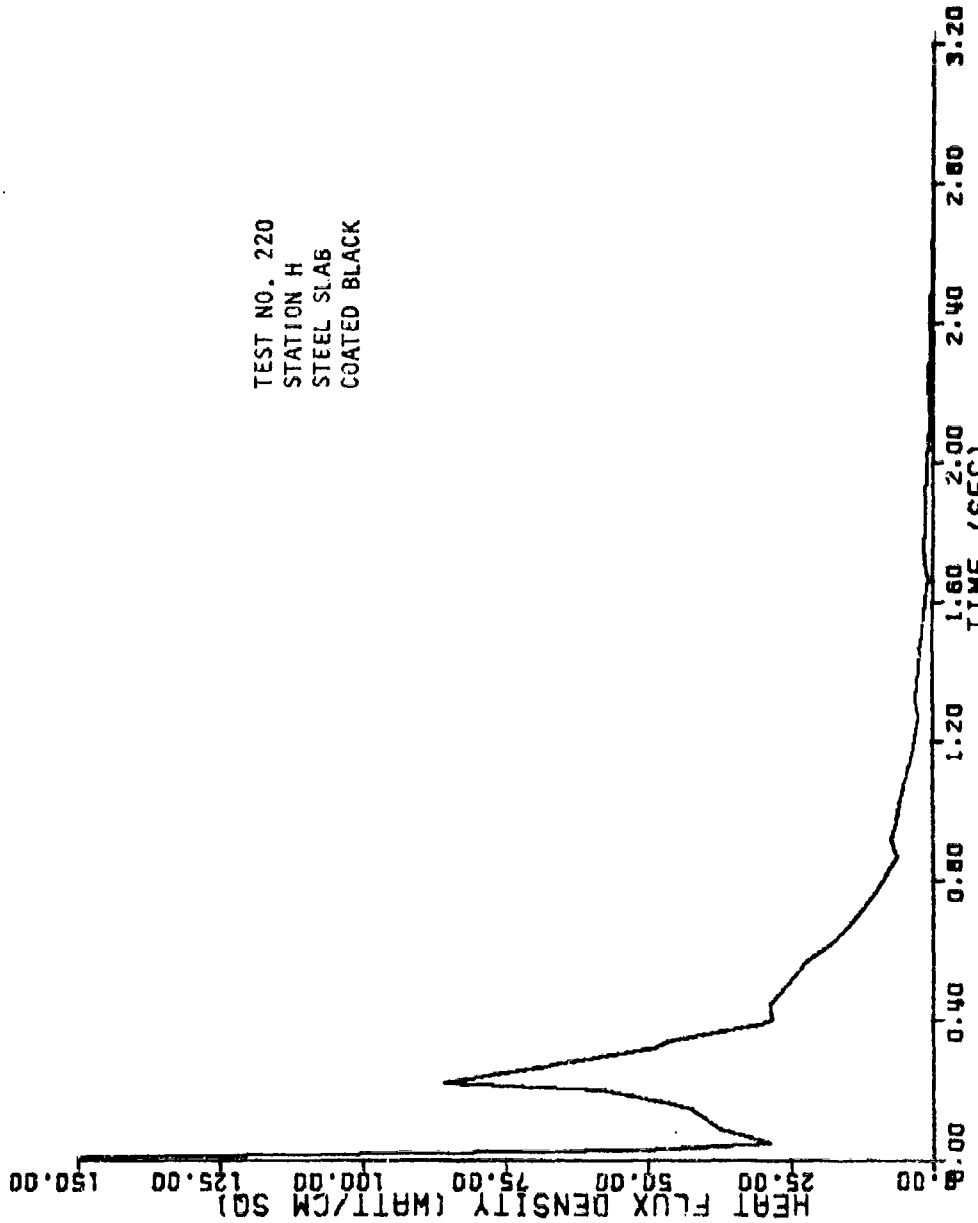

Figure B-51. Heat Flux Density at Station H for Test 220 (100%-lb LO_2/RP-1)

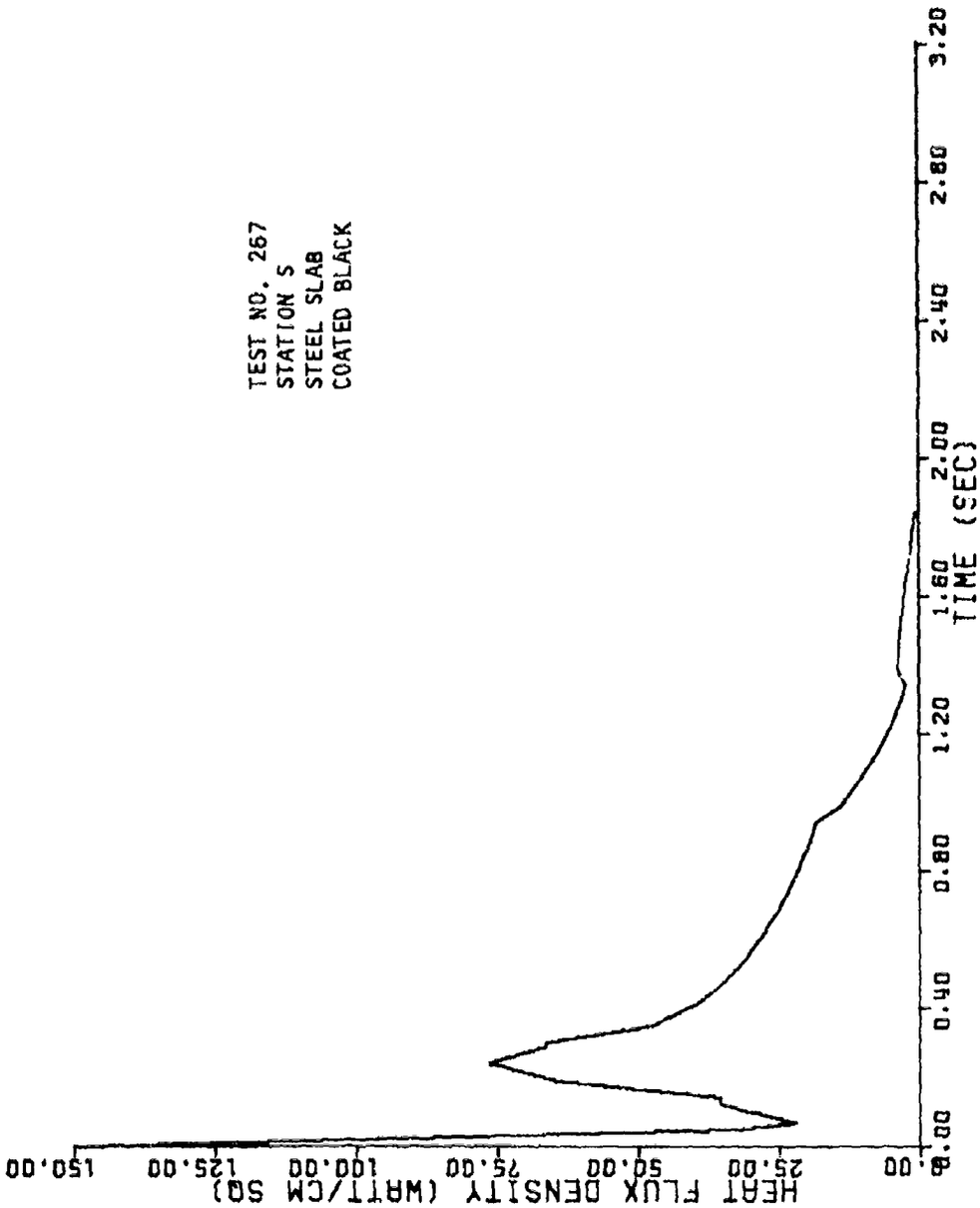

Figure B-52. Heat Flux Density at Station S for Test 267 (1000-lb LO_2/RP-1)

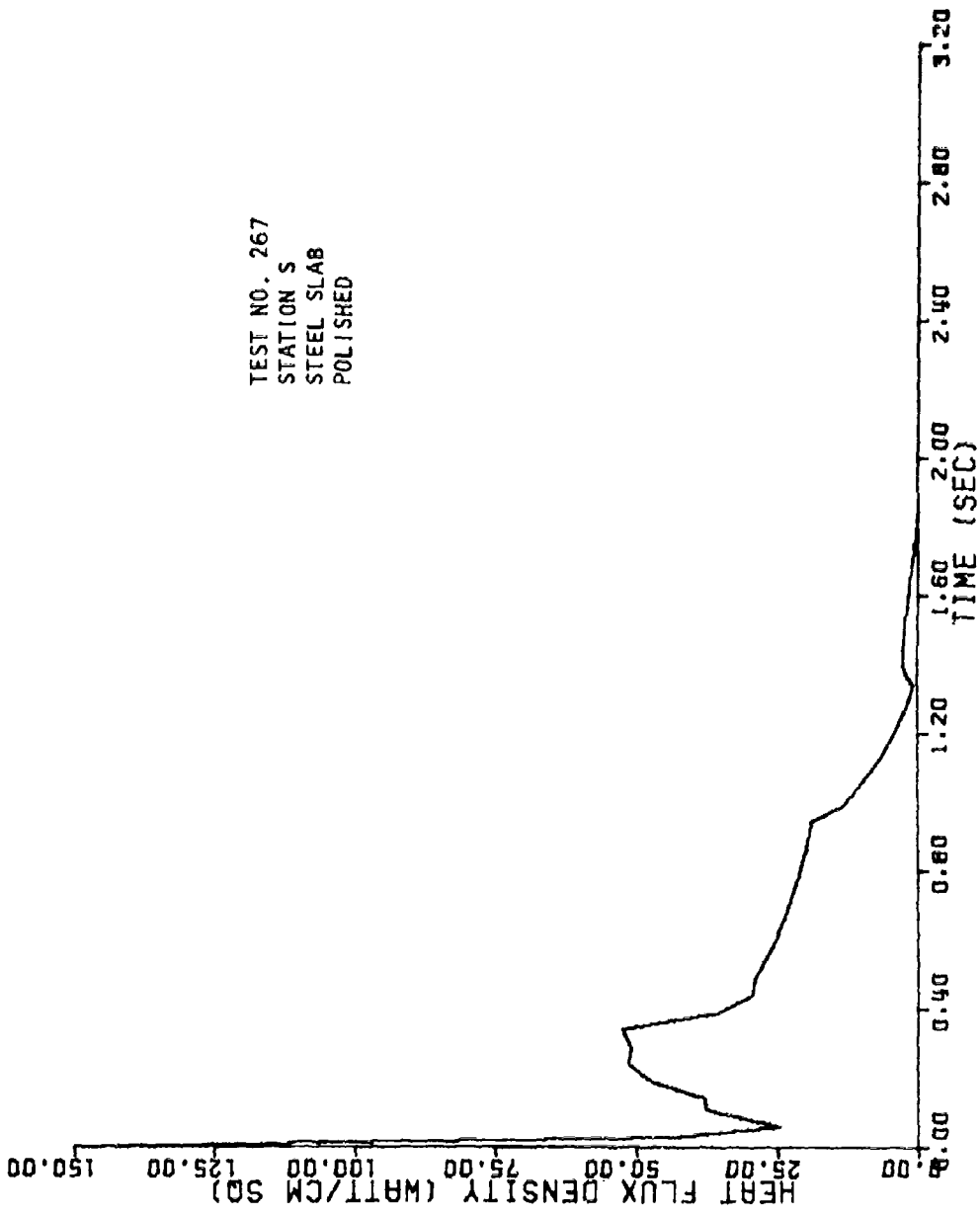

Figure B-53. Heat Flux Density at Station S for Test 267 (1000-lb LO_2/RP-1)

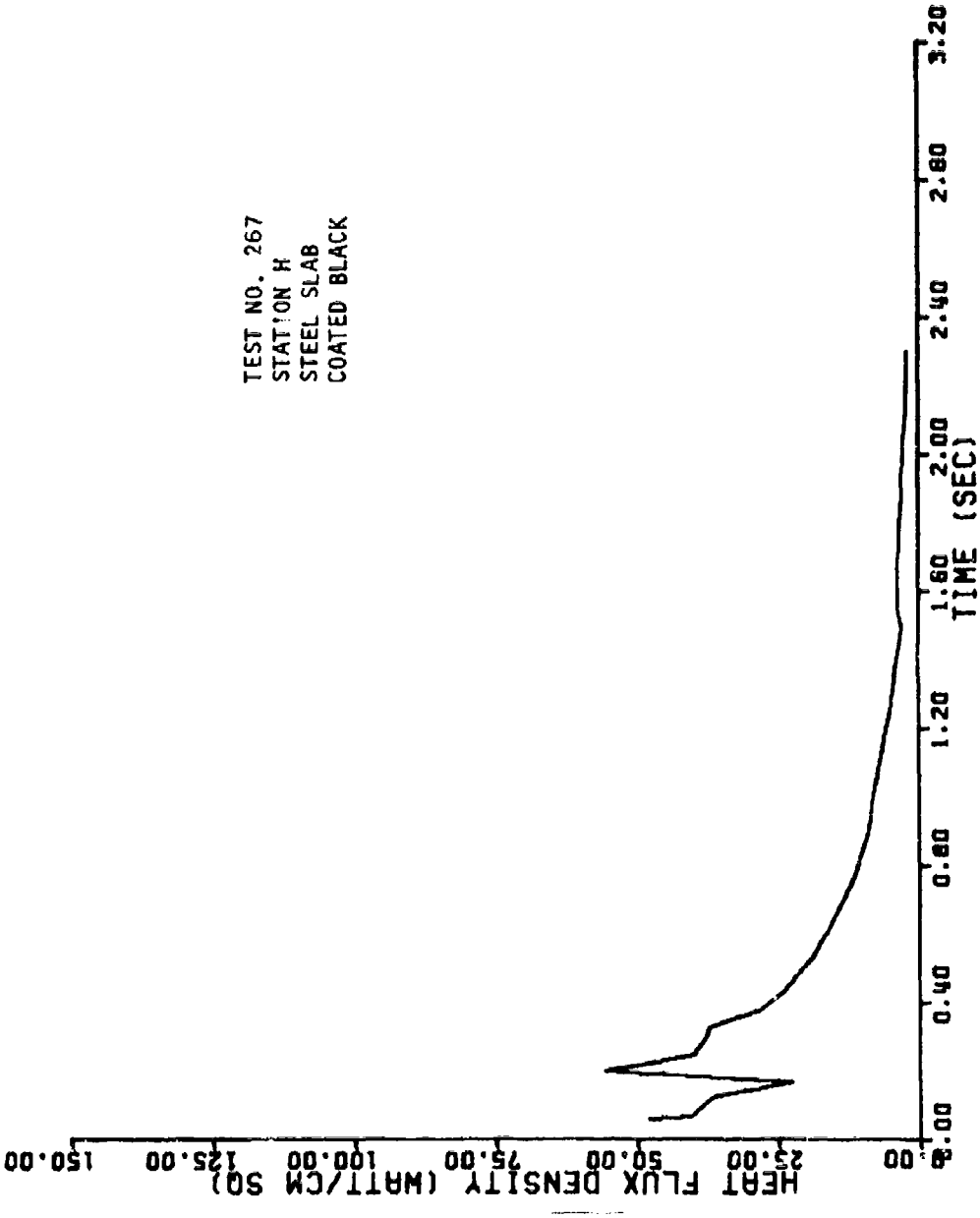

Figure B-54. Heat Flux Density at Station H for Test 267 (1000-lb LO_2/RP-1)

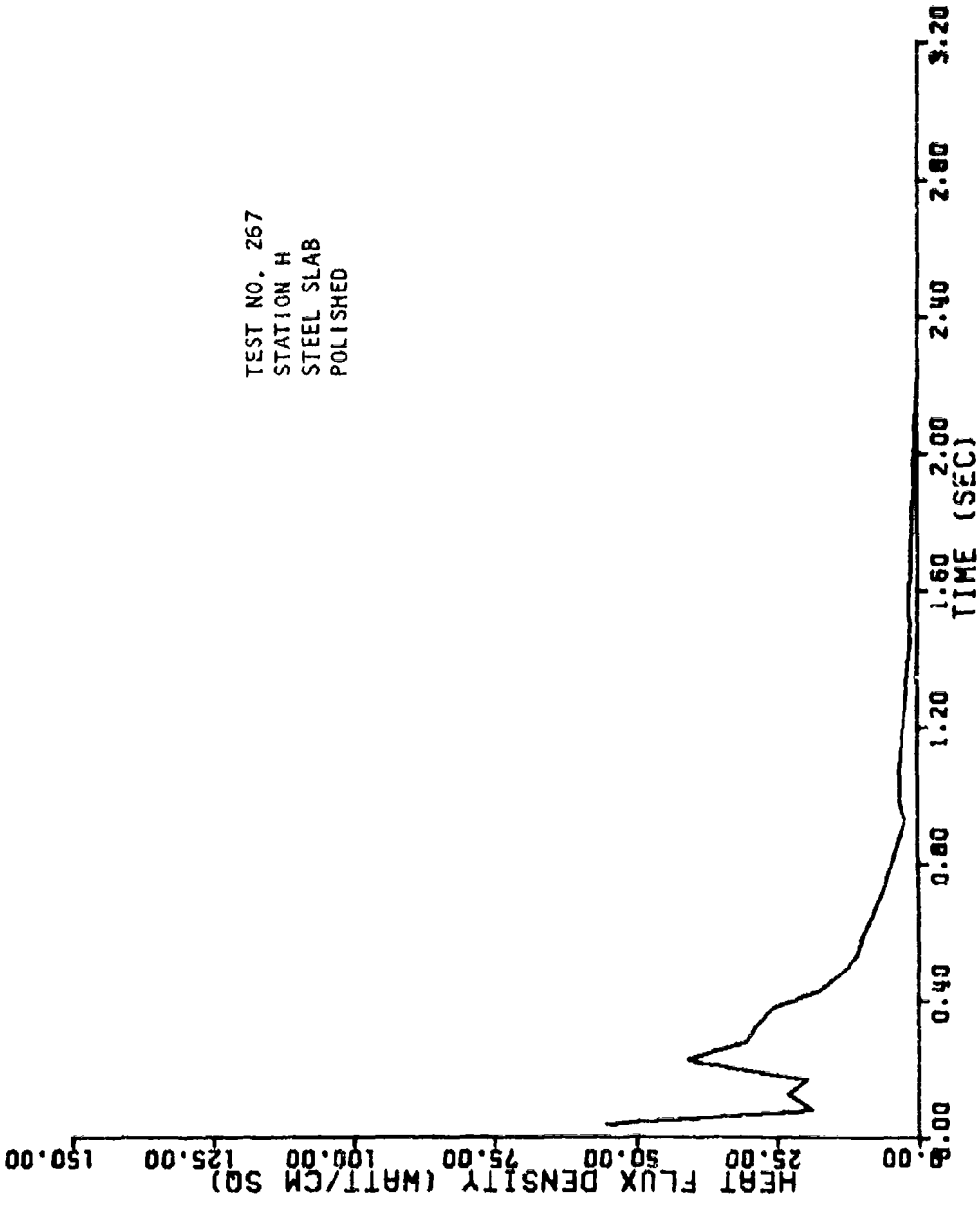

Figure B-55. Heat Flux Density at Station H for Test 267 (1000-lb LO_2/RP-1)

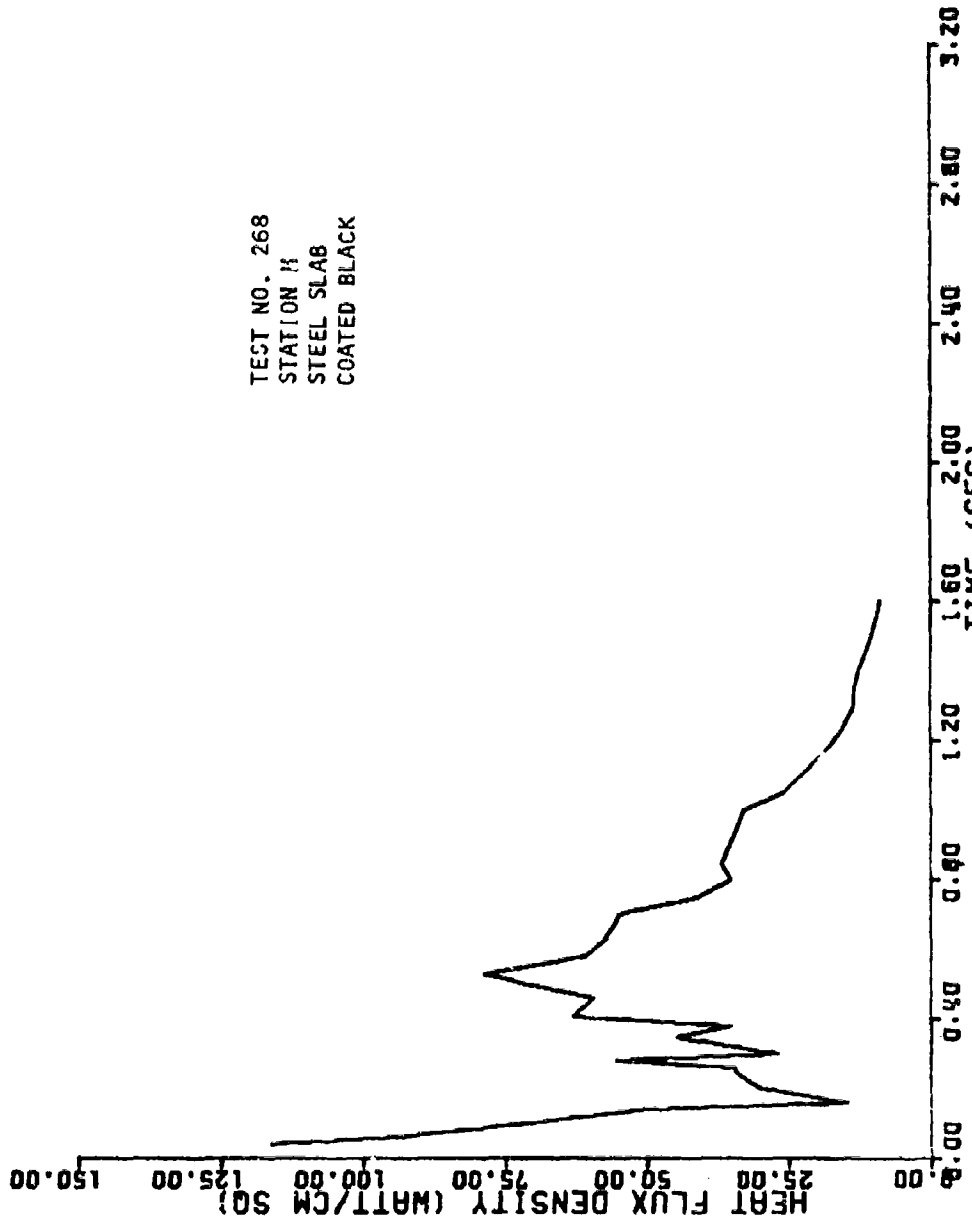

Figure B-56. Heat Flux Density at Station H for Test 268 (1000-lb LO_2/RP-1)

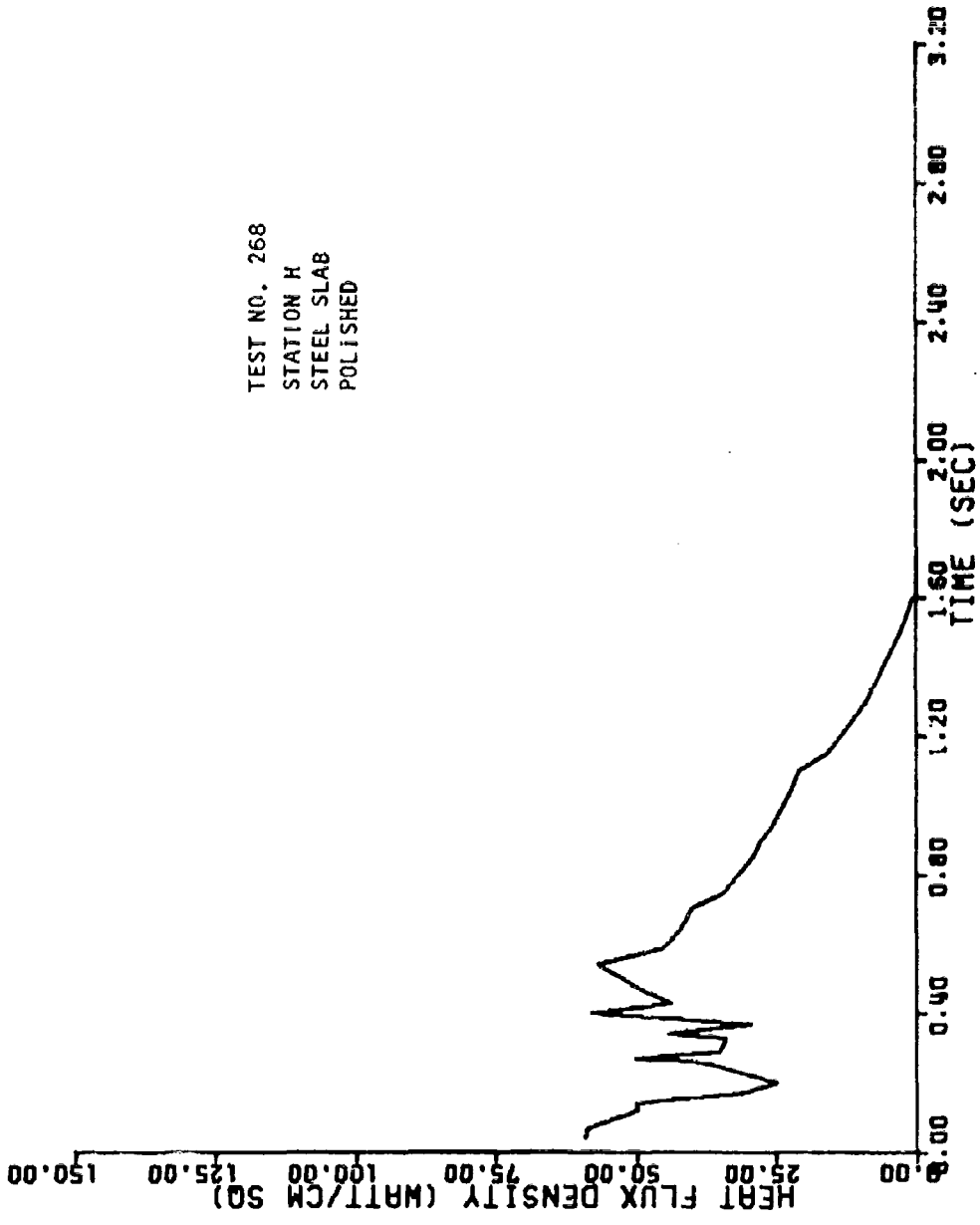

Figure B-37. Heat Flux Density at Station H for Test 268 (1000-lb LO_2/RP-1)

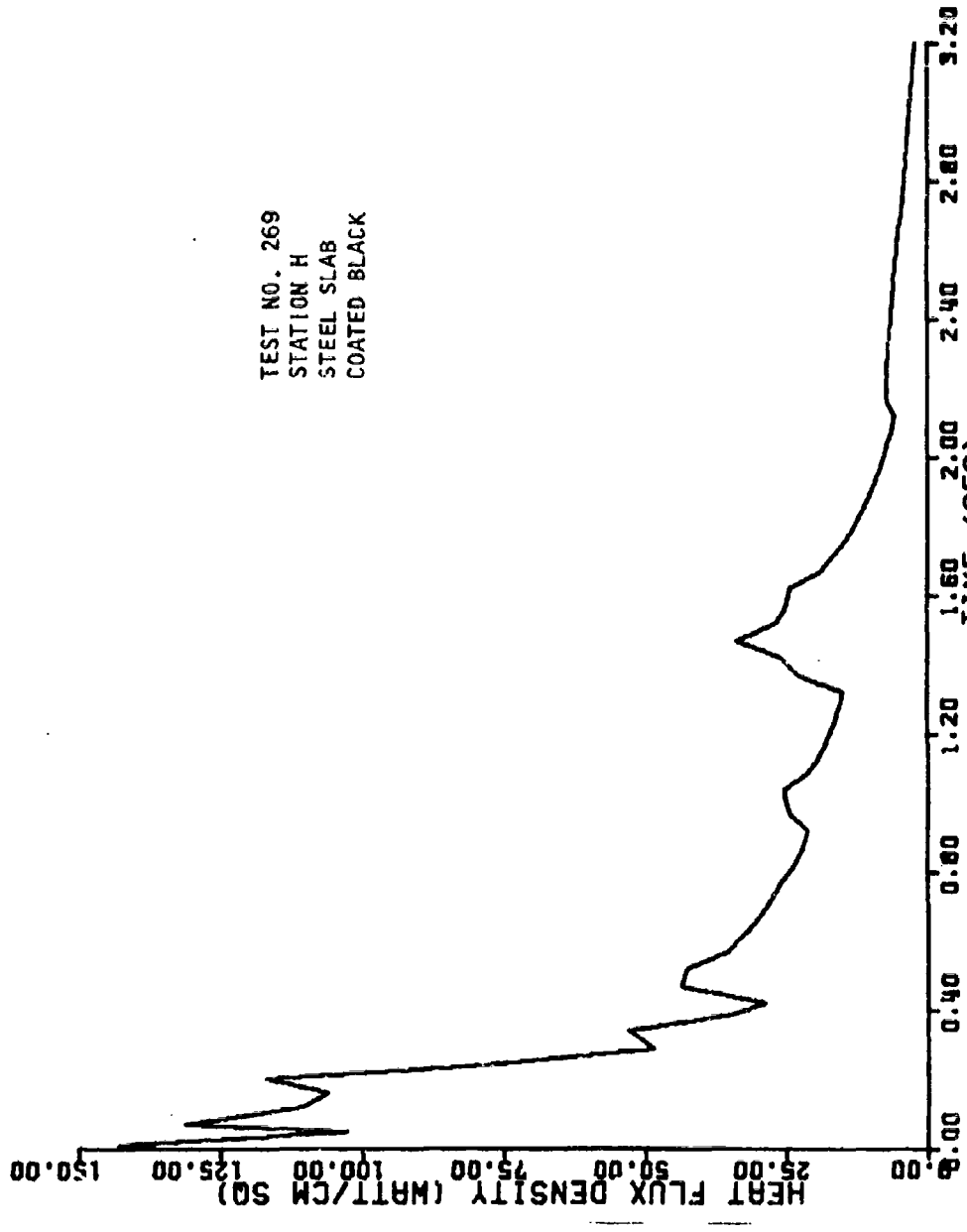

Figure B-58. Heat Flux Density at Station H for Test 269 (1000-lb LO_2/RP-1)

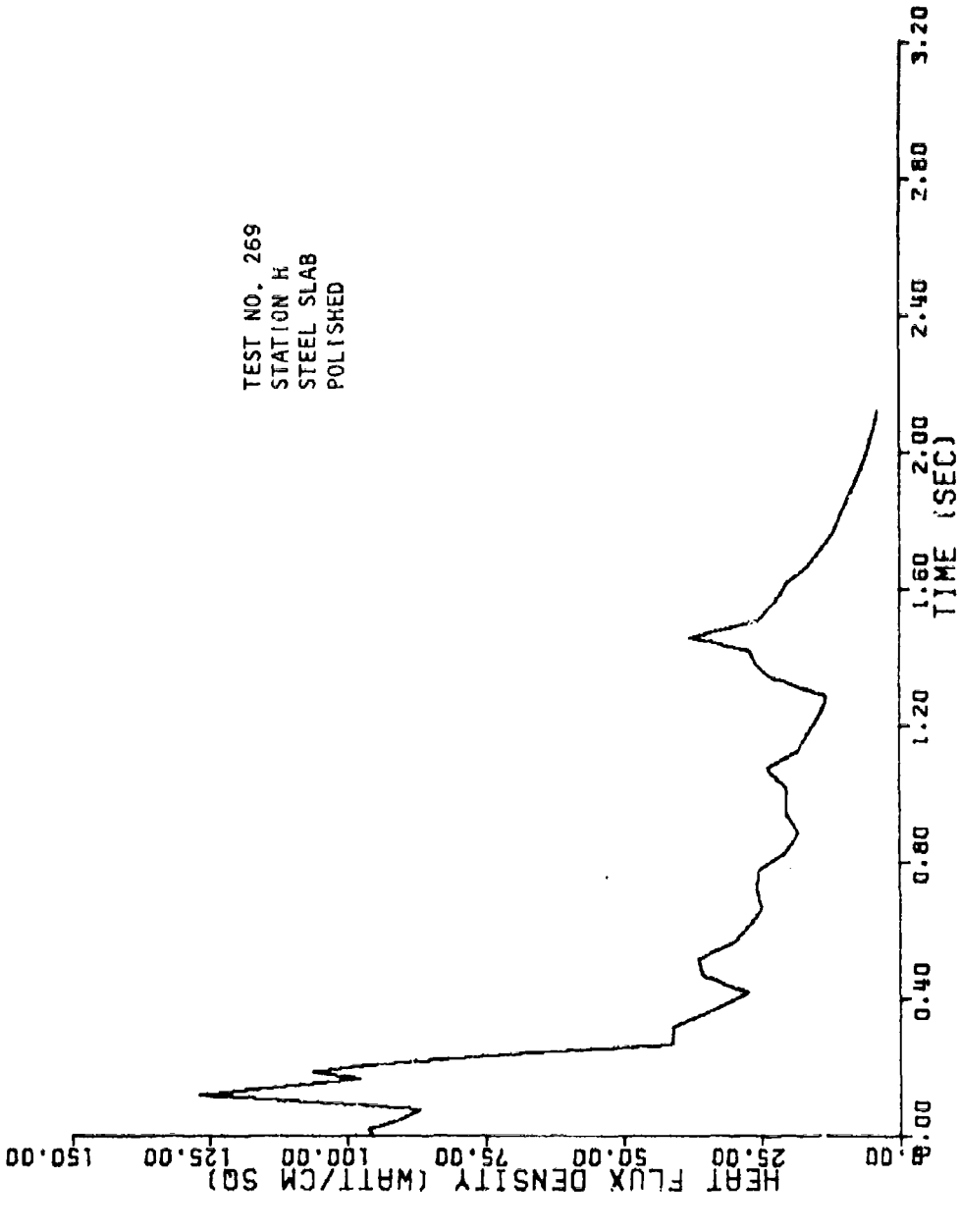

Figure B-59. Heat Flux Density at Station H for Test 269 (1000-lb LO_2/RP-1)

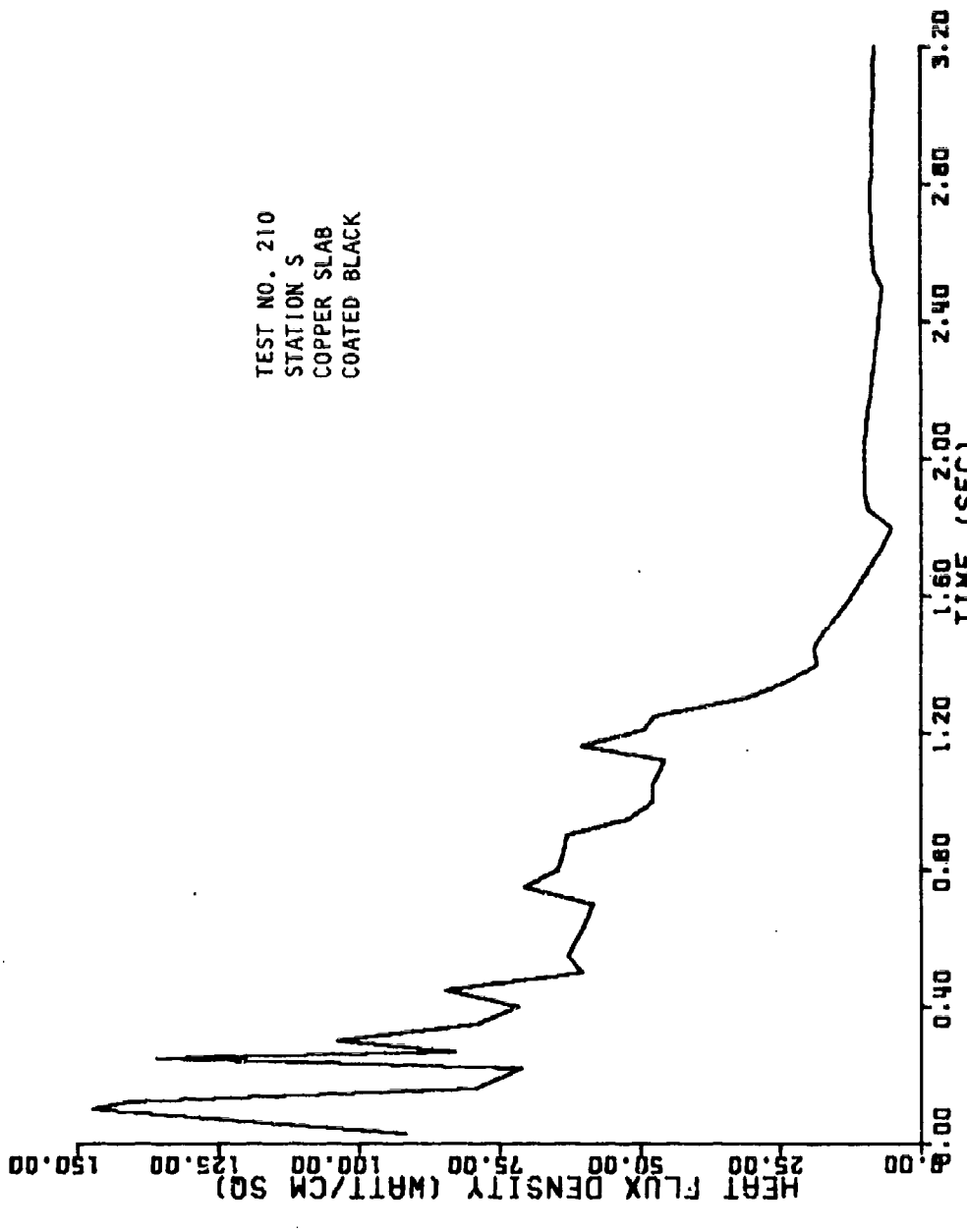

Figure B-60. Heat Flux Density at Station S for Test 210 (1000-lb LO_2/LH_2)

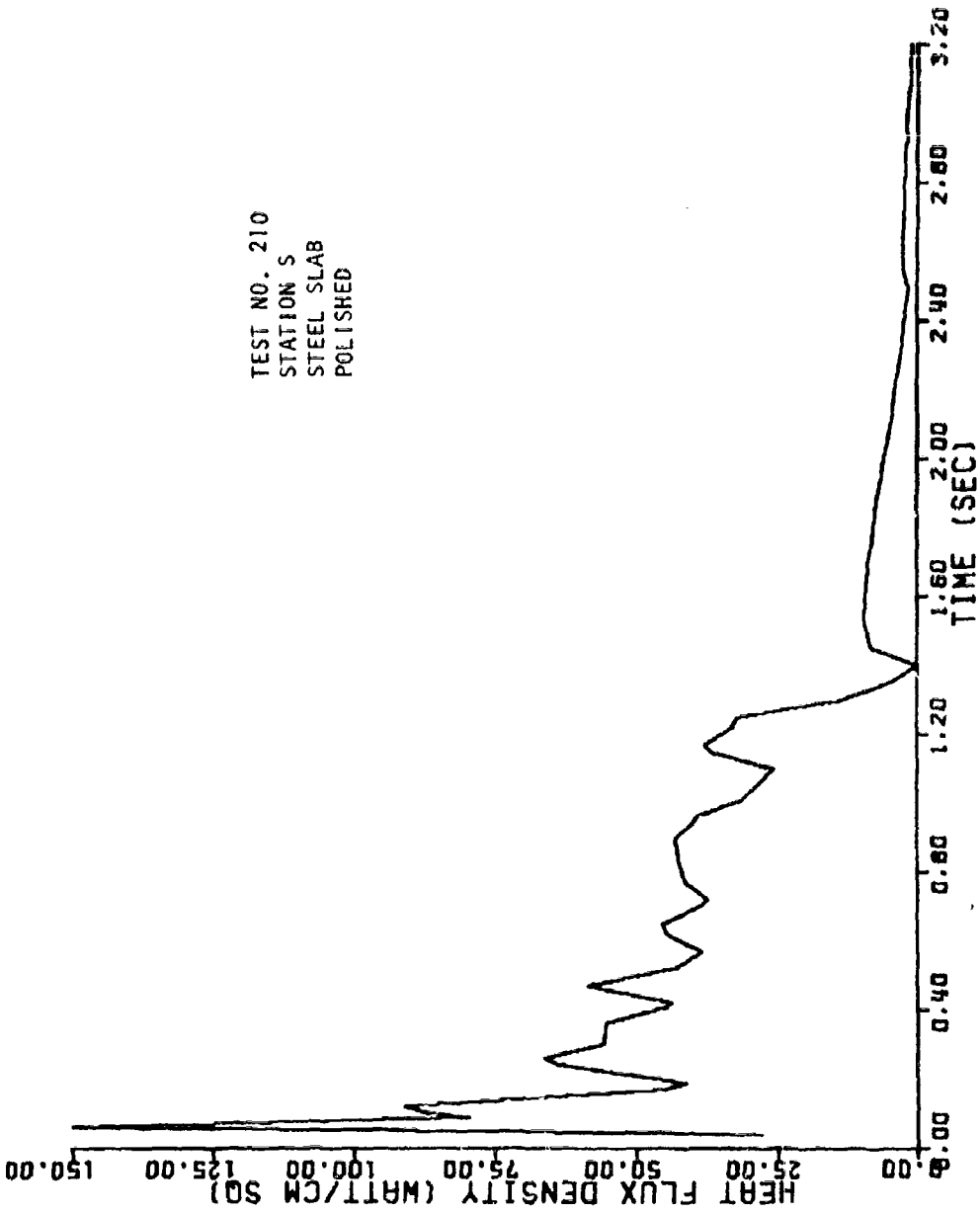

Figure B-61. Heat Flux Density at Station S for Test 210 (1000-lb LO_2/LH_2)

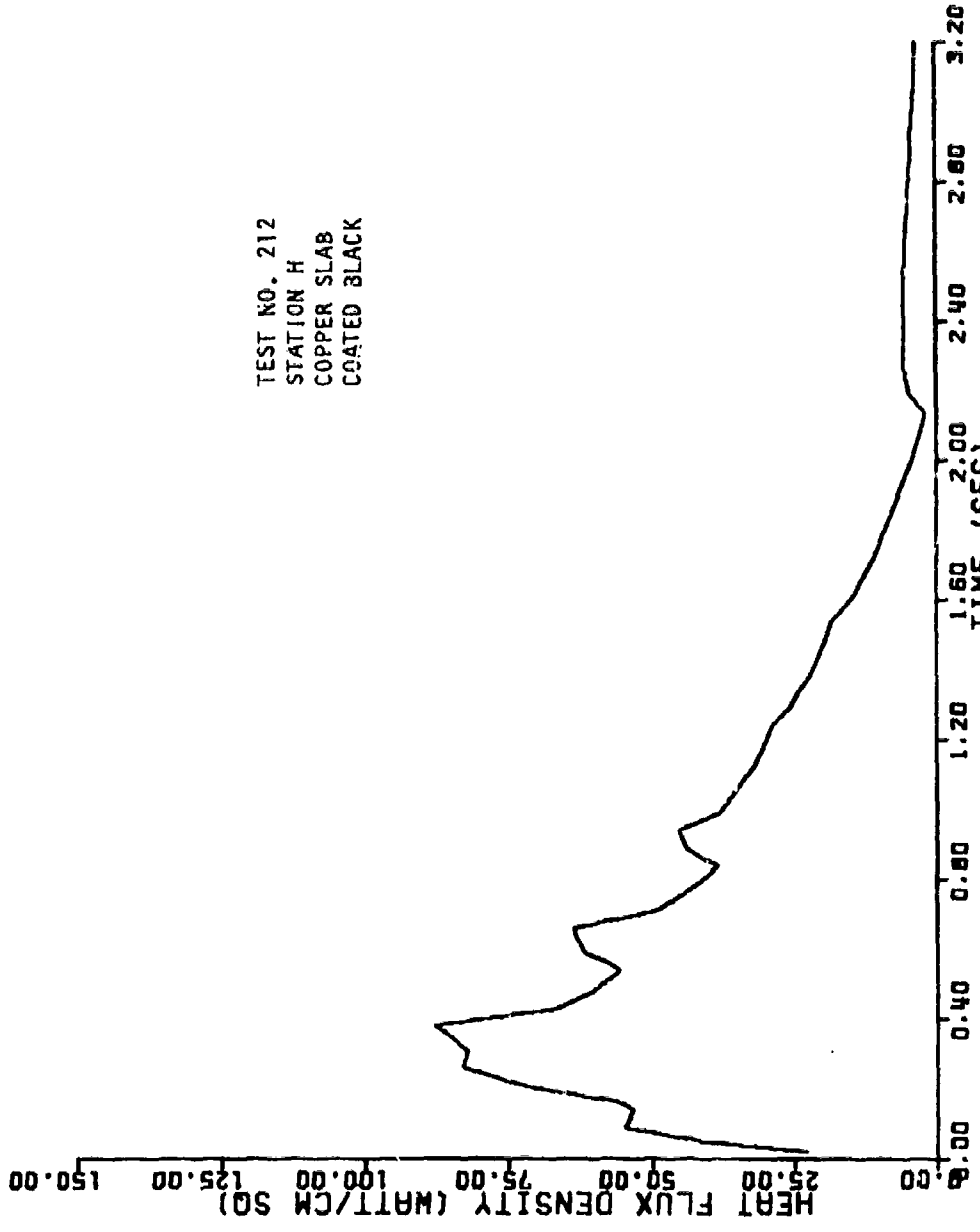

Figure B-62. Heat Flux Density at Station H for Test 212 (1000-lb LO_2/LH_2)

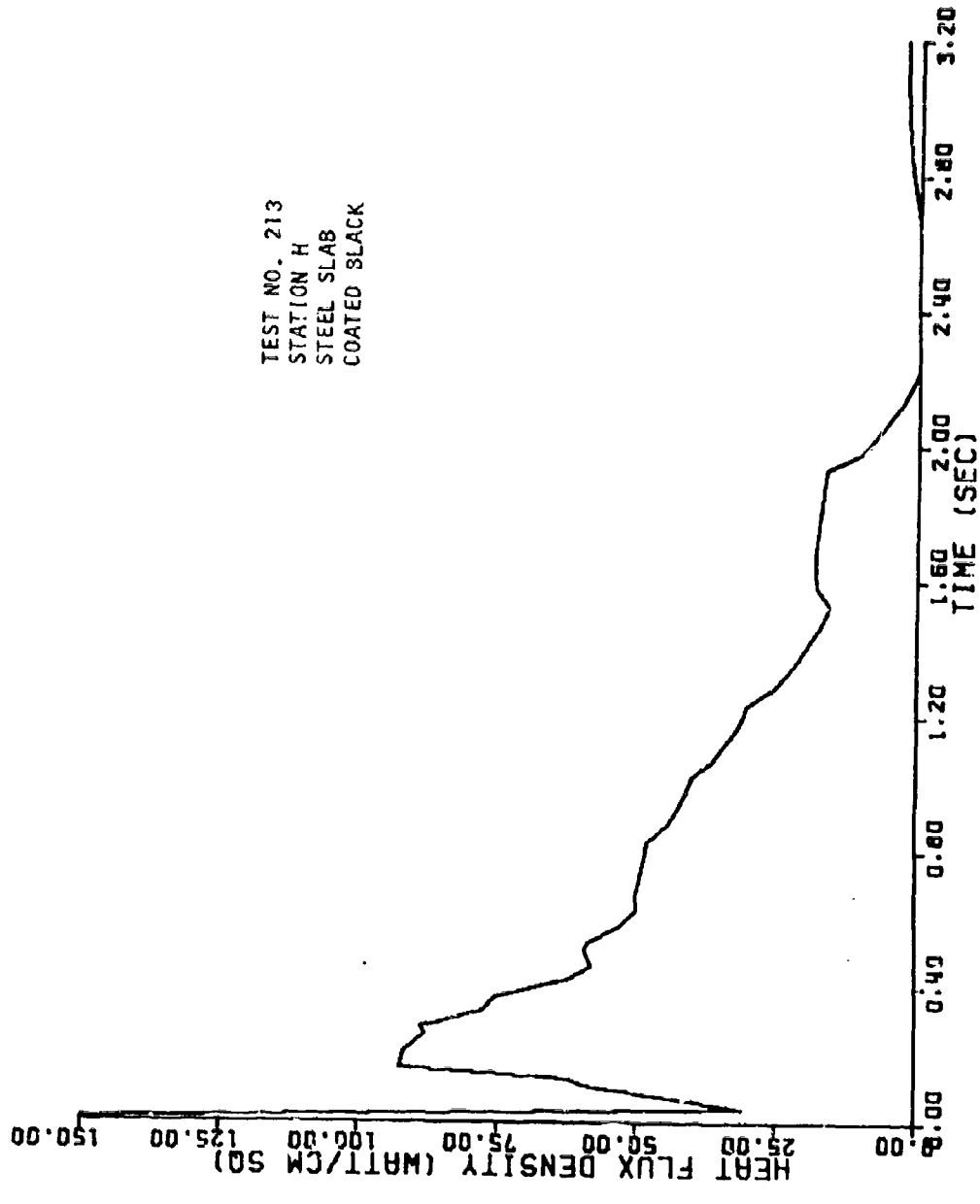

Figure B-63. Heat Flux Density at Station H for Test 213 (1000-lb LO_2/LH_2)

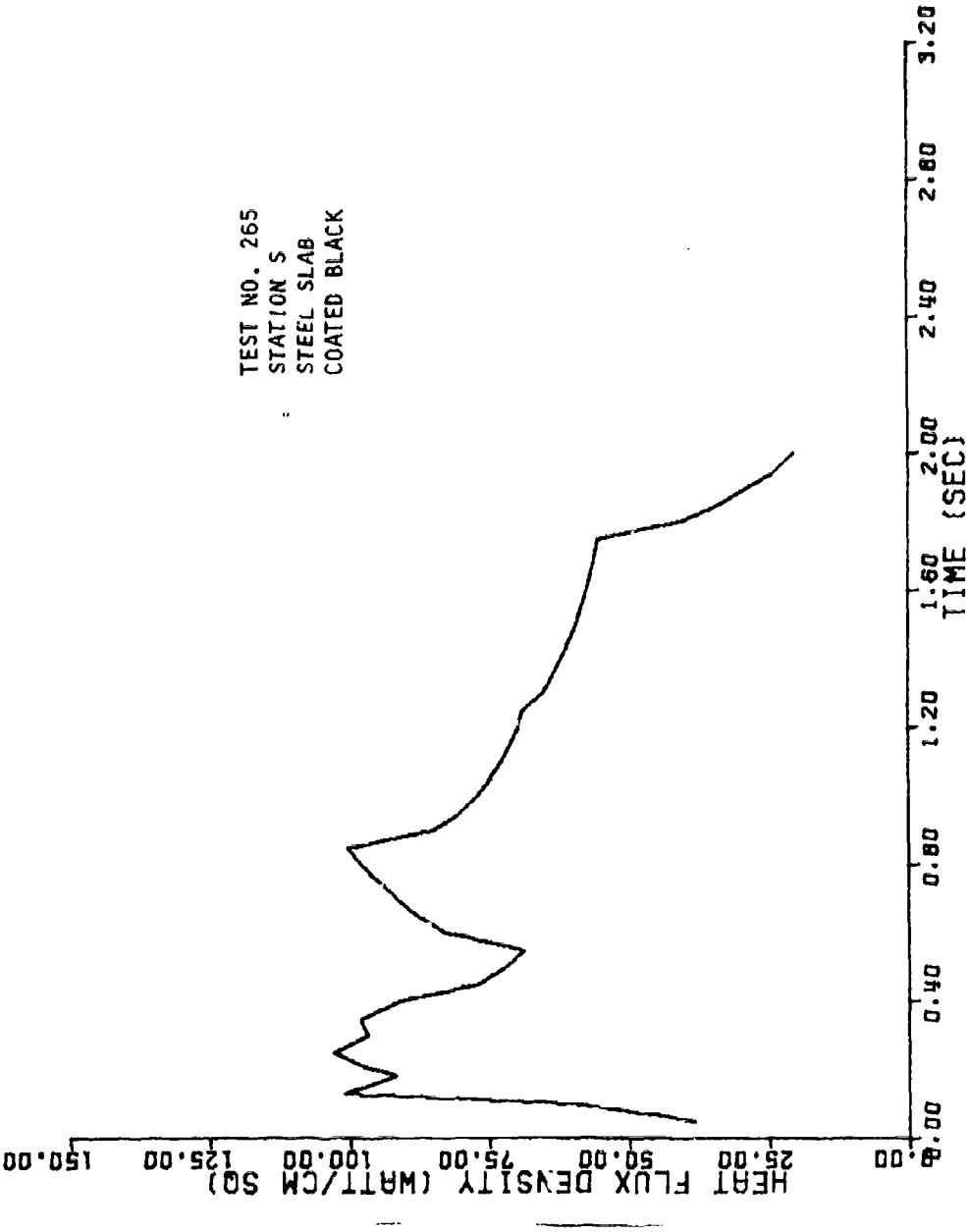

Figure B-64. Heat Flux Density at Station S for Test 265 (1000-lb LO_2/LH_2)

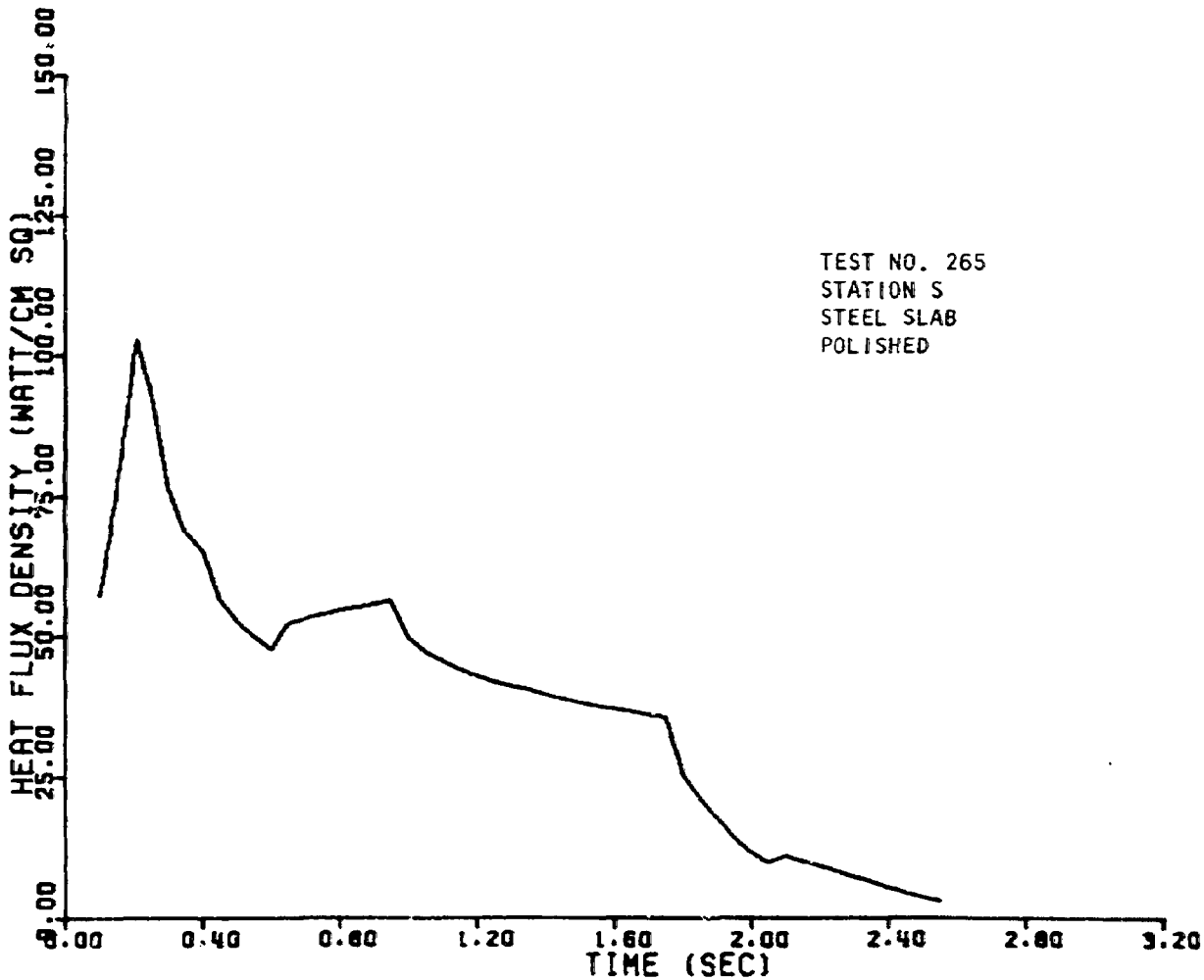

Figure B-65. Heat Flux Density at Station S for Test 265 (1000-lb LO_2/LH_2)

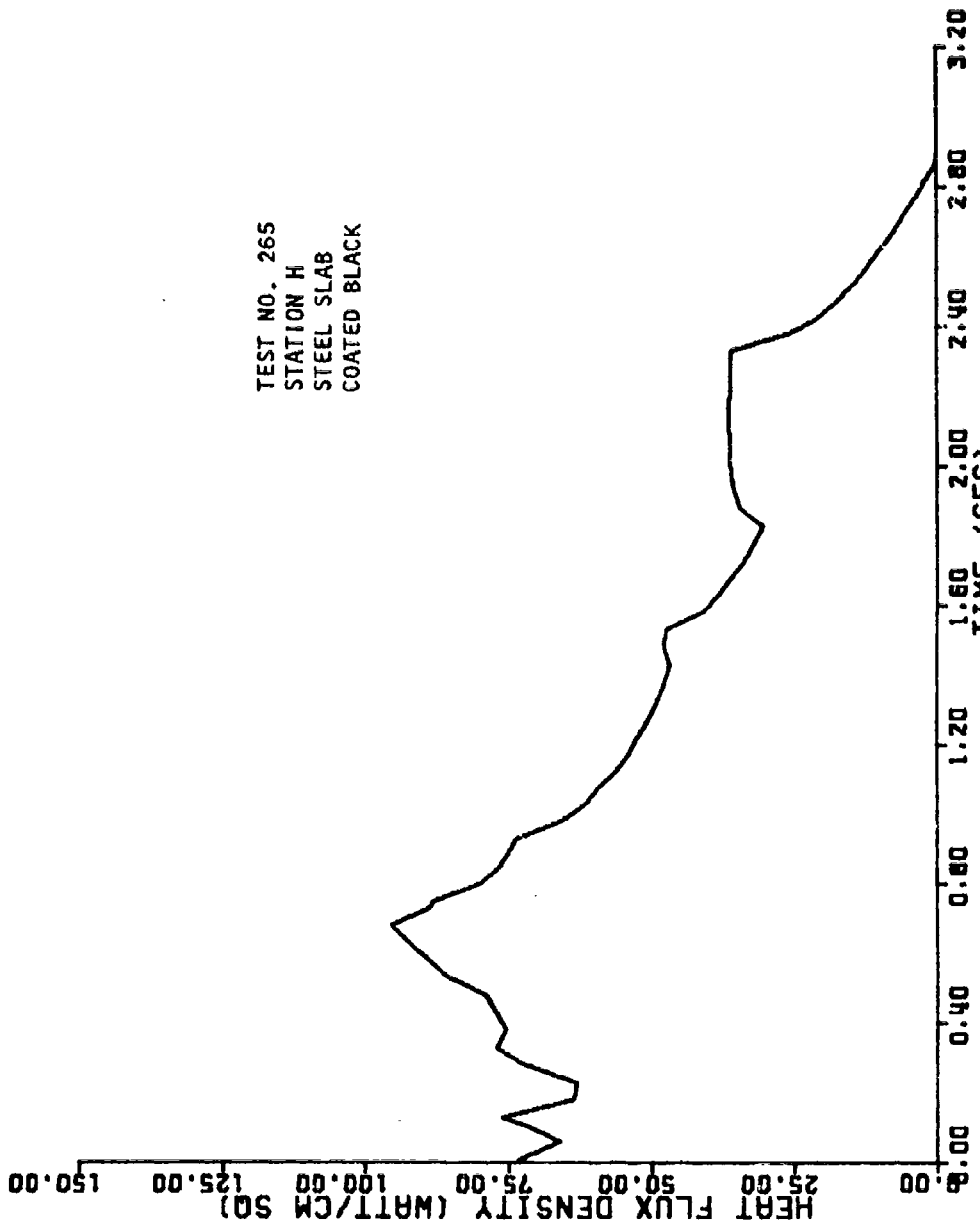

Figure B-66. Heat Flux Density at Station H for Test 265 (1000-lb LO_2/LH_2)

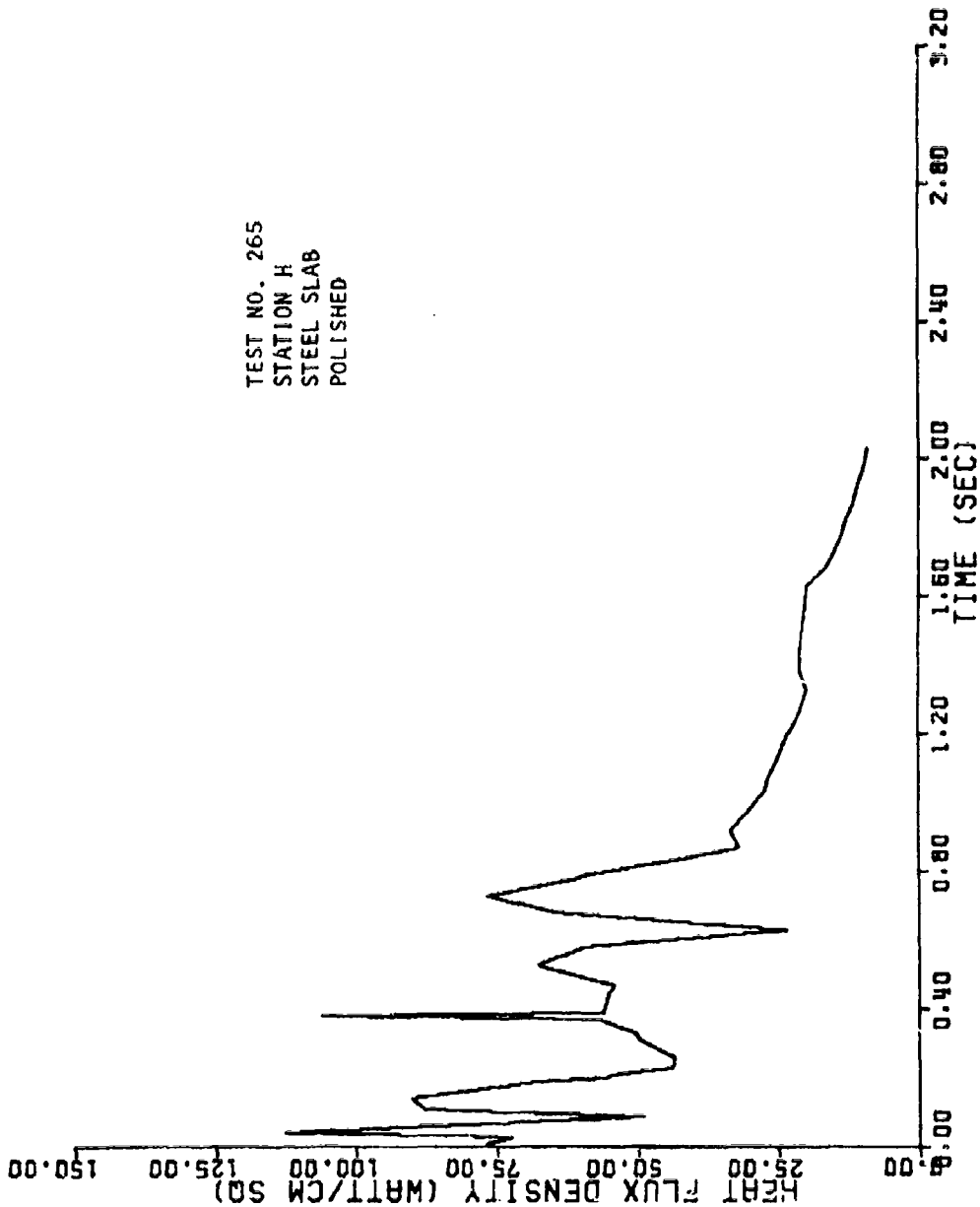

Figure B-67. Heat Flux Density at Station H for Test 265 (1000-lb LO_2/LH_2)

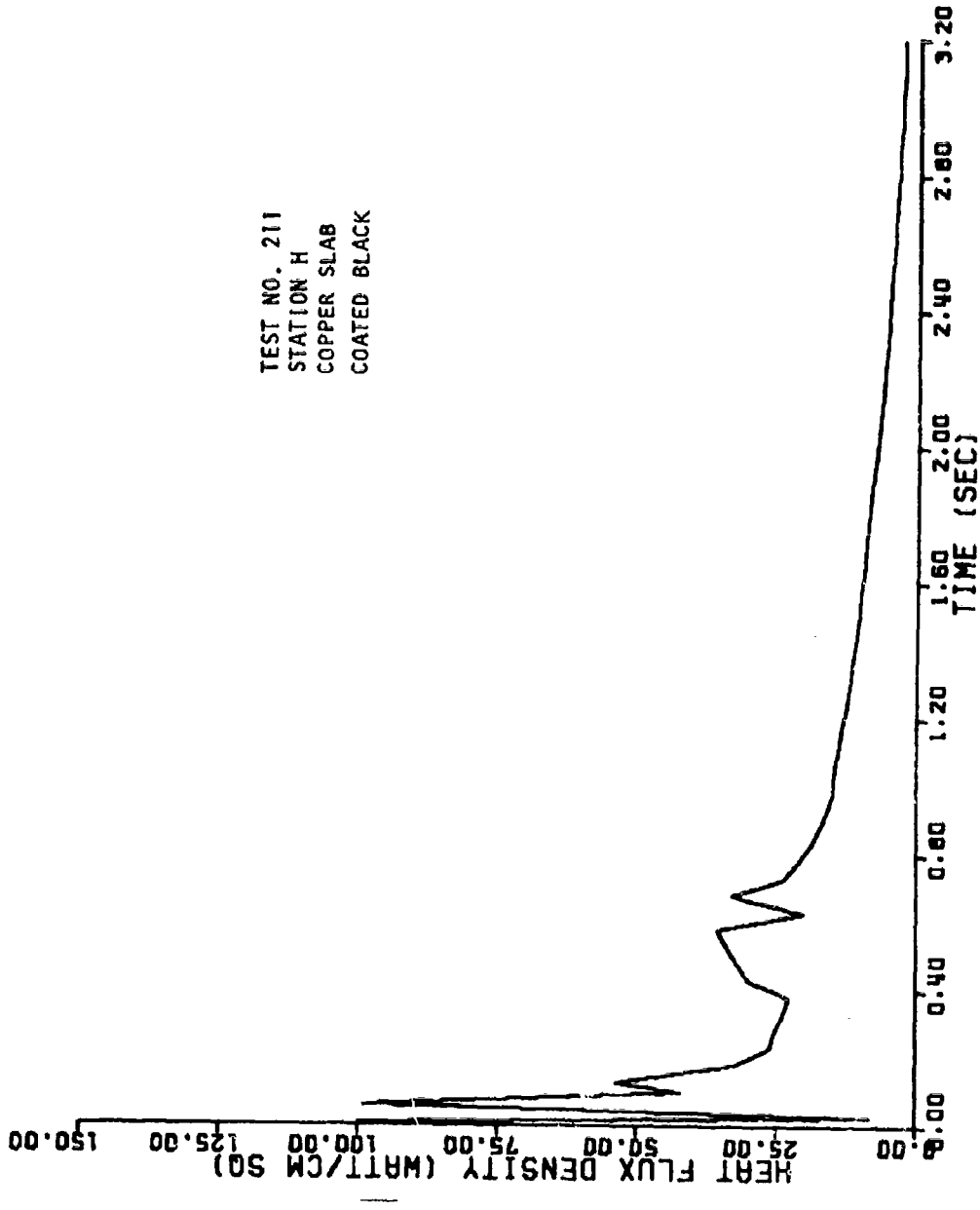

Figure B-68. Heat Flux Density at Station H for Test 211 (1000-lb LO_2/LH_2)

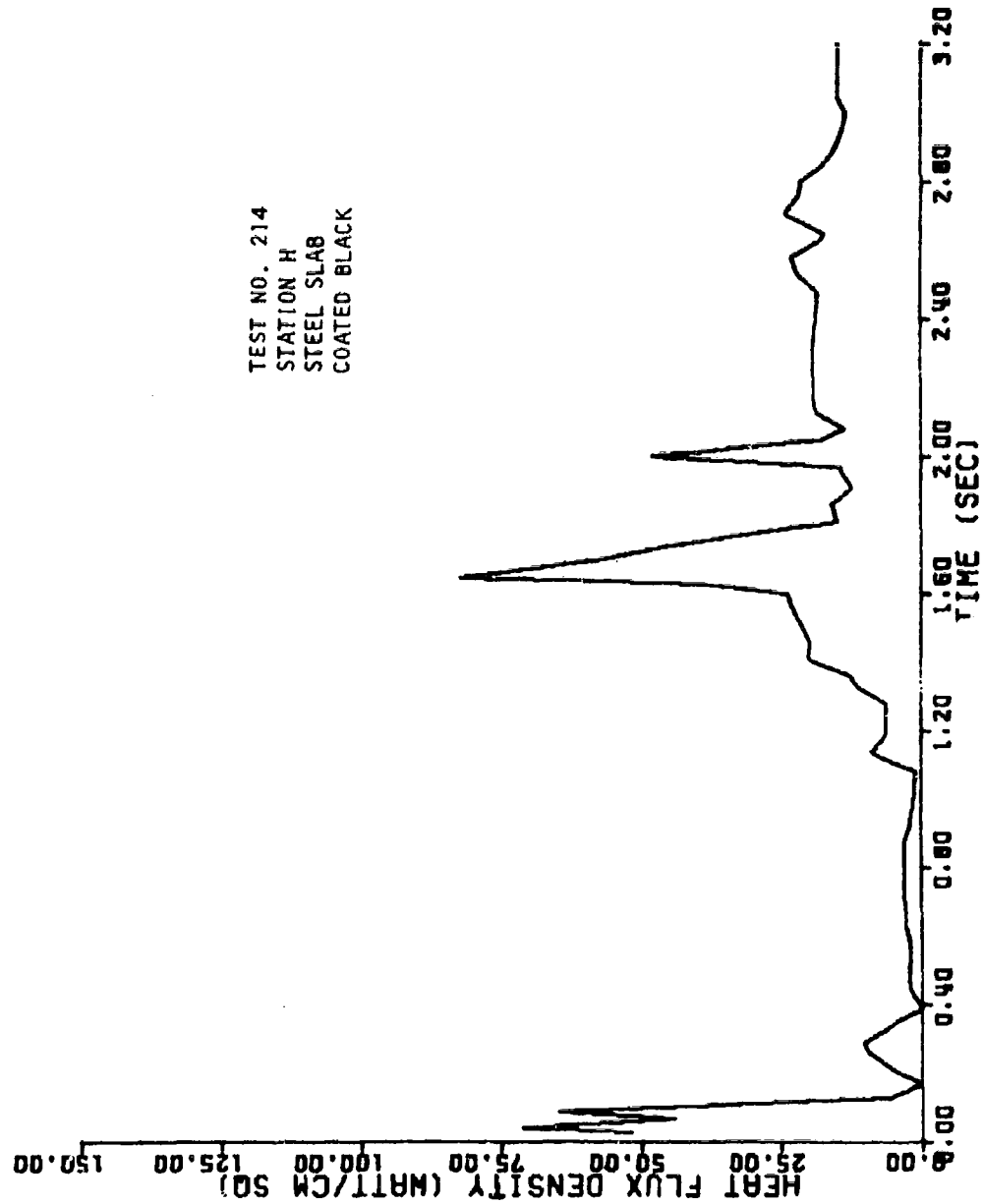

Figure B-69. Heat Flux Density at Station H for Test 214 (1000-lb LO_2/LH_2)

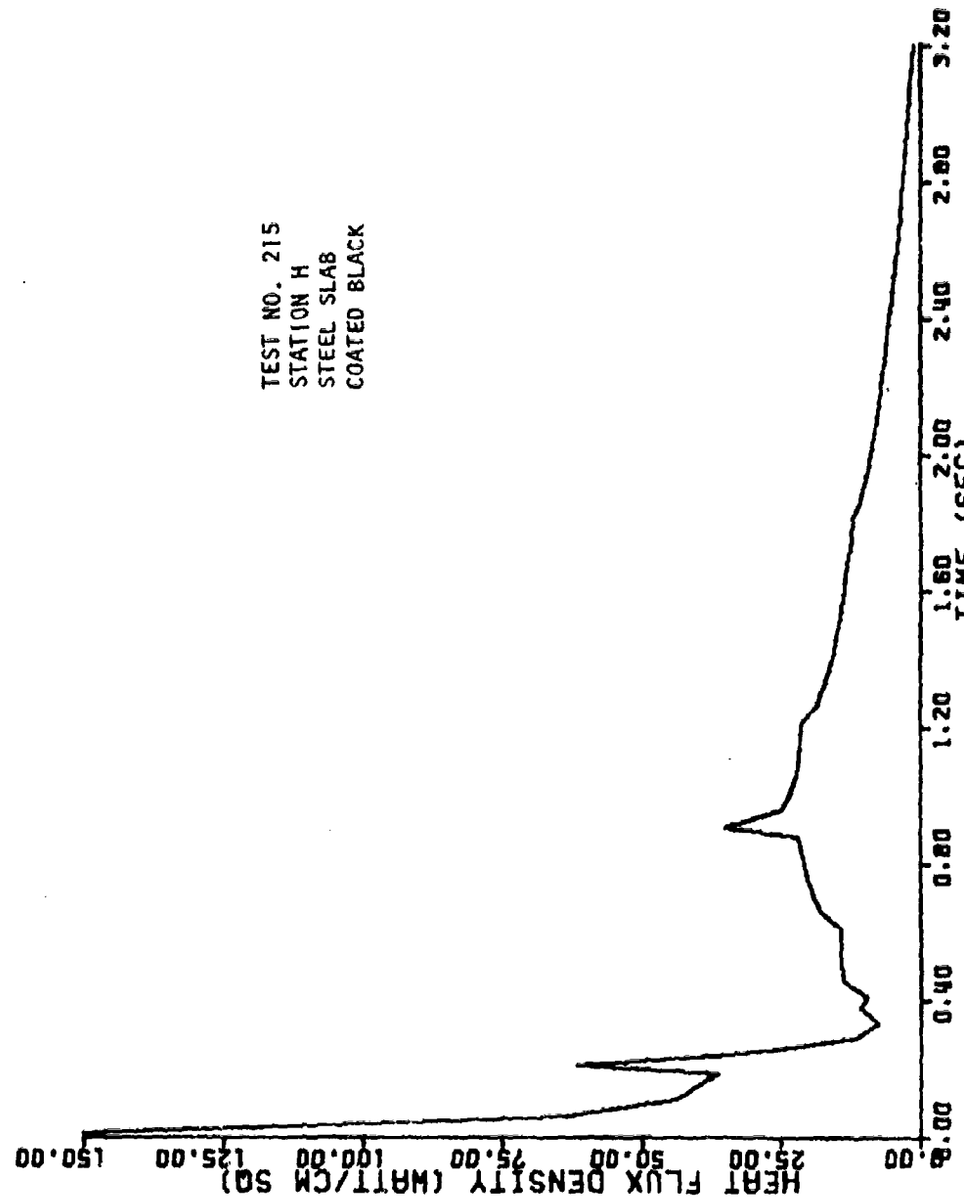

Figure B-70. Heat Flux Density at Station H for Test 215 (1000-lb LO_2/LH_2)

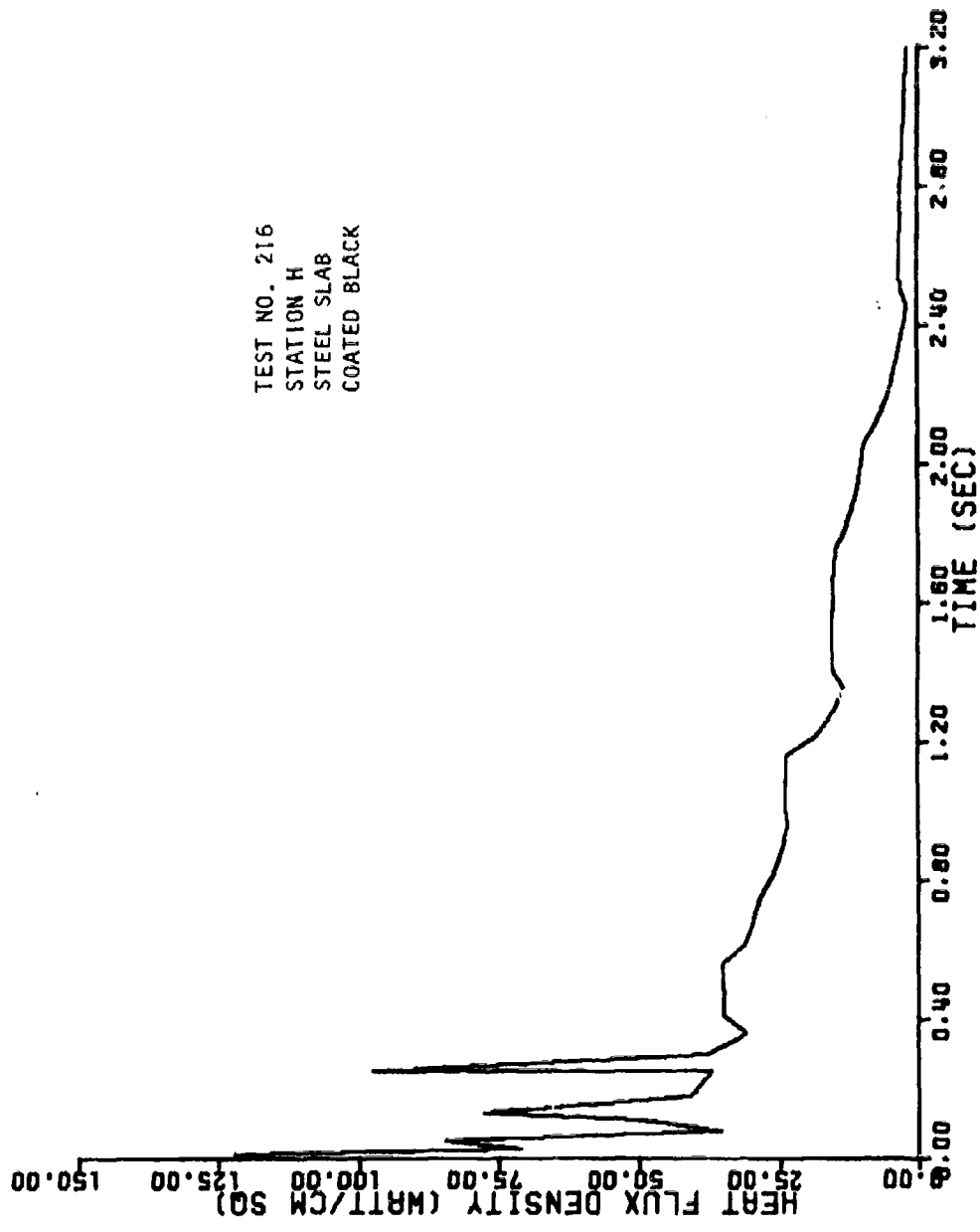

Figure B-71. Heat Flux Density at Station H for Test 216 (1000-lb LO_2/LH_2)

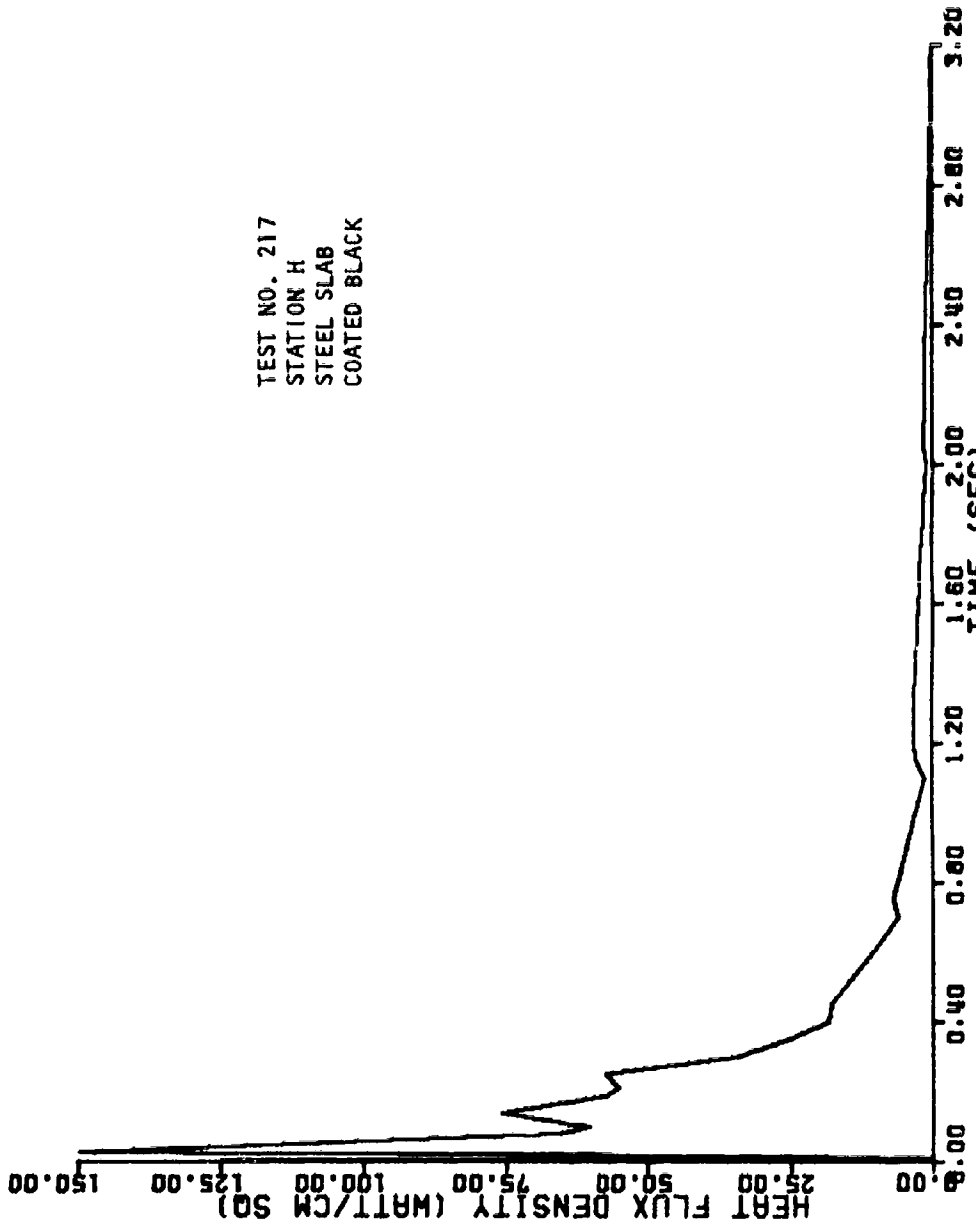

Figure B-72. Heat Flux Density at Station H for Test 217 (1000-lb LO_2/LH_2)

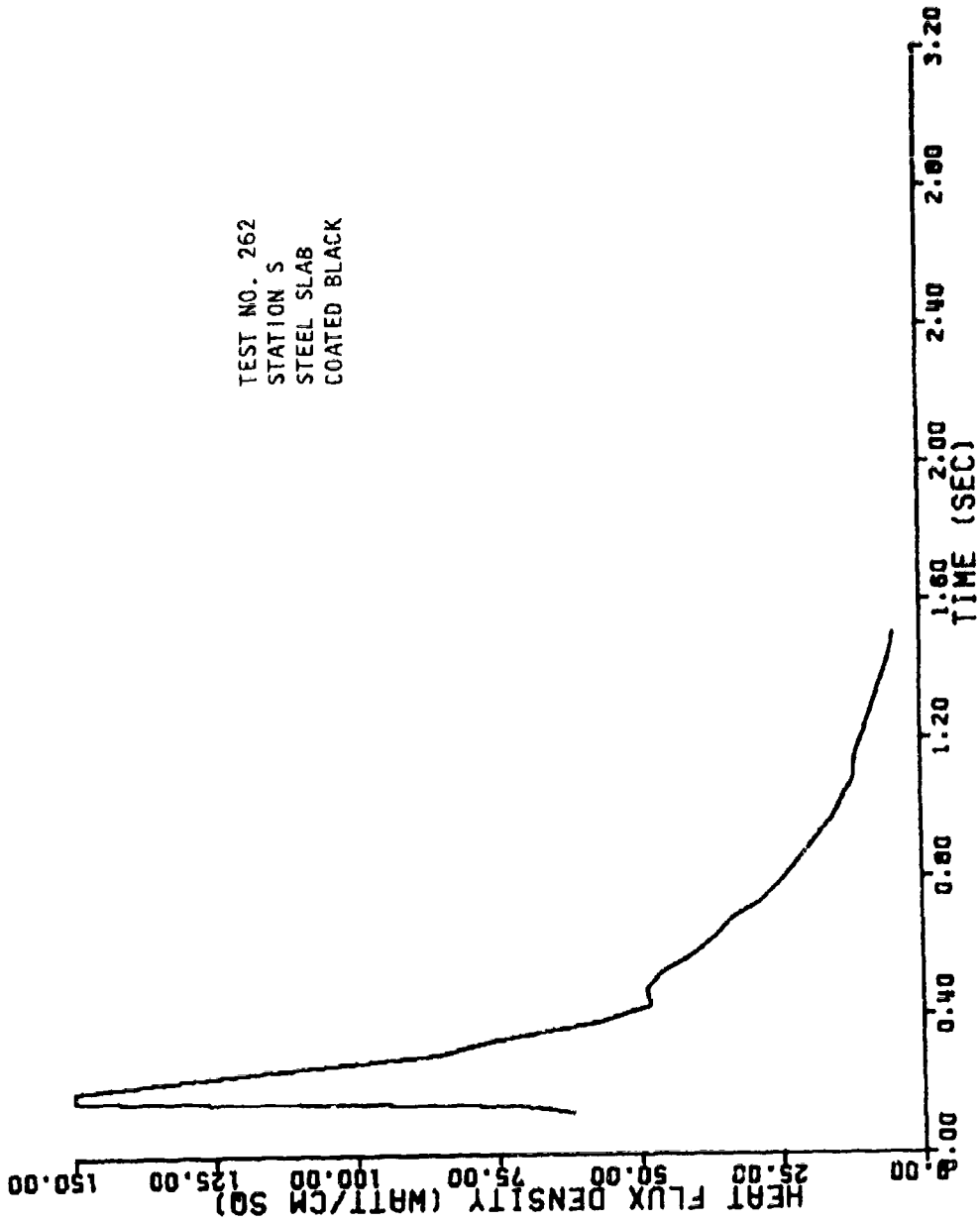

Figure B-73. Heat Flux Density at Station S for Test 262 (1000-lb LO_2/LH_2)

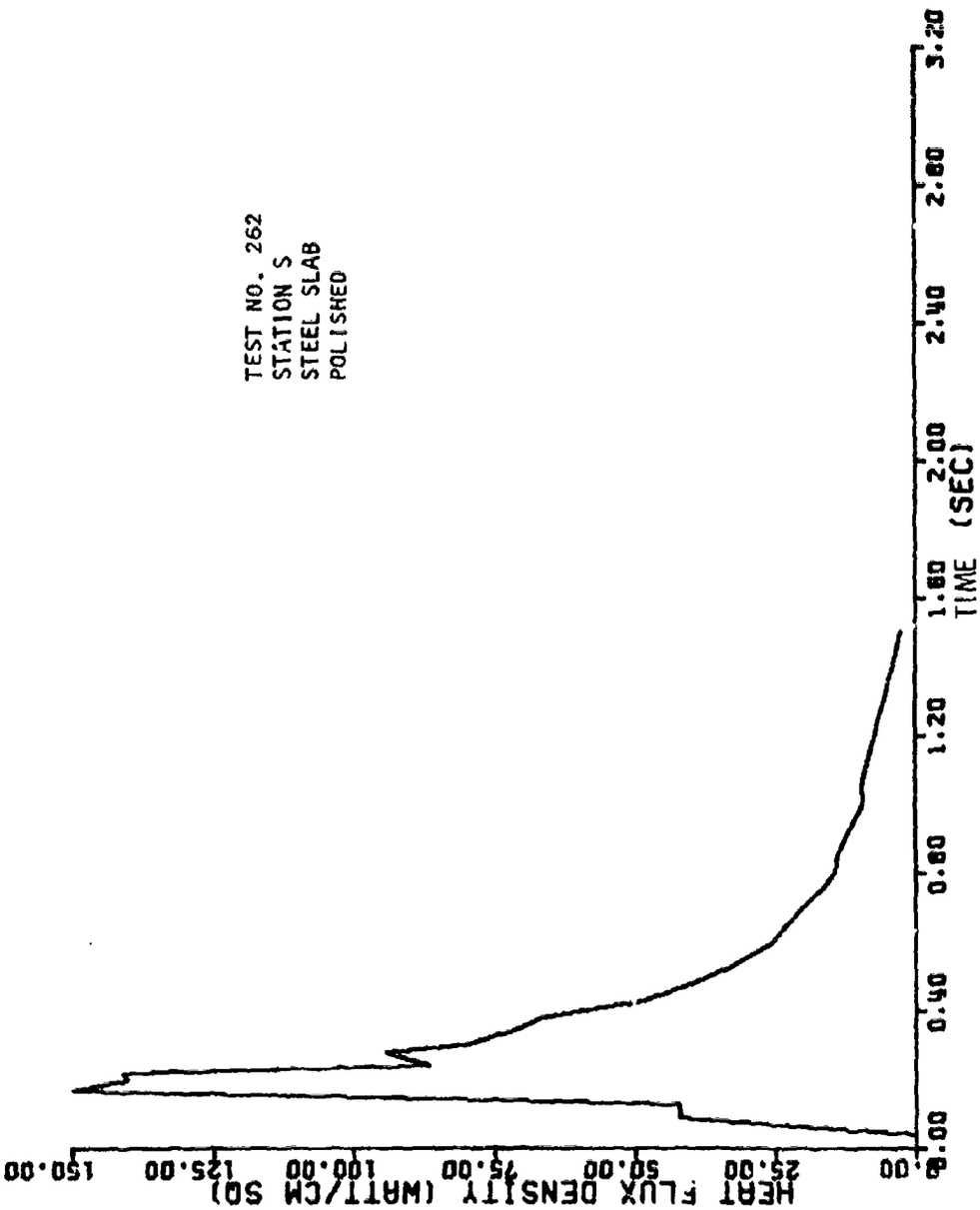

Figure B-74. Heat Flux Density at Station S for Test 262 (1000-lb LO_2/LH_2)

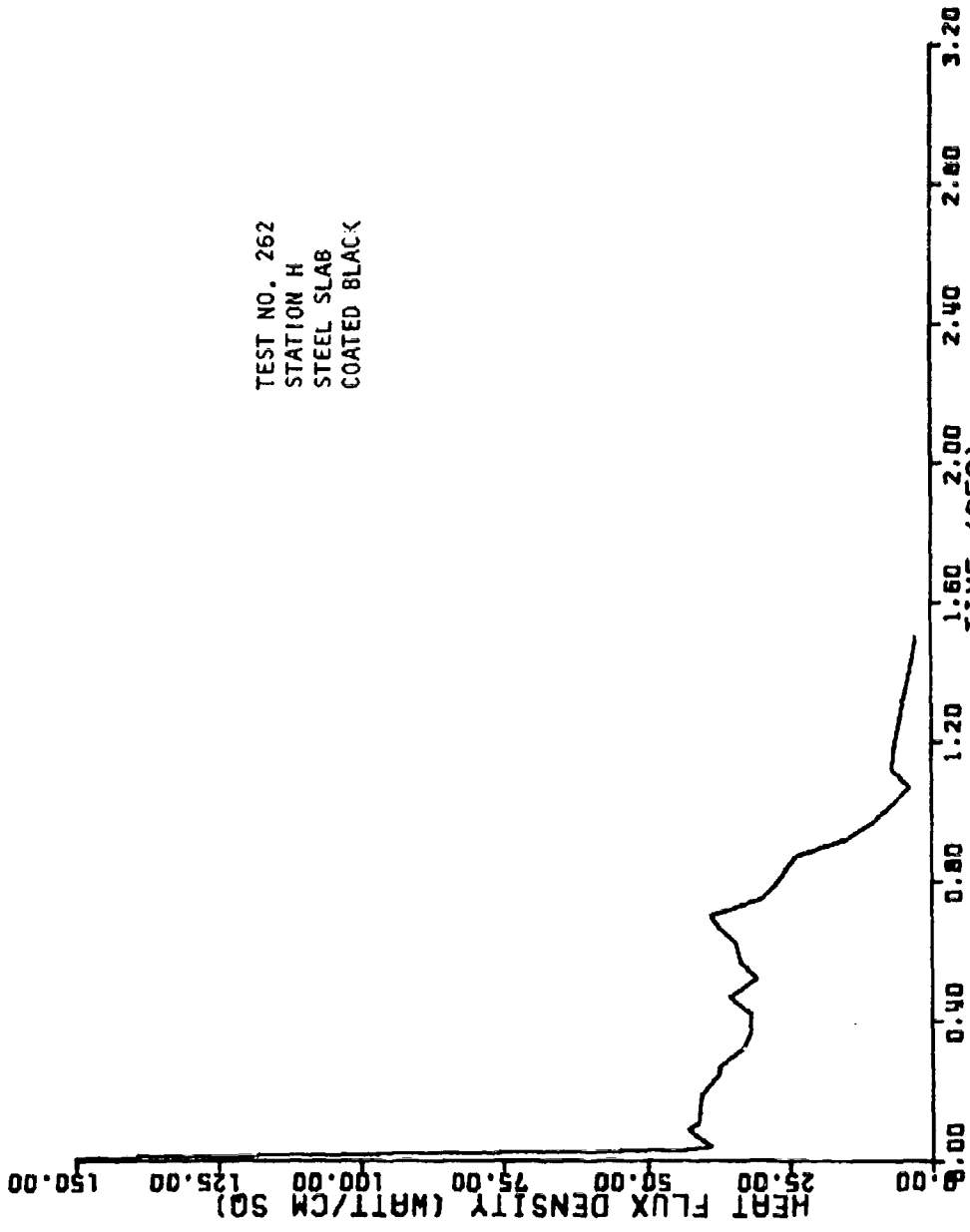

Figure B-75. Heat Flux Density at Station H for Test 262 (1000-lb LO_2/LH_2)

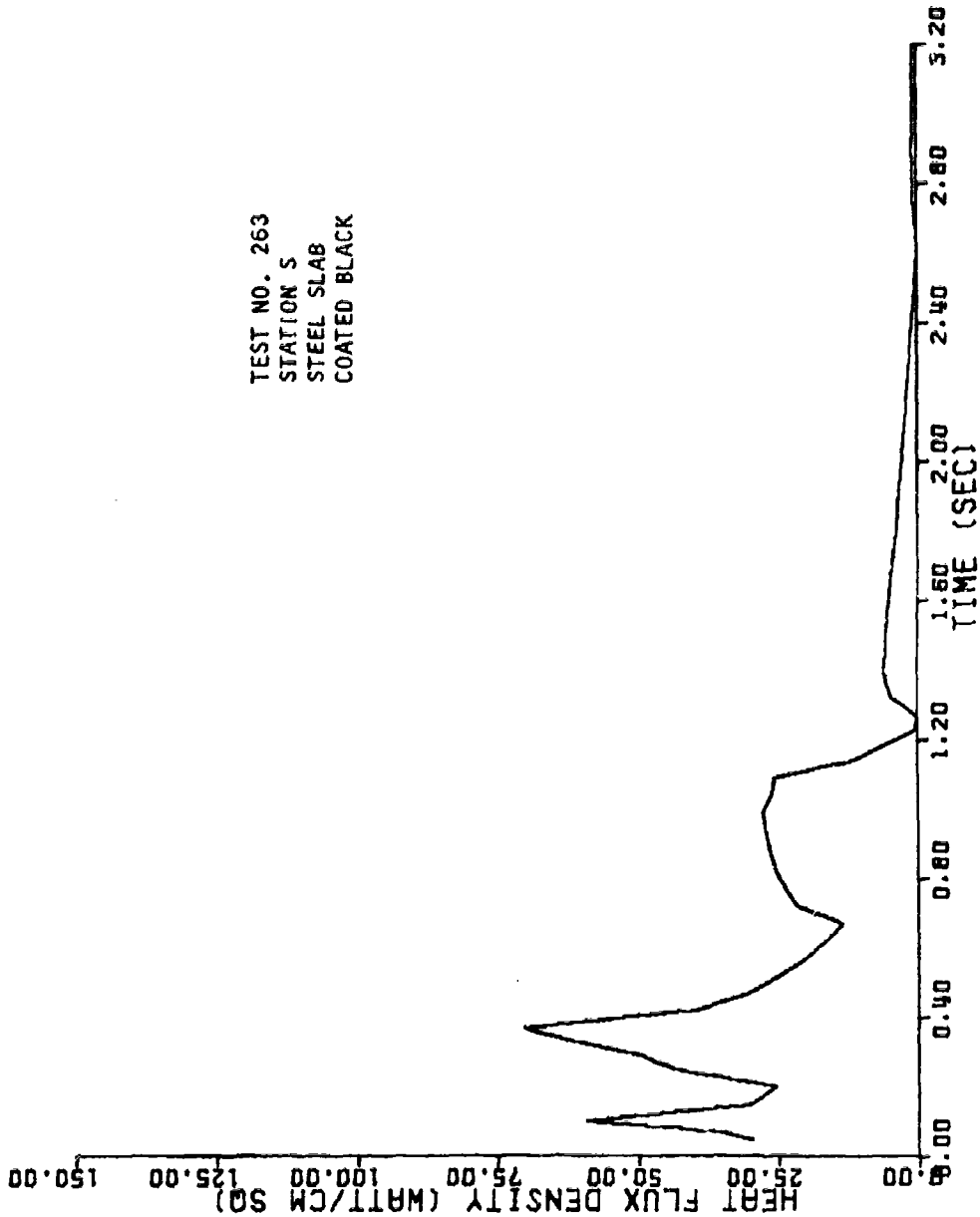

Figure B-76. Heat Flux Density at Station S for Test 263 (1000-lb LO_2/LH_2)

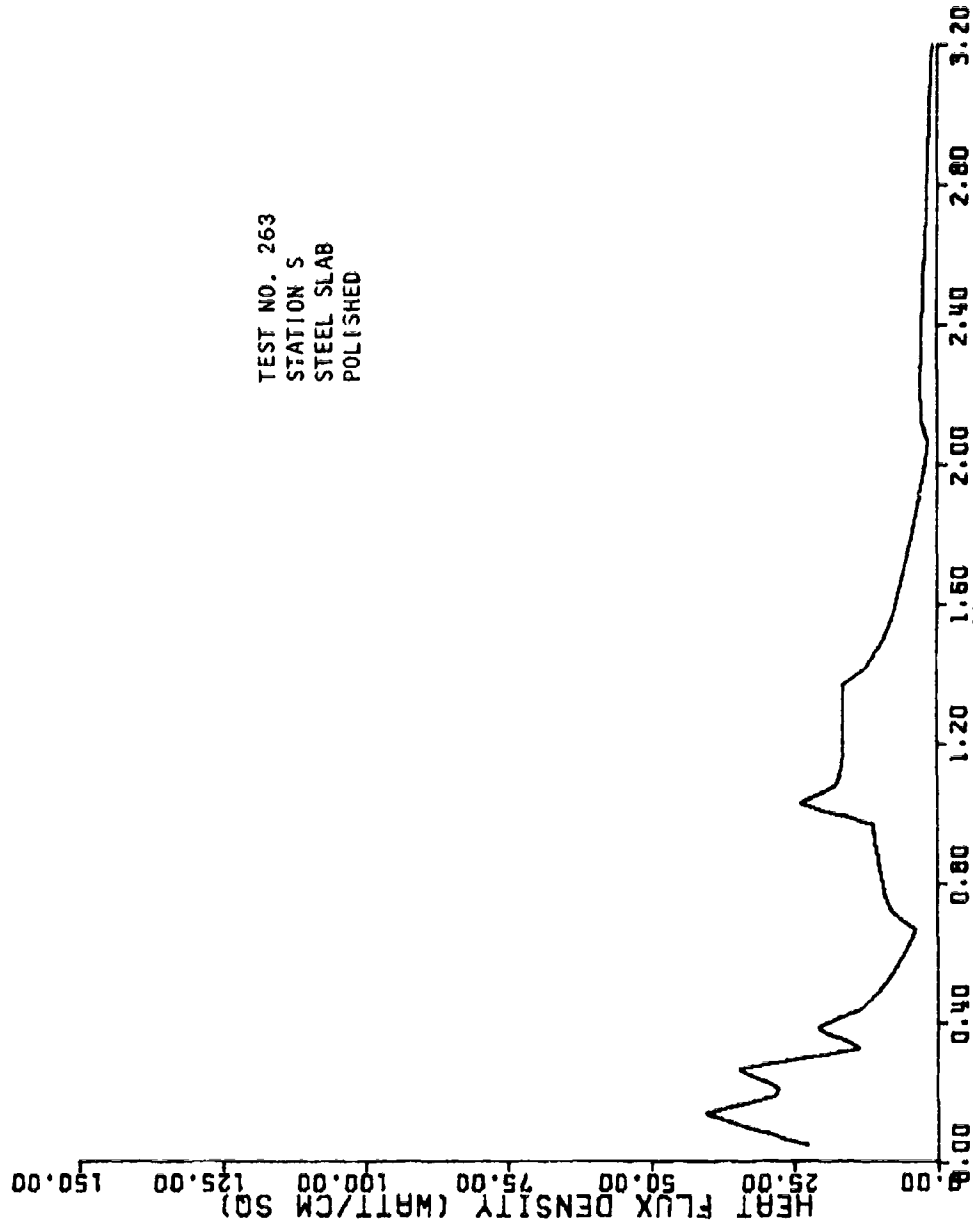

Figure B-77. Heat Flux Density at Station S for Test 263 (1000-lb LO_2/LH_2)

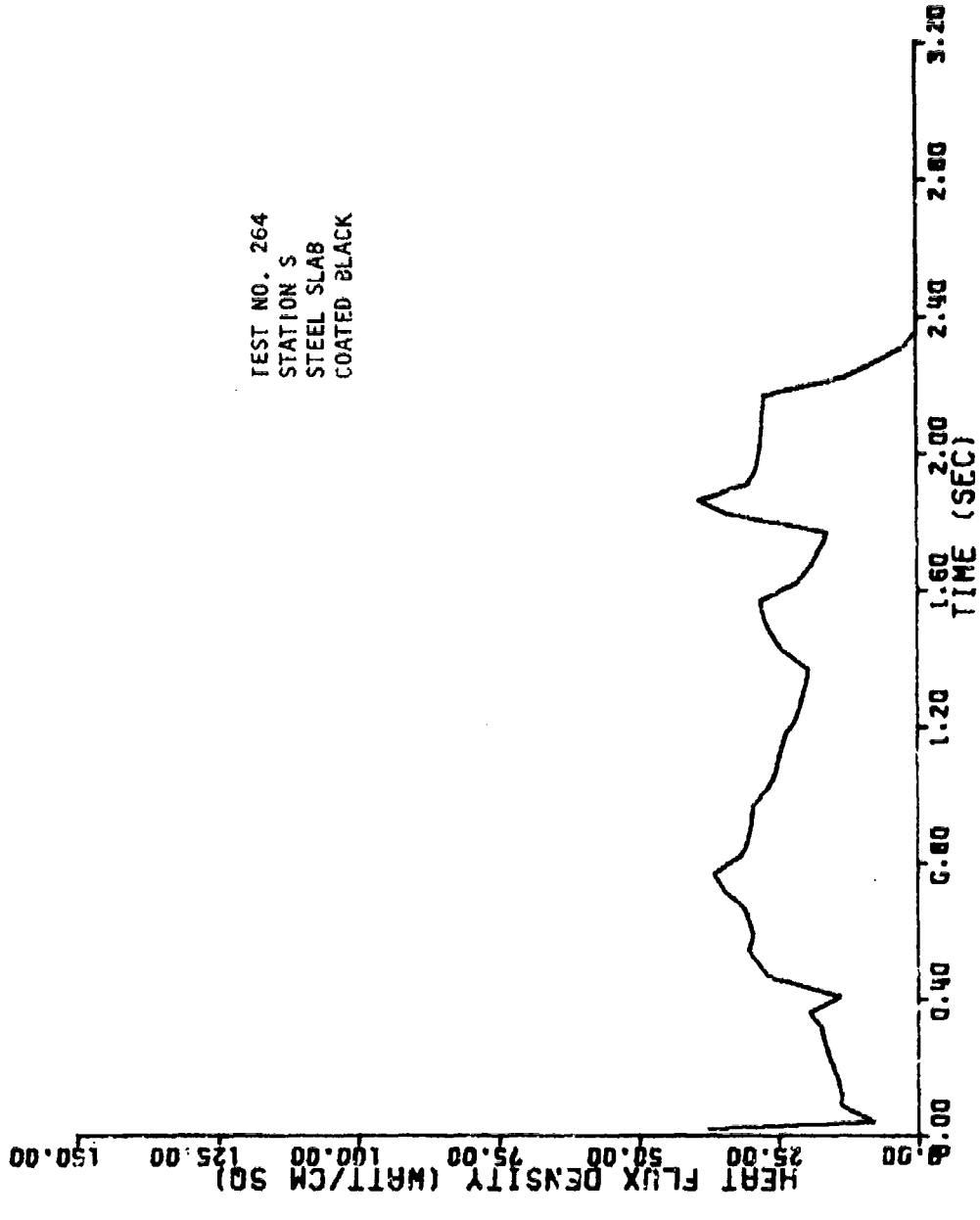

Figure B-78. Heat Flux Density at Station S for Test 264 (1000-lb LO_2/LH_2)

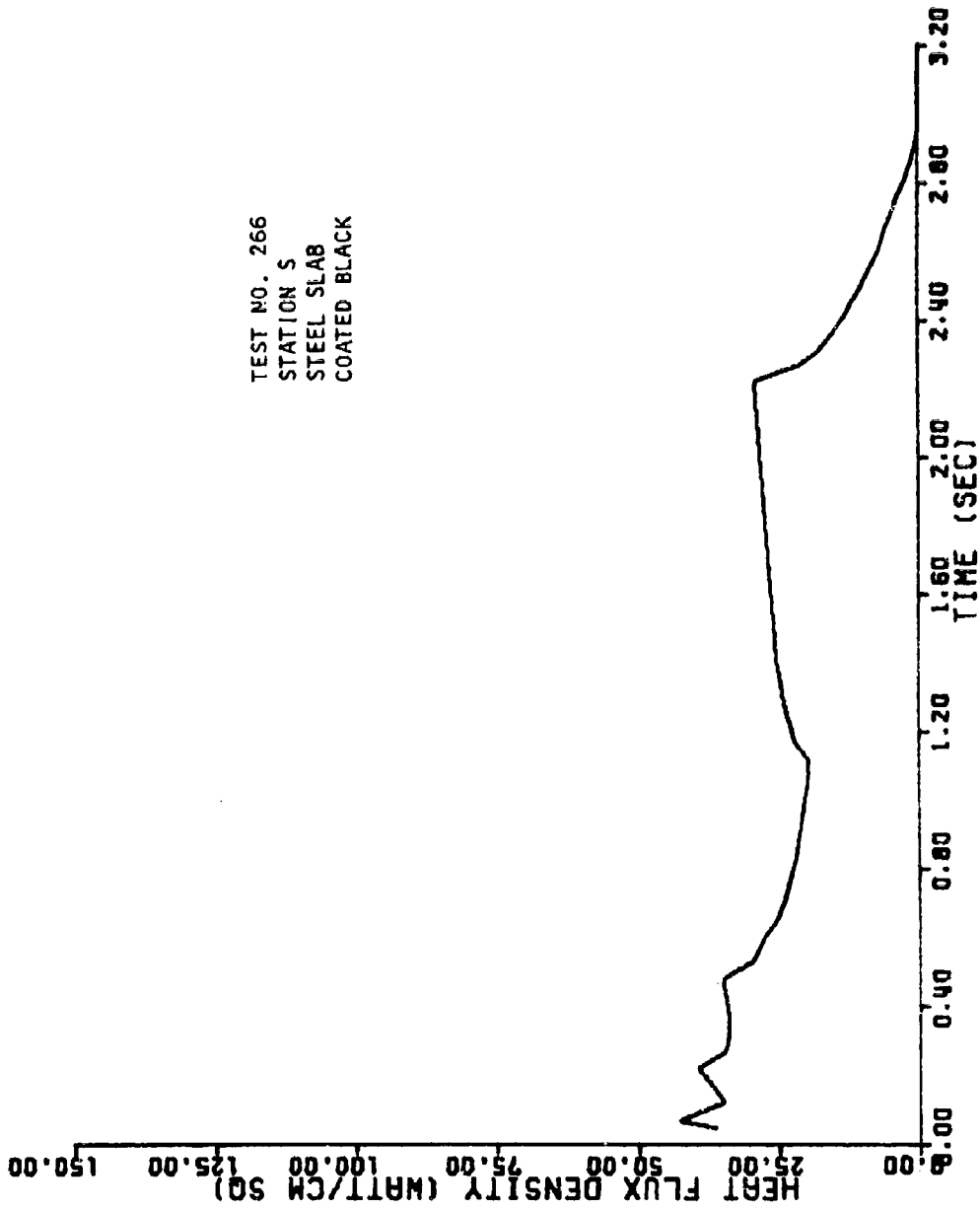

Figure B-79. Heat Flux Density at Station S for Test 266 (1000-lb LO_2/LH_2)

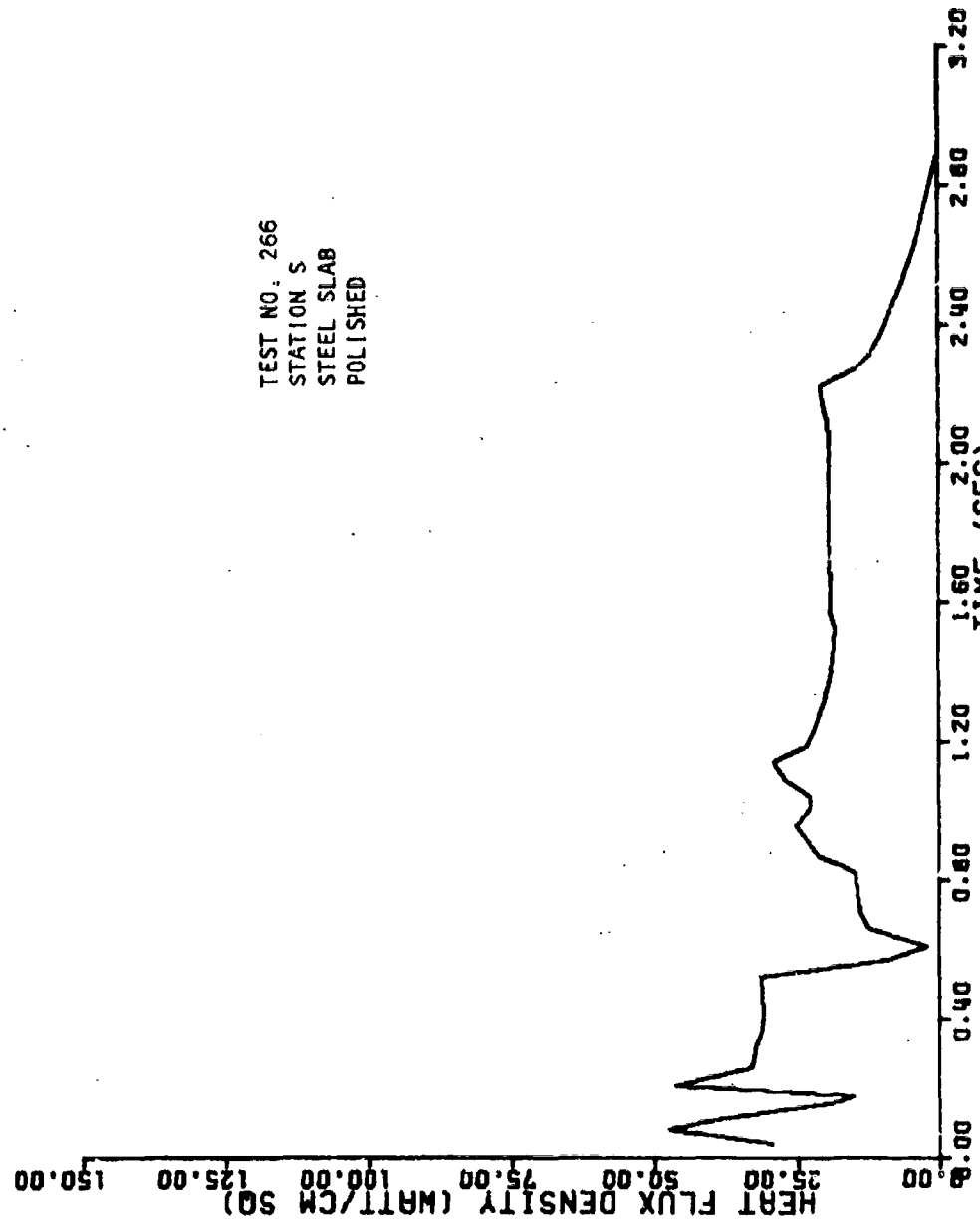

Figure B-80. Heat Flux Density at Station S for Test 266 (1000-lb LO_2/LH_2)

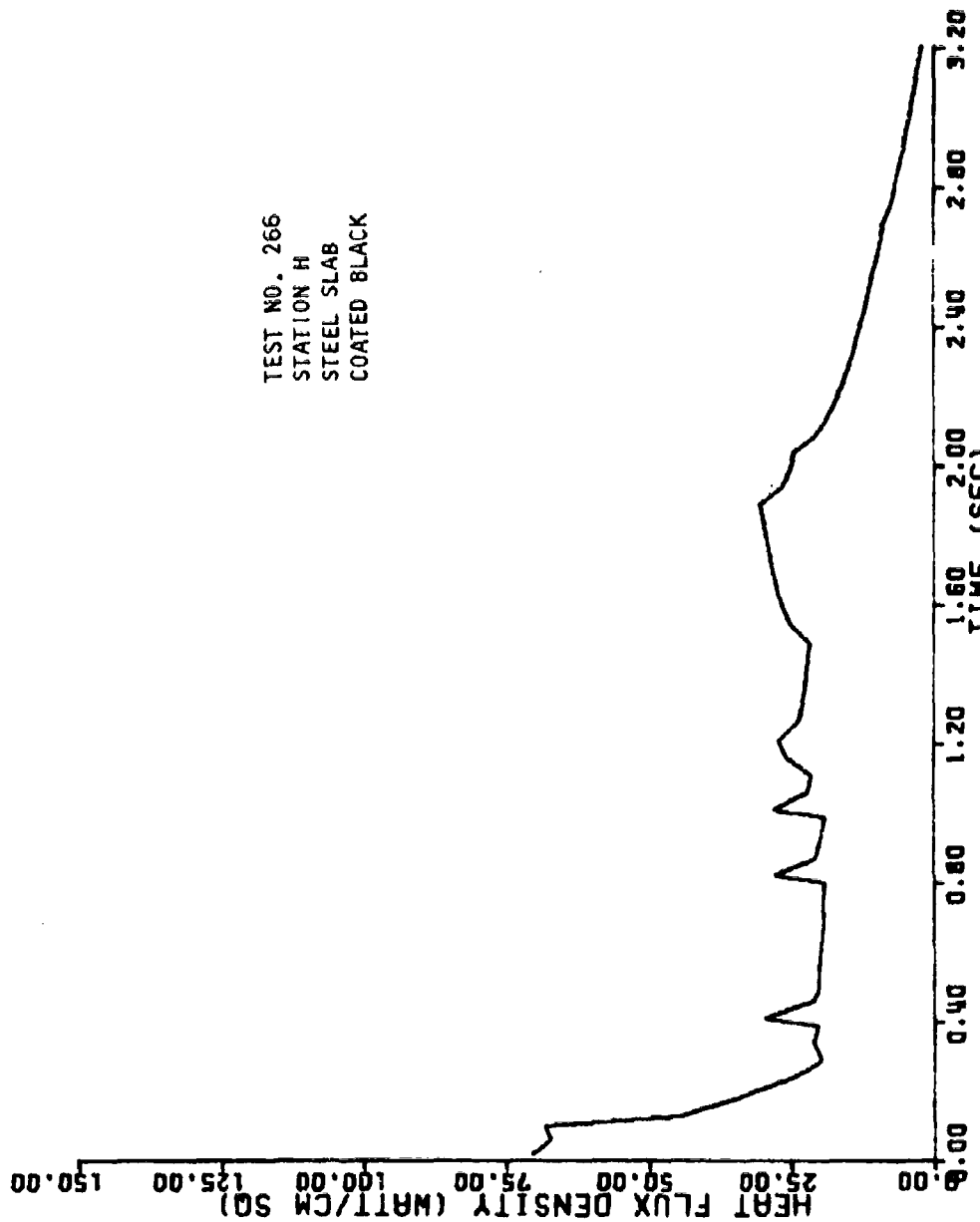

Figure B-81. Heat Flux Density at Station H for Test 266 (1000-lb LO_2/LH_2)

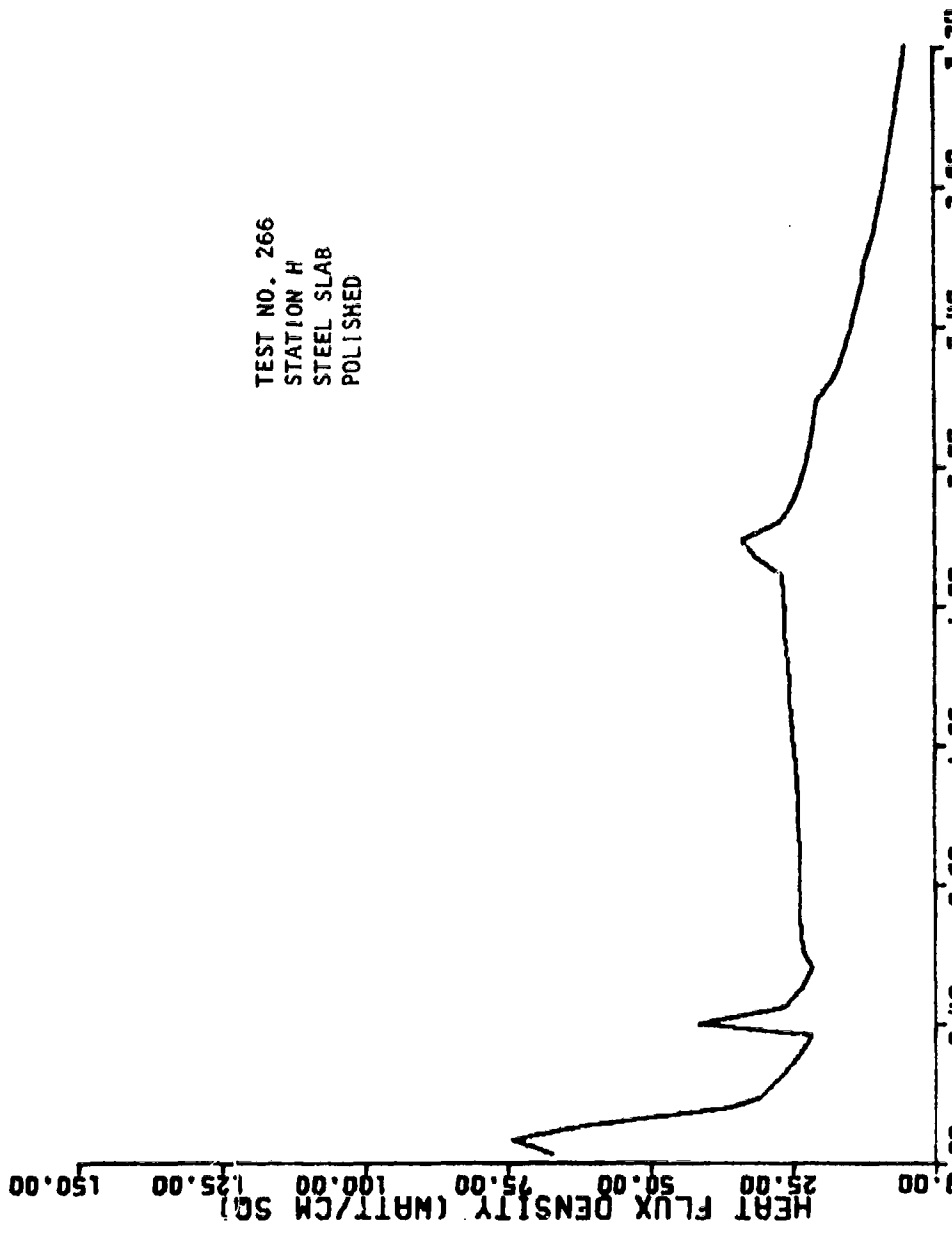

Figure B-82. Heat Flux Density at Station H for Test 266 (1000-lb LO_2/LH_2)

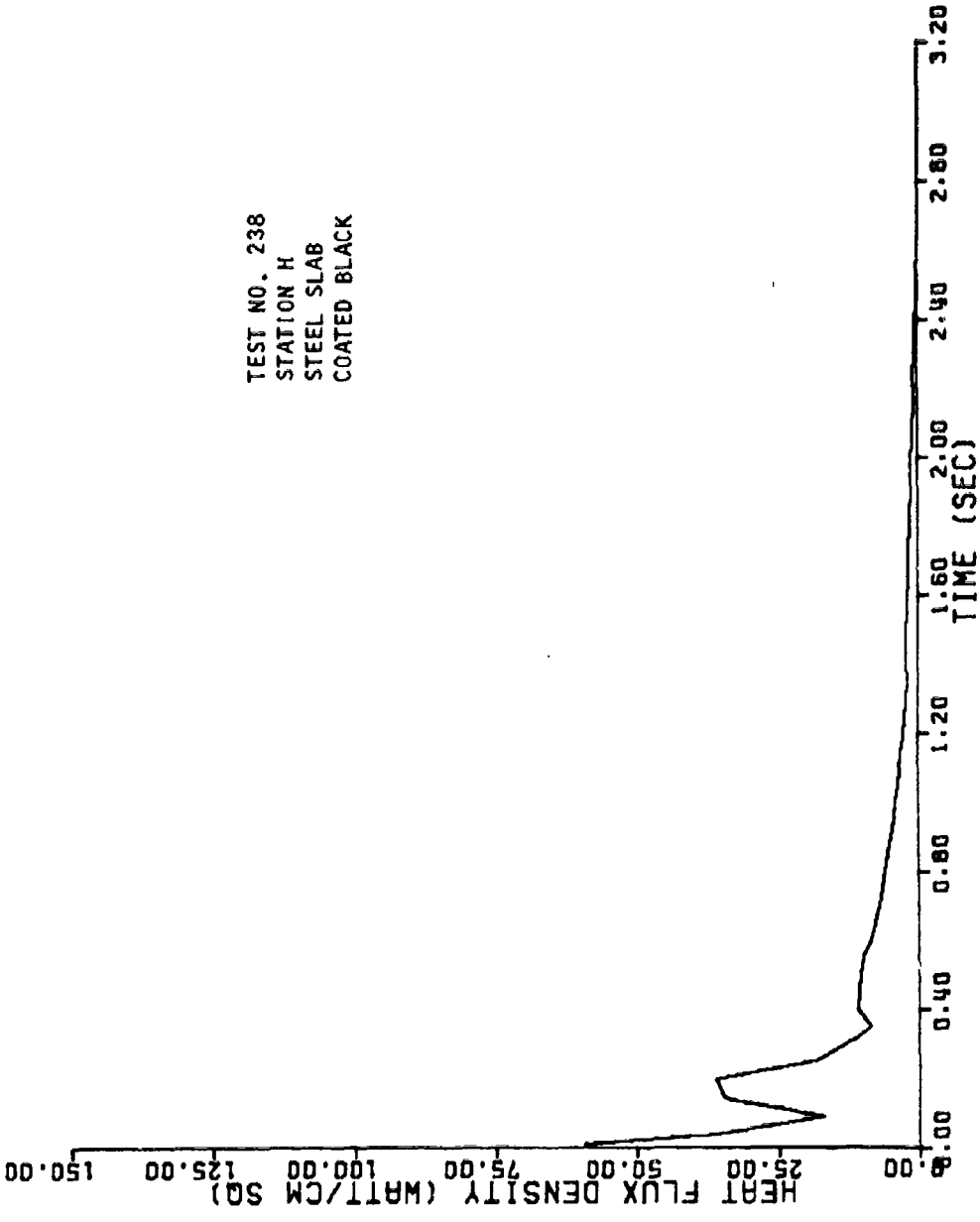

Figure B-83. Heat Flux Density at Station H for Test 238 (200-lb LO_2/RP-1)

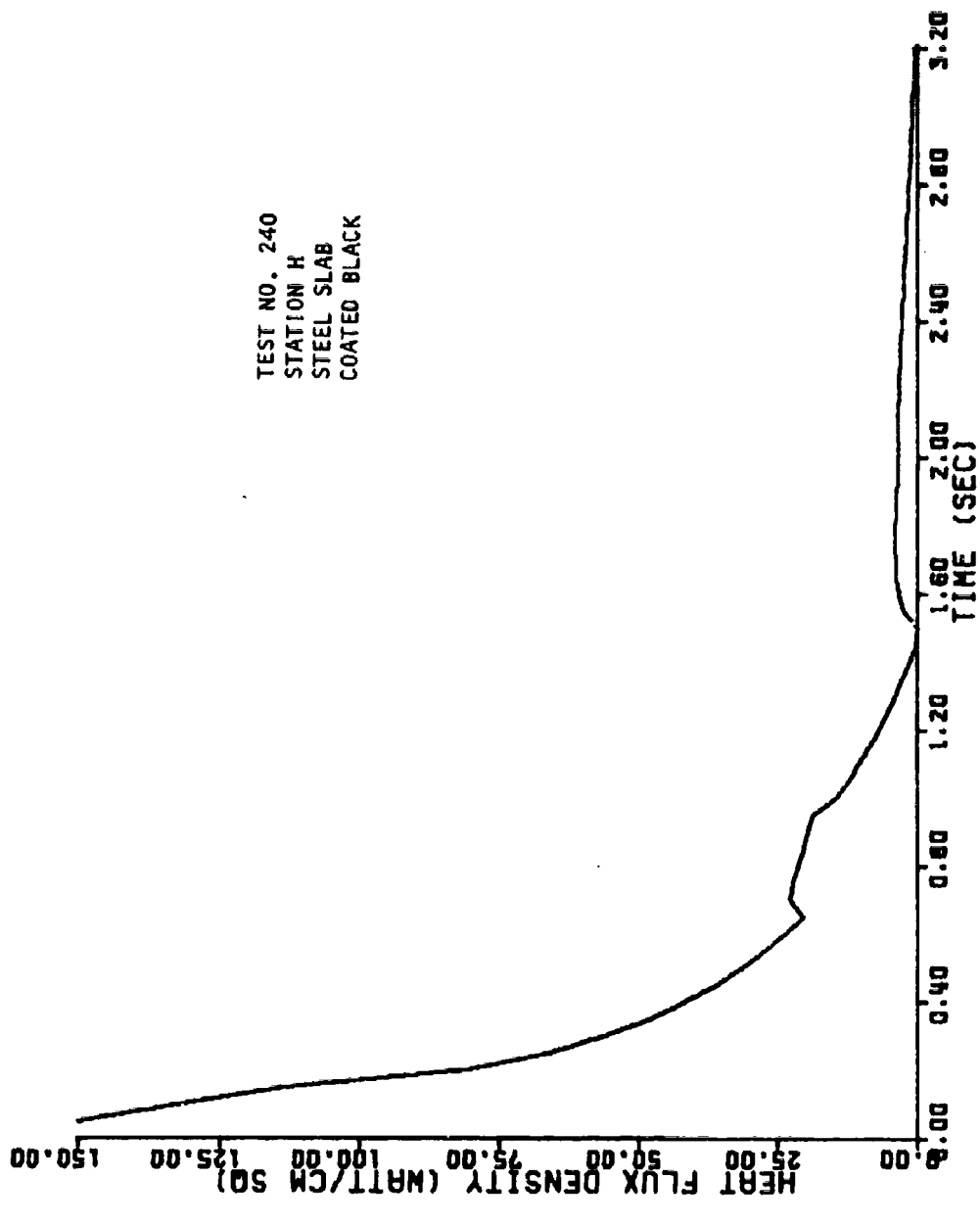

Figure B-84. Heat Flux Density at Station H for Test 240 (200-lb LO_2/RP-1)

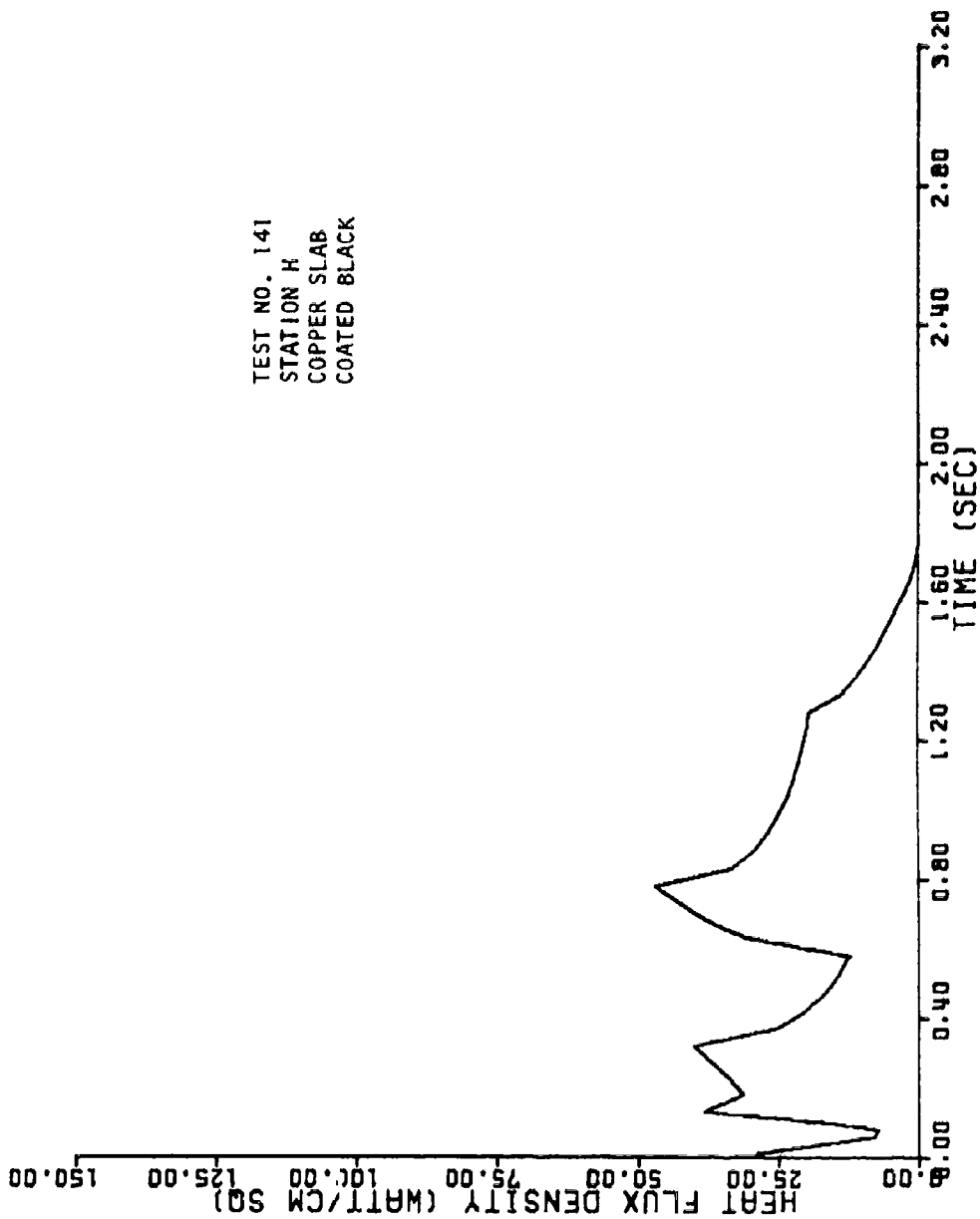

Figure B-85. Heat Flux Density at Station H for Test 141 (200-lb LO_2/RP-1)

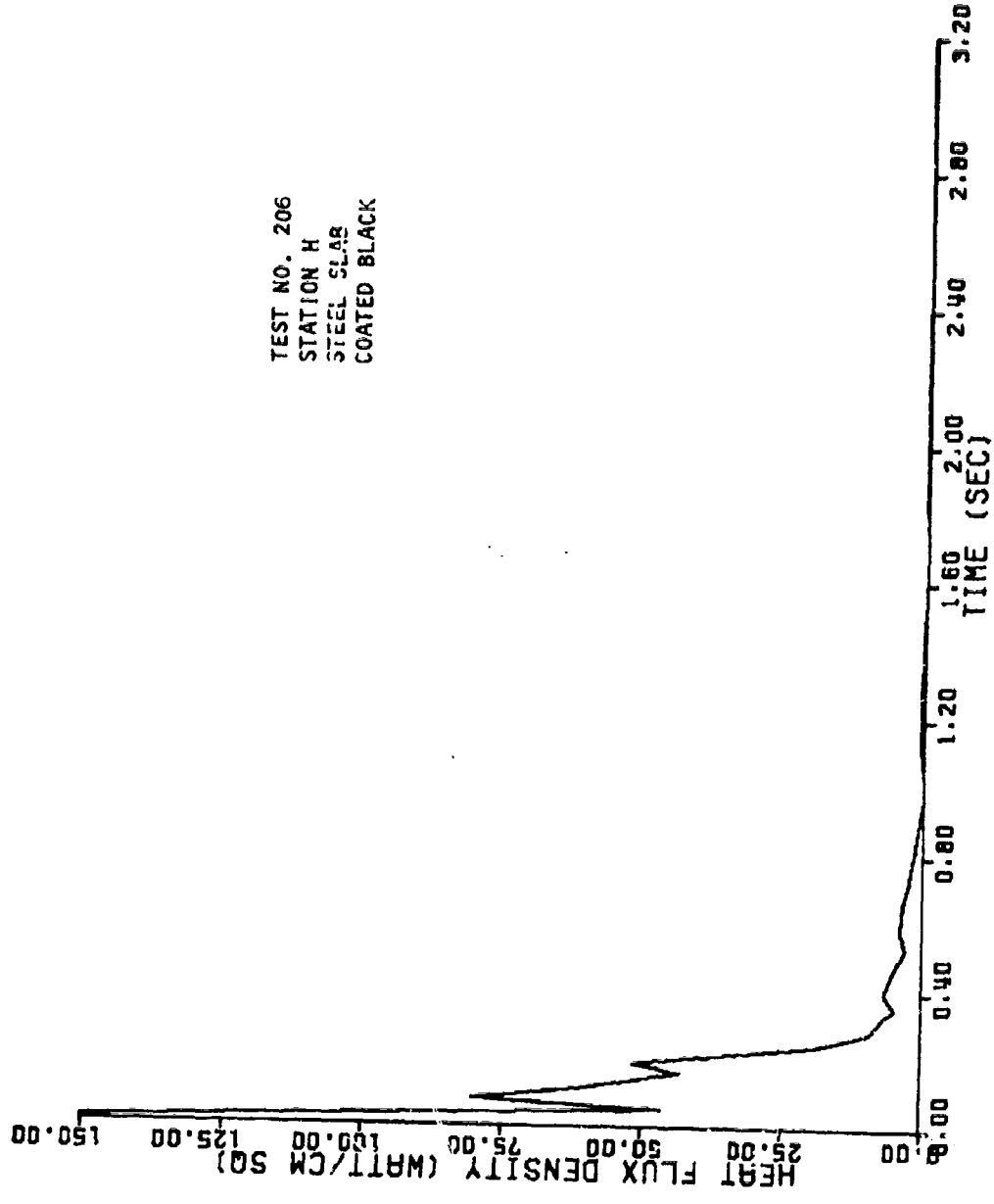

Figure B-66. Heat Flux Density at Station H for Test 206 (200-lb LO_2/RP-1)

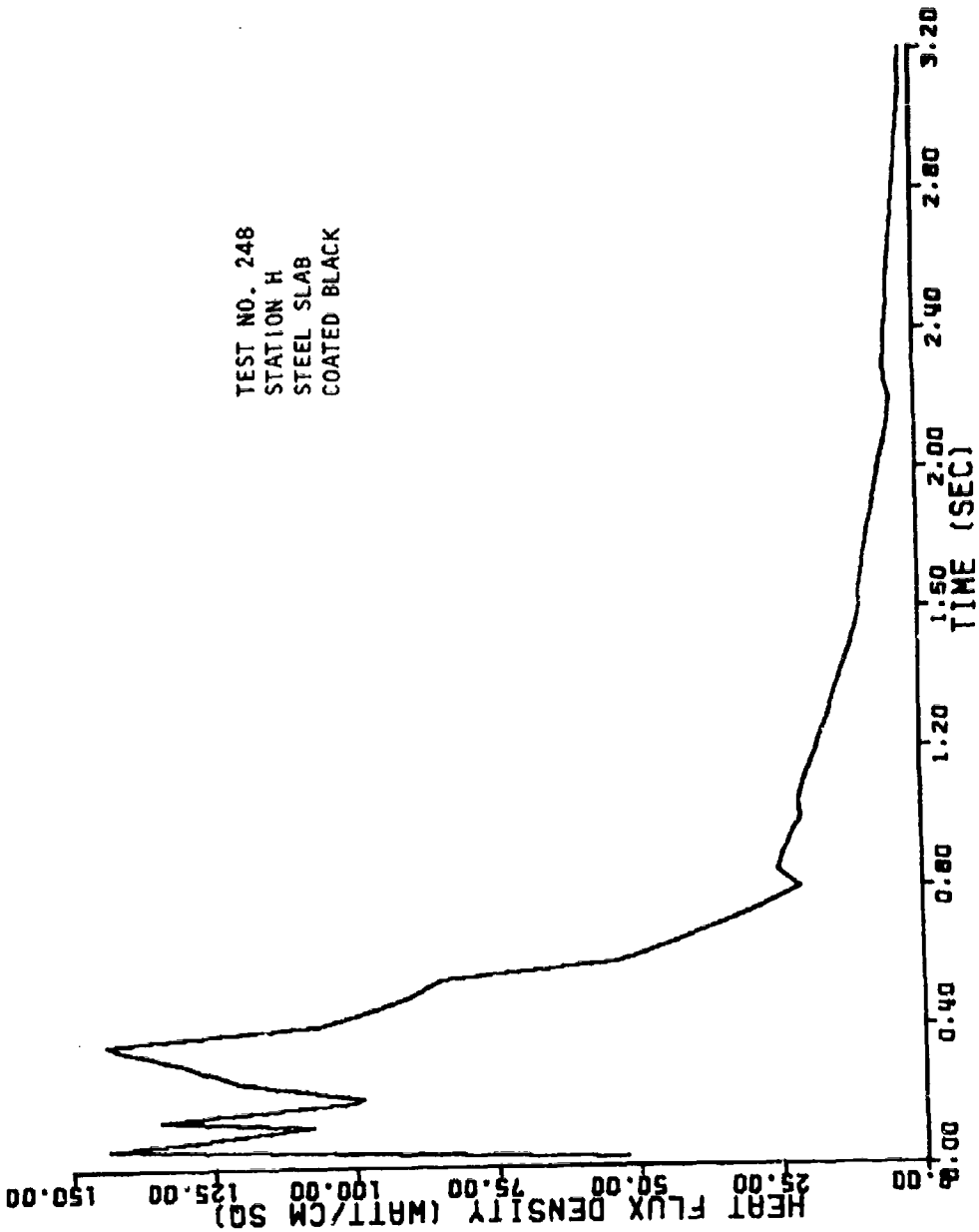

Figure B-87. Heat Flux Density at Station H for Test 248 (200-lb LO_2/RP-1)

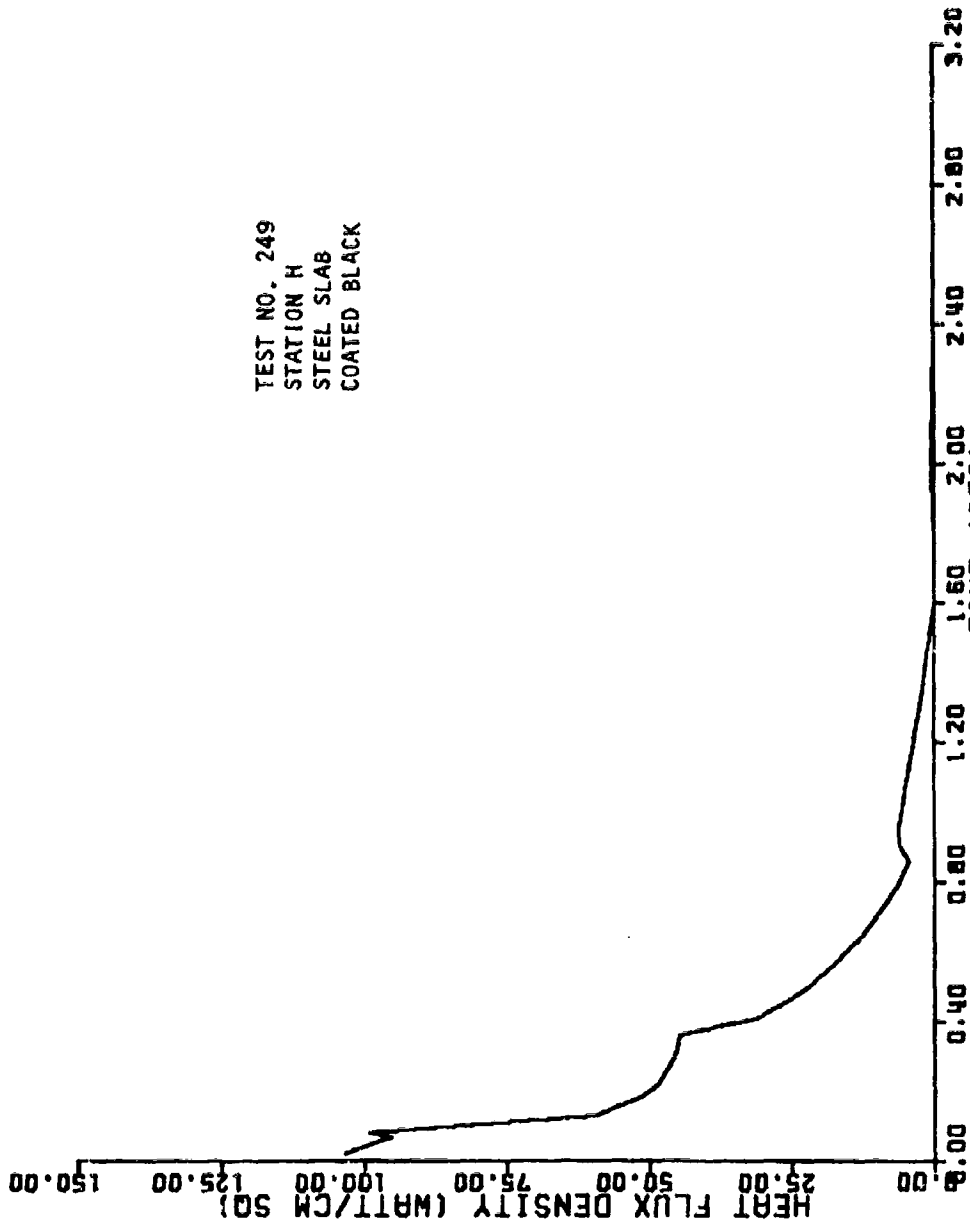

Figure B-88. Heat Flux Density at Station H for Test 249 (200-lb LO_2/RP-1)

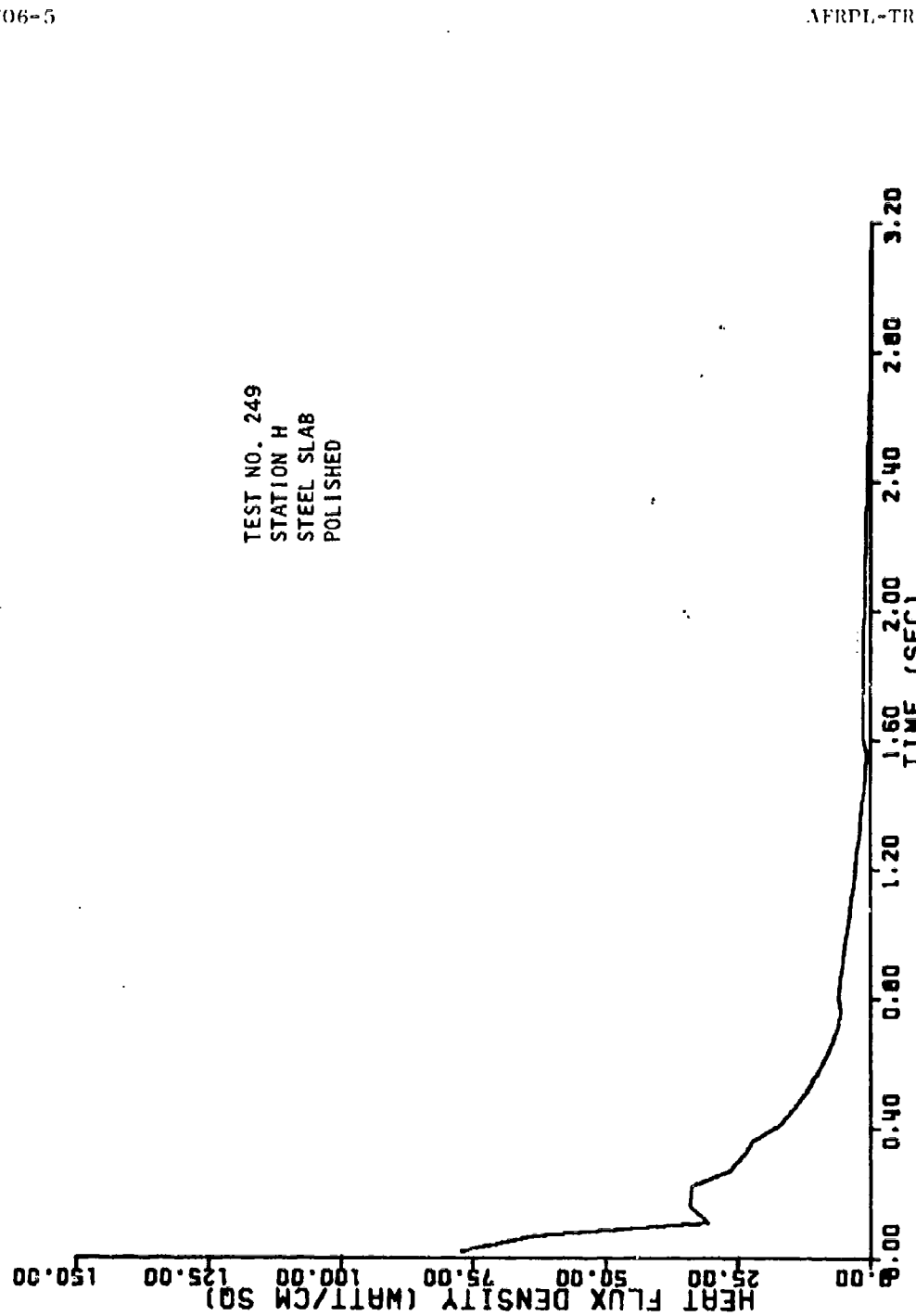

Figure B-89. Heat Flux Density at Station H for Test 249 (200-lb LO_2/RP-1)

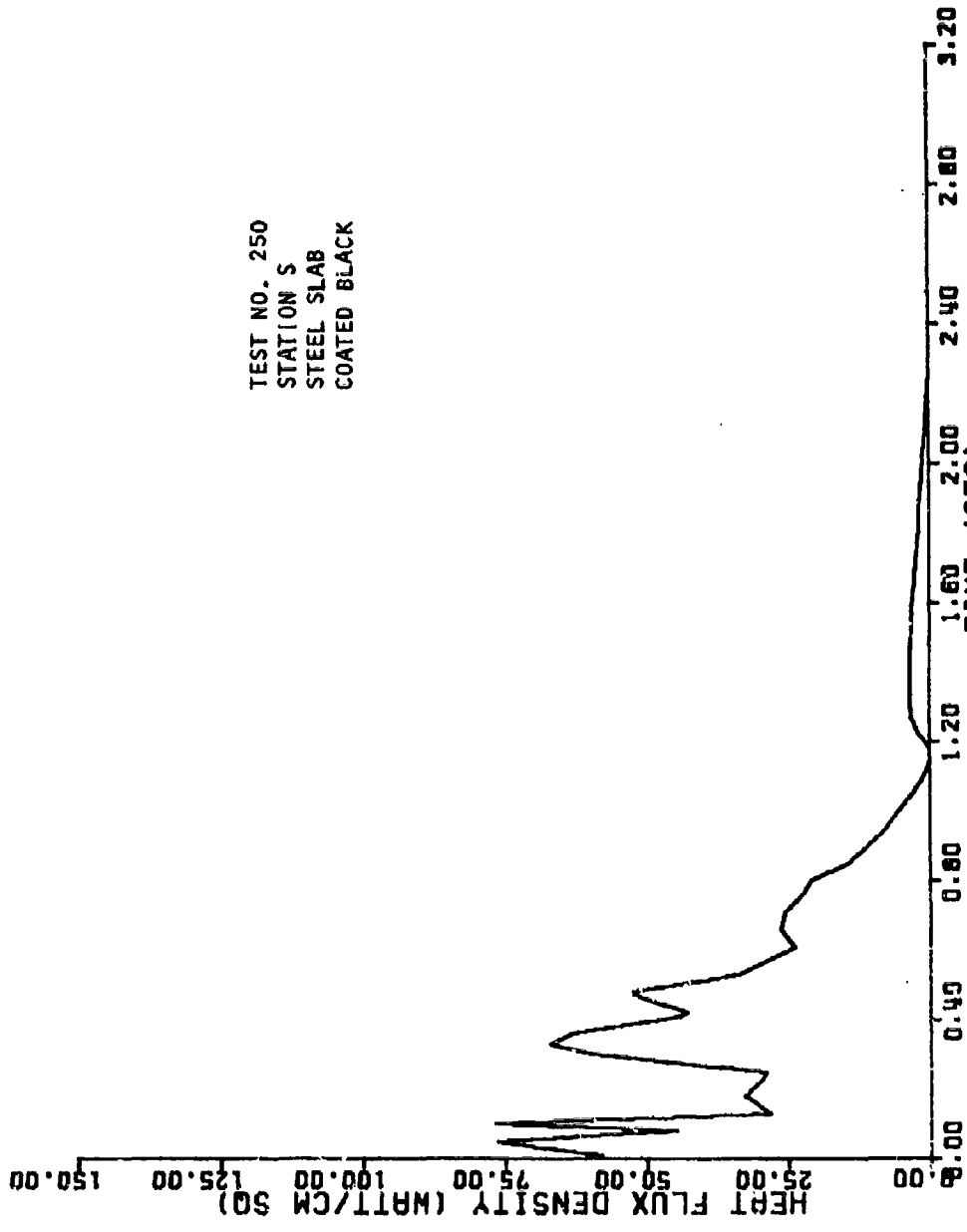

Figure B-90. Heat Flux Density at Station S for Test 250 (200-lb LO_2/RP-1)

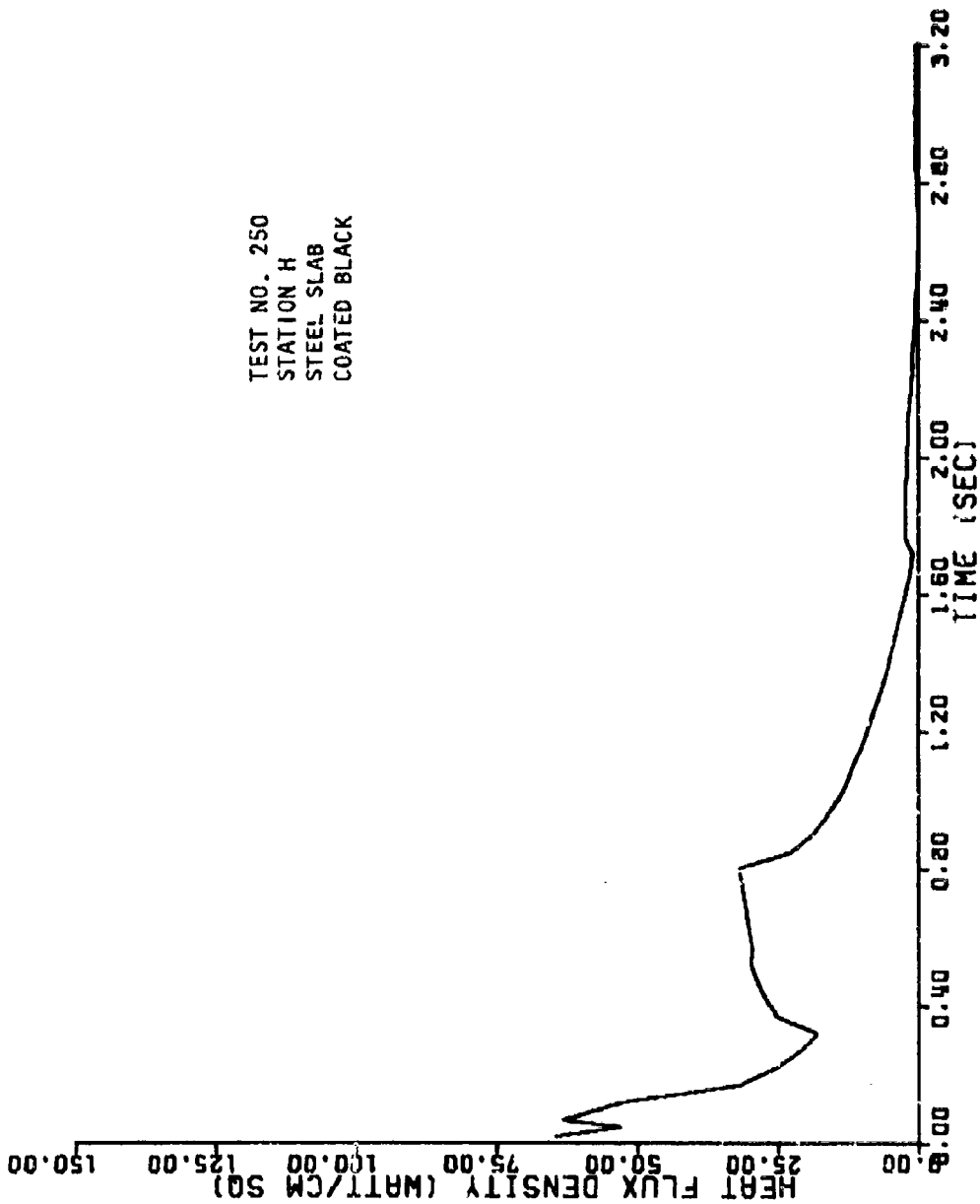

Figure B-91. Heat Flux Density at Station H for Test 250 (200-lb LO_2/RP-1)

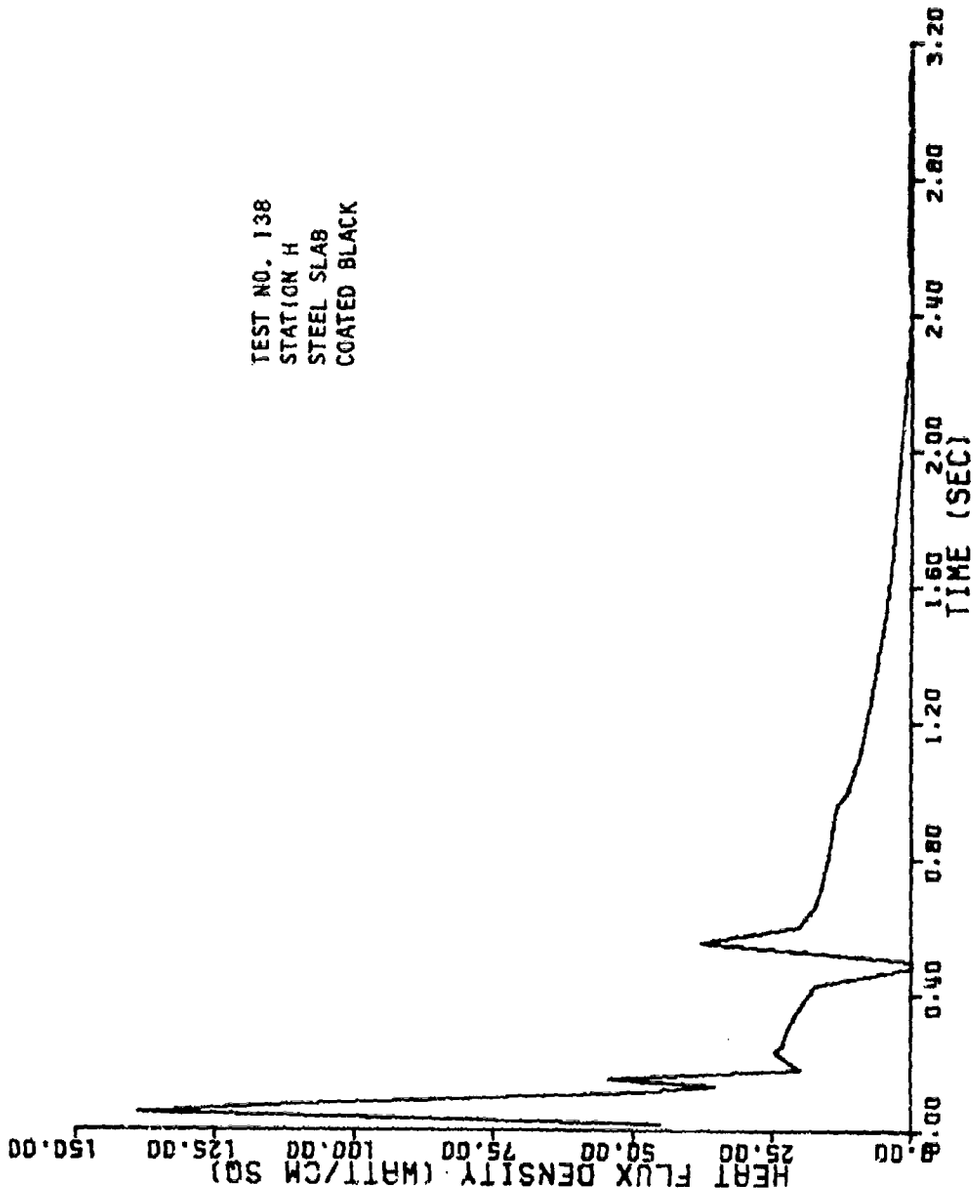

Figure B-92. Heat Flux Density at Station H for Test 138 (200-lb LO_2/LH_2)

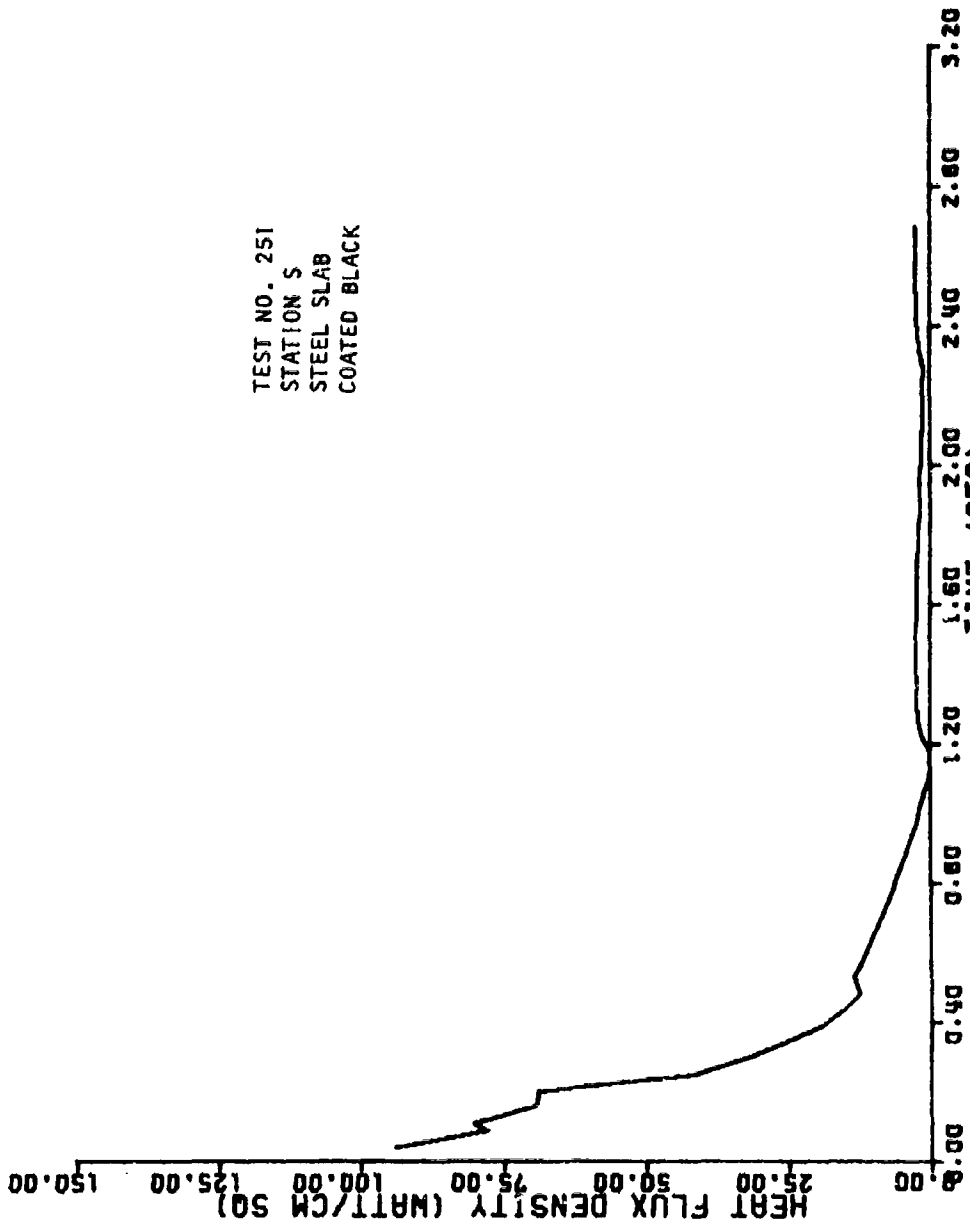

Figure B-93. Heat Flux Density at Station S for Test 251 (200-lb LO_2/LH_2)

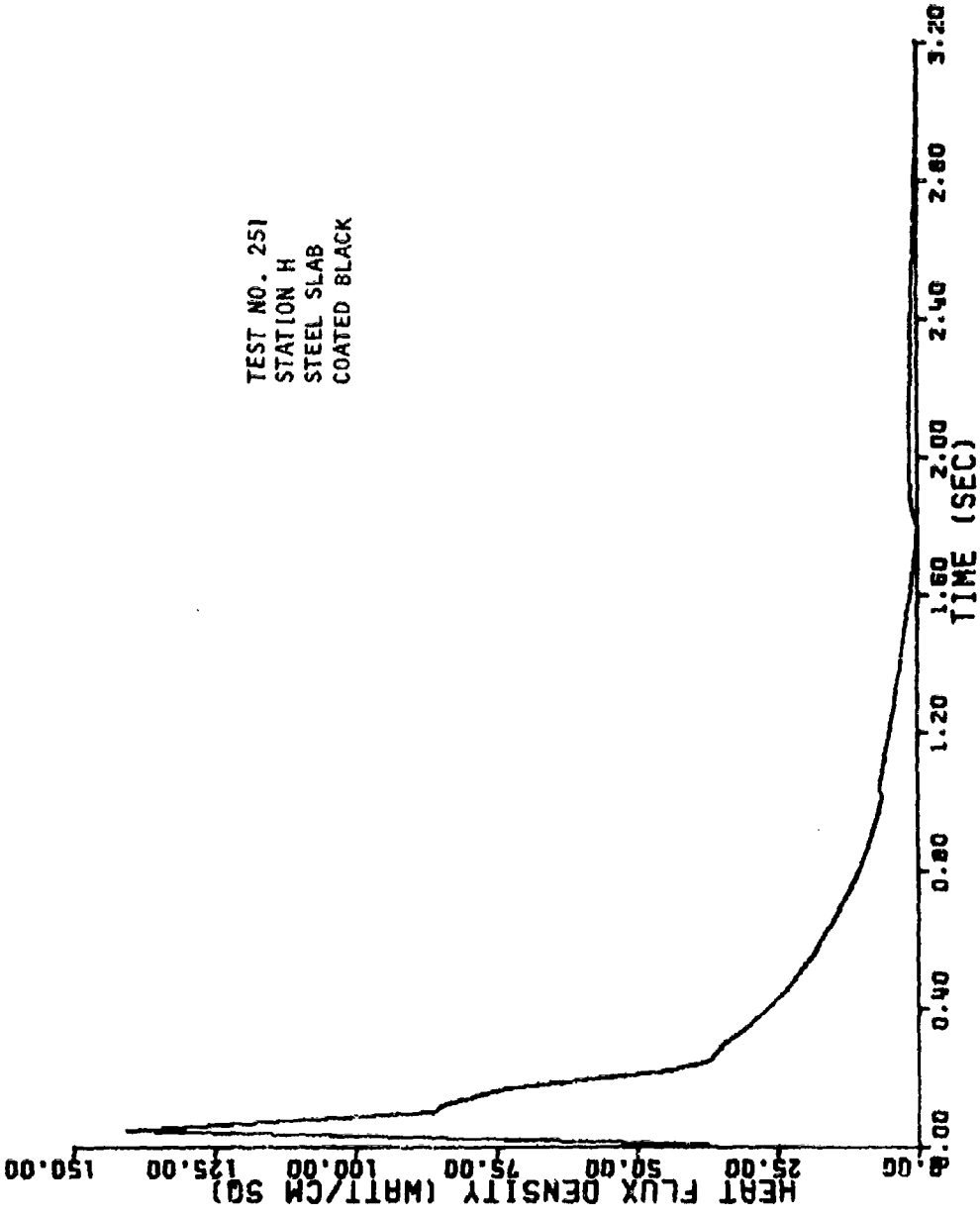

Figure B-94. Heat Flux Density at Station H for Test 251 (200-lb LO_2/LH_2)

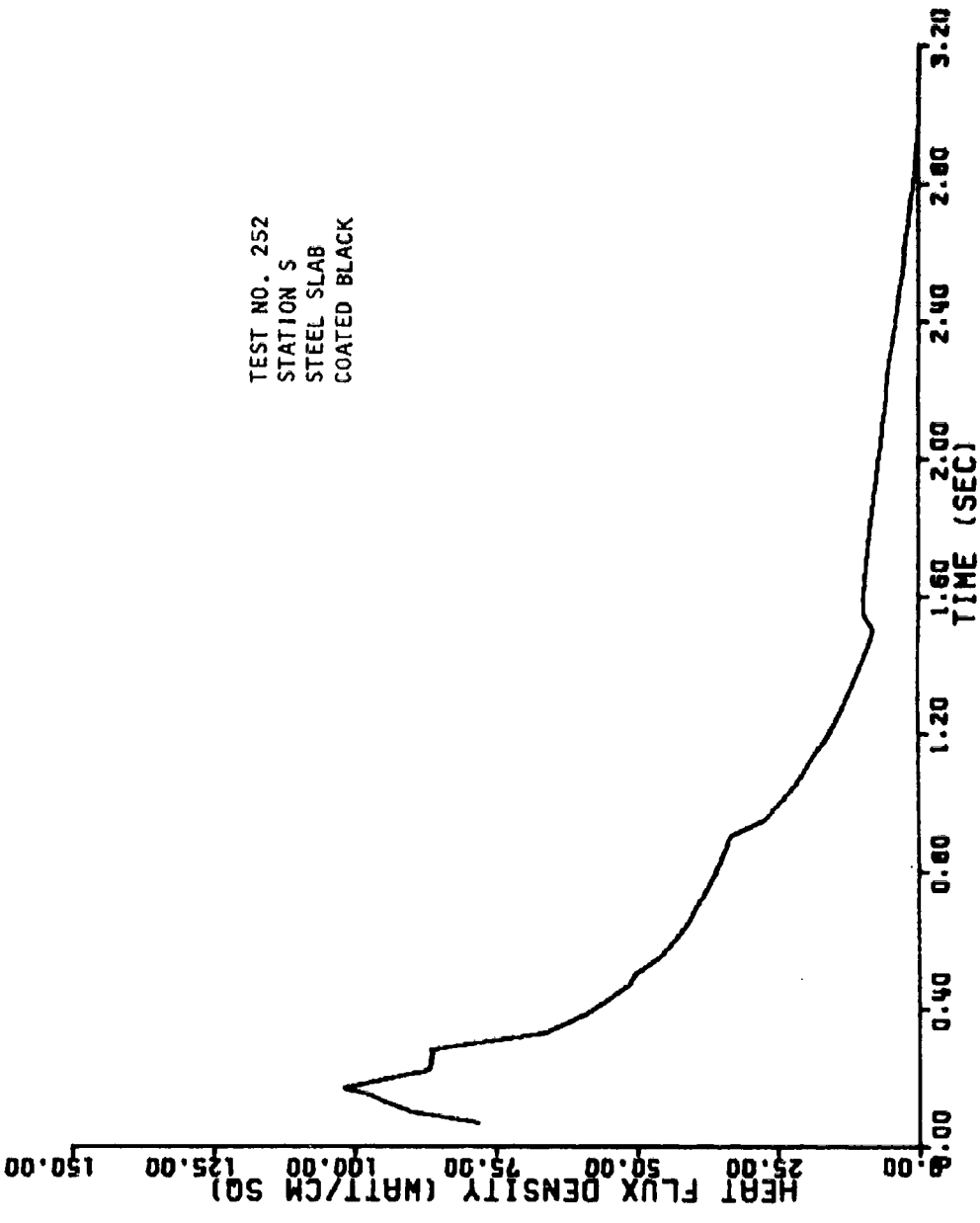

Figure B-95. Heat Flux Density at Station S for Test 252 (200-lb LO_2/LH_2)

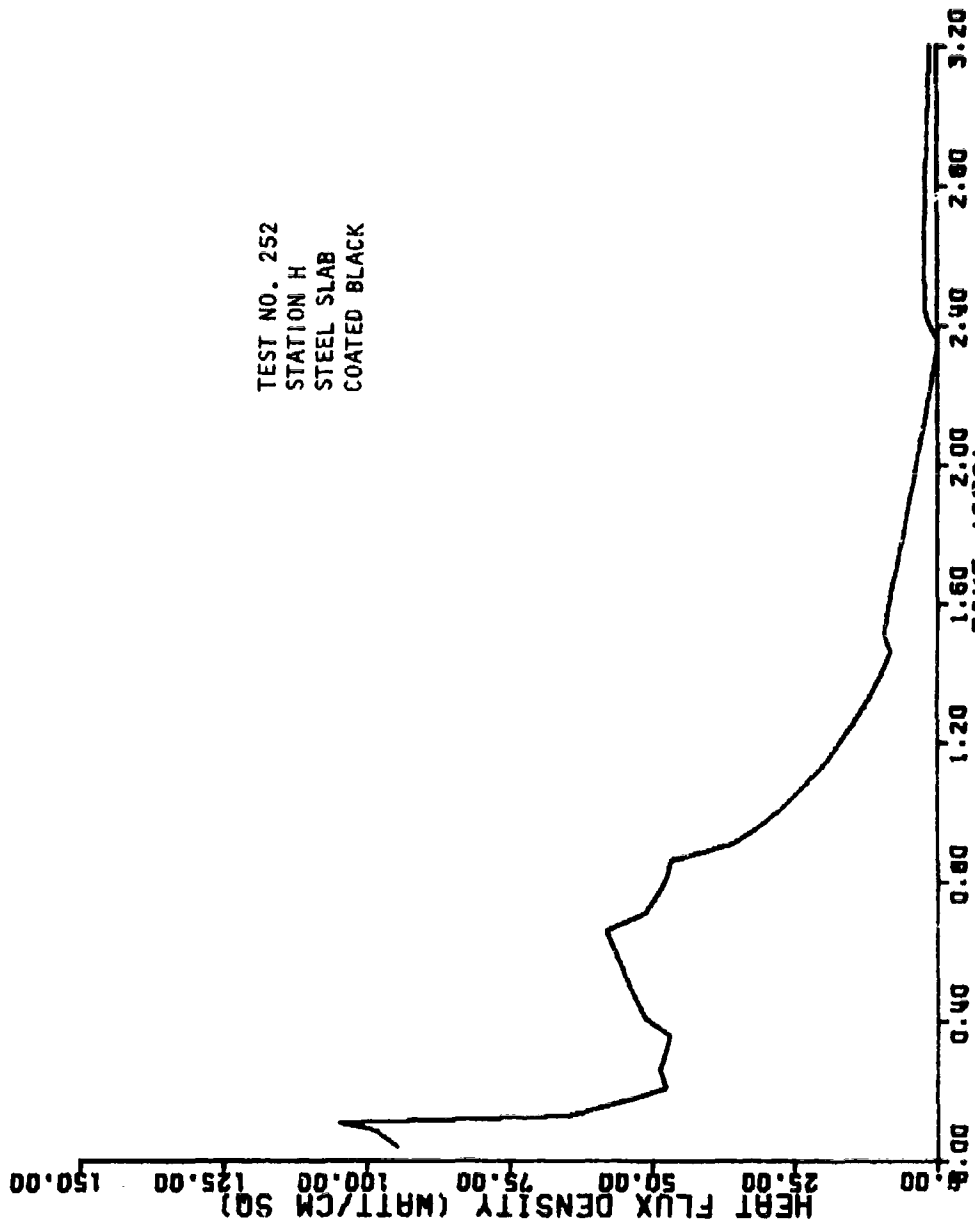

Figure B-96. Heat Flux Density at Station H for Test 252 (200-lb LO_2/LH_2)

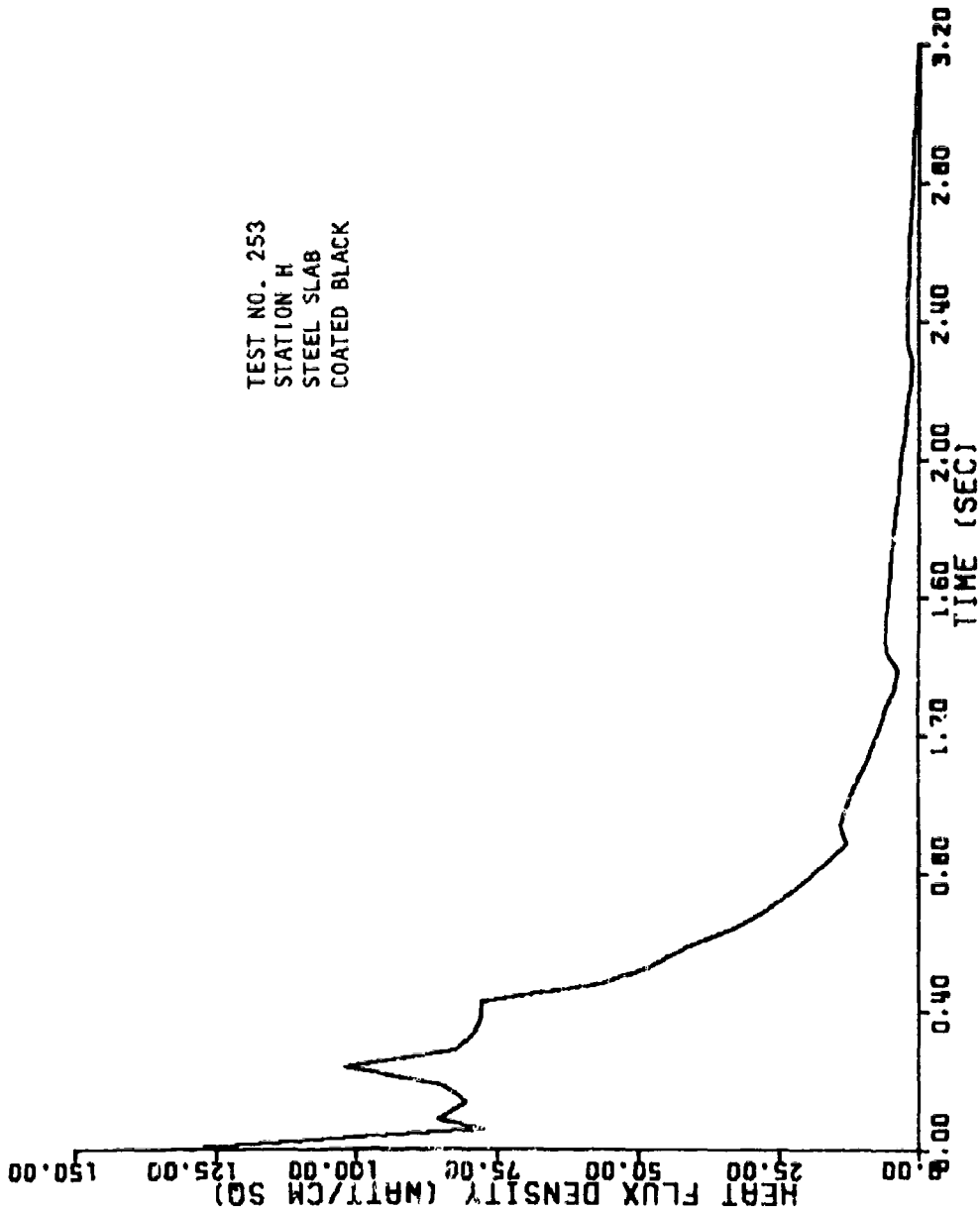

Figure B-97. Heat Flux Density at Station H for Test 253 (200-lb LO_2/LH_2)

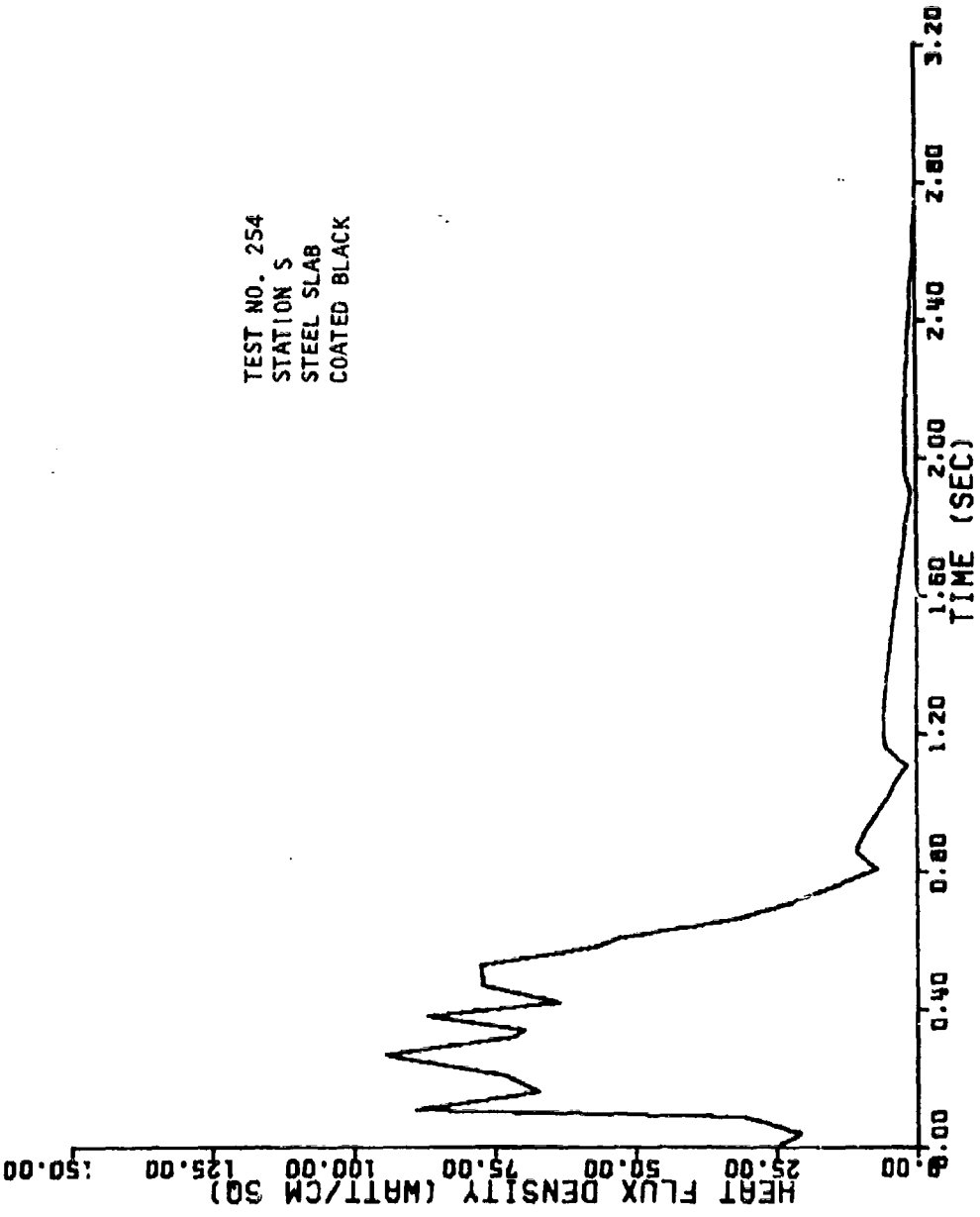

Figure B-98. Heat Flux Density at Station S for Test 254 (200-lb LO_2/LH_2)

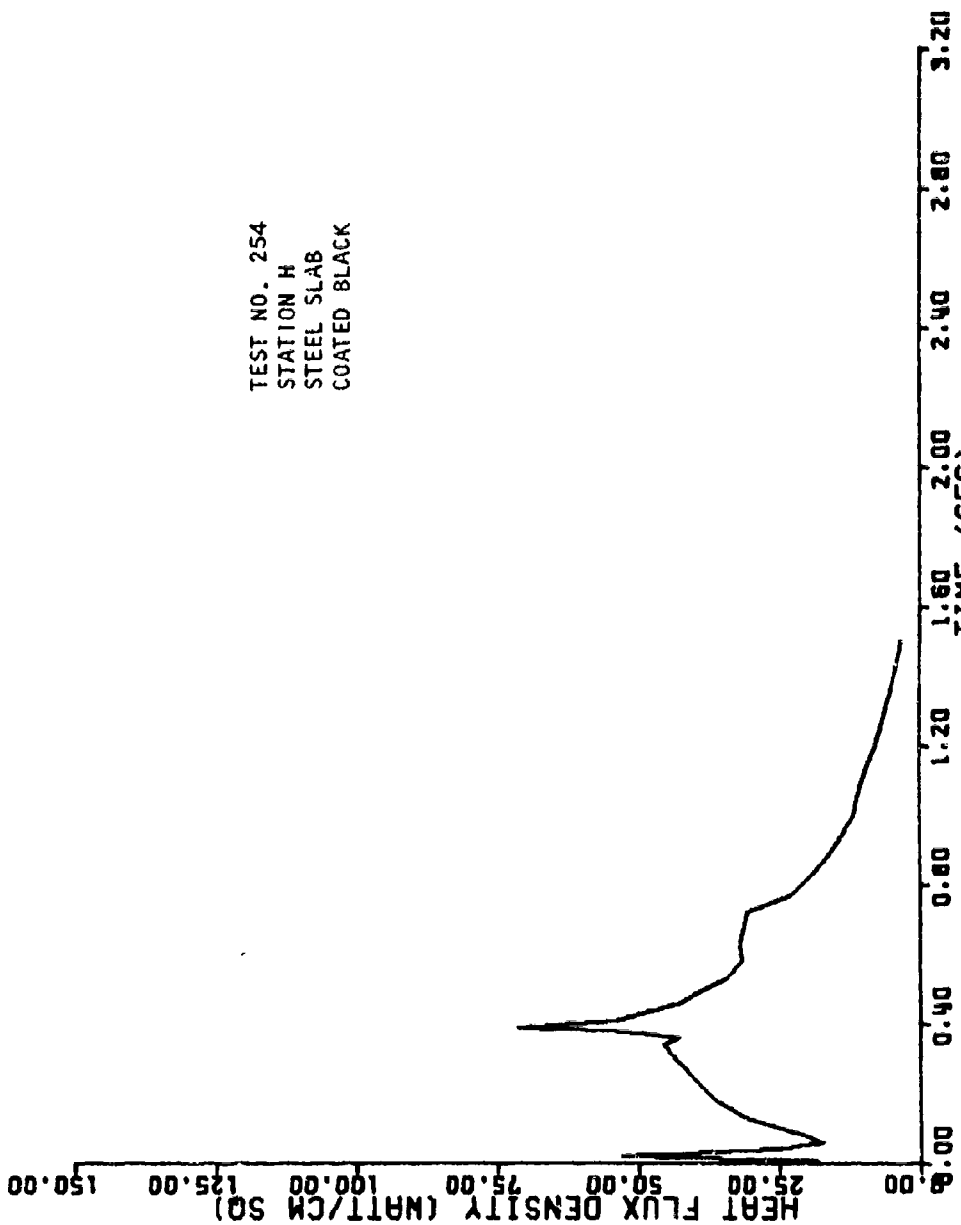

Figure B-99. Heat Flux Density at Station H for Test 254 (200-lb LO_2/LH_2)

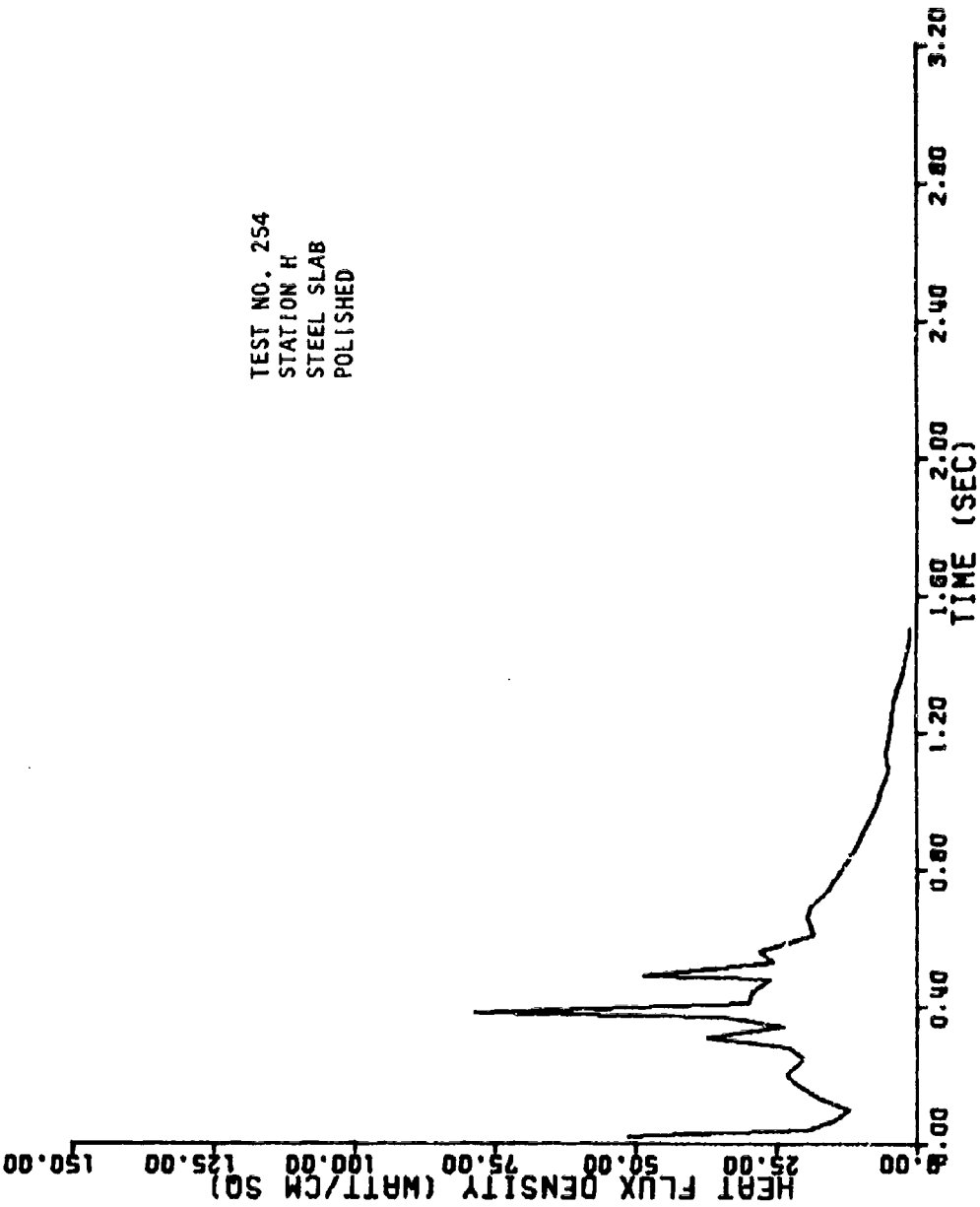

Figure B-100. Heat Flux Density at Station H for Test 254 (200-lb LO_2/LH_2)

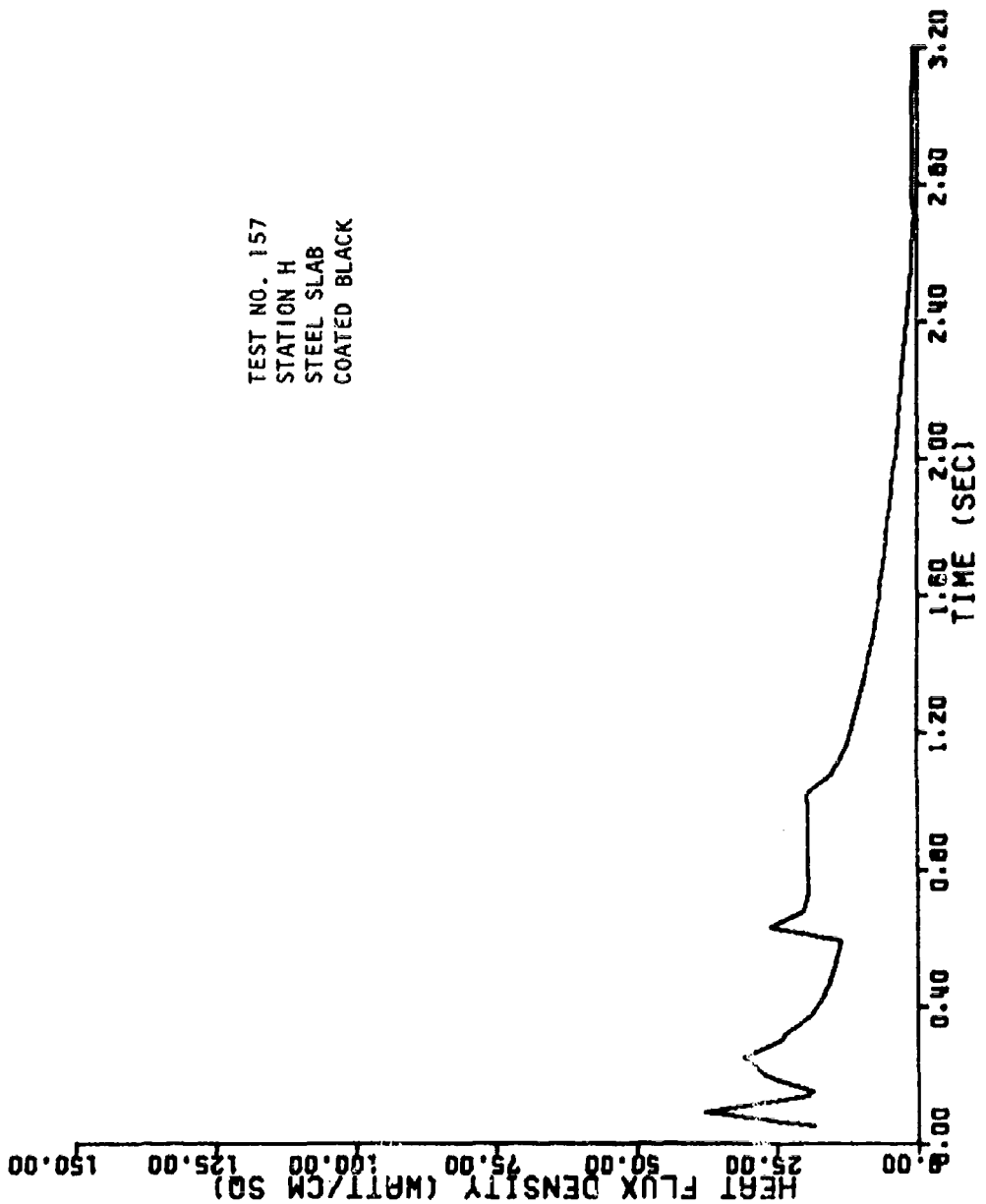

Figure B-101. Heat Flux Density at Station H for Test 157 (260-lb N_2O_4 /50% UDMH-50% N_2H_4)

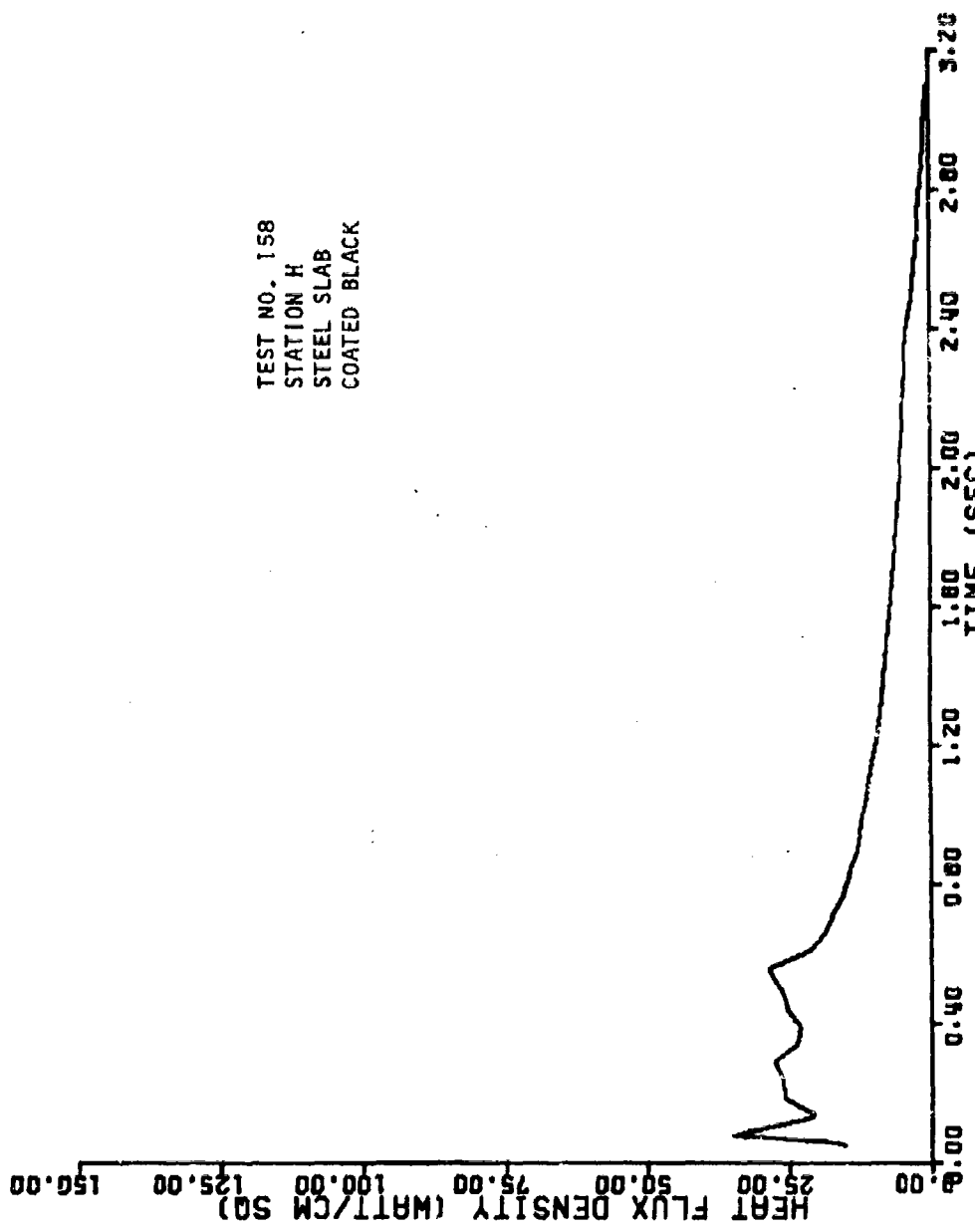

Figure B-102. Heat Flux Density at Station H for Test 158 (200-lb N_2O_4/50% UDMH-50% N_2H_4)

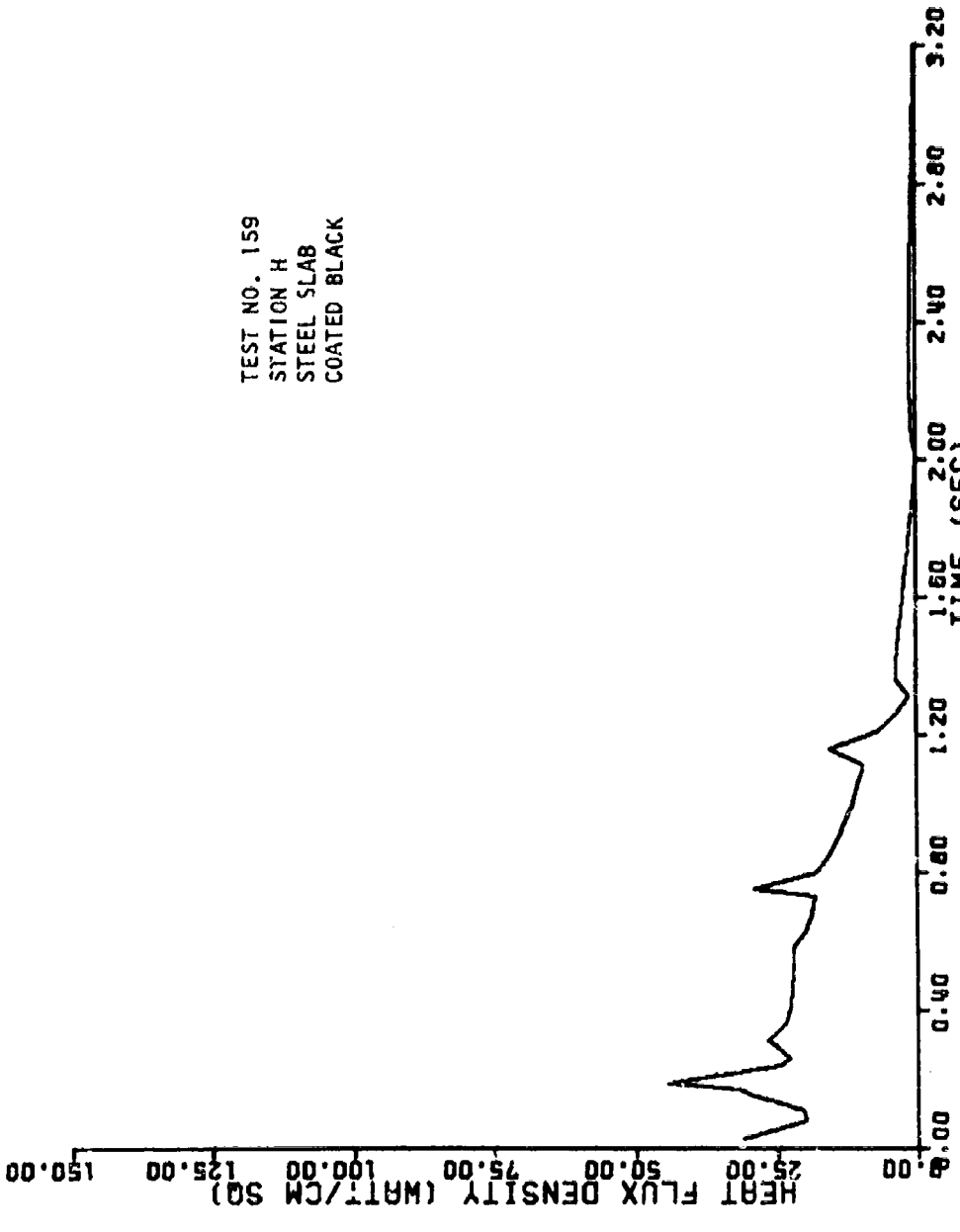

Figure B-103. Heat Flux Density at Station H for Test 159 (200-lb N_2O_4/50% UDMH-50% N_2H_4)

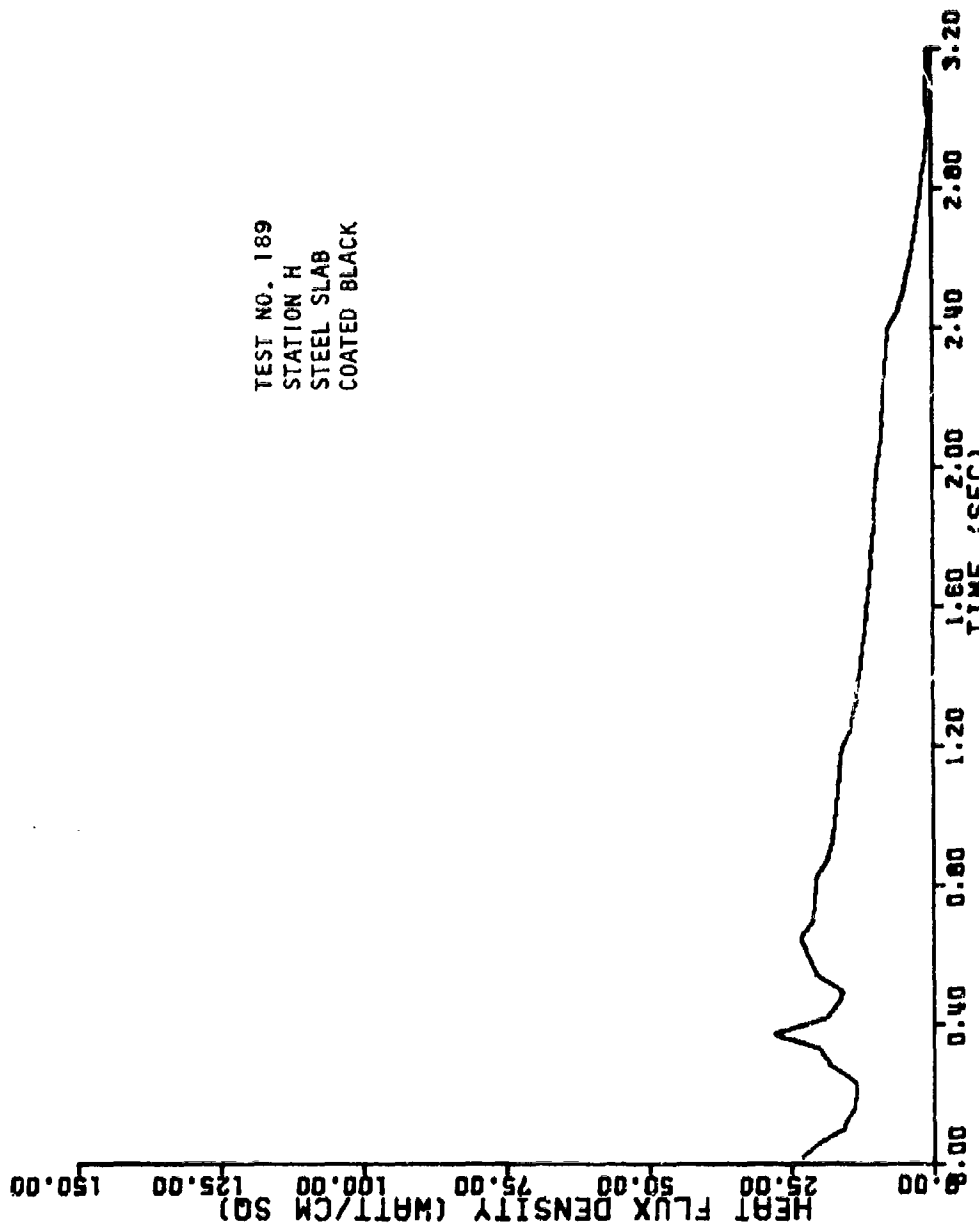

Figure B-104. Heat Flux Density at Station H for Test 189 (1000-lb N_2O_4/50% UDMH-50% N_2H_4)

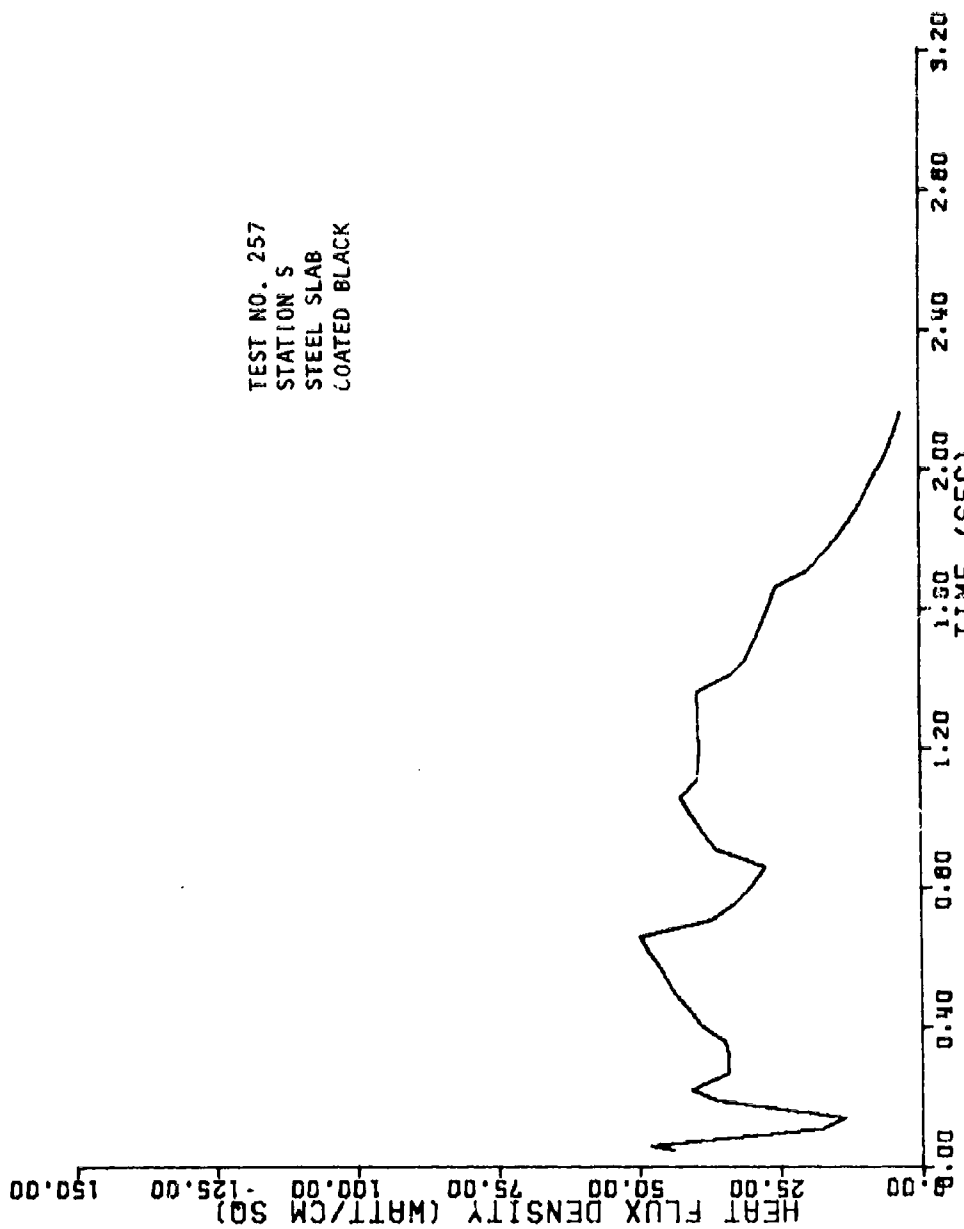

Figure B-105. Heat Flux Density at Station S for Test 257 (1000-lb N_2O_4/50% UDMH-50% N_2H_4)

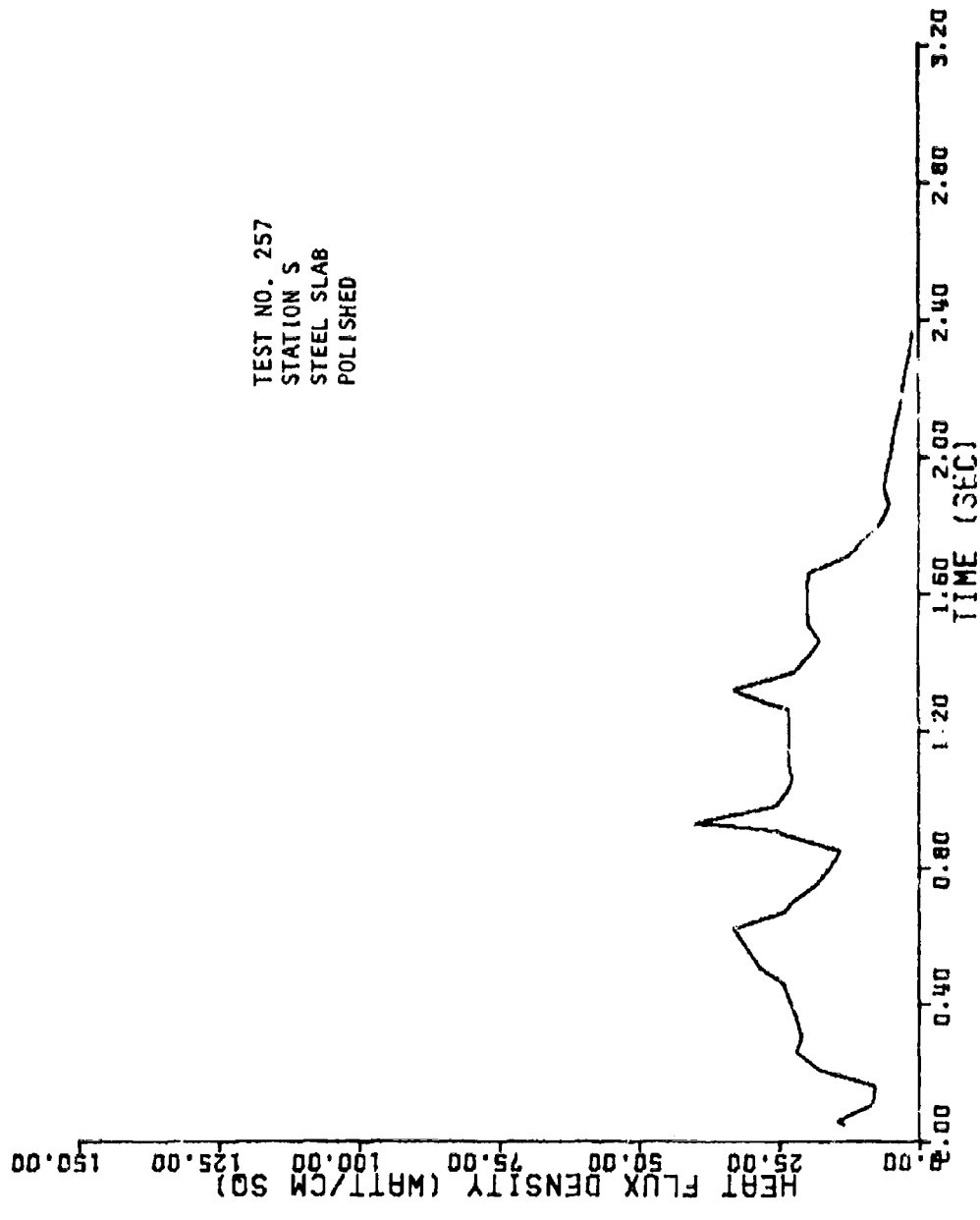

Figure B-106. Heat Flux Density at Station S for Test 257 (1000-lb N_2O_4/50% UDMH-50% N_2H_4)

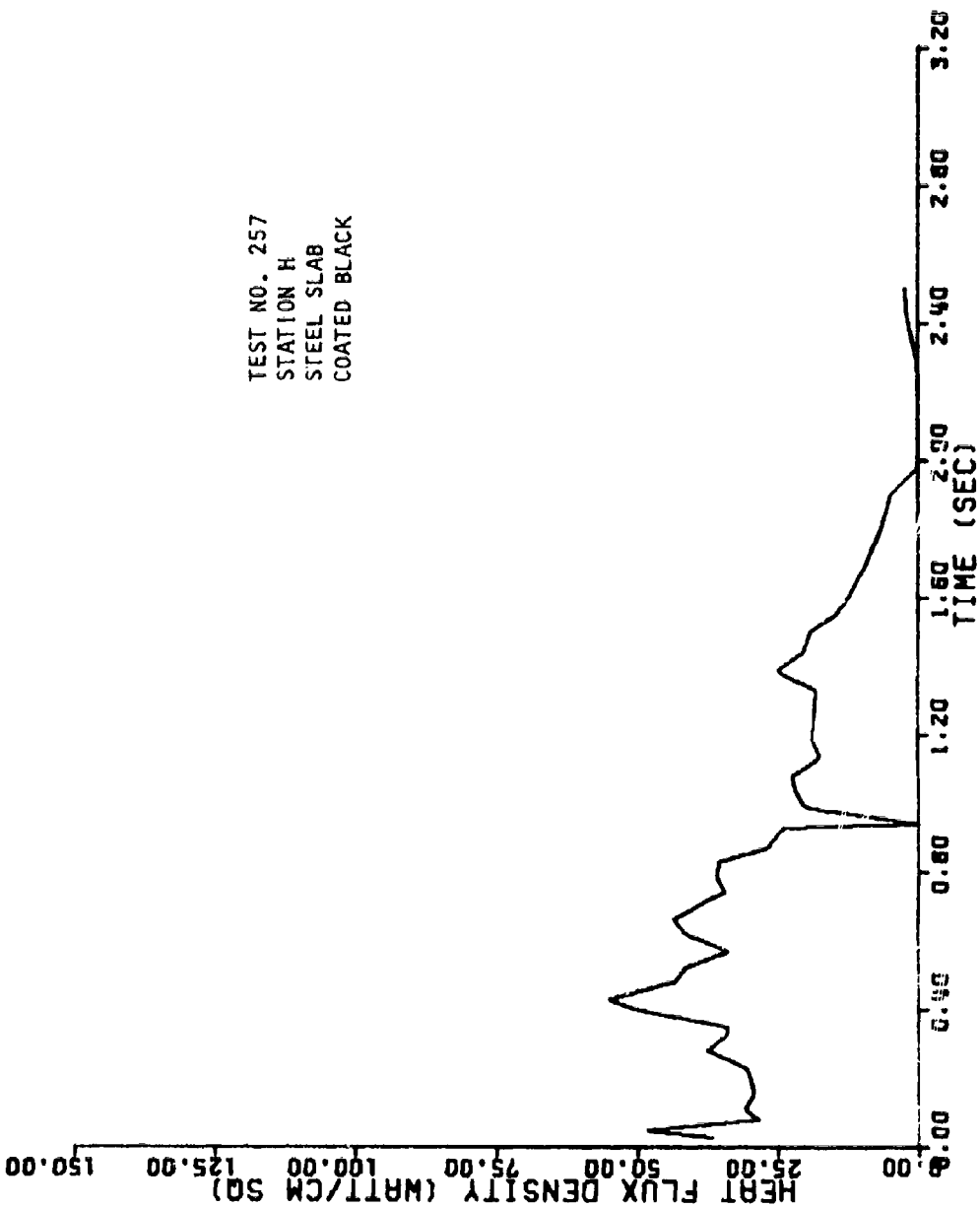

Figure B-107. Heat Flux Density at Station H for Test 257 (1600-lb N_2O_4/50% UDMH-50% N_2H_4)

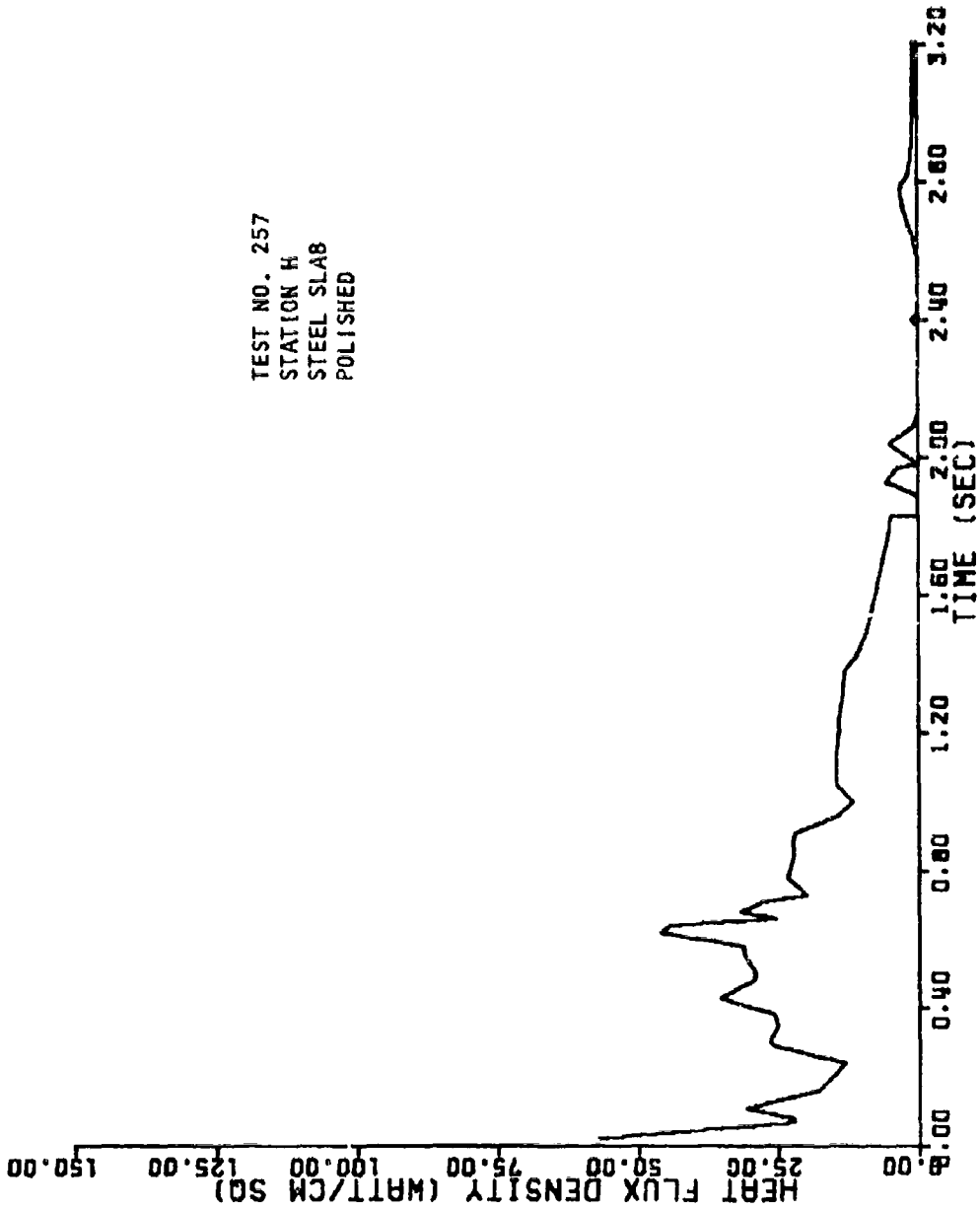

Figure B-108. Heat Flux Density at Station H for Test 257 (1000-lb N_2O_4/50% UDMH-50% N_2H_4)

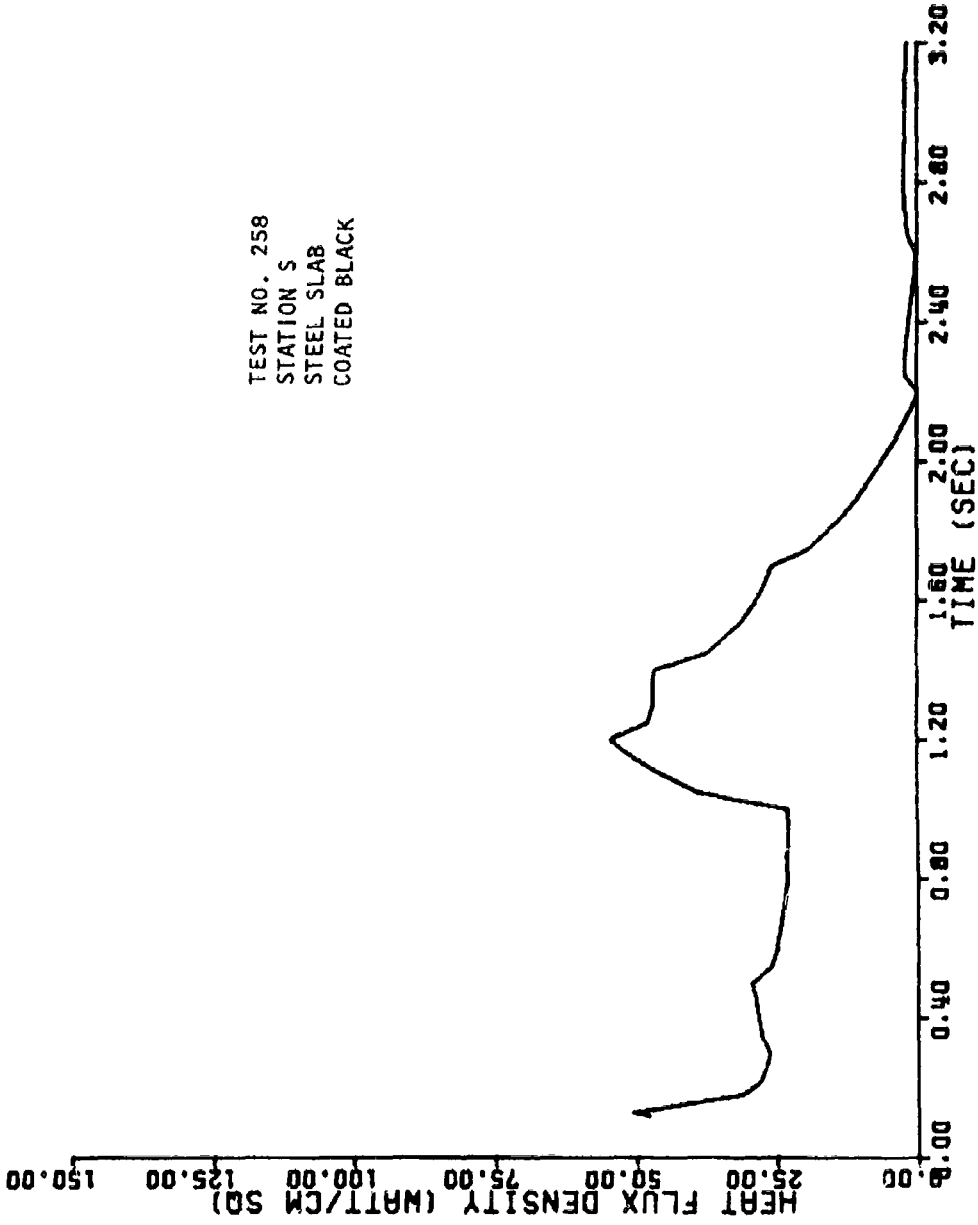

Figure B-109. Heat Flux Density at Station S for Test 258 (1000-lb N_2O_4/50% UDMH-50% N_2H_4)

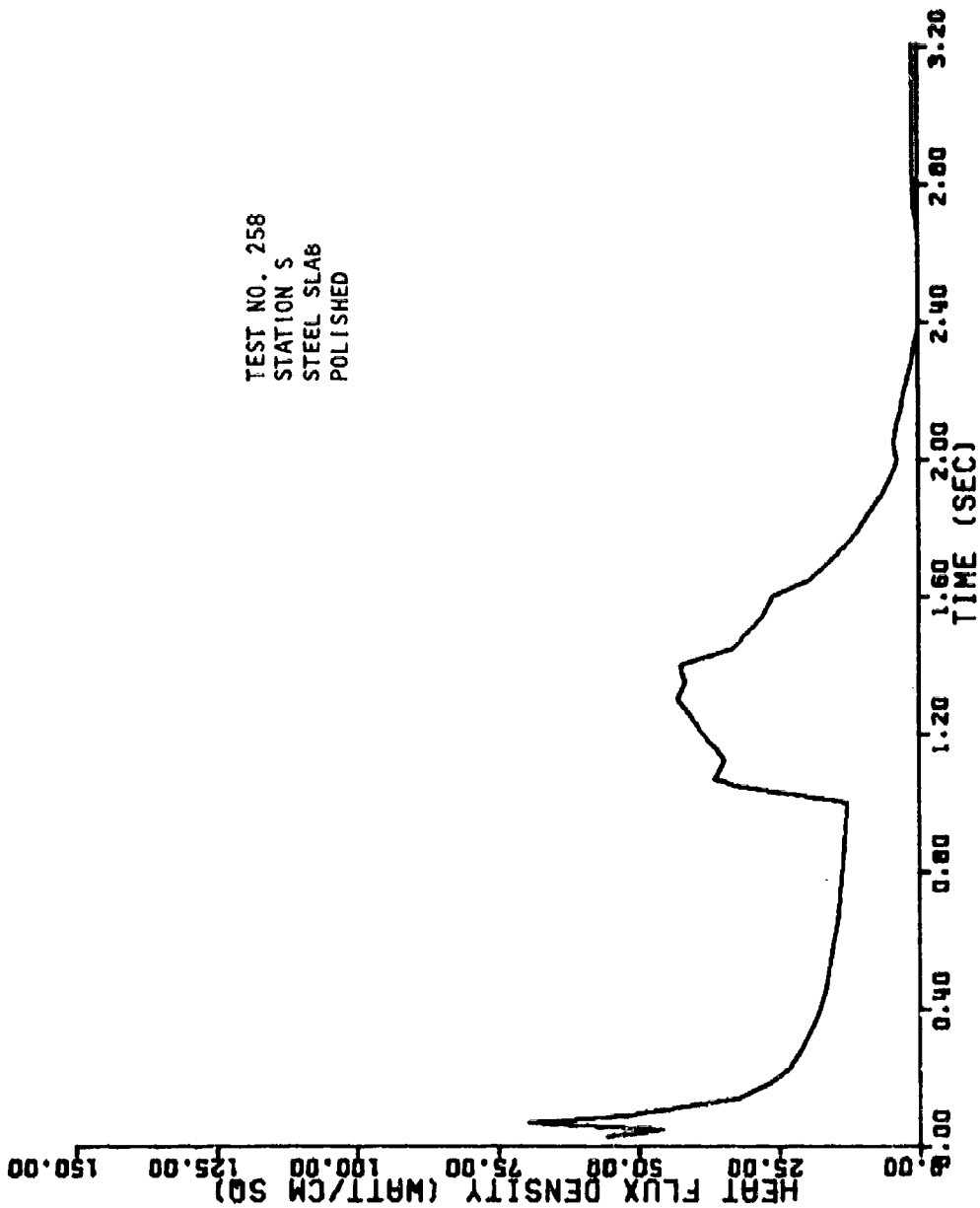

Figure B-110. Heat Flux Density at Station S for Test 258 (1000-lb N_2O_4/50% UDMH-50% N_2H_4)

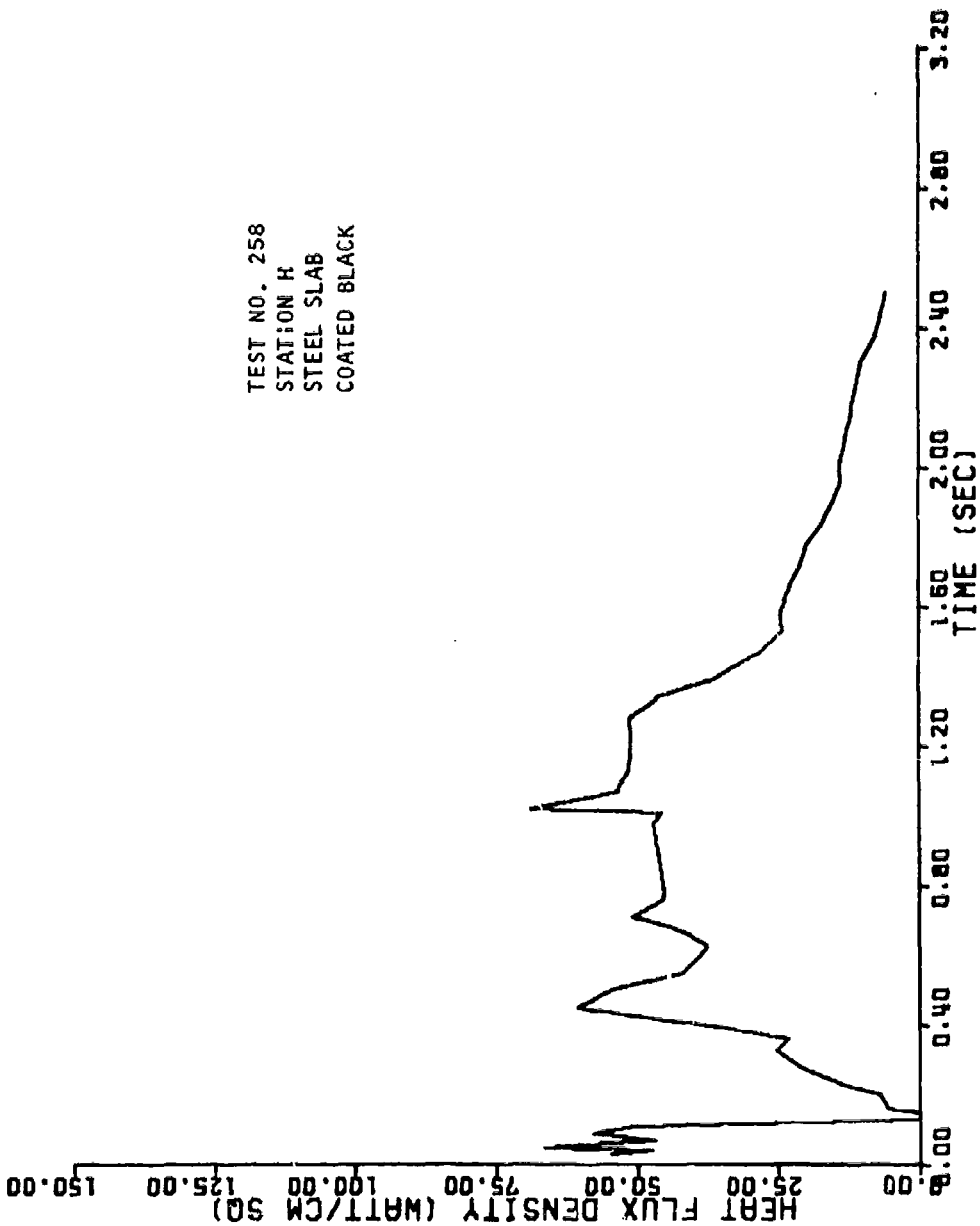

Figure B-111. Heat Flux Density at Station H for Test 258 (1000-lb N_2O_4/50% UDMH-50% N_2H_4)

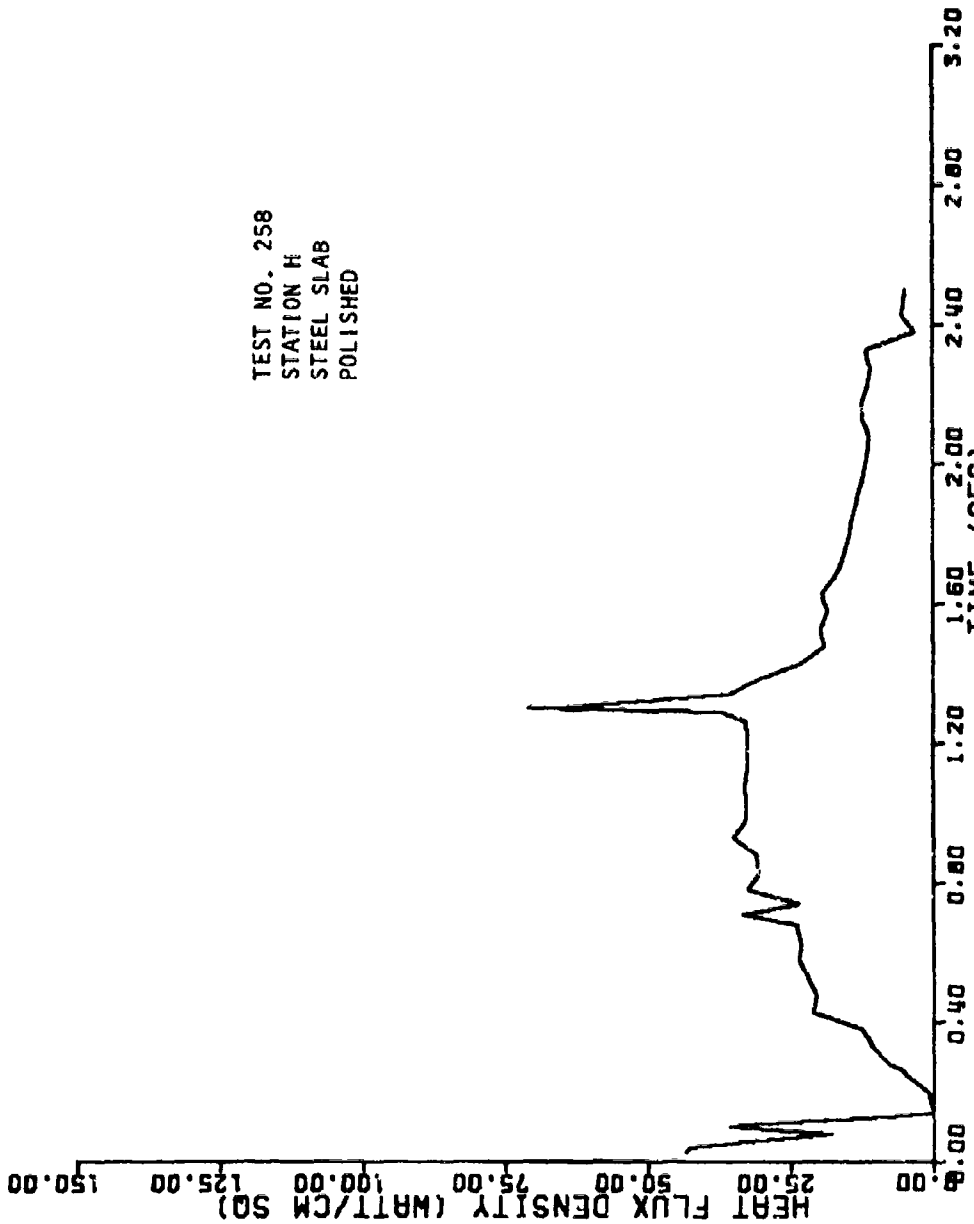

Figure B-112. Heat Flux Density at Station H for Test 258 (1000-lb N_2O_4/50% UDMH-50% N_2H_4)

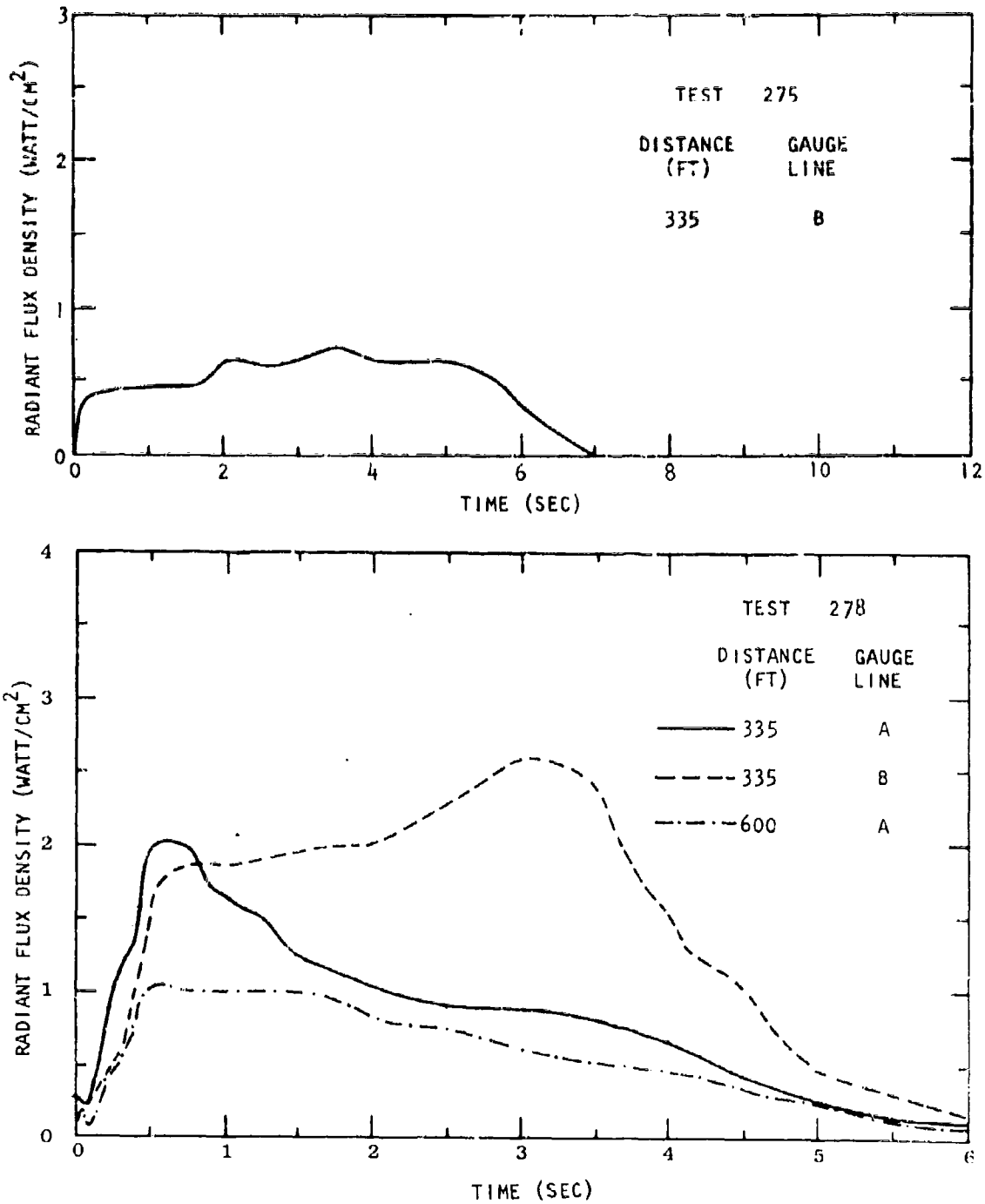

Fig. B-113. Radiant Flux Density Outside the Fireball from Tests 275 and 278 (25,000-lb LO_2/RP-1)

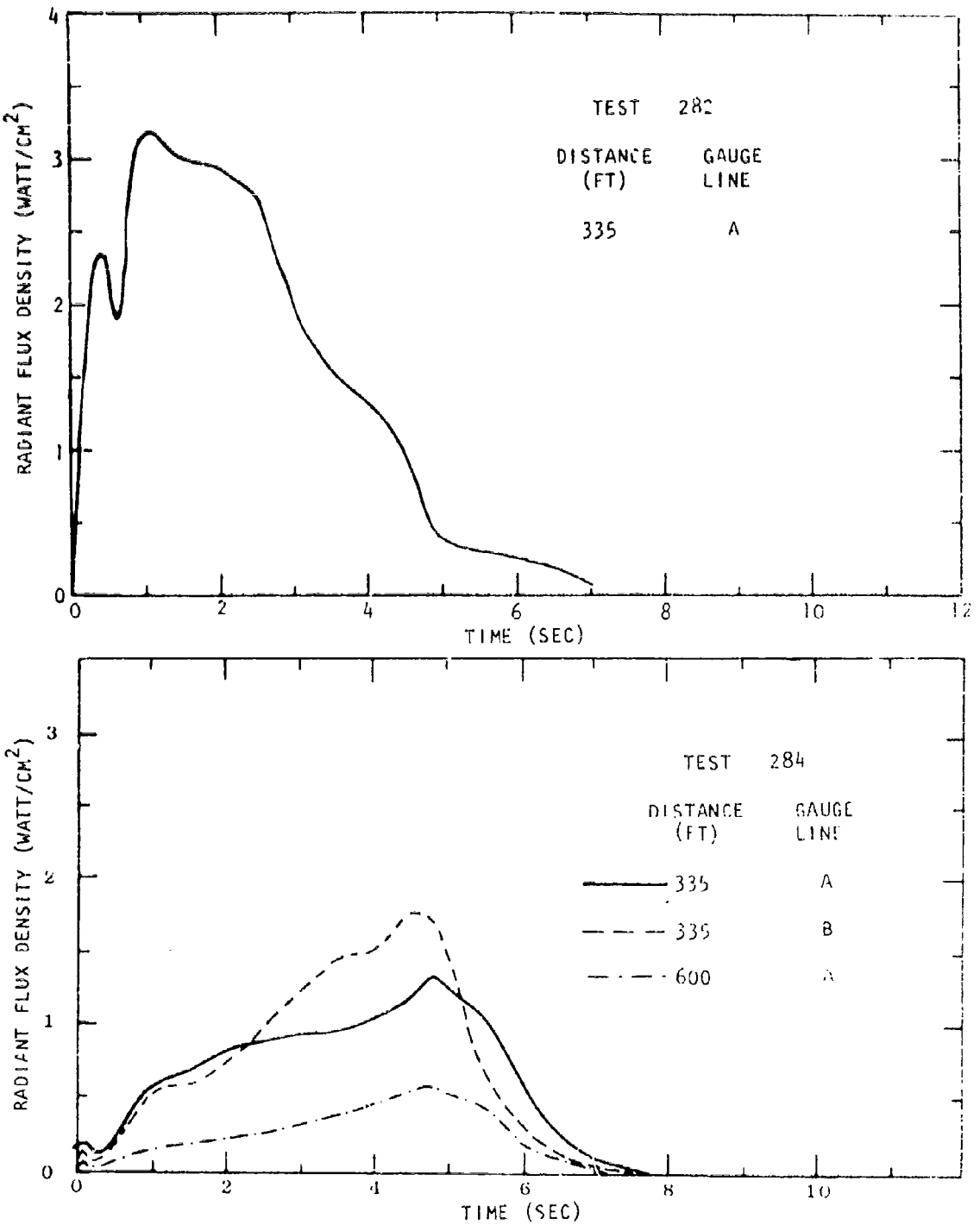

Fig. B-114. Radiant Flux Density Outside the Fireball from Tests 282 and 284 (25,000-lb LO_2/RP-1)

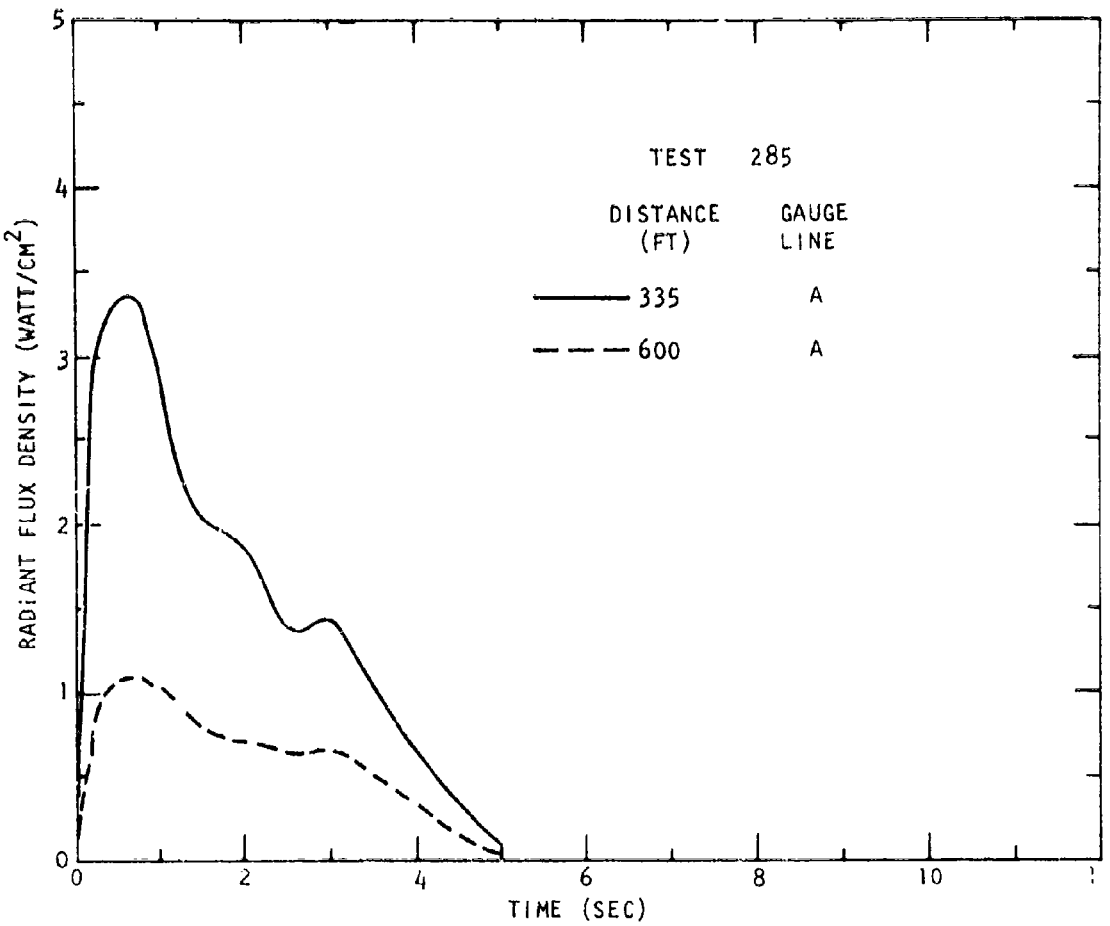

Fig. B-115. Radiant Flux Density Outside the Fireball from Test 285 (25,000-lb LO_2/RP-1)

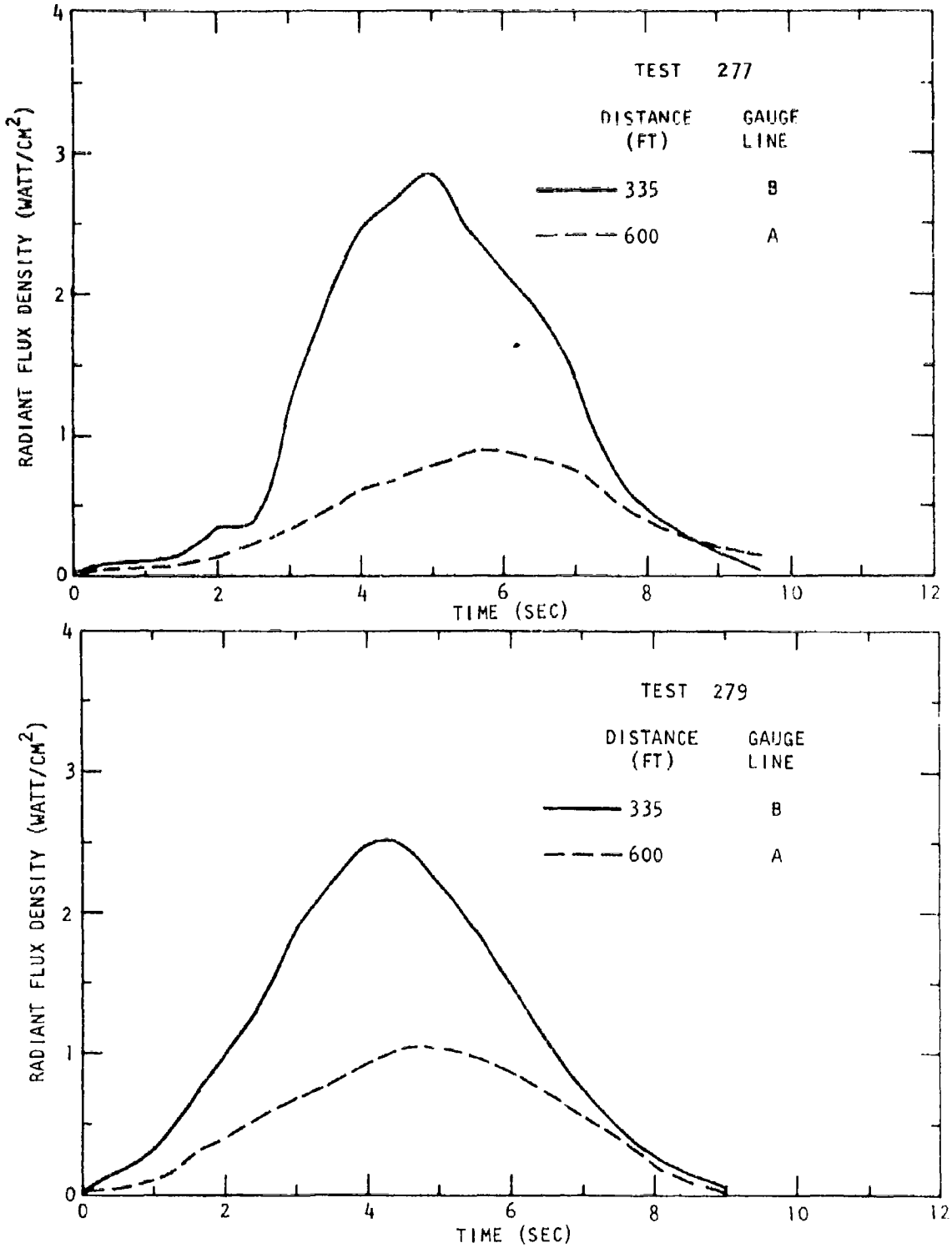

Fig. B-116. Radiant Flux Density Outside the Fireball from Tests 277 and 279 (25,000-lb LO_2/LH_2)

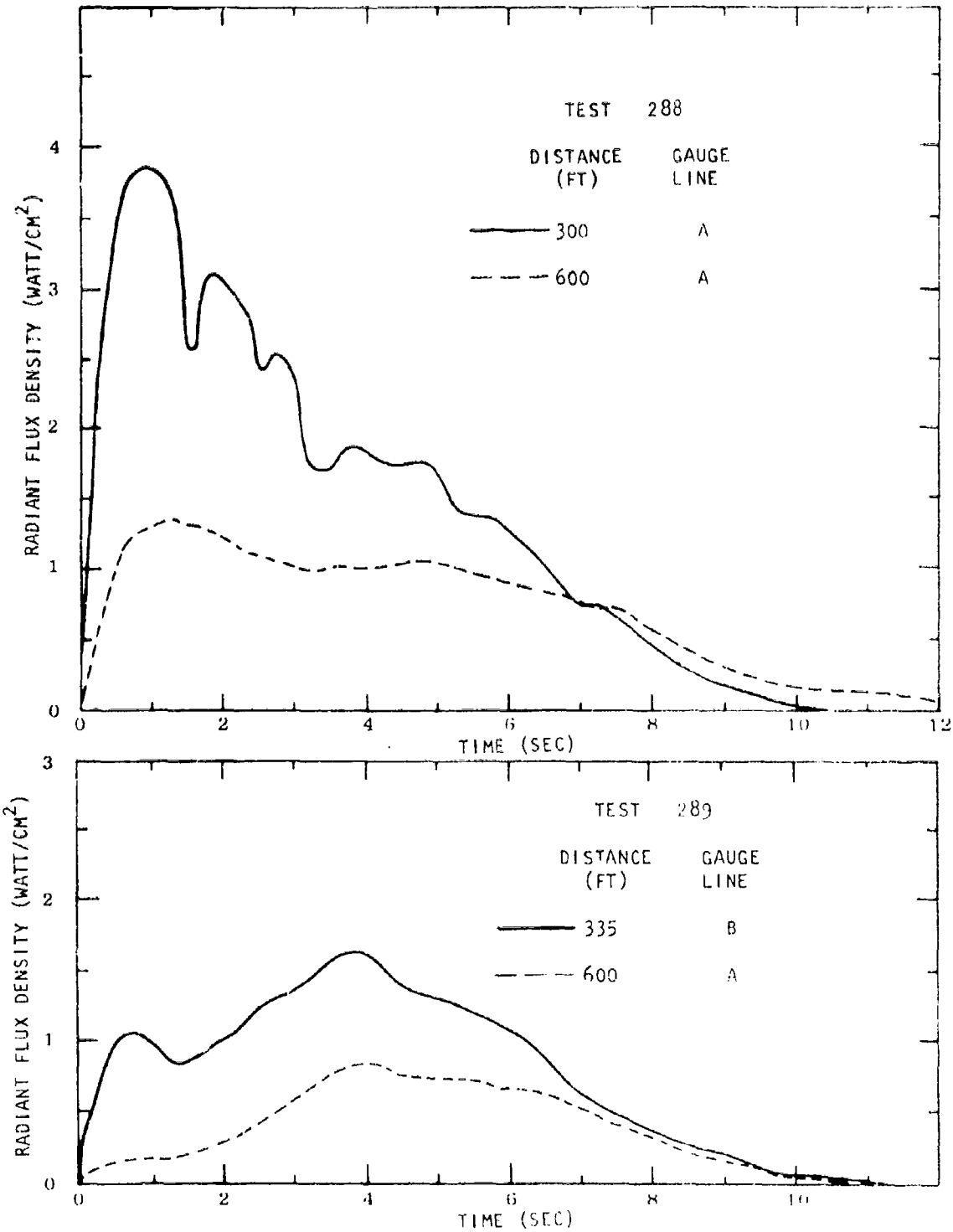

Fig. B-117. Radiant Flux Density Outside the Fireball From Tests 288 and 289 (25,000-lb LO_2/LH_2)

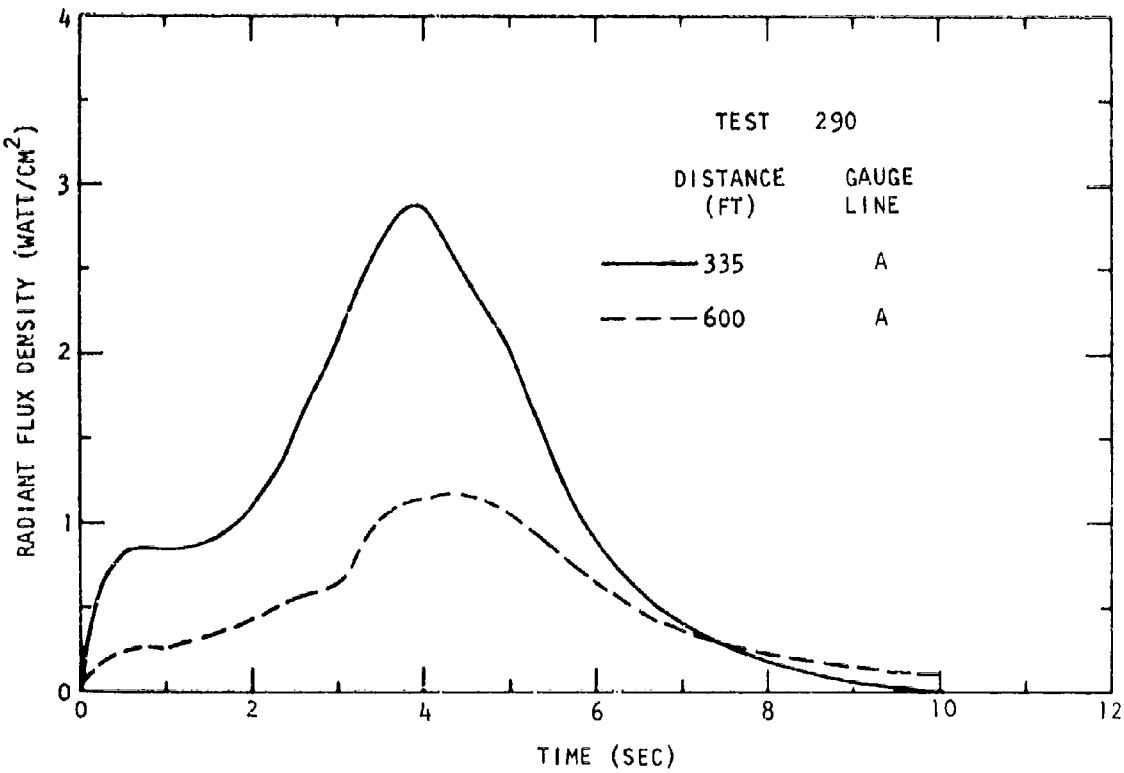

Fig. B-118. Radiant Flux Density Outside the Fireball from Test 290 (25,000-lb LO_2/LH_2)

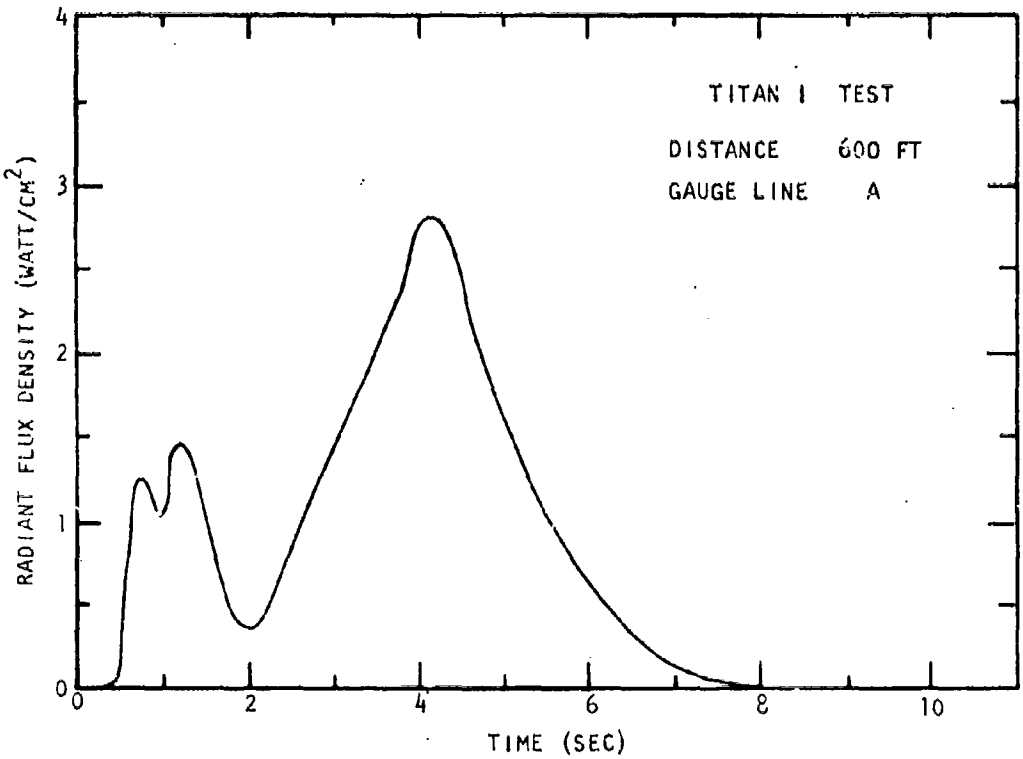

Fig. B-119. Radiant Flux Density Outside the Fireball from the Titan I Test

Appendix C
LIST OF SYMBOLS

Appendix C
LIST OF SYMBOLS

SYMBOL	DESCRIPTION	EXAMPLE UNIT
A	Area irradiated	cm^2
c	Specific heat	watt-sec/gm-°C
C	Psuedo-curvature; Eq. (A.5)	$°C/sec^2$
d	Data trace deflection	cm
D	Fireball diameter	feet
e	Sensitivity of radiometer; Eq. (A.8)	volt/-°C
e	Energy per unit time arriving on an elemental area	watt
e_1	Energy emitted per unit time per unit volume	$watt/cm^3$
e_Θ	Energy per unit time within angles Θ and $\Theta + d\Theta$	watt
E	Electromotive force generated per unit temperature rise	volts/°C
F	Data correction factor; Eq. (A.15)	unitless
G	Gain	unitless
k	Absorption coefficient	1/cm
K	Thermal conductivity	watt/cm-°C
K'	Constant in Eqs. (3.1), (A.1), and (A.4)	$watt\text{-}sec^{1/2}/cm^2\text{-}°C$
n	Index of refraction	unitless
q	Heat flux; energy per unit area per unit time	$watt/cm^2$
r	Distance variable in spherical coordinate system	cm
R	Radius of radiometer sensitive element	cm
t	Time	sec
T	Energy fraction transmitted; Eq. (A.13)	unitless
T_s	Surface temperature	°C
V	Electrical potential difference from center to edge of radiometer sensitive element	volts
V	Voltage applied to recording system per unit data trace deflection	volts/cm
V	Volume	cm^3
W	Propellant weight (fuel plus oxidizer)	lb

SYMBOL	DESCRIPTION	EXAMPLE UNIT
δ	Thickness of radiometer sensitive element	cm
Θ	Angular variable in spherical coordinate system	radian
θ	Incident angle	radian
θ'	Refracted angle	radian
κ	Thermal diffusivity	cm^2/sec
ρ	Density	gm/cm^3
τ	Time constant of radiometer	sec
τ	Fireball duration	sec
τ	Dummy variable in Eqs. (3.1) and (A.1)	sec
τ_o	Heating duration; Eq. (5.3)	sec
ϕ	Angular variable in spherical coordinate system	radian

UNCLASSIFIED
Security Classification

DOCUMENT CONTROL DATA - R & D

(Security classification of title, body of abstract and indexing annotation must be entered when the overall report is classified)

1. ORIGINATING ACTIVITY (Corporate author) URS Research Company 1811 Trousdale Drive Burlingame, California	2a. REPORT SECURITY CLASSIFICATION Unclassified 2b. GROUP

3. REPORT TITLE

HEAT TRANSFER HAZARDS OF LIQUID ROCKET PROPELLANT EXPLOSIONS

4. DESCRIPTIVE NOTES (Type of report and inclusive dates)
Final Report

5. AUTHOR(S) (First name, middle initial, last name)
Joseph A. Mansfield

6. REPORT DATE	7a. TOTAL NO. OF PAGES	7b. NO. OF REFS
February 1969	260	5

8a. CONTRACT OR GRANT NO.	9a. ORIGINATOR'S REPORT NUMBER(S)
F04611-69-C-0004 b. PROJECT NO.	706-5
c.	9b. OTHER REPORT NO(S) (Any other numbers that may be assigned this report) AFRPL TR-69-39
d.	

10. DISTRIBUTION STATEMENT

X [redacted]

11. SUPPLEMENTARY NOTES	12. SPONSORING MILITARY ACTIVITY
	AF Rocket Propulsion Laboratory Air Force Systems Command USAF, Edwards, California

13. ABSTRACT

An extensive experimental program, designated Project PYRO, was conducted in order to improve the definition of the hazards associated with liquid rocket propellant explosions. This report is a summary of the thermal or heat transfer measurements from this program. Tests were conducted with propellant quantities ranging from 200 to approximately 100,000 lb for the propellant combinations of LO_2/RP-1 and LO_2/LH_2, and up to 1000 lb for the hypergolic propellant combination of N_2O_4/50% UDMH-50% N_2H_4. From measurements within the fireball, data are given for the total (convective plus radiant) heat flux density, radiant flux density, and fireball temperature, and – from remote measurements – for the fireball temperature (photo-pyrometric) and radiant flux density. The total heat flux density was evaluated through computation from surface temperature vs time measurements of metal slabs; an error analysis of this technique is included. Curves representing conservative upper bounds of the total heat flux density vs time for a given propellant type and quantity are developed from the data. A recommended procedure for extrapolating these curves to comparatively large propellant quantities is given, along with the basis and limitations of extrapolation.

DD FORM 1 NOV 68 1473 REPLACES DD FORM 1473, 1 JAN 64, WHICH IS OBSOLETE FOR ARMY USE.

UNCLASSIFIED
Security Classification

14 KEY WORDS	LINK A		LINK B		LINK C	
	ROLE	WT	ROLE	WT	ROLE	WT
Project PYRO						
liquid rocket propellant explosions						
heat flux density						
radiant flux density						
fireball temperature						